Strange Hadron Production in Ag+Ag Collisions at 1.58A GeV

Dissertation

zur Erlangung des Doktorgrades

der Naturwissenschaften

vorgelegt beim Fachbereich Physik

der Johann Wolfgang Goethe-Universität

in Frankfurt am Main

von

Simon Spies

aus Wiesbaden

Frankfurt 2022

(D 30)

vom Fachbereich Physik der Johann Wolfgang Goethe-Universität als Dissertation angenommen.

Dekan:

Prof. Dr. Harald Appelshäuser

Gutachter:

Prof. Dr. Joachim Stroth

Prof. Dr. Christoph Blume

Datum der Disputation:

09.06.2022

Abstract

Back in the year 1808, Johann Wolfgang von Goethe described the primary aim of the academic Faust in his famous tragedy *"Faust. Der Tragödie erster Teil"* [97] with the monologue *"Dass ich erkenne, was die Welt im Innersten zusammenhält"* (freely translated: "That I may know, what holds the world together at it's innermost core"). In fact, the aim of nuclear physicists conducting fundamental researches is still the same.

In the year 1808, the atom model by John Dalton was published in which atoms are assumed to be the fundamental constituents of matter. Today we know that atoms consist of an electron shell and a nucleus which itself consists of nucleons, namely protons and neutrons, that further consist of quarks and gluons. At the moment, electrons as well as quarks and gluons are assumed to be fundamental particles since they show no evidence of a sub-structure. The reason for the formation of nucleons from quarks and also the formation of nuclei from nucleons is the strong interaction which is mediated by the gluons. Therefore, one can conclude that the strong interaction holds the world together at it's innermost core.

In modern physics, the strong interaction is investigated using large particle accelerators at facilities like CERN, BNL or GSI. The ions are accelerated to relativistic energies and then collided creating a system of matter at extreme temperature and density for a tiny fraction of a second. The particles emerging from this system are then measured in large detector systems like ALICE, STAR or HADES to deduce information on the strong processes occurring in the collision.

In this work Ag(1.58A GeV)+Ag collisions measured with the HADES detector in March 2019 are analyzed. The HADES experiment is specialized on the measurement of fixed-target collisions at few GeV energy. At these energies, the properties of the system created in the collision are comparable to the conditions expected in merging neutron stars. Therefore, the study of heavy-ion collisions at these energies allows to deduce information on the nuclear Equation of State (EoS) relevant for the stability of neutron stars.

The most abundant charged particle emerging from heavy-ion collisions at these energies are protons. Together with the neutrons they constitute the dominant part of the bulk matter and therefore provide a direct access to the properties of the created system at kinetic freeze-out. Another important aspect of these studies is the production of strange hadrons which are not present in the initial nuclei. At these energies even the lightest strange mesons, the kaons, and the lightest hyperons, the Λs, are produced close to their free NN threshold energy. Thus, their production is strongly correlated to effects connected to the surrounding matter. This applies in particular to double strange hyperons, the Ξs, which are produced far below their free NN threshold energy in such collisions. Their measurement allows to investigate whether medium effects are stronger for particles produced further below their free NN threshold. However, the Ξ hyperons have not been

measured in heavy-ion collisions at such low energies before. Finally, also hypernuclei like the ${}^{3}_{\Lambda}\mathrm{H}$, which is the lightest known, are of great interest as they combine effects concerning hyperons and bulk matter phenomena.

Due to the conservation of strangeness under the strong and the electromagnetic interaction, strange hadrons can decay to non-strange hadrons only via the weak interaction. This results in rather long mean lifetimes which lead to characteristic decay topologies. These can be utilized to identify weakly decaying particles. In this work, the identification procedure is enhance using an ANN in addition to the standard hard selection criteria. Acceptance and efficiency effects are corrected using particles simulated with the event generator Pluto, processed by HGeant and finally implemented in real events.

In this thesis, the emission of protons as well as the production of Λ hyperons, K^{0}_{S} mesons and ${}^{3}_{\Lambda}\mathrm{H}$ hypernuclei are analyzed multi-differentially as a function of transverse momentum, rapidity and centrality. Therefore, the 3.03 billion 30 % most central Ag(1.58A GeV)+Ag events recorded by HADES are used. Furthermore, the lifetimes of Λ hyperons, K^{0}_{S} mesons and ${}^{3}_{\Lambda}\mathrm{H}$ hypernuclei are measured. The obtained ${}^{3}_{\Lambda}\mathrm{H}$ lifetime of $(253 \pm 24 \pm 42)$ ps is compatible with the lifetime of free Λ hyperons, as predicted by theoretic calculations due to its low binding energy. Finally, also the double strange Ξ^{-} hyperons are reconstructed. Unfortunately, the fully optimized signals lie below the confidence threshold of 5σ, which is why both an production rate and an upper production limit are estimated using averaged acceptance and efficiency corrections. Never before, ${}^{3}_{\Lambda}\mathrm{H}$ or Ξ^{-} were successfully reconstructed and analyzed in heavy-ion collisions at such low energies. The obtained results are compared to previous measurements and put in context with world data form different energies and collision systems.

Kurzfassung

Im Jahr 1808 beschrieb Johann Wolfgang von Goethe das vorrangige Ziel des Gelehrten Faust in seiner berühmten Tragödie „Faust. Der Tragödie erster Teil“ [97] mit den Worten „Dass ich erkenne, was die Welt im Innersten zusammenhält“. Tatsächlich ist das Ziel heutiger kernphysikalischer Grundlagenforschung noch immer dasselbe.

Im Jahr 1808 wurde das Atommodel von John Dalton publiziert in welchem die Atome als elementare Bausteine von Materie angenommen werden. Heute wissen wir dass Atome in Wirklichkeit aus einer Elektronenhülle und dem Atomkern bestehen, welcher wiederum aus Nukleonen, genauer gesagt Protonen und Neutronen, besteht, die weiterhin aus Quarks und Gluonen aufgebaut sind. Nach aktuellem Forschungsstand sind die Elektronen sowie Quarks und Gluonen die elementaren Bausteine von Materie da diese bislang keine Anzeichen einer Sub-Struktur zeigen. Der Grund warum sich aus Quarks Nukleonen und aus Nukleonen Atomkerne bilden ist die starke Wechselwirkung, welche von den Gluonen vermittelt wird. Es lässt sich demnach schlussfolgern dass die starke Wechselwirkung die Welt im Innersten zusammenhält.

Die starke Wechselwirkung wird heutzutage an großen Beschleunigeranlagen wie zum Beispiel CERN, BNL oder GSI erforscht. Dort werden Ionen auf relativistische Energien beschleunigt und dann zur Kollision gebracht, wobei sich für einen winzigen Bruchteil einer Sekunde ein System bestehend aus Materie bei extrem hoher Dichte und Temperatur bildet. Die Teilchen die aus einem solchen System hervorgehen werden schließlich in großen Detektorsystemen wie zum Beispiel ALICE, STAR oder HADES gemessen, um Informationen über die starken Prozesse, die in der Kollision auftreten, abzuleiten.

In dieser Arbeit werden Ag(1.58A GeV)+Ag Kollisionen, die im März 2019 mit dem HADES Detektor gemessen wurden, analysiert. Das HADES Experiment ist auf die Messung von *fixed-Target* Kollisionen bei Energien von wenigen GeV spezialisiert. Bei diesen Energien sind die Eigenschaften der entstehenden Systeme vergleichbar mit denen die in kollidierenden Neutronensternen vermutet werden. Aus diesem Grund lassen sich anhand von Schwerionenkollisionen bei diesen Energien Informationen über die nukleare Zustandsgleichung, die die Stabilität von Neutronensternen beeinflusst, gewinnen.

Das häufigste geladene Teilchen welches bei diesen Energien aus Schwerionenkollisionen hervorgeht ist das Proton. Gemeinsam mit den Neutronen bilden sie den größten Anteil an Materie und erlauben daher den Zustand des Systems zum Zeitpunkt des kinetischen Ausfrierens direkt zu messen. Ein weiteres wichtiges Forschungsgebiet ist die Entstehung von „seltsamen“ Hadronen welche in den kollidierenden Kernen nicht vorkommen. Bei diesen Energien werden selbst die leichtesten „seltsamen“ Mesonen, die Kaonen, und die leichtesten Hyperonen, die Λs, nahe ihrer Schwellenenergie für isolierte NN Kollisionen produziert. Aus diesem Grund wird ihre Produktion besonders stark von der umgebenden Materie beeinflusst. Dies gilt umso mehr für die doppelt „seltsamen“ Hyperonen, die Ξs, welche in derartigen Kollisionen weit unterhalb ihrer Schwellenenergie für isolierte NN

Kollisionen produziert werden. Ihre Messung erlaubt Rückschlüsse auf den Zusammenhang zwischen Schwellenenergie und der Relevanz von Mediumeffekten zu ziehen. Leider wurden Ξ Hyperonen bisher noch nie in Schwerionenkollisionen bei derart niedrigen Energien gemessen. Schlussendlich kommt auch den Hyperkenen wie zum Beispiel dem ${}^{3}_{\Lambda}\mathrm{H}$, welches der leichteste Bekannte ist, eine große Bedeutung zu, da diese Effekte in Bezug auf Hyperonen und reguläre Baryonen vereinen.

Aufgrund der Erhaltung der Seltsamkeitsquantenzahl durch die starke und elektromagnetische Wechselwirkung können „seltsame“ Hadronen nur durch die schwache Wechselwirkung in „nicht-seltsame“ zerfallen. Dies führt zu verhältnismäßig hohen Lebensdauern und charakteristischen Zerfallstopologien. Diese können benutzt werden um schwach zerfallende Teilchen zu identifizieren. In dieser Arbeit wird das Verfahren durch die Verwendung eines künstlichen neuronalen Netzwerks unterstützt. Akzeptanz- und Effizienzverluste werden mithilfe von simulierten Teilchen des Eventgenerators Pluto, die von HGeant verarbeitet und in reale *Events* implementiert werden, korrigiert.

In dieser Arbeit werden die Emission von Protonen sowie die Produktion von Λ Hyperonen, $\mathrm{K}^{0}_{\mathrm{S}}$ Mesonen und ${}^{3}_{\Lambda}\mathrm{H}$ Hyperkernen multi-differentiell in Abhängigkeit von Transversalimpuls, Rapidität und Zentralität analysiert. Hierzu werden die 3,03 Milliarden 30 % zentralsten Ag(1.58A GeV)+Ag Kollisionen, die von HADES aufgezeichnet wurden, verwendet. Zusätzlich werden die Lebensdauern von Λ Hyperonen, $\mathrm{K}^{0}_{\mathrm{S}}$ Mesonen und ${}^{3}_{\Lambda}\mathrm{H}$ Hyperkernen gemessen. Die gemessene ${}^{3}_{\Lambda}\mathrm{H}$ Lebensdauer von $(253 \pm 24 \pm 42)$ ps ist kompatibel mit der Lebensdauer freier Λ Hyperonen wie es von theoretischen Berechnungen aufgrund der niedrigen Bindungsenergie erwartet wird. Darüber hinaus werden auch die doppelt „seltsamen“ Ξ^{-} Hyperonen rekonstruiert. Leider liegt das vollständig optimierte Signal immernoch unterhalb der Schwelle von 5σ weshalb sowohl die Produktionsrate als auch ein oberes Produktionslimit mithilfe gemittelter Akzeptanz- und Effizienzkorrekturen bestimmt werden. Dies ist das erste Mal dass ${}^{3}_{\Lambda}\mathrm{H}$ und Ξ^{-} erfolgreich in Schwerionenkollisionen bei derart niedrigen Energien rekonstruiert und analysiert werden. Alle Ergebnisse werden letztendlich mit vorherigen Messungen sowie dem weltweiten Datensatz, bestehend aus unterschiedlichsten Energien und Kollisionssystemen, verglichen.

Contents

1. Introduction

1.1. The Standard Model of Nuclear Physics

In the year 1961, M. Gell-Mann proposed the so-called eightfold-way to order the vast amount of new particles discovered at this time [94]. Three years later he and G. Zweig independently extended this theory by the proposal that all hadrons are built from three types of quarks which were not yet discovered [95, 183]. Although these approaches were revised and extended several times since then, they still form the base of what is called today the standard model of nuclear physics.

Currently, the standard model includes three fundamental interactions, the strong, the electromagnetic and the weak one each having its own fundamental gauge-bosons mediating the interaction, namely the gluons, the photons and the Z- and W-bosons respectively. The fourth known fundamental interaction, the gravitation, is not included in the standard model. For each interaction only particles carrying the according charge can couple to the corresponding gauge-bosons and thereby interact. The charge of the strong interaction is called color charge and the charge of the electromagnetic interaction is the electric charge. Within the electro-weak unification theory the electromagnetic and weak interaction are combined in the electro-weak interaction.

Besides the fundamental interactions and their gauge-bosons, the standard model includes six fermions carrying one out of three color charges, the quarks, and six color-neutral fermions, the leptons. Both quarks and leptons are grouped in three families by increasing mass and their electric charge. Table 1.1 lists the fermions included in the standard model and their charges. The most recent addition to the standard model happened in 2012 when the discovery of the Higgs-Boson was announced by the ATLAS (A Toroidal LHC ApparatuS) [1, 2] and the Compact Muon Solenoid (CMS) [77, 78] collaborations. In the scope of the quantum field theory it can be understood as an excitation of the Higgs-field which is responsible for the generation of the rest masses of all fundamental particles.

A very active research area of modern nuclear physics is the search for physics beyond the standard model like for example particles not yet included. The goal is to either disprove or to extend the standard model and thereby solve open questions concerning yet unexplained observations like the cosmologic dark matter and dark energy problem [82]. The ultimate goal from the theory side is to unify the electro-weak and the strong interaction and to integrate the gravitational interaction described by the general theory of relativity. The thereby obtained grand-unification theory would describe all four known fundamental interactions at once. However, nuclear physics itself is still a very active research field focused on studying the strong interaction in more detail to shed light on processes that cannot be described by calculations based on first principles, yet. Strongly interacting baryon-rich matter as studied in this thesis is an example for such processes. Therefore, in the following section the strong interaction is described in more detail.

Class	**Families** 1st	2nd	3rd	**Color Charge**	**Electric Charge**
Quarks	up (u)	charm (c)	top (t)	Yes	2/3 e
	down (d)	strange (s)	bottom (b)		–1/3 e
Leptons	Electron (e^-)	Muon (μ^-)	Tau (τ^-)	No	–1 e
	Electron-Neutrino (ν_e)	Muon-Neutrino (ν_μ)	Tau-Neutrino (ν_τ)		0

Table 1.1.: Overview of the fermions in the standard model of nuclear physics [169, 184].

1.2. The Strong Interaction

In the year 1973, H. Fritzsch, M. Gell-Mann and H. Leutwyler proposed a theory to describe the observed effects of the strong interaction [90] which is called Quantum Chromo Dynamics (QCD) today. The theory was developed in close analogy to the established Quantum Electro Dynamics (QED) theory which describes electromagnetic interactions between electrically charged particles by the exchange of virtual photons. Analogous, in the QCD theory the strong interaction between particles carrying color charge is described by the exchange of gluons. The color charge is defined in analogy to the additive color model with the colors black and white corresponding to a neutral charge and the eligible charge states being three colors that add up to white like red, green and blue.

The fundamental difference between the QED and QCD theory is that in contrast to the photons which are electrically neutral, the gluons themself carry a color and an anti-color charge. Therefore, not only the quarks interact strongly but also the gluons mediating the interaction interact between each other via further gluons. If one attempts to separate two bound quarks, the gluon field between them, also called flux-tube or string, increases due to further gluon-gluon interactions. Once enough energy is stored in the flux-tube, it breaks creating a new quark-antiquark-pair resulting in two independent bound systems. For this reason at larger scales than a few fermi only color neutral objects like baryons (three quarks) or mesons (quark and anti-quark) can exist which is called confinement of quarks. Another consequence is that the strong interaction is not observed at macroscopic scales unlike the electromagnetic or the gravitational interaction. If one reverses the situation and compresses bound quarks, the flux-tube between them decreases and the strong binding ceases. At some point, the quarks can be assumed to move freely within the compressed system which is called asymptotic freedom.

$$\Delta x \Delta p \geq \hbar \tag{1.1}$$

According to Heisenberg's uncertainty principle 1.1, increasing quark distances correspond to decreasing momentum transfer in their interaction and decreasing quark distances correspond to increasing momentum transfer. Therefore, confinement is not only observed at low quark densities but also at low temperatures and asymptotic freedom is not only observed at high quark densities but also at high temperatures.

1.2.1. Theoretical Description

In the theoretical description of interactions the exchange of gauge-bosons is quantified by a factor proportionally influencing the interaction cross-sections called the coupling constant. The coupling constant of the electromagnetic interaction α, also called fine-structure constant, is almost independent from the amount of momentum transferred in the interaction and rises only at very small distances. The gluon-gluon interactions however result in a strong dependence between the coupling constant of the strong interaction α_S and the amount of momentum transferred in the interaction. Therefore, it is also called running coupling constant.

At high momentum transfers or low distances, where α_S is small, strongly interacting particles can be described using perturbative approaches neglecting higher order interaction terms. At low momentum transfers or large distances however these higher order terms contribute significantly to the interaction due to the increase of α_S. An approach to calculate strong interactions in this regime is called lattice-QCD [83]. In this approach the interactions are solved numerically on a finite discrete space-time-grid with quarks positioned at the crossings and gluons connecting them. The obtained results are then extrapolated to a hypothetical infinite space-time-grid which corresponds to the situation in nature. At the moment lattice-QCD calculations are mostly restricted to systems with vanishing or small net-baryon-densities due to the fermion sign problem arising at finite baryochemical potentials. Therefore, strongly interacting baryon-rich matter mostly needs to be described by effective approaches.

1.2.2. Phenomenology of Hadrons

Hadrons are usually observed in two configurations: Baryons which consist of three quarks and mesons which consist of a quark and an anti-quark. Also further configurations like for example penta-quarks consisting of four quarks and an anti-quark are feasible, however, the existence of hadrons consisting of four or more quarks is not yet finally proven. Although under normal conditions quarks cannot exist unbound, their bare rest masses have been extracted from their influence on hadron properties. For the two lightest quark flavors up and down bare rest masses of $\lesssim 5$ MeV/c^2 are found [184]. The lightest baryon, the proton, however has a rest mass of ≈ 938 MeV/c^2 which is about a factor 100 higher than the sum of the rest masses of its constituents. This strong difference between bound and unbound quark masses can be interpreted in two pictures described in the following:

Phenomenologically motivated interpretation: From scattering experiments it is known that the charge distribution of a nucleon has a size of about one fermi. Due to Heisenberg's uncertainty principle 1.1 restricting the positions of quarks to the size of a hadron rises their momenta to the order of few hundred MeV/c. According to Equation 1.2 discovered by A. Einstein these momenta relate to energies and thereby mass. In that sense, the large hadron masses can be understood as a result of confining the quarks inside the volume of a hadron.

$$E = \sqrt{p^2c^2 + m_0^2c^4} \tag{1.2}$$

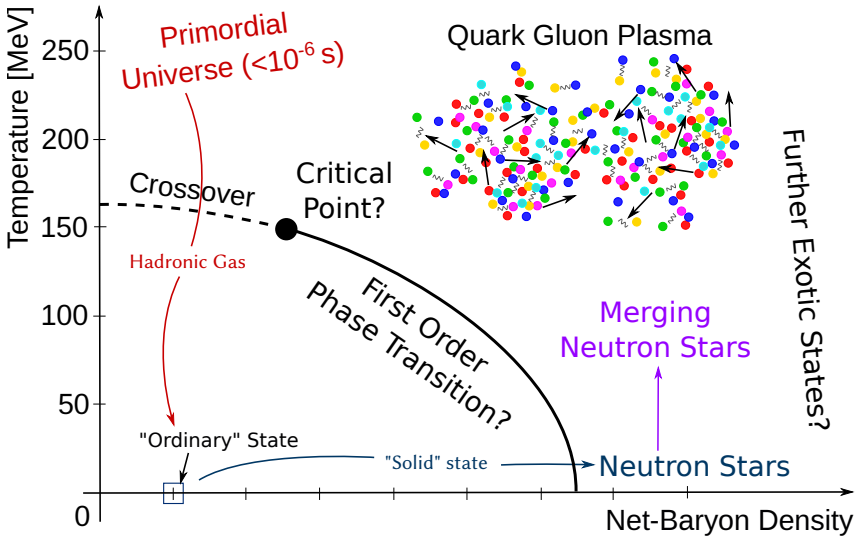

Figure 1.1.: Schematic phase diagram of strongly interacting QCD matter with the net-baryon density on the x-axis and the temperature on the y-axis. Original depiction from [130].

Experimentally motivated interpretation: In deep inelastic scattering experiments it was found that hadrons contain more quarks than initially assumed. Besides the quarks defining the quantum numbers of a hadron which are called valence-quarks, hadrons also contain virtual quark-antiquark-pairs dynamically created in the gluon fields between the valence-quarks which are called sea-quarks. In that sense the large hadron masses can be understood as a result of the large amount of energy stored in the dynamically created sea-quarks as well as the gluons inside a hadron.

Unfortunately, up to now there is no theory which completely describes the dynamically generated masses for all hadrons. One particular open question concerns the masses of mesons: While the lightest mesons, the pions, have masses around 140 MeV/c^2, the second lightest mesons are more then three times as heavy with masses around 500 MeV/c^2 although free strange quarks are associated with a mass of only $\approx$ 93 MeV/c^2 [184]. Also the chiral partners of the pions, the σs, have masses around 500 MeV/c^2. This breaking of the chiral symmetry is described in the QCD theory by a different coupling to the virtual quark-antiquark condensates filling the QCD vacuum. It is assumed that in a hot or dense medium in which the quarks approach asymptotic freedom the condensates melt, the chiral symmetry is restored and chiral partners have the same spectral distribution.

1.2.3. Phases of Strongly Interacting Matter

If matter is heated up such that molecular, atomic and nuclear binding effects can be neglected, it can be described as a gas of hadrons in which the quarks are confined. As already mentioned before, if the temperature or quark density is increased much further, the confinement of the quarks ceases due to the effect of asymptotic freedom. In this state, which is called Quark Gluon Plasma (QGP), the quarks are still strongly coupled but can move freely in the entire medium. The transition from the hadron gas into the QGP state can be described as a transition between thermodynamic phases. The corresponding phase diagram is shown in Figure 1.1 in a schematic way with the net-baryon density on the x-axis and the temperature on the y-axis. The net-baryon density can also be replaced by the baryochemical potential since they are strongly correlated.

Lattice-QCD calculations predict at vanishing baryochemical potentials a transition from the hadron gas to the QGP phase as well as a restoration of the chiral symmetry at temperatures around 160 MeV [66, 117]. The transition happens continuously and is therefore a crossover transition. Predictions suggest that at higher baryochemical potentials the transition becomes a higher order phase transition which implies the existence of a critical point somewhere in between [58, 102, 117, 159]. Unfortunately, lattice-QCD calculations for non-zero baryochemical potentials are still challenging. However, thanks to recent developments, the existence of a critical point in the region of temperatures larger than 135 MeV and baryochemical potentials lower than 270 MeV is highly unlikely [154]. Due to the limited theoretical predictions, the region of intermediate to high baryochemical potentials is primarily explored from the experimental side. One very promising physics program to determine the position of the critical point in the QCD phase diagram is the beam energy scan conducted by the STAR (Solenoidal Tracker At RHIC) [104] collaboration [38]. The region of highest baryochemical potentials and vanishing temperatures is not reachable through heavy-ion collisions and therefore only sparsely explored. It can only be described with effective approaches with further exotic states of matter like for example a color superconductor or a quarkyonic phase being feasible.

1.2.4. Exotic Matter in the Universe

The conditions required for QCD matter to form exotic states are barely reached anywhere in our universe. The hottest natural material on earth is found in its innermost core, but its temperature corresponds to "only" ≈ 0.5 eV. Even the temperature at the hottest place in our entire solar system, which is the center of our sun, corresponds to "only" ≈ 1.3 keV and is therefore still considered "cold" with respect to the QCD phase diagram. Also the high macroscopic densities of matter at these places are irrelevant since they result from a compression of the volumes normally taken up by the electron shells rather than a compression of the nucleons themselves.

There are only two types of objects in our universe where matter in exotic QCD phases is expected: black holes and neutron stars. Both of them are remnants of heavy stars that burned up their entire fuel and therefore collapsed due to the gravitational force to extremely dense objects. While neutron stars are stabilized against further compression by the fermi pressure as a result of the Pauli principle, black holes collapse into a point-like singularity and therefore develop an event horizon. Since it is impossible to gather any information from beyond the event horizon, details about the conditions inside a black hole are an unsolved mystery. Neutron stars on the other hand do not develop an event horizon and can therefore be studied using telescopes.

The matter inside a neutron star is still considered "cold" with respect to the QCD phase diagram. However, due to the extreme gravitational compression, the volumes normally taken up by the electron shells completely vanish and the density of the nucleons packed in the nuclear cores is increased. Recent astrophysical observations in combination with theoretical models conjecture that the high nuclear densities result in the formation of exotic quark matter in the cores of neutron stars [47]. Recently, the collision of two neutron stars in a so called neutron star merger event is also in the focus of nuclear physics. Simulations of such merger events show that in the collision parts of the neutron

star matter are heated up to temperatures of $\approx$ 50 MeV [136]. As it will be discussed in the following Section 1.3, matter under similar conditions can be produced and studied in the laboratory using heavy-ion collisions. In our universe an asymmetry between matter and anti-matter is observed and systems with vanishing baryochemical potential do not exist. However, it is assumed that shortly after the big bang, quarks and anti-quarks were produced symmetrically in pairs. As the universe expanded, the temperature decreased and the matter condensed from the QGP phase forming the very first hadrons. The corresponding high temperature low baryochemical potential region of the QCD phase diagram can be studied on earth using heavy-ion collisions, which will be discussed in more detail in the following Section 1.3.

1.3. Heavy-Ion Collisions

Heavy-Ion Collisions (HICs) are the only possibility to create and study QCD matter under extreme conditions in the laboratory. In the collision of heavy-ions accelerated to relativistic energies the nucleons are compressed and heated up creating a system of high temperature and density for a few fm/c ($\approx 10^{-23}$ s) until it expands again. Due to the short lifespan of the system its properties are only indirectly accessible in most studies using the measurements of particles emerging from the system in combination with effective models.

The temperature and the baryochemical potential of the created system strongly depend on the kinetic energy of the incident ions. At the highest energies of few TeV per nucleon like provided by the Large Hadron Collider (LHC) at the European Organization for Nuclear Research (CERN), the ions are almost translucent and the nucleons are barely decelerated during the collision [84]. The particles emerging from such collisions are created from energy as matter-antimatter-pairs with high momenta. Therefore, the system is characterized by a vanishing baryochemical potential and high temperatures. In contrast to that, at energies of few GeV per nucleon like provided by the SIS18 accelerator at GSI, the ions are strongly decelerated in the collision and the nucleons participate in the created system [155]. Most particles emerging from such collisions are or consist of nucleons from the colliding nuclei. Therefore, the system is characterized by a high baryochemical potential and moderate temperatures. At the moment, the vanishing temperature part of the QCD phase diagram cannot be explored by heavy-ion collisions, since the matter is always heated up to non-negligible temperatures there.

The time evolution of a Ag(1.58A GeV)+Ag collision with an impact parameter of 3 fm simulated with the UrQMD transport model [59, 69] is schematically depicted in Figure 1.2. The four sub-figures can be roughly associated with the following phases of the collision:

Pre-Collision Phase: Initially, the two Lorentz-contracted nuclei approach each other in their common Center of Mass (CM) system. All nucleons from a nucleus carry approximately the same proportion of the total momentum, however, not exactly due to their fermi-momenta.

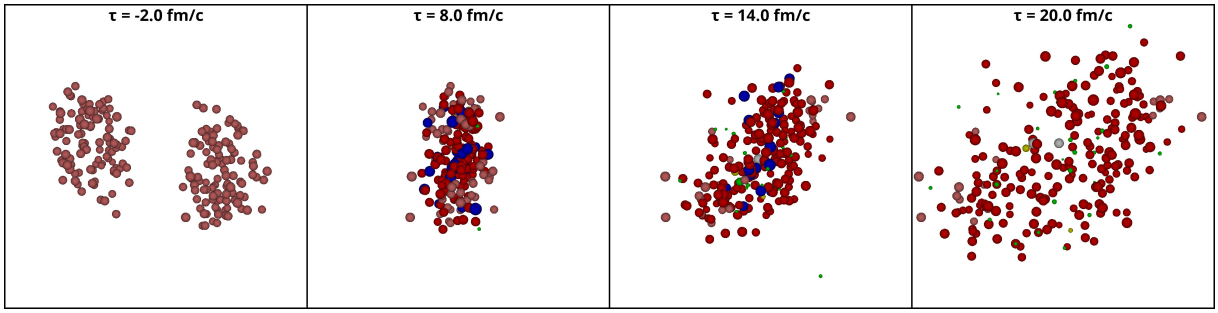

Figure 1.2.: Schematic depiction of the time evolution of a Ag(1.58A GeV)+Ag collision with an impact parameter of 3 fm simulated with UrQMD [59, 69]. The depictions show the particles in the CM system of the colliding nuclei. Nucleons that have not interacted (spectators) are depicted light red and those that interacted (participants) are depicted dark red. Nuclear resonances are depicted blue, hyperons white, strange mesons yellow and all other mesons green. The nucleon diameters correspond to their average inelastic strong interaction length and the remaining particles are scaled according to their masses. The depictions are generated by the UrQMD viewer developed by P. Klaus in [121].

High-Density Phase: In this simulation, about 8 fm/c after the first interactions between the nuclei took place, a high nuclear density in the reaction zone is reached. As the nucleons are strongly decelerated by nucleon-nucleon reactions, they remain in the reaction zone and contribute to the high density system which is also called fireball. As it was explained before there are multiple scenarios on what happens inside this fireball: For example, the matter might experience a phase transition to the QGP or another exotic phase [167]. Furthermore, the spectral functions of hadrons inside the fireball are expected to be modified due to coupling to the medium and the chiral symmetry is restored to some extend due to melting of the quark-antiquark condensates [55, 57, 64]. Besides that, the high-density phase also comprises the highest rate of nucleon-nucleon interactions. Only if a sufficient amount of nucleon-nucleon interactions take place over the short lifespan of the system, it can be assumed to approach a thermal equilibrium. As it will be shown later on, many measurements are "well" described by a thermal ansatz which suggests the conclusion that a thermal equilibrium is (almost) achieved.

Expansion Phase: Immediately after the fireball reaches its maximum density, it starts to expand due to the high pressure gradient between its center and the surrounding matter resulting in a decrease of both temperature and density. In non-central heavy-ion collisions, the expansion is not azimuthally symmetric and depends on the orientation of the reaction plane (cf. Section 1.3.4) [19, 21, 22]. The azimuthal asymmetry with respect to the reaction plane is called flow and parametrized using Fourier coefficients. The first three coefficients are called directed flow v_1, elliptic flow v_2 and triangular flow v_3. Additionally, also an anisotropy between the longitudinal and the transverse expansion is observed as a result of the nucleons being not fully stopped in the collision. This effect is also visible in Figure 1.2. In Section 1.4 different approaches to describe the expansion profile of the fireball are discussed.

Post-Freeze-Out Phase: At some point, the expansion has progressed so far that inelastic particle-particle interactions cease due to increasing mean nucleon distances. Except for resonance decays, the chemical composition of the particles remains unchanged with respect to the strong interaction. Though it can still change due to electromagnetic and weak decays, this point in time is called chemical freeze-out. At a later point also the elastic particle-particle interactions cease. After this point, which is called kinetic freeze-out, the momenta of the particles remain unchanged again with the exception of electromagnetic and weak decays. The two freeze-out points are very important in the study of heavy-ion collisions, since they represent in most analyses the chemical and kinetic state of the particles as they are finally measured in the detectors.

1.3.1. HIC Experiments and the QCD Phase Diagram

The baryochemical potential and the temperature are collective thermodynamic properties to describe the macroscopic state of a medium and can therefore not be measured directly. While the temperature at the kinetic freeze-out can be obtained from the kinetic distributions of the measured particles using the functions described in Section 1.4, the baryochemical potential can be obtained for the chemical freeze-out using a Statistical Hadronization Model (SHM) [72]. In this model the multiplicities of particles emerging from the fireball are described by Equation 1.3. In this equation i indexes the various particle species with multiplicities M_i, the degeneracy factors g_i, the energy E_i and the baryon numbers B_i. V represents the volume of the fireball, μ_B its baryochemical potential and T its temperature. As it will be described in the following Section 1.3.2, at low collision energies the additional canonic suppression factor F_{Si} is required to describe the production rates of strange hadrons. Furthermore, as the particle multiplicities are measured in the detectors, any feeddown effects from electromagnetic and weak decays occurring after the chemical freeze-out need to be considered, too.

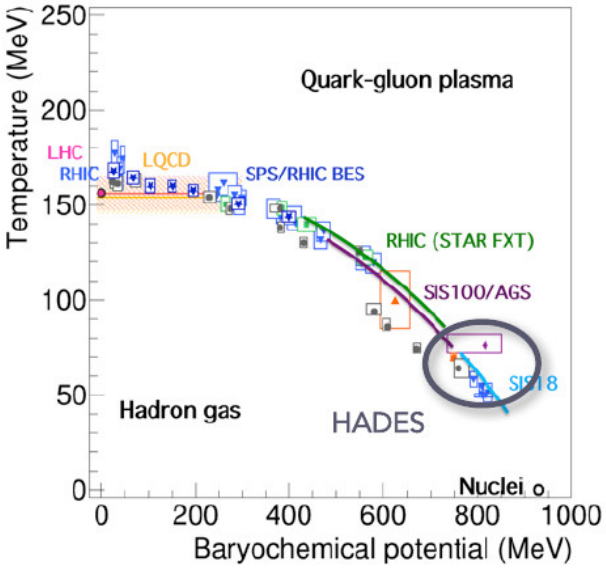

Figure 1.3.: Depiction of the chemical freeze-out points measured by various experiments in the baryochemical potential temperature plane. The data are taken from [23, 36, 45, 46, 60, 81, 128] and the depiction was created by T. Galatyuk.

$$M_i = g_i V \int \frac{d^3p}{(2\pi)^3} \exp\left(-\frac{E_i - B_i\mu_B}{T}\right) (\times F_{Si})\,. \tag{1.3}$$

Using a χ^2 minimization, the baryochemical potential and temperature which describe the measured multiplicities best are determined. As it is shown in multiple publications,

a reasonable description of all multiplicities can be achieved from low SIS18 energies to high LHC energies [36, 45, 81, 173]. The thereby obtained chemical freeze-out points are depicted in Figure 1.3 in the baryochemical potential temperature plane. Furthermore, the plot shows the region with available lattice-QCD calculations as well as the regions covered by future physics programs and accelerator facilities. HADES is measuring at the highest baryochemical potentials currently available. The recently conducted beam energy scan by the STAR collaboration connects this region to the highest available energies. Therefore, almost the entire range is nowadays explored by current heavy-ion collision experiments.

Figure 1.3 also shows that all measured chemical freeze-out points from lowest to highest energies align on a common trajectory. This hints at a global freeze-out criterion valid from lowest to highest energies. One commonly discussed global freeze-out criterion candidate is the average energy per particle $\langle E \rangle / \langle N \rangle$. Assuming the chemical freeze-out to occur as soon as $\langle E \rangle / \langle N \rangle$ drops below ≈ 1 GeV in the SHM reproduces the measured chemical freeze-out points with fair agreement [81]. Alternative freeze-out criteria are discussed in this reference as well.

1.3.2. Strangeness Production at SIS18 Energies

All particles emerging from a heavy-ion collision at SIS18 are either nucleons from the colliding ions, recombinations of the quarks contained in them or newly produced particles like for example pions. The production of new particles is possible since according to A. Einstein mass and energy are equivalent and can be converted into each other according to Equation 1.2. However, sufficient energy to produce the rest masses of the new particles has to be available. In the microscopic transport picture a heavy-ion collision is described by a superposition of multiple Nucleon-Nucleon (NN) collisions. One commonly used measure for the energy available to produce new particles is the energy available in the collision of a projectile with a target nucleon $\sqrt{s_{\mathrm{NN}}}$. In a fixed-target collision it is defined by Equation 1.4. In a relativistic heavy-ion collision the rest masses of the projectile m_p and the target m_t are both the nucleon rest mass and the projectile energy E_p is the total energy of a projectile nucleon with the kinetic energy E_{beam}. The result has to be understood as only an approximate since many body effects like for example fermi momenta are ignored.

$$\sqrt{s} = \sqrt{m_p^2 c^4 + m_t^2 c^4 + 2 E_p m_t c^2} \tag{1.4}$$

In an isolated collision a specific reaction channel is only possible if $\sqrt{s}$ exceeds the sum of rest masses of the particles in the output channel. This sum is therefore called the energetic threshold $\sqrt{s_{\mathrm{thres}}}$ of the reaction. In a heavy-ion collision however, individual NN collisions are not isolated due to collective effects. Remaining with the assumption that a heavy-ion collision is properly described by a series of NN collisions, in a first NN collision a nuclear resonance R could be created. In a following RN reaction, $\sqrt{s}$ could exceed $\sqrt{s_{\mathrm{NN}}}$ due to the higher mass of the resonance. Furthermore, also by elastic NN collisions, the kinetic energy of a single nucleon can be increased resulting in an increased $\sqrt{s_{\mathrm{NN}}}$ in subsequent collisions. Therefore, in a heavy-ion collision also reaction channels with $\sqrt{s_{\mathrm{thres}}} > \sqrt{s_{\mathrm{NN}}}$ are possible and called “sub-threshold” in the following.

At SIS18 collision energies strange hadrons are extraordinary important, since strangeness is the only quark flavor that is generated entirely as particle antiparticle pairs in the collision. Hypothetically also the heavier quark flavors could be produced, however, this would require a large accumulation of energy which is highly unlikely. Since strange quarks can only be produced as quark-antiquark-pairs in strong processes, the amount of produced strangeness in one collision balances out which results in the strangeness-balance equation 1.5:

$$\underbrace{M(\Lambda) + M(\Sigma) + 2M(\Xi) + 3M(\Omega) + M\left(\overline{K}\right)}_{S<0} = \underbrace{M(K)}_{S>0}. \tag{1.5}$$

In this equation M represents the multiplicities of the various particle species. The left side of the equation corresponds to the particles containing one or more strange quarks that carry a strangeness of –1 for historic reasons. Those are the single strange baryons Λ and Σ, the multi-strange baryons Ξ and Ω as well as the anti-kaons. The right side of the equation corresponds to the particles containing an anti-strange quark which therefore carry a strangeness of +1. Since at SIS18 energies the production of anti-baryons is highly unlikely, these are only the kaons. Most of these particles appear in multiple charge and/or excitation states. In this equation the species names always correspond to all existing states. The ϕ meson which consist of a strange and an anti-strange quark does not appear in the strangeness balance equation since it carries an overall strangeness of 0 and thereby always conserves strangeness.

In the SHM the conservation of strangeness poses a challenge at low collision energies. At high collision energies enough strange hadrons are produced to conserve strangeness on average which is described by a grand canonical ensemble. At low collision energies however, the conservation of strangeness results in a canonical suppression of the production of strange hadrons which is accounted for in the SHM by the canonical suppression factor F_{Si} [72]. This factor describes the probability to produce for each strange hadron an according amount of anti-strange hadrons to balance the strangeness. Since the strange and anti-strange quark need to be produced close to each other in space, one realization is to calculate the production probabilities in F_{Si} within a canonical volume V_C which is always smaller than the entire volume of the fireball V. In systematic studies it turned out that the SHM describes the measured multiplicities of strange hadron with these modifications well [81, 106, 174].

Assuming strangeness to be produced in isolated NN collisions, the most straight-forward production channel is the production of a kaon-antikaon-pair according to Equation 1.6:

$$N + N \rightarrow N + N + K + \overline{K}. \tag{1.6}$$

The exact threshold of this channel depends on which charge states of the nucleons and the kaons are chosen, but is always $\approx$ 2.87 GeV. Due to the baryon dominance of the systems created at SIS18 energies, there is a more favorable strangeness production channel involving a hyperon given by Equation 1.7:

$$N + N \rightarrow \Lambda + K + N \tag{1.7}$$

Independent of the chosen charge states, this channel has a threshold of only ≈ 2.55 GeV. Exchanging the Λ hyperon in this channel by a Σ hyperon gives another possible strangeness production channel with a threshold of ≈ 2.63 GeV. For the production of multi-strange hyperons more kaons need to be produced along with them to counter balance the strangeness. For example the most favorable production channel of the Ξ hyperons is given by Equation 1.8:

$$N + N \rightarrow \Xi + K + K + N \tag{1.8}$$

However, this production channel already has a threshold of ≈ 3.25 GeV again depending on the chosen charge states. It is obvious that the production of double strange hyperons is suppressed against the production of single strange hyperons. Even further suppressed is the production of the triple strange Ω hyperon whose most favorable production channel has an threshold of ≈ 3.62 GeV.

Due to the multitude of nucleons participating in a heavy-ion collision, interactions between produced strange hadrons and further particles are possible. One example of such secondary reactions are the so called strangeness exchange reactions in which the strange quark from a meson is transferred to a baryon or vice-versa. An according reaction is given by Equation 1.9:

$$N + \overline{K} \leftrightarrow \Lambda + \pi. \tag{1.9}$$

With the vacuum rest masses of the particles, the sum of masses of the state involving the hyperon is lower compared to the state involving the anti-kaon which makes the hyperon-state energetically favored due to a higher phase-space factor. However, as it will be discussed is the following Section 1.3.3, the in-medium anti-kaon mass is expected to be lower than its free mass which might favor the anti-kaon state.

1.3.3. In-Medium Modifications

The presence of hot and/or dense matter influence the properties of the particles inside them [148]. One example for this effect is the melting of the quark-antiquark condensates present in the QCD vacuum which results in the restoration of the chiral symmetry. However, hadrons also couple to the medium itself which modifies their properties additionally. One example of such couplings to the medium is the excitation of resonance-hole-pairs by mesons which is schematically shown by the Feynman-diagram in Figure 1.4. In case of strange mesons, the coupling is realized via hyperon resonances. As it was already mentioned in the previous section, only anti-kaons which carry a strange quark can couple directly to hyperons which is not possible for kaons which

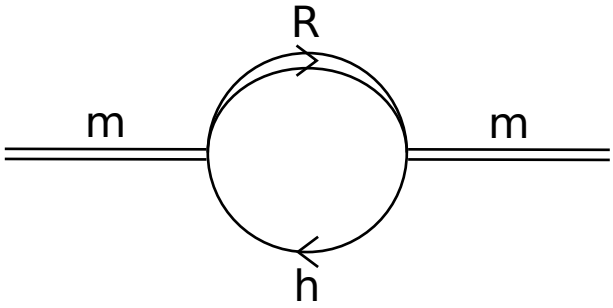

Figure 1.4.: Schematic depiction of a meson (m) coupling to a medium via resonance (R)-hole (h) excitation.

carry an anti-strange quark. In a baryon dominated medium, like created in heavy-ion collisions at SIS18 energies, the effective coupling is attractive for anti-kaons resulting in a decreased effective mass and repulsive for kaons resulting in an increased effective mass [85, 115, 125].

Since the microscopic description of interactions with the medium is difficult, the couplings are often described by the mean-field approach in which the microscopic interactions with the medium are effectively described by interactions with fields created by the medium. These fields are constrained via potentials which reflect the attraction of anti-kaons and the repulsion of kaons.

1.3.4. Centrality

The colliding nuclei are extended particles and can be described roughly by spherical bags with diffuse surfaces filled with nucleons. Their radius can be approximated with the nuclear charge radius which amounts to 5.3 fm in case of Ag nuclei [89]. Assuming an inelastic nucleon-nucleon cross-section of 25 mb, the inelastic strong interaction length amounts to $\approx$ 0.9 fm. Since the radii of the colliding nuclei are significantly larger, in a heavy-ion collision not all nucleons undergo inelastic interactions if the nuclei do not collide central. The degree of centrality of a collision is quantified by the distance of closest approach between the centers of mass of the colliding nuclei which is also called impact parameter.

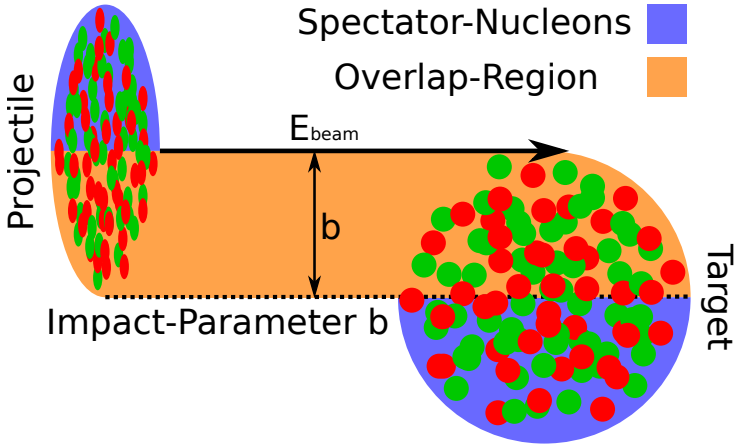

Figure 1.5.: Schematic depiction of a peripheral Ag(1.58A GeV)+Ag heavy-ion collision. Similar depiction already used in [170].

Figure 1.5 schematically depicts its definition in a peripheral Ag(1.58A GeV)+Ag fixed-target collision. The collision is shown in the laboratory system which is why only the projectile nucleus is Lorentz-contracted. The protons (red circles) and neutrons (green circles) are depicted with their average inelastic strong interaction length as diameter in relation to the projectile and target nuclei depicted with their nuclear charge radii. Therefore, in this simplified geometric model all nucleons in the orange overlap-region can be assumed to interact inelastic in the collision and are therefore called participants. On the other side, all nucleons in the blue region are assumed not to participate in the collision and are therefore called spectators. In Section 3.5 a more involved geometric Glauber model [134] is described which is used to estimate the amount of participants with higher precision.

It is obvious that the amount of participants strongly depends on the impact parameter and therefore the degree of centrality of the collision. Furthermore, the amount of participants can be understood as a measure for the size of the medium created in the collision. Since it is the aim of many studies to investigate the effects of this medium on the production and emission of particles, it is important to define event classes with similar amount of participants. For this purpose, the centrality of a collision is defined as the probability of a similar collision being more central (having a smaller impact parameter) than the current one. In other words, the centrality amounts to the cross-section of all more central collisions as a proportion of the total inelastic cross-section. Therefore, the centrality class of the 0-10 % most central collisions corresponds to the 10 % of all inelastic collisions with the smallest impact parameters.

Another important property to classify the emission of particles is the so-called reaction plane which is spanned by the longitudinal axis and the impact parameter. At collision energies $\sqrt{s_{NN}}$ of few GeV the spectator nucleons shield the emission of particles from the collision zone in direction of the reaction plane. Therefore, particles are emitted preferential perpendicular to the reaction plane which is called out-of-plane emission and is measured by negative elliptical flow coefficients [19]. At higher collision energies, the situation reverses as the spectator nucleons pass the collision zone faster than it expands. This leads to particles from the collision zone being emitted preferential parallel to the reaction plane which is called in-plane emission and is measured by positive elliptical flow coefficients [21, 22].

Unfortunately, neither the impact parameter nor the reaction plane can be directly measured with sophisticated methods. Since the reaction plane is not required for the analyses described in this thesis, it will not be further discussed. The method used to estimate the impact parameter and thereby the centrality of an event is described in Section 3.5.

1.4. Phase-Space Distribution Models

The kinematics of particles emitted from the collision zone of a heavy-ion collision are a result of the complicated sub-processes occurring between the involved particles. Microscopic transport models, like for example the UrQMD model [59, 69], simulate heavy-ion collisions by initializing the nucleons within the colliding nuclei and then simulate the entire chain of nucleon-nucleon, nucleon-resonance, resonance-resonance and further particle-particle interactions. However, since especially resonance-resonance interaction cross-section are almost impossible to measure, models like for example the additive quark model [98, 176] are used to estimate them which is a source for uncertainties. Fortunately, in most cases even analytic models based on simple assumptions describe the measured kinematic distributions reasonably well. In the multi-differential analyses described in Chapter 4, such models are used to extrapolate the measured kinematic distributions to regions of the entire phase-space not covered by the measurement. In the following, two commonly used analytic models as well as variations of them are described.

1.4.1. Isotropic Statistical Model

The model labeled Isotropic-Statistical (IS) model in this thesis is based on the SHM which was successfully used to describe the production of various particles from SIS18 energies of few GeV up to LHC energies of few TeV [36, 45, 81, 173]. The central assumption of this model is that particles are emitted from a thermalized fireball which results in momentum distributions described by the Boltzmann-like Equation 1.10:

$$\left(\frac{d^3N}{d^3p}\right)_{IS} = C \cdot \exp\left(-\frac{E}{T_{Eff}}\right) \tag{1.10}$$

Under this assumption the kinematic distributions of the particles are described by only two free parameters: T_{Eff} is the effective temperature of the fireball and C is a scaling constant which combines physical constants and the multiplicity of the particle. Note that if the model is applied to particle multiplicities, the parameters reflect the state of the fireball at chemical freeze-out, in contrast to applying the model to kinematic distributions where the parameters reflect the state of the fireball at kinetic freeze-out.

Conversely, in multi-differential analyses of the kinematic distributions of particles, the transverse momentum components p_x and p_y are transformed to the radial component p_t (transverse momentum) and an azimuthal angle ϕ. Since there is no reason for an anisotropy in azimuthal direction if the analysis is performed independent from the orientation of the reaction plane (cf. Section 1.3.4), the azimuthal component can be eliminated from the equations. Instead of the transverse momentum p_t sometimes the transverse mass m_t is used. Both formulations can be converted into each other using the relation $p_t \cdot dp_t = m_t \cdot dm_t$. In the following, always the transverse mass m_t is used as it results in more compact equations. Furthermore, the longitudinal momentum component p_z is transformed to the Lorentz-additive longitudinal rapidity y according to $dp_z = E \cdot dy$. The Lorentz-additivity of the rapidity y allows to describe the boost between the laboratory system and the center-of-mass system of the fireball in a fixed-target collision by a fixed rapidity offset. With this transformations the IS kinematic distributions are described by Equation 1.11:

$$\left(\frac{d^2N}{dm_t dy}\right)_{IS} = 2\pi \cdot C \cdot m_t^2 \cdot \cosh(y) \cdot \exp\left(-\frac{m_t \cdot \cosh(y)}{T_{Eff}}\right). \tag{1.11}$$

Examining the argument of the exponential function of Equation 1.11 one notices that for a fixed rapidity, the transverse mass spectrum can be interpreted as yet another Boltzmann-like function with the temperature given by Equation 1.12. These temperatures are also referred to as Boltzmann-temperatures:

$$T_B = \frac{T_{Eff}}{\cosh(y)}. \tag{1.12}$$

The transverse kinematic distribution over the entire phase-space can be obtained by integrating over rapidity. This integral can be solved analytically by using the modified Bessel function $K_1(x)$ yielding Equation 1.13:

$$\left(\frac{dN}{dm_t}\right)_{IS} = \int_{-\infty}^{\infty} \left(\frac{d^2N}{dm_t dy}\right)_{IS} (m_t, y)\, dy = 4\pi \cdot C \cdot m_t^2 \cdot K_1\left(\frac{m_t}{T_{Eff}}\right). \tag{1.13}$$

In a similar manner, the longitudinal kinematic distribution over the entire phase-space can be obtained by integrating over the transverse mass. Analytic integration yields Equation 1.14:

$$\begin{aligned}\left(\frac{dN}{dy}\right)_{IS} &= \int_{m_0}^{\infty} \left(\frac{d^2N}{dm_t dy}\right)_{IS} (m_t, y)\, dm_t \\ &= 2\pi \cdot C \cdot T_{Eff} \cdot \exp\left(-\frac{m_0 \cdot \cosh(y)}{T_{Eff}}\right) \cdot \left(m_0^2 + 2m_0 \frac{T_{Eff}}{\cosh(y)} + 2\frac{{T_{Eff}}^2}{\cosh(y)^2}\right).\end{aligned} \tag{1.14}$$

Equation 1.14 can be transformed into a Gaussian function, by approximating the polynomial bracket as constant and substituting the $\cosh(y)$ in the exponential function by its second order Taylor expansion around 0. The width of this Gaussian function, which is also referred to as the thermal width of the rapidity spectrum, is defined by Equation 1.15:

$$\left(\frac{dN}{dy}\right)_{IS} \propto C \cdot \exp\left(-\frac{y^2}{2\sigma^2}\right) \quad \text{with} \quad \sigma = \sqrt{\frac{T_{Eff}}{m_0}}. \tag{1.15}$$

While the isotropy of the fireball integrated over all reaction plane angles is well justified in the two transverse directions, the longitudinal direction is special since it is the direction of the beam axis and therefore the direction of the initial momentum of the beam-ions. Depending on the kinetic beam energy, the colliding ions are not fully stopped in the collision, which results in an additional residual expansion of the fireball in longitudinal direction and therefore an anisotropic fireball. This longitudinal anisotropy is not reflected by the default IS model.

The simplest solution to overcome this problem is to apply the model to the transverse and longitudinal spectra independently, allowing for different transverse and longitudinal parameter values. Another approach, which was proposed in [164], is to extend the IS model by an additional parameter η to describe the longitudinal anisotropy, e.g. by assuming two identical IS fireballs positioned at $\pm\eta$ around the center-of-mass rapidity of the collision system. This approach is referred to as Double Isotropic-Statistical (DIS) model in this thesis and is defined by Equation 1.16. Despite its simplicity, it is found that this approach describes the measured kinematic distributions quite well.

$$\left(\frac{d^2N}{dm_t dy}\right)_{DIS} = \left(\frac{d^2N}{dm_t dy}\right)_{IS} (m_t, y-\eta) + \left(\frac{d^2N}{dm_t dy}\right)_{IS} (m_t, y+\eta) \tag{1.16}$$

A more sophisticated assumption to describe the longitudinal anisotropy is that the IS fireball spans the rapidity range from $-\eta$ to $+\eta$ around the center-of-mass rapidity of the collision system, which is the original proposal from [164]. Mathematically this corresponds to integrating the IS model from $-\eta$ to $+\eta$. This approach is called Integrated Integrated Isotropic-Statistical (IIS) model in this thesis and is defined by Equation 1.17:

$$\left(\frac{d^2N}{dm_t dy}\right)_{IIS} = \int_{-\eta}^{\eta} \left(\frac{d^2N}{dm_t dy}\right)_{IS} (m_t, y + x)\, dx. \tag{1.17}$$

Since unfortunately the additional integral of the IIS model cannot be easily solved analytically, in this work it is approximated using the numerical Gauss-Legendre integration method. In this work it is found that using 50 sampling points for the numerical integration provides a fair compromise between speed and accuracy.

1.4.2. Siemens-Rasmussen Model

The Siemens-Rasmussen (SR) model in an extension of the IS model proposed by P.J. Siemens and J.O. Rasmussen in 1979 [168]. In order to explain the kinematic distributions of protons and pions from ion collisions at several hundred MeV which are not well described by purely thermal models, they proposed to extend the thermal fireball by a (mean) expansion velocity β. This velocity is also called blast-wave velocity or simply blast. With this extension, the model can be understood to produce particles with thermal kinematic distributions, but due to the expansion of the thermal source itself, the particles experience an additional radial boost defined by the blast velocity. Applying the extension results in the momentum distribution defined by Equation 1.18 using the Lorentz-factor γ and the parameter α defined by Equation 1.19:

$$\left(\frac{d^3N}{d^3p}\right)_{SR} = C \cdot \exp\left(-\frac{\gamma E}{T_{Eff}}\right) \cdot \left[\left(1 + \frac{T_{Eff}}{\gamma E}\right) \frac{\sinh(\alpha)}{\alpha} - \frac{T_{Eff}}{\gamma E} \cosh(\alpha)\right] \tag{1.18}$$

$$\gamma = \frac{1}{\sqrt{1-\beta^2}} \quad \text{and} \quad \alpha = \beta\gamma \frac{p}{T_{Eff}} \tag{1.19}$$

Like the IS model, the SR model is transformed into the transverse mass and rapidity system for practical usage, resulting in Equation 1.20:

$$\left(\frac{d^2N}{dm_t dy}\right)_{SR} = 2\pi \cdot m_t^2 \cdot \cosh(y) \cdot \left(\frac{d^3N}{d^3p}\right)_{SR} \tag{1.20}$$

Due to the more complicated terms in the SR model equations, the integrals for the transverse or longitudinal kinematic distributions over the entire phase-space cannot be easily solved analytically. Therefore, they are approximated again using the numerical Gauss-Legendre integration method with 50 sampling points. Since in this special case the method can only be applied with finite integral borders, the transverse integration is performed in the range $m_t \in [0, 10000]\,\mathrm{MeV/c^2}$ and the longitudinal integration is performed in the range $y \in [0, 5]$ and the result is multiplied with 2 as the model is symmetric by definition. Since the distribution is decreasing exponentially towards high transverse masses and high absolute rapidities, these approximations are justified.

The default SR model assumes a radial symmetric blast-wave and is therefore not capable to describe the longitudinal anisotropy which was already discussed in Section 1.4.1. However, the same approaches discussed for the IS model can be applied to the SR model

resulting in the Double Siemens-Rasmussen (DSR) model defined by Equation 1.21 and the Integrated Siemens-Rasmussen (ISR) model defined by Equation 1.22:

$$\left(\frac{d^2N}{dm_t dy}\right)_{DSR} = \left(\frac{d^2N}{dm_t dy}\right)_{SR}(m_t, y-\eta, \beta) + \left(\frac{d^2N}{dm_t dy}\right)_{SR}(m_t, y+\eta, \beta) \tag{1.21}$$

$$\left(\frac{d^2N}{dm_t dy}\right)_{ISR} = \int_{-\eta}^{\eta}\left(\frac{d^2N}{dm_t dy}\right)_{SR}(m_t, y+x, \beta)\, dx \tag{1.22}$$

The two dimensional integral that arises in the equation for the longitudinal kinematic distribution over the entire phase-space of the ISR model is again solved numerically, this time applying an adaptive quadrature integration algorithm [96]. In the analyses described in the sections of Chapter 4, these models are used to extrapolate the measured distributions to region of the phase-space not covered by the measurement. The systematic uncertainties of these extrapolations are determined by comparing the results of different models.

1.5. State of the Art and Aim of the Thesis

The investigation of fixed-target heavy-ion collisions with beam energies around 1-2 GeV per nucleon started in the early 1970s with first experimental setups at the Lawrence Berkeley National Laboratory (LBNL) in the USA and the Joint Institute for Nuclear Research (JINR) in the USSR. In the year 1984 these studies were continued by an experimental program at the Bevalac accelerator of the LBNL involving the Plastic-Ball spectrometer [56], the Streamer-Chamber experiment [103], the Equation Of State (EOS) experiment [151] and the DiLepton Spectreometer (DLS) [182]. Shortly afterwards experiments at higher energies using the Alternating Gradient Synchrotron (AGS) accelerator at the Brookhaven National Laboratory (BNL) and the Super Proton Synchrotron (SPS) accelerator at CERN followed. At GSI the investigation of heavy-ion collisions using the SIS18 accelerator started in the early 1990s when the KaoS (Kaon Spectrometer) [166], the FOPI (FOur PI) [156] and the TAPS (Two-Three-Arm Photon Spectrometer) [140] experiment were taken into operation.

The primary goal of the KaoS spectrometer was the measurement of Kaons utilizing a double-focussing quadrupole-dipole magnetic spectrometer. The production of Kaons was measured in light (C+C), intermediate (Ni+Ni) and heavy (Au+Au) ion collision systems at various beam energies between 0.6 and 2.0A GeV allowing to study both system size and energy dependence of the production of strangeness around its free NN threshold energy. Due to the limited geometrical acceptance of the spectrometer, it was not capable of reconstructing short lived particles from their decay daughters. Summaries of the physics results obtained by the KaoS collaboration are given in [87, 88].

One of the most astonishing observations made by the KaoS collaboration is that the ratio of produced K^+ and K^- mesons is almost independent of the size of the collision [88]. Despite the strong difference between the free NN production threshold energies of K^+ and K^- mesons, as pointed out in Section 1.3.2, their production rates scale in the same way. A similar observation involving also Λ hyperons as well as K^0_S and ϕ mesons was made by

the HADES collaboration in Au+Au collisions [18]. However, the K^- and ϕ results suffer from large statistical uncertainties. For the HADES Ag+Ag data the increased amount of recorded events leads to a significant decrease of the statistical uncertainties. In this thesis the production of Λ hyperons and K^0_S mesons is studied which, in combination with the K^+, K^- and ϕ mesons that are studied in parallel in [122], allows to test the observed universal scaling of strange particles with A_{Part} with a higher precision than ever before.

Due to its large geometrical acceptance, in contrast to KaoS, the FOPI experiment was able to reconstruct short lived particles, like for example Λ hyperons as well as K^0_S and ϕ mesons. The measurements of FOPI were conducted again from light (Ca+Ca) up to heavy (Au+Au) ion collision systems over a wide range of beam energies from 0.1 to 1.9A GeV. After its decommissioning the physics program of FOPI was continued by the HADES experiment.

KaoS observed that the inverse slopes of the transverse spectra of K^+ mesons lay significantly above the ones of K^- mesons. At FOPI, an unexpected high ratio between the production rates of ϕ and K^- mesons was measured [131], which lead to the assumption that a significant amount of all K^- mesons originates from the $\phi \rightarrow K^+ + K^-$ decay thus significantly influencing the overall K^- transverse slope [144]. This assumption was later confirmed by measurements of the HADES collaboration and it showed that the production of K^+ and K^- mesons can be described with the same transverse slope if the feeddown contribution from the ϕ decay is subtracted [17]. Further studies of the production of strangeness conducted by FOPI are described in [107, 126, 143]. Besides that, also the azimuthal emission anisotropies (flow) and in particular their energy dependence was studied by FOPI [44, 155].

In this thesis the emission/production of protons, Λ hyperons, K^0_S mesons, ${}^3_\Lambda H$ hypernuclei and Ξ^- hyperons is investigated using the recent HADES Ag(1.58A GeV)+Ag data sample. These particles have been studied by HADES before in Ar(1.76A GeV)+KCl collisions [30, 31, 33, 34] as well as Au(1.23A GeV)+Au collisions [17, 18, 175]. Due to the intermediate system size and intermediate energy of the Ag+Ag collisions, their study will allow to analyze the effects of system size and energy in a very systematic way. Furthermore, thanks to the large amount of recorded events, the precision of the measurements is strongly enhanced and particles that could not be measured in the previous data samples, like for example the ${}^3_\Lambda H$ and the Ξ^- in Au+Au or the ${}^3_\Lambda H$ in Ar+KCl, might become accessible.

In Chapter 1 the physical background for the performed analyses is briefly summarized. Furthermore, in Section 1.4 some analytical models that are going to be used in the analyses later on are defined and described. In Chapter 2 the technical prerequisites for the conducted analyses are described. This chapter primarily consists of Section 2.2 which describes the physical setup of the HADES detector system and Section 2.3 which describes the most important steps required to analyze data recorded by the HADES experiment. In Chapter 3 several analysis methods that have been either newly developed, altered or investigated within the scope of this project are described. All these methods are of general nature and can be used for various different analyses. In the sections of Chapter 4 the individual particle analyses performed in the scope of this project as well as their results are described. Finally, in Chapter 5 the results obtained in the previous chapter are summarized and interpreted.

2. The HADES Experiment

2.1. The Research Facility GSI / FAIR

The HADES experiment is one of several experiments located at the GSI Helmholtz Center for Heavy-Ion Research in Darmstadt, Germany. The researches conducted there cover the fields of nuclear-, atomic-, plasma- and biophysics as well as material science.

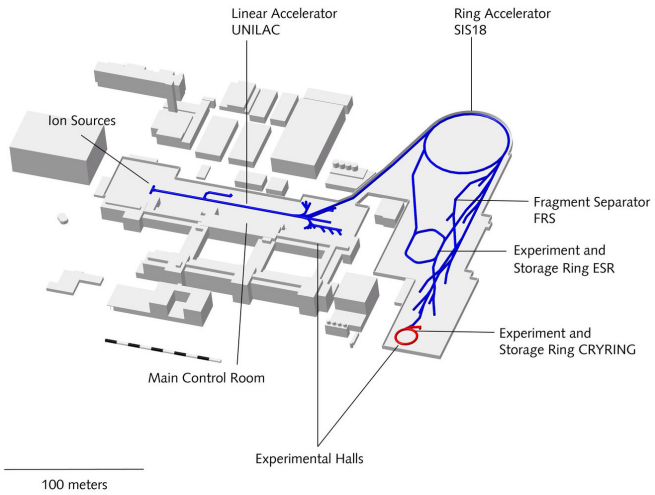

Figure 2.1.: Schematic view of the GSI accelerator infrastructure [101].

The key feature of the facility is its accelerator infrastructure, which is schematically shown in Figure 2.1. It allows to accelerate ions up to the heaviest natural element, uranium, to energies of 1-2 GeV per nucleon. The positively charged ions produced in the Ion Sources at low kinetic energies are first accelerated by the UNIversal Linear ACcelerator (UNILAC) up to energies of 11.4 MeV per nucleon [100]. To reach higher energies, the ions are accelerated further by the Heavy-Ion Synchrotron 18 Tm (SIS18) ring accelerator. Afterwards, the ions can either be used directly for experiments like HADES or to produce a secondary beam of rare nuclei in the FRagment Separator (FRS). Furthermore, the setup involves the Experimental Storage Ring (ESR) storage ring that allows to store and cool accelerated ions (cf. [100]).

At the moment the GSI facility is being extended to the Facility for Antiproton and Ion Research (FAIR). One of the most important aspects of this extension is the construction of the new Heavy-Ion Synchrotron 100 Tm (SIS100) ring accelerator. It will allow to accelerate ions, injected by the upgraded SIS18 accelerator, to 29 GeV in case of protons, corresponding to 14.5 GeV per nucleon for deuterons and $\approx$ 10 GeV per nucleon for heavy-ions [172]. This will open up new possibilities to various kinds of researches and further additions to the current facility, like an improved fragment separator, an improved storage ring and an additional storage ring designed specifically for anti-protons, are planned.

The physics program of FAIR involves a phase 0 in which experiments are operated at the current SIS18 accelerator. Yet, they already employ detector technology developed for future FAIR experiments. In the scope of FAIR Phase-0 the HADES experiment measured Ag+Ag collisions at 1.58A GeV beam energy in March 2019, which are analyzed in this thesis. The following Section 2.2 describes the setup and capabilities of the HADES detector system.

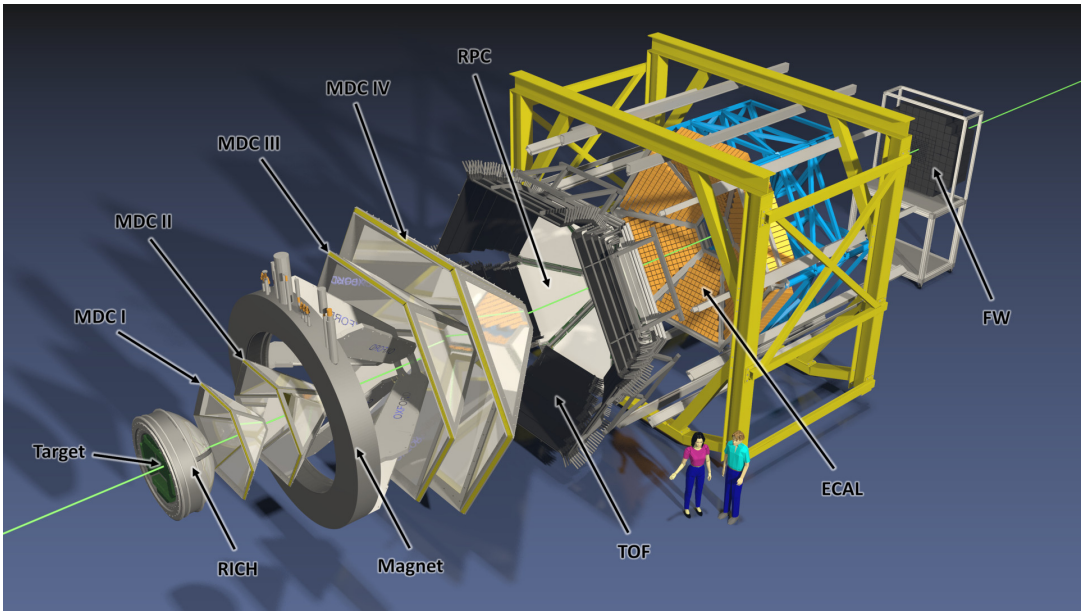

Figure 2.2.: Exploded view of the HADES detector setup. The original image from [162] has been altered to include the improved RICH-detector, the new ECAL-detector and the FW-detector.

2.2. The HADES Detector System

The apronym HADES stands for High Acceptance DiElectron Spectrometer. Its setup is shown in Figure 2.2 in an exploded view for better visualization of the different subcomponents. As the name implies, the detector is specifically designed for the measurement of e^+e^- pairs, especially those produced by decays of the vector mesons ρ, ω and ϕ. Due to their short lifetimes and the non-strongly interacting decay products, these probes transport information on the hot and dense phase created in the collision almost undisturbed to the detector. However, a precise measurement of e^+e^- pairs from vector meson decays is challenging.

In general, the vector mesons ρ, ω and ϕ can be produced directly in elementary NN collisions: $N + N \rightarrow N + N + (\rho, \omega, \phi)$. In case of the ω, the energetic threshold of this channel amounts to $\sqrt{s} \gtrsim 2.66$ GeV assuming a ω mass of 0.78 GeV [184]. However, in heavy-ion collisions at SIS18 energies the available energy in elementary NN collisions is often below. For example, in Ag+Ag collisions at 1.58A GeV beam energy, which are analyzed in this thesis, $\sqrt{s_{NN}}$ amounts to 2.55 GeV. Therefore, the vector mesons ρ, ω and ϕ are produced below their free NN threshold energy, which leads to low production rates of $\lesssim 10^{-2}$ per event. In addition, the branching ratios of their dileptonic decay channels are pretty small and amount to only $\approx 10^{-4}$ [184].

Measuring a statistically significant amount of e^+e^- decays of vector mesons, despite their low production probabilities, requires a detector with the following features:

- **High event rates** are achieved by the fast DAQ system, described in Section 2.2.9, of the HADES experiment that allows to record in average up to 11,000 Ag+Ag events at 1.58A GeV beam energy per second.

- **High geometric acceptance**: Due to the low e^+e^- mass, which leads to high opening angles in the vector meson decays, this is of special importance. In azimuthal direction the HADES detector setup is divided into six identical but independent sectors covering the full azimuthal angle (See Figure 2.2). In polar direction the detectors span angles between 18° and 85° in forward direction.
- To achieve **high reconstruction efficiencies**, an efficient track reconstruction method, described in Section 2.3.3, was developed for the HADES experiment.
- **Low e^+e^- background**: There are two main contributions to the e^+e^- background with respect to the reconstruction of vector mesons via their dileptonic decay channels:
  - **Hadrons**, mostly charged pions, wrongly identified as e^+ or e^-: This background can be suppressed very efficiently using the RICH detector of the HADES experiment, which is only sensitive to highly relativistic particles. It is being described in Section 2.2.3.
  - **High energetic photons** converted to e^+e^- pairs in matter: This background is reduced by minimizing the amount of heavy material, created particles are traversing, which is achieved by the target setup, described in Section 2.2.2.

In addition to its capabilities in the reconstruction of e^+e^- pairs, the HADES detector is very well suited to measure hadrons. Its high event rates in combination with its high geometric acceptance and reconstruction efficiencies allow to conduct very detailed analyses even for rarely produced hadrons, which is the topic of this thesis. In the following sections the individual sub-detectors of the HADES experiment are described. Further information on the capabilities of the HADES experiment can be found in [32].

2.2.1. The START and VETO Detector

Out of all detectors of the HADES experiment, only the START- and the VETO detector are directly exposed to the high intensity heavy-ion beam. Thus, they require high resistivity against radiation. Despite their high production costs, diamond detectors, produced with the Chemical Vapor Deposition (CVD) method, are used, because they furthermore provide a precise time resolution and a high heat conductivity, which allows to run them without any external cooling [32].

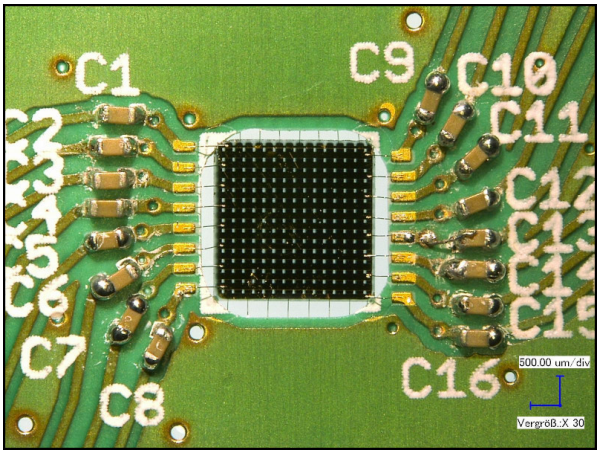

Figure 2.3.: Photo of the START detector.

Looking in the direction of the beam, the START detector, shown in Figure 2.3, is the first detector of the HADES experiment, located 5.27 cm in front of the first target segment. It is 60 μm thick and has an active area of 4.7 mm × 4.7 mm read out by 16 strips with a pitch of ≈ 300 μm per side, orientated in x- and y-direction respectively.

When a beam ion traverses the START detector and reacts in the target, the time measured by the START detector is used as the time of the heavy-ion reaction, despite the spacial distance between the detector and the target, causing a constant offset. Furthermore, the START detector is used to monitor the intensity and the focusing of the beam. Due to its relevance, high efficiencies of $\gtrsim 95$ % are required. However, the continuous irradiation damages the atomic structure of the diamond and thereby leads to decreasing efficiencies. To cope with this effect, the detector can be moved in x- and y-direction.

The VETO detector, shown in Figure 2.4, is located 54.68 cm behind the target. It has an active area of 8 mm $\times$ 8 mm and is read out by eight pads. The VETO detector's main purpose is to reject triggered events in which either no nuclear reaction took place in the target or in which another beam ion traversed the target simultaneously with the actual colliding ion, making it impossible to guarantee that the correct reaction time was measured by the START detector. The criteria used to identify problematic events are described further in Section 3.2.

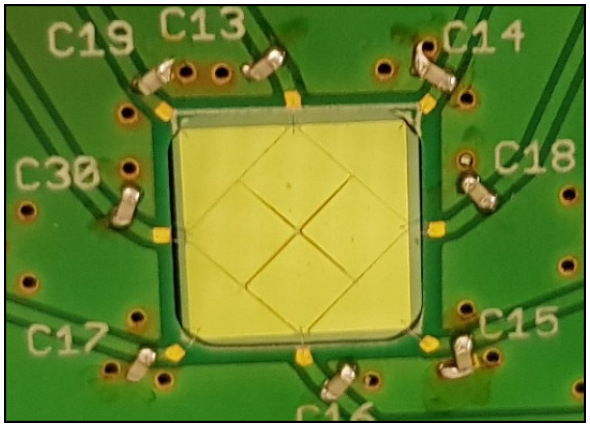

Figure 2.4.: Photo of the VETO detector.

2.2.2. The 15-fold Silver Target

Concerning the conversion of photons and the energy loss of charged particles, heavy elements are exceptionally crucial as both effects scale quadratic with the atomic number of the traversed material (Z^2). Therefore, the heavy-ion target of the HADES experiment, shown in Figure 2.5, was designed to allow particles created in the collision to leave the target without traversing much material. This is achieved by reducing the thickness of the target material to 40 µm, which on the other hand decreases the nuclear interaction probability to 0.1 %. By concatenating 15 identical target segments with 3 mm gaps, a total nuclear interaction probability of 1.5 % is achieved whilst remaining a photon conversion probability of below 1 % [15].

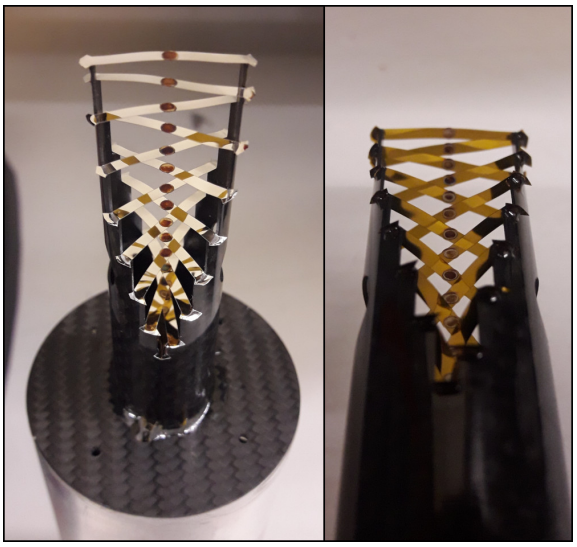

Figure 2.5.: Photos of the 15-fold silver target used in the analyzed beam time.

As every heavy-ion beam has a cloud of beam ions, called "halo", around its focus, also the amount of material around the actual target needs to be minimized. The 15 Silver disks of 2.2 mm diameter are glued to thin kapton strips, attached to the actual mounting structure entirely made of carbon fibers, providing a high structural stability at low weight. Nevertheless, a contamination of Ag+C events needs to be considered in the later analyses.

2.2.3. The RICH Detector

Particles, created in nuclear reactions in the target, traverse the Ring Imaging CHerenkov (RICH) detector first. It comprises a radiator gas volume which was filled with Isobutane in the analyzed Ag+Ag beam time. At a refraction index of 1.0015 in the relevant photon energy range [163], only highly relativistic charged particles with $\gamma \gtrsim 18$ reach velocities above the speed of light in the gas and thereby emit Cherenkov light. The emitted light is then reflected by a parabolic mirror towards photo multipliers placed in backward direction to prevent them from measuring charged particles, which they are also sensitive to.

With this setup the detector is almost exclusively sensitive to electrons and positrons at the relevant collision energies, because the next lightest charged particles, the pions, require a momentum of $\gtrsim$ 2500 MeV/c to emit Cherenkov light in the radiator gas. As Cherenkov light is always emitted conically with a fixed angle towards the particle track, it is detected as characteristic rings by the photo multipliers. Matching the centers of these rings with the reconstructed particle tracks, allows to identify electron and positron tracks. More details on the RICH detector can be found in [20].

2.2.4. The MDC Detectors

The track reconstruction is based on 24 trapezoidal shaped Mini Drift Chambers (MDCs) in four planes (MDC I - MDC IV) for each of the six sectors. With this setup the full azimuthal angle except the frames and the coils is covered as well as polar angles between 18° and 85°. The first two chambers of each sector are placed in front of the magnet, described in Section 2.2.5, and the latter two are placed behind it, allowing to deduce the particle momenta from the deviation of the tracks in the magnetic field. The full track reconstruction and particle identification method is described in Section 2.3.3.

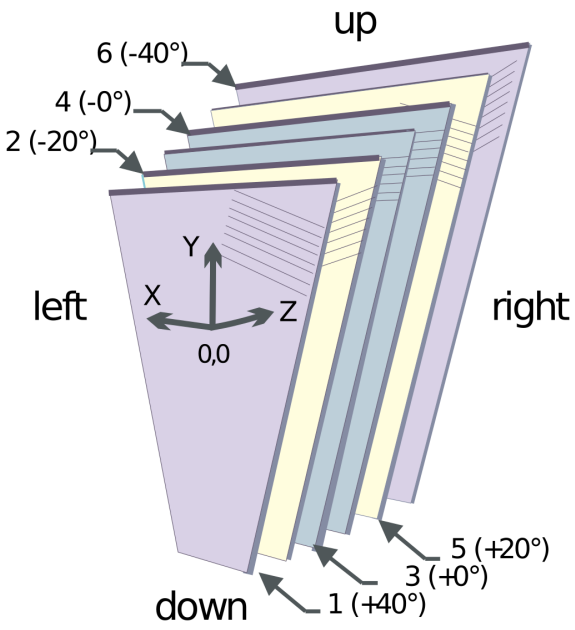

Figure 2.6.: Schematic view of the sense wire layers of a MDC chamber [132].

The chambers operate on the principle of multiple proportional counters with a common gas volume. In the analyzed Ag+Ag beam time, an admixture of 70 % Argon and 30 % Carbon Dioxide was used [137]. In this admixture, Argon serves as counting gas, whilst Carbon Dioxide serves as quenching gas to absorb ionizing radiation from the recombination of electron-hole pairs, which otherwise would induce secondary signals not related to the actually measured particle.

In order to meet the requirement of a low material budget to reduce multiple scattering and photon conversion, the anodes and cathodes of the chambers are made from thin

wires distributed over 13 planes per chamber. Every second layer is equipped solely with cathode wires of 80-100 µm diameter inclined by 90° towards the x-direction of the chamber coordinate system defined in Figure 2.6. Every other layer is equipped alternating with field wires that serve as further cathodes and sense wires of 20-30 µm diameter that serve as anodes as well as read-out wires. As shown in Figure 2.6, the wires of the sense wire layers are inclined by ±40°, ±20° and twice 0°. Due to their different orientations, the point a particle traversed the chamber at, corresponds to the intersection point of multiple active sense wires.

During operation, a negative potential of ≈ 2000 V, varying between the different planes, is applied to the cathode and field wires while the sense wires remain at ground potential. This causes ionization electrons, created along the trajectory of a charged particle, to drift along the field lines towards the sense wires, as it is shown in Figure 2.7. Once the electrons reach sufficient energy, they ionize further gas atoms and thereby increase the total amount of free electrons. This effect, also referred to as avalanche effect, occurs mostly close to the sense wires where the density of the electric field rises strongly. The time, the ionization electrons need to drift to the sense wire, rises monotonically with the distance between the ionizing particle and the sense wire. Thus, its distance of closest approach can be deduced from the time of the measured signal, resulting in a total spacial resolution of a few hundred microns.

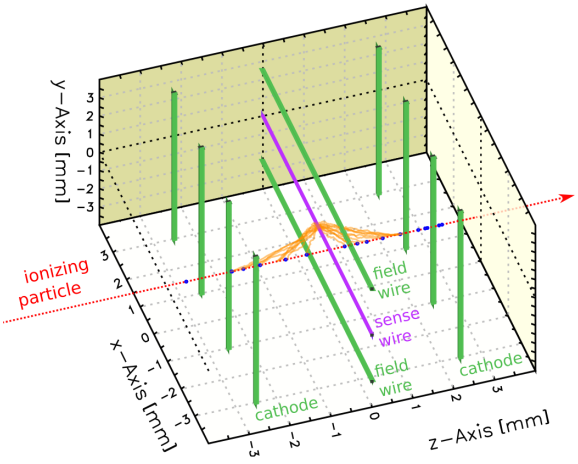

Figure 2.7.: Schematic view of a drift cell from one of the two innermost sense wire layers with an ionizing particle passing through. The ionization electrons are depicted as thin orange lines [179].

Another important quantity that can be measured by the MDCs is the specific energy loss of a particle in the detector gas. It can be described by the Bethe-Bloch-Equation 3.7 [184], which is explained in Section 3.4.2. Since the chambers are being operated at voltages where they are in proportional mode, the amount of energy, initially deposited, can be deduced from the integral of the measured signal. However, since the signal amplitude is not measured directly, this integral is not trivial to determine. Therefore, it is estimated using the Time over Threshold (ToT) method. For this method, it is assumed that all signals have equal shapes and only differ in their height. In that case, the time a signal stays above a fixed threshold scales proportional with the integral of the signal.

Section 2.3.3 describes how particle tracks are reconstructed and identified based on the quantities measured by the detectors. Further information, specifically on the MDCs, can be found in [32, 132, 179].

2.2.5. The Magnet

The magnet of the HADES experiment is used to generate a toroidal magnetic field between the two inner and the two outer planes of MDCs. It consists of six coils made from a copper-niobium-titanium alloy [158] that are located at the borders of adjacent sectors, where the MDCs are not sensitive due to their frames. The coils are cooled by a liquid nitrogen and liquid helium cooling system down to 4.7 K, where they reach superconductivity. Thus, currents up to 3464 A can be generated despite the compact coil setup and an inhomogeneous magnetic field of 0.9 - 3.6 T strength is induced. With standard polarity, positively charged particles are deflected towards low and negatively charged particles towards high polar angles, allowing to reconstruct their momenta from the strength of the deflection, as described in Section 2.3.3.4. Since especially the electron positron identification by the RICH detector would suffer from a residual magnetic field, the coil geometry was optimized to provide an almost field free region around the target. Further information on the magnet and its cooling plant can be found in [32, 158].

2.2.6. The META Detectors

The Multiplicity Electron Trigger Array (META) is located directly behind the fourth plane of MDCs. It is a generic term for the RPC detector, described in Section 2.2.6.1, and the TOF detector, described in Section 2.2.6.2. Both detectors are used to measure the time of flight of particles. In combination with the length of their reconstructed trajectories, this allows to calculate the speed of the particles, which, in combination with the momentum, enables us to identify the particle as described in Section 3.4.1. Furthermore, the detector signals are used as an input for the CTS, described in Section 2.2.9.

2.2.6.1. The RPC Detector

The Resistive Plate Chamber (RPC) detector covers polar angles between 18° and 45°. Due to the forward boost of the CM in fixed target collisions, this region comprises a high track density. Thus, a detector with high granularity as well as short dead times is required.

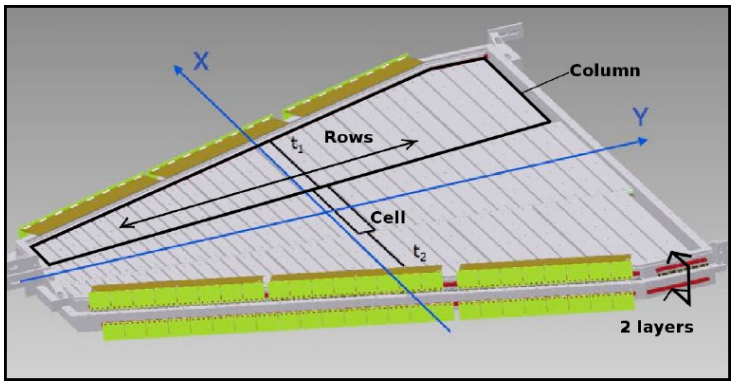

Figure 2.8.: Schematic view of the internal column, row and cell structure of the RPC detectors [161].

Each of the six RPC detectors consists of two overlapping layers with three columns of 31 individual cells, as it is shown in Figure 2.8. Every cell contains three 2 mm thick aluminum electrodes separated by two 2 mm thick glass electrodes. The detector gas, which is an admixture of 90 % Freon ($C_2H_2F_4$) and 10 % Sulfur Hexaflouride (SF_6) [123], is filled in 270 µm wide gaps between the aluminum and glass electrodes. During operation, a positive potential of ≈ 6000 V is applied

to the center aluminum electrode that acts as an anode whilst the outer two aluminum electrodes are held at ground potential and thereby act as cathodes. When an ionizing particle traverses the cell, it triggers an avalanche of ionization electrons in the detector gas due to the strong electrical field and thereby induces a clear electrical signal in the center aluminum electrode which is read out on both ends of the cell.

Since particles traverse the electrical field twice in each cell, high efficiencies of $\gtrsim 95$ % are achieved. On average, the time resolution amounts to 77 ps in case of a single hit in the detector and 83 ps in case of multiple hits in adjacent cells [68]. In polar direction the spacial resolution of the detector is limited by the sizes of the cells which range from 2.2cm at lowest polar angles to 5cm at highest polar angles. In azimuthal direction the sizes of the cells range from 12 cm at lowest polar angles to 52 cm at highest polar angles. In azimuthal direction the position of a detected hit is calculated from the delay between the measurements on both ends of the cell resulting in a spacial resolution of up to 6 mm [63]. Because the total gas volume of the detector is small and the applied high voltage is far above the region of linear gas amplification, the correlation between the RPC signals and the initially deposited energy, and thereby the specific energy loss of the particles, is rather weak. Further information on the RPC can also be found in [62].

2.2.6.2. The TOF Detector

The polar angle region between 44° and 88° is covered by the Time Of Flight (TOF) detector. Every one of its six sectors consists of eight modules that comprise eight plastic scintillator rods made from BC408 material with lengths between 1 and 2 m. The scintillation light, generated by ionizing particles in the rods, is read out on both sides by individual PhotoMultiplier Tubes (PMTs).

The time of a hit can be averaged over the times measured by the two PMTs per rod taking into account the time the scintillation light needs to traverse the full length of the rod. Thus, a temporal resolution of 150 ps is achieved. The position of a detected hit along the rod (azimuthal direction) can be calculated from the delay between the signals from the two PMTs which results in a spacial resolution of ≈ 2.5 cm in azimuthal direction. In polar direction, the spacial resolution of the detector is limited by the widths of the rods. They amount to 2 cm for the rods of the four innermost modules and 3 cm for the rods of the four outermost modules (cf. [40]).

The intensity of the induced scintillation light scales with the amount of energy a particle deposited in the scintillation material. Therefore, the signal shapes are correlated to the specific energy losses of the particles. Since the density of the scintillation plastic is higher than the density of the detector gas in the MDCs, the particles loose more energy, which makes the energy loss measurement of the TOF detector more accurate than the one of the MDC detector.

2.2.7. The ECAL Detector

The Electromagnetic CALorimeter (ECAL) is positioned directly behind the RPC detector and covers approximately the same polar angle region. It was used for the first time in the analyzed Ag+Ag beam time and replaced the older PRE-SHOWER detector. The main purpose of the calorimeter is to detect photons, which previously could only be reconstructed from their conversion dilepton pairs. Furthermore, the ECAL can be used to improve the identification of measured particle tracks, especially the separation of electrons/positrons and pions.

Every sector of the ECAL consists of 163 modules. Each module contains a 9.2 cm $\times$ 9.2 cm $\times$ 42 cm CEREN25 lead glass block. When relativistic particles traverse the lead glass, they deposit their energy effectively generating showers of photons which are measured by PMTs. The total energy of the particle is then calculated from the amplitude of the measured signal. In the analyzed Ag+Ag beam time only four of the six sectors of the ECAL were equipped with modules resulting in an azimuthal acceptance of $\approx 2/3$. Further information on the ECAL can be found in [93].

2.2.8. The FW Detector

The Forward Wall (FW) detector is located 6 - 7 m behind the target and covers polar angles between 0.33° and 7.17°. Like the full HADES experiment it is constructed symmetrically around the beam axis going through its center and thereby covers the full azimuthal angle, however, it does not follow the general six-sector layout of the HADES experiment. The main purpose of the FW detector is the measurement of the spectator protons and light nuclei. Their azimuthal distribution is related to the angle of the event plane, which was described in Section 1.3.4. Furthermore, the spectator's polar distribution as well as their amount relates to the centrality of the collision.

The FW consists of 288 quadratic plastic scintillator modules made from BC408 material that are read out by individual PMTs. Due to the forward boost in fixed target heavy-ion collisions, the particle density drops with increasing polar angle. Therefore, the module size is increasing at higher polar angles to remain similar hit rates in all modules. Since the strong irradiation of the heavy-ion beam would damage the modules, the FW has a 8 cm $\times$ 8 cm hole in its center. It is surrounded by five rings of 4 cm $\times$ 4 cm modules (140). Around these center modules two rings of 8 cm $\times$ 8 cm modules (64) are placed and afterwards follow 3 rings, with 12 modules missing at the edges of the outer ring, of 16 cm $\times$ 16 cm modules (84).

2.2.9. The CTS and DAQ System

The Data AcQuisition (DAQ) system of the HADES experiment collects and stores the data of all sub-detectors. It consists of the Front-End Electronics (FEEs) of the individual detectors, the Central Trigger System (CTS) and the Event Builders (EBs).

When a beam ion is detected by the START detector, the CTS is activated and a decision whether the ion reacted in the target and whether the reaction is of physical relevance is

taken. A first level trigger decision is taken based on raw detector hit information like the amount of total hits in the META detectors. A second level trigger decision can be taken based on detector data preprocessed by Image Processing Units (IPUs) to select events that contain lepton candidates, however, in the heavy-ion beam times the second trigger level is usually not used. When the CTS takes a positive trigger decision, it sends a global reference time signal as well as the positive trigger decision to the detector FEEs. This starts the read-out of the data from the respective detectors and sends them to the EBs via a global gigabit switch. The EBs collect all data and finally write them to disk in the HADES List mode Data (HLD) file format. When the FEEs have finished the read-out and transmitted the data, they notify the CTS system. Only after all FEEs finished the read-out and notified the CTS, the next trigger decision can be taken. Therefore, the maximum event rate to be recorded by the DAQ is limited by the slowest FEE in the system.

In the analyzed Ag+Ag beam time the LVL1 trigger decisions were taken based on the sum of hits in the RPC and the TOF detector. This number is correlated to the amount of particle tracks in the event, which corresponds to the centrality of the collision (cf. Section 1.3.4). Two Physics Triggers (PTs) were defined. The PT2 trigger required 5 hits and the PT3 trigger 20 hits in the RPC and TOF detector. However, to reduce the amount of peripheral events, only every 32^{nd} event with a positive PT2 but negative PT3 trigger decision was recorded.

Further information on the DAQ and CTS system of the HADES experiment can be found in [133].

2.3. The HADES Software Framework

The software required to analyze HADES data is contained in the HYDRA (HADES sYstem for Data Reduction and Analysis) software framework. It is entirely based on the ROOT framework [150], commonly used in high-energy experiments, and employs a similar modular structure. Each sub-detector of the setup has its own module containing the classes required to decode the raw data, store parameters, apply calibrations, reconstruct hits, store final data, simulate detector responses and further tools specifically for the particular sub-detector. Furthermore, the framework contains global classes to control the full reconstruction process and distribute data from various sources among all sub-processes as well as classes combining data from different detectors to final physical objects like particle tracks. After the reconstruction process, the reconstructed objects and information are stored in the HADES Data Summary Tape (DST) file format that allows to perform analyses without having to run computation intensive tasks, like the reconstruction of particle tracks, every time an analysis is run.

The following sections describe the steps required to extract information on physical objects from the detectors raw data stored in the HLD file format. Since the final data of this process are stored in the DST file format, the whole process is also called DST production.

2.3.1. Collision Time Estimation

As stated in Section 2.2.1, the START detector is used to measure the time a beam ion traversed the target. If the ion collides with a target nucleus, the time measured by the START detector is used as the time the collision took place. However, due to the high intensity of the beam, often there are multiple hit candidates in the START detector and the correct one needs to be identified.

In the first step, the raw START detector hits, extracted from the HLD data, are calibrated using the parameters obtained from the calibration process described in Section 3.1. Next, the first calibrated START detector hit in a rough time window of ± 25 ns around the zero point in time is selected as the preliminary hit defining the collision time. Afterwards, the raw hit data from the META detectors RPC and TOF are calibrated and translated to single physical hits. Multiple hits that most probably are caused by the same particle are merged together in clusters. In the next step, the three fastest hits in the RPC and TOF detector are selected and their times are normalized to a distance of 2100 mm to the target region. Since the three fastest particles of a reaction most probably have velocities close to the speed of light which amounts to roughly 300 mm/ns, their times of flight normalized to a distance of 2100 mm has to be close to 7 ns. Finally, the three fastest times of flight are averaged and the START detector hit closest to -7 ns, is selected as the hit determining the most probable collision time. In case no START detector hit is found in an interval of ± 2 ns around -7 ns, the event gets discarded. Multiple hits in the START detector with a temporal difference of less than 0.5 ns were most probably caused by the same ion. In that case their measured times are averaged.

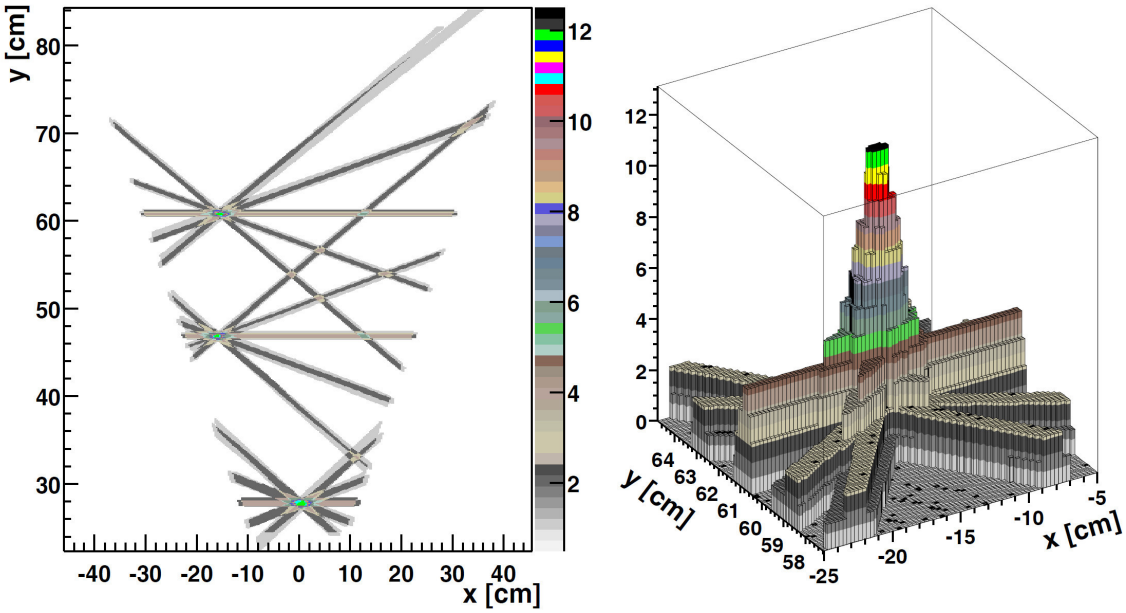

Figure 2.9.: Active wires projected onto the common projection plane between MDCs I and II or III and IV respectively. The 2D view in the left shows three clusters at the intersection points of multiple activated wires. The 3D view in the right demonstrates how the required thresholds to identify a cluster remove random intersections between activated wires [32].

In the following steps, the data of the other detectors are processed and particle tracks are reconstructed as described in Section 2.3.3. To improve the precision of the collision time estimation further, the tracks of the most abundant particle species, namely protons and pions, are identified by rough selection criteria. Using Equation 2.1 with their reconstructed momenta as well as their well known rest masses [184], their expected velocities and thereby their expected times of flight can be calculated. Finally, the measured collision time is adjusted to improve the accordance between the measured times of flight and the times of flight calculated from the momenta according to:

$$\beta = \frac{p}{\sqrt{p^2 + m_0^2}} \tag{2.1}$$

2.3.2. Collision Vertex Estimation

Like the collision time, the spacial position of the collision, also called primary collision vertex, is an observable required for many subsequent measurements. Identifying a particle using the method described in Section 3.4.1 requires the total flight length of the particle in addition to its time of flight. As almost all particles, created in a collision, emerge directly from the primary collision vertex, integrating a particle trajectory between the primary collision vertex and the measured META hit, gives the total flight length of the particle. In the HADES experiment three different methods to estimate the primary collision vertex are used. They are sorted by increasing precision, however, they also increasing levels of the particle track reconstruction:

MDC-Cluster-Vertex: This vertex is determined as the first step of the track reconstruction and serves as a starting point for the cluster finding in the inner two MDCs, described in Section 2.3.3. To determine it, a common projection plane between MDC planes I and II is defined, as shown in Figure 2.10. For each of the 15 target segments as well as for the START detector, the active wires from MDCs I and II are projected to the projection plane with the corresponding positions serving as the view points of the projections. Figure 2.9 gives an example of how such a projection looks like. Afterwards, the resolutions of the intersection points of multiple active wires are quantified. Finally, the target segment with the best resolution is selected as the position of the MDC-Cluster-Vertex. Obviously, due to the applied method, the vertex has no resolution in the xy plane and only 16 possible z positions, corresponding to the 15 target segments and the START detector. Nevertheless, the found target segment matches the one found by the more precise Track-Candidate-Vertex in most cases.

Inner-MDC-Track-Segment-Vertex: As the name implies, this vertex requires at least one successfully reconstructed inner track segment. First, the inner track segments are extrapolated towards the target region assuming straight tracks due to the vanishing magnetic field in this region. Afterwards, the Inner-MDC-Track-Segment-Vertex is determined as the average point of closest approach of all extrapolated inner track segments. The quality of the vertex is estimated using a χ^2 value in combination with the distances of closest approach of all inner track segments. Unlike the MDC-Cluster-Vertex, the Inner-MDC-Track-Segment-Vertex provides non-discrete positions in x, y and z direction.

Track-Candidate-Vertex: This vertex is estimated based on fully reconstructed track candidates and thereby requires the full track reconstruction to be executed in advance. The track candidates are extrapolated towards the target region using the Runge-Kutta parametrization from the final step of the track reconstruction procedure. Afterwards, the Track-Candidate-Vertex is determined analogue to the Inner-MDC-Track-Segment-Vertex as the point of closest approach of all track candidates. Additionally, a χ^2 value quantifying the quality of the vertex is calculated.

In general, the precision of all methods for the estimation of the primary collision vertex increases with the amount of available particle tracks. Therefore, the event vertex reconstruction is more precise for central collisions than for peripheral ones. Due to the use of fully reconstructed tracks, which provide a precise Runge-Kutta parametrization of the trajectory, the Track-Candidate-Vertex yields the highest resolution and is therefore used throughout this thesis. However, the precision can be increased further during the analysis as described in Section 3.7.

2.3.3. Reconstruction of Particles

The reconstruction of particles involves several steps required to deduce their properties from raw detector hits. At first, their trajectories are reconstructed from the hits in the four MDC planes in combination with the known magnetic field between plane II and III. This procedure is referred to by the term "Tracking" and requires a sophisticated method to distinguish between actual trajectories and random combinations, especially in heavy-ion collisions with large amounts of particles traversing the detectors. Afterwards, the reconstructed trajectories are matched with the hits in the META detectors and the momentum of the particle is reconstructed based on its deflection in the magnetic field. The full process is schematically shown as a flowchart in Figure 2.11 and can be divided into four steps which will be explained in more detail in the following sections.

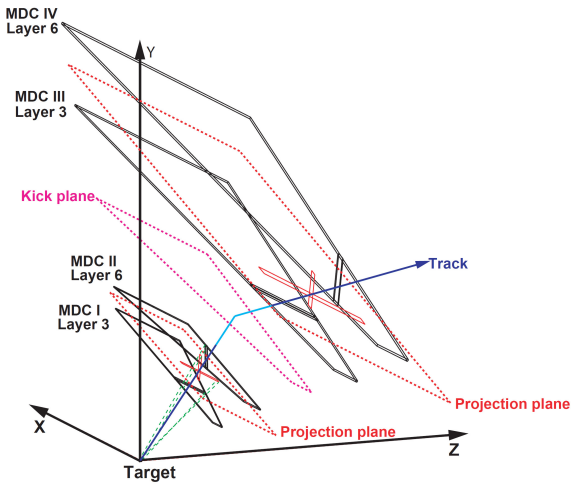

Figure 2.10.: Schematic view of the virtual projection planes between MDCs I and II or III and IV respectively. Furthermore, the virtual kick-plane in the center of the magnetic field region is shown as well as a trajectory showing how the deflection in the magnetic field can be approximated by an instantaneous deflection at the intersection point with the kick-plane [32].

2.3.3.1. Inner Clusters and Track Segments

In the first step, after the MDC-Cluster-Vertex (cf. Section 2.3.2) has been determined, the clusters and track segments of the two inner MDC planes I and II are searched. Therefore, the areas around each active wire corresponding to the measured drift times are projected to the hypothetical projection plane located between the chambers, with the MDC-Cluster-Vertex serving as the view point of the projection. Such a projection is exemplary shown in Figure 2.9. Using the projection, the intersection points of multiple active wires are searched. To suppress random intersections a minimum amount of active wires contributing to an intersection point are required ($N_W > N_{thres}$). Iteratively, the intersection point with the highest resolution not yet processed is selected as a cluster. This process corresponds to the yellow box in Figure 2.11.

Off-Vertex-Cluster

In heavy-ion collisions most particles originate from the primary collision vertex. Therefore, in the first iteration of the inner cluster and track segment finding routine, the MDC-Cluster-Vertex (cf. Section 2.3.2) is used as the view point of the projection of the active wires. However, there are also charged particles created at secondary vertices like in case of weakly decaying hadrons. Since the clusters of their trajectories are not pointing to the primary collision vertex, they are called Off-Vertex-Cluster. Using the standard cluster finding method, their reconstruction efficiencies are low compared to those originating from the target region. The effi-

ciencies are increased by processing all active wires that have not been assigned to a cluster in the first iteration of the cluster finding routine in a second iteration. This second iteration corresponds to the orange box in Figure 2.11 and aims at finding intersection points of multiple active wires independent from their pointing. Therefore, first a list of all active wires that have not been assigned to a cluster in the first iteration is created. In this list, combinations of two wires from MDC I and two wires from MDC II intersecting each other and with a minimum angle of 40° between them, are searched. Afterwards, the line connecting the intersection points is created and all active wires close to this line are added. If this amount of active wires exceeds a threshold lower than the one used in the first iteration, an Off-Vertex-Cluster is created and added to the list of all clusters found. This procedure is repeated until no further Off-Vertex-Cluster are found.

Finally, the inner track segments are build from the identified cluster. Therefore, straight tracks are assumed, due to the vanishing magnetic field in the region of the two inner MDC planes. For each cluster found, an inner track segment is created and adjusted to the spacial positions measured by the MDC wires participating in the cluster using a χ^2 minimization technique. The resulting χ^2 value can afterwards be used as a quality indicator for the inner track segment as well as the complete track created from it.

Especially the cluster and track segment reconstruction in the inner two MDC planes suffers from fake correlations due to the high track density. To cope with these contamination, dedicated fake-rejection criteria like for example the already mentioned minimum amount of wires contributing to a cluster are applied.

2.3.3.2. Outer Clusters and Track Segments

The reconstruction of clusters and track segments in the outer MDC planes III and IV follows the same principle as for the inner MDC planes I and II. However, due to the deflection of the particles in the magnetic field, the primary collision vertex cannot be used as the view point for the projection towards the common projection plane. This problem is solved by approximating the continuous deflection of the particles in the magnetic field by an instantaneous deflection when the particles cross a virtual plane in the center of the magnetic field, called kick-plane, which is schematically shown in Figure 2.10. Using this approximation, the intersection points of the extrapolated inner track segments with the kick-plane can be used as the view points for the projection of the active wires from the outer MDC planes towards their common projection plane.

Using these view points, the clusters in the outer two MDC planes are identified individually for each found inner track segment with the same method already used for the inner two MDC planes. Afterwards, the outer track segments are created from the identified clusters in the outer MDC planes, again using the same method as for the inner two MDC planes, resulting in another χ^2 value that can be used as a quality indicator for the outer track segment as well as the complete track created from it. Finally, similar fake rejection criteria as for the inner track segments are applied to the outer track segments. The individual combinations of an inner MDC track segment with the outer MDC track segments found using its intersection point with the kick-plane, are now called a track candidate.

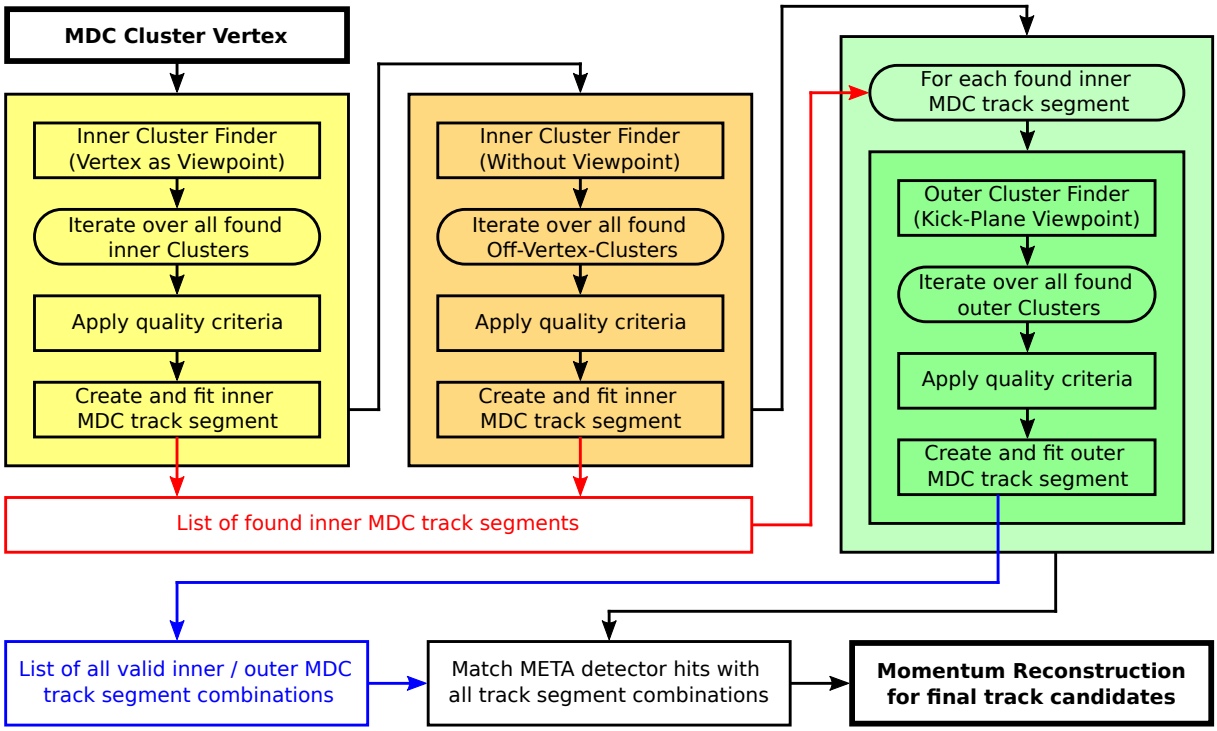

Figure 2.11.: Flowchart of the track reconstruction procedure. The colored arrows show how the found inner MDC track segments (red) and the found combinations of an inner and an outer MDC track segment (blue) are accumulated in global lists. The boxes represent the executed steps with the rounded boxes corresponding to loops. Their sequence is shown by the black arrows, starting with the MDC-Cluster-Vertex as input for the two iterations of the inner MDC cluster and track segment finding procedure, depicted in yellow and orange and described in Section 2.3.3.1. Afterwards follow the outer MDC cluster and track segment finding procedures, depicted in green and described in Section 2.3.3.2, the matching with the META detector hits, described in Section 2.3.3.3 and the momentum reconstruction, described in Section 2.3.3.4 which results in final track candidates.

2.3.3.3. META Hit Matching

In the next step, the reconstructed outer track segments are matched against the reconstructed hits in the META detectors to assign time of flight measurements to the reconstructed trajectories. Therefore, the track segments are extrapolated towards the planes of the META detectors and the intersection points are calculated. The accordance between an intersection point and a possible hit in the META detectors is quantified by the so called META Match Quality (MMQ) parameter which is calculated by Equation 2.2.

$$MMQ = \sqrt{\frac{dx^2}{\sigma_x^2} + \frac{dy^2}{\sigma_y^2}} \tag{2.2}$$

In this equation dx and dy represent the distance between the calculated intersection point and the measured hit in the coordinate system of the plane of the META detector. σ_x and σ_y represent the corresponding spacial resolutions of the META detector at the

hit position which strongly depend on the position in polar direction due to the setup of the META detectors. The resulting MMQ value can be interpreted as the distance between the intersection point and the META hit given in standard deviations. Finally, all combinations of outer segments and META hits with a MMQ value smaller than 10 are accepted. In heavy-ions collision events with high hit densities in the META detectors, further restrictions on the distance in y-direction are applied in the analyses later on. These restrictions, which will be described in more detail in Section 3.3, are required to reduce the amount of tracks matched with wrong META hits, since the spacial resolution of the META detectors in y-direction is limited solely by their cell sizes. Similar procedures are also used to match the outer segments with the hits in the ECAL detector and the inner segments with the centers of the rings, measured by the RICH detector.

2.3.3.4. Momentum Reconstruction

The momentum of a charged particle is reconstructed from its deflection in the magnetic field. Using Equation 2.3 [184] the momentum of a particle p can be calculated from its deflection radius R, its charge number z, its pitch angle to the magnetic field λ and the magnetic field strength B. Since only the sign of the charge number can be deduced from the direction of the deflection, but not its absolute value, an absolute charge of 1 is assumed for all particle tracks. Therefore, the reconstructed momentum is actually the momentum over charge ratio p/z, which needs to be considered for particles carrying multiple elementary charges like Helium or Lithium nuclei.

$$p \cos \lambda = zeBR \tag{2.3}$$

In the HADES experiment three different methods are used to calculate the momentum of a particle from its reconstructed trajectory. In the following, the three methods are explained, sorted by increasing precision, however, they also increase in the required computational power:

Kick-Plane Method: This method is the most simple and fastest approach to estimate the momentum of a charged particle track. It utilizes the same approach used to determine the view points for the reconstruction of clusters and track segments in the outer two MDC planes III and IV, as described in Section 2.3.3.2. Therefore, the continuous deflection of a particle in the magnetic field is approximated by a single instantaneous deflection as the extrapolated trajectory crosses the kick-plane located in the center of the magnetic field as shown in Figure 2.10. Unfortunately, due to the strong inhomogeneity of the magnetic field, the momentum resolution of this method is limited, which requires more sophisticated methods.

Cubic Spline Method: This method is an extension of the kick-plane method, providing a higher precision in the reconstruction of the momenta. Using the intersection points of the inner and outer track segments with the center planes of the four MDC detectors, the trajectory in the region of the magnetic field between MDC plane II and III is interpolated using a cubic spline model. Afterwards, the trajectory between MDC plane II and III is divided into 49 segments of equal length and the continuous deflection of the particle is approximated by 50 instantaneous deflections

at the edges of these segments. Using the analytic derivative of the cubic spline at these points together with a precise map of the magnetic field, allows to calculate the momentum for each of the 50 points individually. The final momentum is obtained by averaging the 50 individually reconstructed momenta and applying systematic corrections obtained from simulations. Although the obtained momenta are more precise than the ones of the kick-plane method, some effects like the non-toroidal magnetic field geometry close to the edges of the sectors where the coils sit, or the remaining magnetic field in the regions of the inner and outer track segments are not taken into account. This makes the more accurate Runge-Kutta method necessary, especially for low momenta particles.

Runge-Kutta Method: This method provides the highest precision of all methods for the momentum reconstruction implemented for the HADES experiment and is therefore the standard method used in high-end analyses. However, it also requires the most computational power compared to the other methods. It utilizes the Runge-Kutta method [124, 157] to solve the differential equation of motion of a charged particle over the complete spacial range of its trajectory numerically. The Lorentz force is hereby calculated using the three dimensional map of the magnetic field together with the estimated momentum. Afterwards the accordance between the Runge-Kutta trajectory and the measured hits in the four MDC detectors is quantified by a χ^2 technique yielding the ${\chi^2}_{\mathrm{RK}}$ value. In an iterative χ^2 minimization procedure, starting with the results from the cubic spline method, the momentum is adjusted so that the measured MDC hits are best described by the Runge-Kutta trajectory. Furthermore, the final ${\chi^2}_{\mathrm{RK}}$ value can be used as a quality indicator for the momentum reconstruction as well as the complete track reconstruction.

Further information on the reconstruction of particle tracks as well as the momentum determination methods in the HADES experiment can be found in [32].

2.3.4. Simulated Events

The term "Simulated Events" refers to events consisting of particles with known properties generated according to a given model for which the responses of the detectors are simulated and that pass through the same reconstruction procedure like the experimental data. In the analysis of experimental data they are of great importance since the comparison of initially generated particles with the particles finally reconstructed allows to deduce properties of the detector and the applied procedures that cannot be deduced from experimental data. These properties include but are not limited to the spacial acceptance of the detectors, inefficiencies due to the limitations of the detectors and the electronics as well as the efficiencies and resolutions of the applied reconstruction and analysis procedures. However, the generation of simulated events that match the properties of experimental data is challenging.

For the HADES experiment primarily two generators for simulated particles are used. Both of them are based on the Monte-Carlo (MC) method to generate randomized results that fulfill given criteria on average. In the following, they will be shortly introduced:

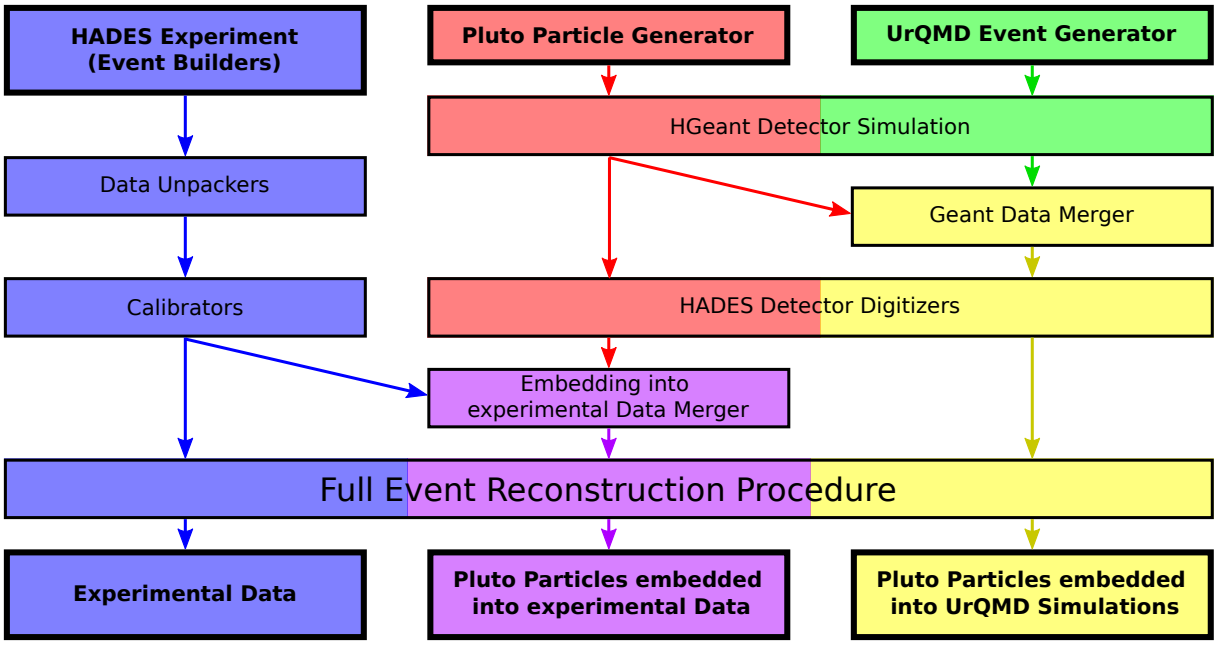

Figure 2.12.: Flow chart of the steps to produce DSTs prepared for further analyses from experimental data (blue), Pluto particles (red) and UrQMD events (green). The features of DSTs with Pluto particles embedded into UrQMD simulations (yellow) or into experimental data (purple) are discussed in Section 2.3.4.

The UrQMD Transport Model: For the HADES experiment version 3.3p2 of the Ultra relativistic Quantum Molecular Dynamics (UrQMD) event generator is used to simulate the reactions occurring in the collision of two nuclei with given energies using a microscopic transport approach. Information on the underlying methods and implementations as well as the capabilities and limitations of the model can be found in [59, 69].

The Pluto Particle Generator: Unlike the UrQMD event generator, Pluto does not simulate the underlying reactions leading to a final state, but only the final state itself by assuming the particles to be emitted from a source with a given kinematic distribution. Furthermore, for unstable particles it can be specified via which decay channels and with which branching ratio they are supposed to decay for which also the daughter particles are simulated. Further information on the underlying methods and implementations as well as the capabilities and limitations of the generator can be found in [91].

The use of purely simulated events poses some problems: Due to the complicated underlying processes, the kinematic distributions of the particles are usually unknown. Limitations of the generator can influence the generated particle species, like for example UrQMD does not generate any nuclei in the final state. In a realistic simulation rarely produced particles, like particles containing strangeness at HADES energies, or rare decay channels, like the dilepton channel of vector mesons, occur also rarely. Thus, they do require large amounts of simulated events to gain a significant amount of the process of interest in the analysis.

These problems are dealt with by using Pluto to generate purely the specific particle or decay channel of interest with a given kinematic distribution and embedding one of this particle into each simulated UrQMD event. Unfortunately, for the previous Au+Au dataset it was shown that using this method the simulated reconstruction efficiencies of particle tracks involving an Off-Vertex-Cluster (cf. Section 2.3.3.1) are significantly higher than expected from particle tracks not involving Off-Vertex-Cluster [170]. These observations were confirmed in the analyzed Ag+Ag data. It was concluded that these problems are a result of several sources of spurious particles present in experimental data but not taken into account in purely simulated events. Therefore, a procedure to embed the particles generated by the Pluto event generator into experimental events has been developed.

Figure 2.12 shows the processes conducted to produce the three kinds of DSTs (experimental events and Pluto particles embedded into either experimental or UrQMD events) schematically. Experimental data are first processed by the so called Unpackers that convert the raw bytestream from the detectors FEEs stored in the HLD files (cf. Section 2.2.9) into information on the hits detected by the individual sub-detectors. Afterwards, detector specific calibration procedures are applied to the raw hit information by the Calibrators. The resulting information are then processed by the track reconstruction procedure already described in Section 2.3.3.

In case of simulated particles, first the interactions of the particles in the detector material as well as the magnetic field are simulated. Therefore, the HGeant package, based on the GEometry And TRacking (GEANT) 3.21 package [73], comprising the full three dimensional geometry of the HADES detector system as well as all used materials and their properties, is used. The package samples all processes occurring when a particles traverses the detector system, like interactions with matter (e.g. energy loss or multiple scattering), the interaction with the magnetic field due to the Lorentz force, but also the decays of unstable particles, using a Monte-Carlo approach. After the interactions have been simulated for Pluto and UrQMD particles independently, they are merged to generate simulation data with Pluto particles embedded into UrQMD events. In the next step, the detector hits in the sub-detectors are generated from the interactions simulated by GEANT with the help so called Digitizers by mimicking the response behavior of the detector as well as the connected electronics. In case of Pluto particles embedded into UrQMD events, the resulting hits are now processed by the same event reconstruction procedure that is used for experimental data. In case of Pluto particles embedded into experimental events, the simulated hits of the Pluto particles from the Digitizers are merged with the calibrated hits of experimental data from the Calibrators taking into account specific detector properties like resolutions to decide whether two hits need to be merged into one. Afterwards, the hits are also processed by the event reconstruction procedure.

For simulated particles, the original particle properties are transported through the complete chain of simulation and reconstruction steps. Since they finally are processed by the exact same event reconstruction procedure as experimental events, the differences between experimental and simulated events are limited to differences between the used event generator and reality as well as the accuracy of the simulation of the detector responses. The accordance between experimental and simulated events will be discussed in Section 3.3.

2.4. The March 2019 Ag+Ag Beam Time

In March 2019 the HADES collaboration conducted a measurement campaign, also called "beam time", of heavy-ion collisions. ^{107}Ag ions were impinged on the Silver target, described in Section 2.2.2, which is made of natural Silver [127], consisting of 51.8 % ^{107}Ag and 48.2 % ^{109}Ag [65] isotopes. The measurement campaign was split into three different phases of datataking for physics analyses as well as additional datataking periods for commissioning and calibration purposes. The specifications of the different phases are summarized in the following Table 2.1:

Property	**Phase 1**	**Phase 2**	**Phase 3**
Collision system	^{107}Ag + ^{107}Ag (51.8 %) and ^{107}Ag + ^{109}Ag (48.2 %)		
Beam energy	1.58A GeV	1.23A GeV	
Beam intensity	1.5 – 3.5 MHz		
Magnet current	3200 A	2500 A	200 A
Duration	430.9 h	39.1 h	6.3 h
Events recorded	13.64×10^9	1.32×10^9	0.24×10^9
Mean event rate	8.8 kHz	9.4 kHz	10.7 kHz
Data recorded	333.6 TB	29.3 TB	5.5 TB
Mean data rate	215.1 MB/s	208.2 MB/s	239.9 MB/s

Table 2.1.: Specifications and characteristics of the three phases of the March 2019 measurement campaign.

With a grand total of 15.28 billion recorded collisions and 368.1 TB raw data including commissioning and calibration data, the March 2019 beam time comprises the largest amount of data ever collected by the HADES collaboration in a single beam time. In the analysis described in this thesis only data from the major phase 1 of the beam time are analyzed. The trigger settings used for the datataking are described in Section 2.2.9.

The experimental data are recorded in blocks of events, so called runs. For the March 2019 beam time one of these runs contains on average 450,000 events corresponding to 50 seconds of datataking. In total 32966 runs were recorded. In the procedures described in the following Chapter 3 data collected within such a run are often used to study the performance of the detector system over the whole beam time. Furthermore, since it is almost impossible to ensure a constant performance over the full duration of the beam time of almost an entire month, many methods are applied on single runs in order to take performance variations of the detector system into account. Therefore, it is assumed that all performance changes within the duration of one run are negligible.

3. Analysis Methods

In this chapter all methods and procedures required to perform the physics analyses, which will be described in Chapter 4, are explained. These include the filtering of events and tracks, the identification of particles, the estimation of the centrality of the collision as well as further methods specifically for the reconstruction of weakly decaying particles. Additionally, the calibration procedure for the START detector required to assure precise reaction time measurements is described in the following Section 3.1.

3.1. START Detector Calibration

The calibration procedure of the START detector can be split into two steps: First, the constant delays[1] between all strips of the START detector and all pads of the VETO detector are compensated by individual offsets. In the second step, the offsets are adjusted for each run of the beam time individually making use of the measured times of flight and momenta of π^- tracks. After this calibration the the START detector reaches a time precision of approximately 50 ps (σ).

The primary aim of the first step of the calibration procedure is to compensate constant delays between the strips of the START detector and the pads of the VETO detector such that all measured times can be correlated to each other. One of the most dominant source of delays between the strips and pads are differences in the length of the wires that connect the detector with its FEE. At an electrical signal speed of approximately 2/3 of the speed of light, which corresponds to ≈ 20 cm/ns, divergences of only a few millimeter in the wire lengths result in non-negligible delays due to the signal transmission times. Furthermore, different thresholds to suppress electrical noise as well as different amplifications in the strips and pads lead to delays of the measured times. This is a consequence of signals with low amplitudes needing more time to exceed a certain threshold than signals with high amplitudes, in the following also referred to as time-walk effect. Fortunately, if a single strip of the START detector or pad of the VETO detector is considered the time-walk effect between the signals of different beam-ions can be neglected since all beam-ions have the same charge and energy and thereby induce similar shaped signals.

The calibration is executed in the following way: First, all START and VETO hits within an event are collected and the delays between the START and VETO hits are calculated. For each possible combination of a START strip with a VETO pad the distribution of these delays is plotted. The distributions show a peak structure as a result of correlated START and VETO hits caused by the same beam-ion and a continuous background as a result of uncorrelated hits caused by different beam-ions. Next, the most abundantly hit strip of the START detector is searched. For the analyzed Ag+Ag beam time this is strip 3 in x-direction. For the eight delay distributions corresponding to the eight

[1] Differences between the measured times when a single beam-ion is detected by multiple strips or pads.

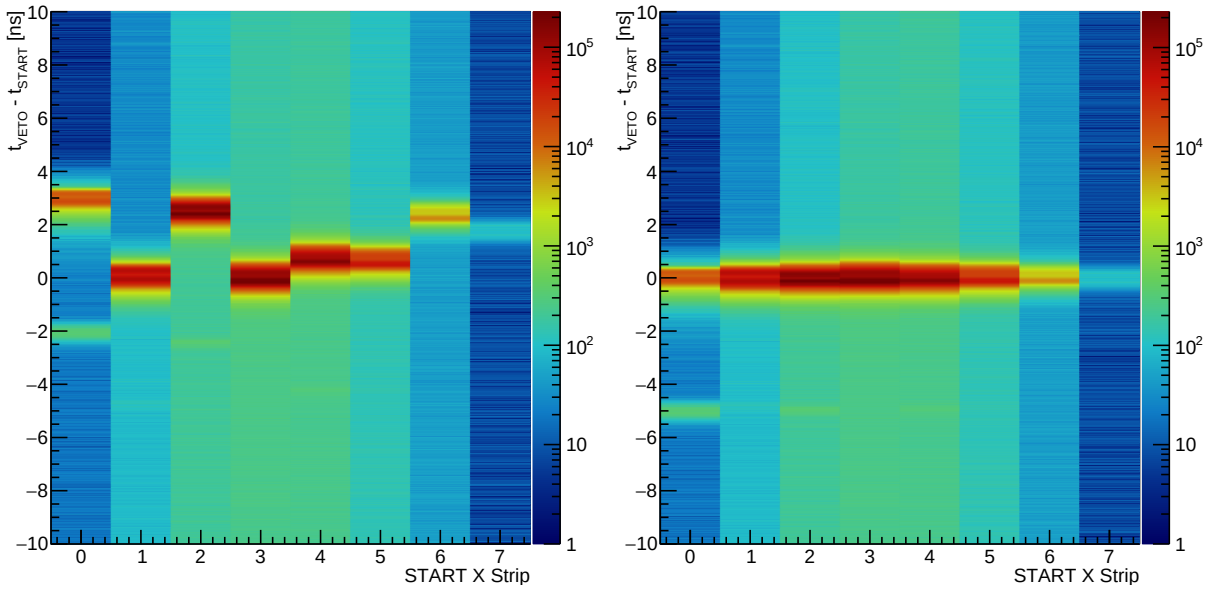

Figure 3.1.: Delays between the eight most abundantly hit strips in x-direction of the START detector and the most abundantly hit pad 4 of the VETO detector. The left plot shows the distributions before and the right plot after the first step of the START detector calibration procedure has been applied.

VETO pads and the single selected START strip, the most probable value of the peak structure is determined using a Gaussian fit function. These values are used as offsets to compensate the constant delays between the VETO pads and thereby constitute the calibration for the VETO detector. Afterwards, the procedure is repeated conversely to determine the calibration offsets for the START strips: First, the most abundantly hit pad of the VETO detector (Pad 4 in the analyzed Ag+Ag beam time) is determined. Now, the most probable values of the delay distributions of the various START strips with this single selected VETO pad are determined and used as offsets to compensate the delays between the START strips.

Figure 3.1 shows the delay between the START and VETO hits along the y-axis for the eight most abundantly hit START strips in x-direction on the x-axis and the single selected VETO pad 4 used to determine the calibration offsets for the START strips. The distributions before the calibration procedure is applied are shown in the left and the the distributions afterwards in the right. In both plots the peak structures due to correlated START and VETO hits as well as the uncorrelated background are clearly visible. The applied calibration offsets compensate the delays between the various START strips in general. However, some START strips (e.g. strip 0) show a second peak structure at least one order of magnitude less abundant than the primary peak structure and shifted by 5 ns. Furthermore, if one investigates the peak structures precisely, one notices sub-structures. Both effects can be attributed to changes in the detector performance over time which are not accounted for in the first step of the START detector calibration. Nevertheless, a time precision of $\approx$ 110 ps (σ) is achieved on average after the first calibration step.

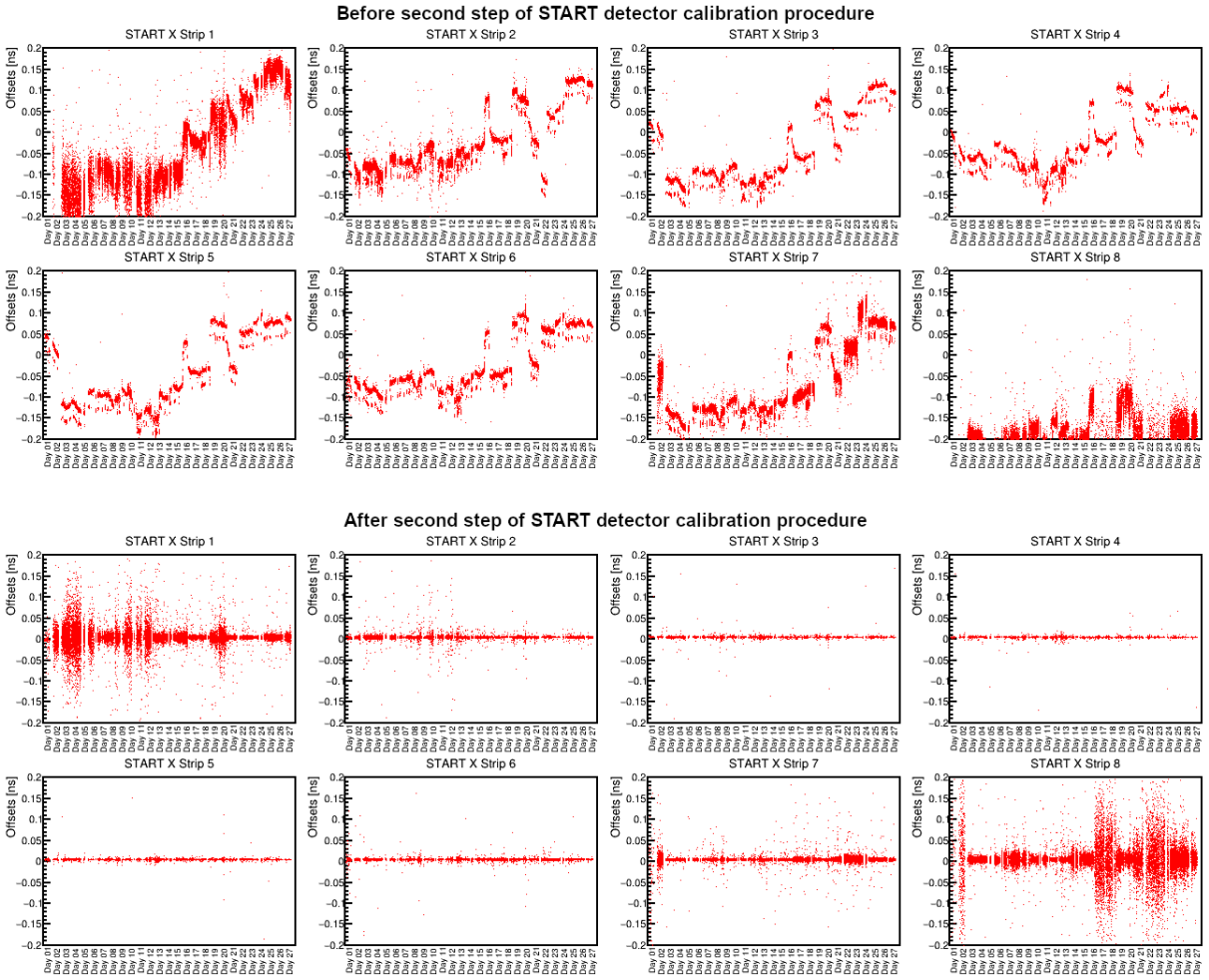

Figure 3.2.: Average temporal difference between times of flight measured by the RPC detector and times of flight calculated from the measured momentum for π^- tracks for each run of the whole beam time. Only the eight most abundantly hit strips in x-direction of the START detector are shown. The upper two rows show the differences before and the lower two rows after the second step of the START detector calibration procedure has been applied.

To improve the precision of the time measurement further, changes in the detector performance over time, that generate the previously mentioned sub-structures as well as the shift of the secondary peak (see Figure 3.1), need to be taken into account. These performance changes are a result of changing delays due to the time-walk effect when the signal thresholds or the amplification voltages are changed. Such changes are inevitable in order to keep the required detection efficiency although the crystal structure of the detector gets damaged by the irradiation from the heavy-ion beam. Furthermore, also temperature changes in the detector material or its FEE can lead to non-negligible delays. To compensate for such effects, in the second step of the START detector calibration procedure the offsets for the START strips are adjusted individually for each run using the measured momenta of π^- tracks.

Without a proper reaction time measurement, the identification of particles using the method described in Section 3.4.1 is impossible. π^- tracks however can be identified requiring just a negative polarity and a momentum larger than 300 MeV/c as contributions from other charged hadrons are negligible small under those selections. As the RPC detector provides a better time resolution than the TOF detector, only π^- measured in the RPC detector are taken into account. Using Equation 2.1 the speed of the identified π^- tracks is calculated from the nominal pion mass [184] and the measured momentum. Together with the length of the reconstructed trajectory between the primary event vertex and the META detector hit, the expected time of flight is calculated. Next, the distributions of the differences between the actually measured time of flight and the calculated time of flight are created for each strip of the START detector and each run of the beam time. Like in the first step of the calibration procedure, the means of those distributions are determined using a Gaussian fit function and are used as additional offsets for each run individually. Together with the offsets determined in the first step, the calibration parameters for the START detector are now complete.

Figure 3.2 shows the offsets determined in the second step of the START detector calibration procedure. Each of its panels represents one of the eight most abundantly hit strips of the START detector in x-direction. The offsets off all runs of the beam time are given by the small red dots with their position within the beam time on the x-axis. The upper two rows show the offsets finally used for the calibration. One clearly sees that all strips of the START detector show comparable trends since in most cases the conditions of all strips of the detector change simultaneously. As a cross check and in order to determine the final temporal precision of the detector, the offsets are recalculated after the full event reconstruction procedure has been repeated with the final calibration parameters. These offsets are displayed in the lower two rows of Figure 3.2. Ideally, they should all show exactly 0. However, since in the event reconstruction procedure many criteria are defined relative to the measured reaction time, the sample of π^- tracks changes which is why the determined offsets get smeared around 0 by statistical fluctuations and the resolution of the measurement. Nevertheless, the plots show that the procedure successfully compensates fluctuations in the performance of the START detector over the beam time.

Finally, after the full calibration procedure for the START detector has been applied a time precision of $\Delta t_0 \lesssim 50$ ps (σ) is achieved on average. This result falls in line with the temporal resolution determined for the previous Au+Au beam time in which a similar detector setup like for the analyzed Ag+Ag beam time was used [145].

3.2. Event Selection Criteria

The triggered and recorded collisions, called events in the following, are tainted by events that have to be excluded from the physics analyses for various reasons. The following list gives some examples:

- **Peripheral events:** The size of the hot and dense phase created in a collision scales with the number of participating nucleons and thereby with the centrality of the collision. Therefore, central events are of greater importance than peripheral ones for analyses aiming to study the hot and dense phase.
- **Events that cannot be analyzed by the standard reconstruction methods:** Events for which an important information, like the reaction time, measured by the START detector, is missing. In this case the flight times of charged particles and thereby their masses cannot be deduced by the standard method (cf. Section 3.4.1).
- **Events originating from reactions outside the target:** These occur when beam-ions react with material like the START detector or the mounting structure of the target. Since these materials contain mostly Carbon, a significant proportion of events from the Ag+Ag beam time were actually Ag+C collisions.
- **Events including particles from more than one collision (Pile-Up):** In case two reactions occur shortly after each other, the detectors are not able to distinguish between particles from one or the other reaction. Therefore, the particles cannot be clearly assigned to the two reaction times which hampers proper time of flight measurements or to the two primary event vertices which strongly influences the Off-Vertex-Topology parameters described in Section 3.6. Furthermore, due to the larger amount of particles measured simultaneously, the efficiencies of both the detectors and the reconstruction procedures suffer. Such events are mostly caused by quick intensity fluctuations of the heavy-ion beam.
- **Events in which a part of the detector system was not operational:** Problems with parts of the detector systems causing slightly lowered efficiencies do not bias the physics results since the simulations are tuned to reproduce the average efficiencies of the detector systems. However, if a significant part of the detector system fails the influences are not averaged out which is why the affected events need to be removed.

Problematic events are identified in two steps: In the first step, nine predefined quality criteria are applied. Afterwards, the average amounts of the most abundant hadrons, π^-, π^+ and protons, as well as e^+ and e^- per event are calculated for each sector and each run. In case one of these averages diverges more than a fixed proportion from the corresponding daily average, all events from this run are not used in the analyses later on. This procedure will be described in more detail in Section 3.2.1.

The following list defines the nine quality criteria used in the first step of the event selection procedure. They are listed in the same order like in Figure 3.3 which shows the proportions of events remaining accepted after applying the criteria sequentially and the proportion of events rejected by each criterion.

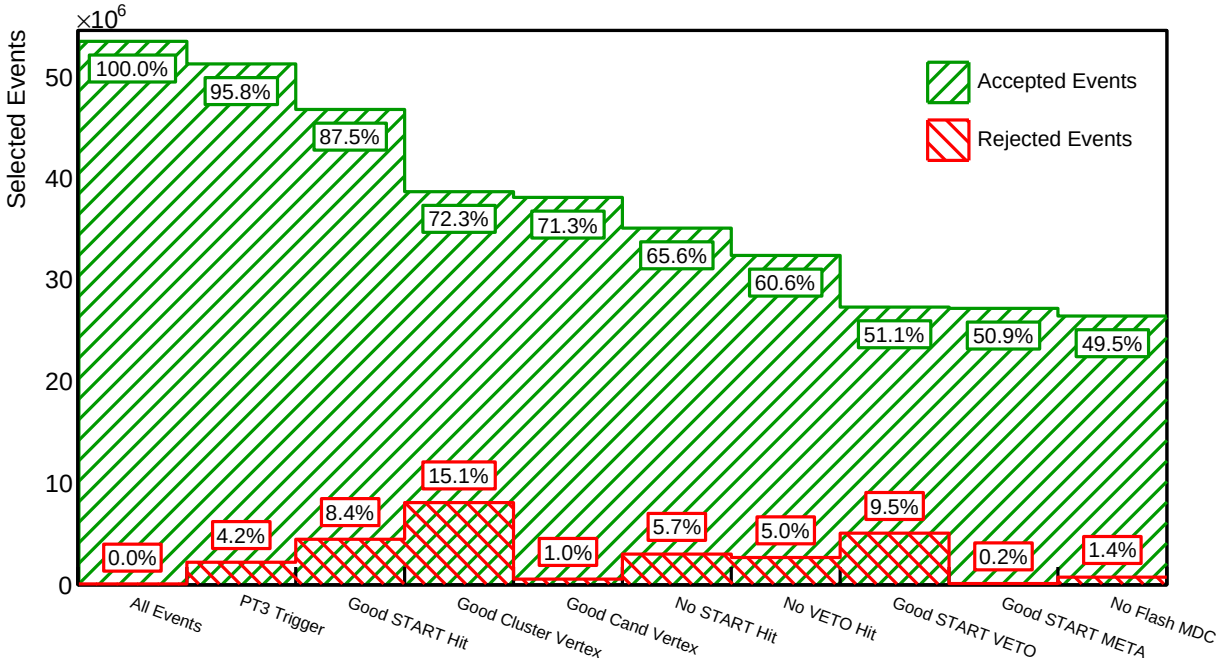

Figure 3.3.: Event reduction by the various criteria to discard problematic events. The green bars show the amount of events accepted after the corresponding selection criteria have been applied sequentially, the red bars show how many events are removed. The plot was generated with a sub-sample of $\approx$ 54 million recorded events which are representative for all events analyzed in this thesis.

- **Physics Trigger 3:** As the name implies, this criterion requires a positive PT3 Trigger decision as a first pre-selection of central collisions. In the analyzed beam time, the PT3 Trigger requires 20 hits in the RPC and TOF detector which is fulfilled by the $\approx 55\%$ most central Ag+Ag events. A more accurate centrality estimation is performed using the method described in Section 3.5 later on.
- **Good START Hit:** This criterion requires that both steps of the collision time estimation, described in Section 2.3.1, succeed. The first step of the procedure is considered successful if a preliminary START detector hit is found. The second step is considered successful if in addition a START detector hit inside the defined ± 2 ns window is found. The purpose of this criterion is to reject events in which the flight times of charged particles cannot be determined by the delay between their META hit and the selected START hit. Knowing the flight times of charged particles is required to identify them via the method described in Section 3.4.1.
- **Good Cluster Vertex:** This criterion is based on the MDC-Cluster-Vertex, which is determined as described in Section 2.3.2. It requires a successfully estimated event vertex with a position corresponding to one of the 15 target segments. Thereby, events, in which a Ag+C or Ag+Au reaction took place in the START detector, are almost entirely removed. This is necessary, because the centrality estimation, described in Section 3.5, assumes pure Ag+Ag events. Furthermore, since these collision systems are asymmetric, particles emerging from them have different kinematic distributions and therefore bias the physics results.

- **Good Candidate Vertex:** This criterion is strongly correlated to the previous one since it also rejects events from outside the target region by the estimated primary vertex. However, it utilizes the more precise Track-Candidate-Vertex whose estimation procedure is also described in Section 2.3.2. The criterion requires a successfully estimated vertex with a z-coordinate larger than -70 mm which roughly corresponds to the region of the target.
- **No additional START Hit:** This criterion is used to reject events in which multiple beam ions reacted in the target less than 15 ns after each other. In such events it is difficult to disentangle the particles of the different collisions. Thereby, it is also difficult to assign appropriate flight times to the particles which biases the particle identification method described in Section 3.4.1. The rejection is achieved by requiring that in a time window of $\pm$15 ns around the START detector hit, selected as described in Section 2.3.1, no further START detector hit was recorded. Since a single beam ion, traversing the START detector, can induce multiple hits due to crosstalk between adjacent channels as well as the two sides of the START detector which are treated independently, hits within a time window of $\pm$0.5 ns around the selected hit are accepted.
- **No VETO Hit:** This criterion requires that in the same time window used by the previous criterion of $\pm$15 ns around the selected START detector hit no VETO detector hit was recorded. Since only beam ions that did not react in the target are measured in the VETO detector and an event is only recorded when a Physics Trigger (cf. Section 2.2.9) decides that a reaction took place, this situation implies that at least two beam ions traversed the START detector shortly after each other. If, however, only one of them is detected due to detector inefficiencies, it cannot be guaranteed that exactly this ion reacted in the target and thereby the correct reaction time was measured.
- **Good START VETO:** This criterion is used to ensure that the detector signals of a collision that triggered an event are not tainted by detector signals from a secondary reaction that occurred later in time. Therefore, events in which a second reaction took place before all sub-detectors were read out need to be identified. This is achieved by identifying all START detector hits in a time window of 15-350 ns after the selected START detector hit and requiring each of them to have a correlated VETO detector hit within $\pm$2 ns around them.
- **Good START META:** This criterion has the same purpose as the previous one, but uses META detectors hits instead of VETO detector hits. This is advantageous as the presence of late hits in the META detectors proves that there is a contamination actually inducing detector hits. To identify the problematic events, first all START detector hits in a time window of 80-350 ns after the selected START detector hit are identified. Afterwards, all META detector hits measured in a time window of 7-12 ns after one of these secondary START detector hits are counted. Finally, the event is rejected if this amount exceeds the threshold of 4 hits.

- **No Flash MDC:** During the analysis of the Ag+Ag data it turned out that in some events almost all sense wires from one or more MDC chambers recorded hits. Such large amounts of active cells are unphysical and render an accurate reconstruction of MDC track clusters as described in Section 2.3.3 impossible, which is why these events need to be identified and removed. In further investigations it turned out that these commonly show low times over threshold and occur over the full recorded range of time, even prior to the trigger signal. Therefore, in order to reject these events with noise without biasing real events, the amount of activated sense wires with a time over threshold of less than 30ns that occurred earlier than 5 ns before the trigger signal are counted for each MDC chamber. Finally, in case a threshold of 20 is exceeded in one chamber, the event is removed (cf. [141]).

As it is shown in Figure 3.3 applying all of these nine criteria sequentially rejects approximately 50% of all events. The largest fraction of events is rejected by the Good Cluster Vertex criterion which primarily rejects Ag+C events from the START detector. Using Monte-Carlo Glauber-Model calculations, described in Section 3.5, it can be estimated that approximately the 25% most central Ag+C reactions fulfill the PT3 trigger condition and are thereby recorded by the HADES DAQ system.

The second largest proportion of events is rejected by the Good START VETO criterion. The reason therefore are primarily fluctuations in the ion rate of the heavy-ion beam within milliseconds, also called micro-spill-structure, leading to multiple ions traversing the experiment shortly after each other. This situation increases the probability of multiple collisions overlapping in time and more events need to be discarded. However, since the criterion requires a VETO hit, also actually unproblematic events are rejected if the VETO detector did not detect an beam-ion due to inefficiencies.

In addition, to clearly identify time ranges in which the reconstruction of particle tracks was influenced by problems in any of the involved sub-systems, a second step of selecting events, which will be described in the following Section 3.2.1, is required.

3.2.1. Run-wise Sector Selection

The aim of the run-wise sector selection is to determine the performance in measuring and reconstructing particle tracks for each of the six sectors in each run individually. This allows to identify and reject ranges of time in which a part of the detector system showed a significant diverging performance which cannot be accounted for in simulations and thereby also in the estimation of reconstruction efficiencies.

The performance of the track reconstruction is determined using the amount of tracks corresponding to the most abundant hadron species, namely protons, π^+ and π^-, as well as tracks identified as either e^+ or e^- tracks. The hadron tracks are identified using the corresponding 3σ regions in the momentum-velocity-plane, which are obtained as described in Section 3.4.1, on top of the standard track selection criteria, described in Section 3.3. The e^+ and e^- tracks are identified by requiring a successfully matched ring, measured in the RICH detector, in addition to the standard track selection criteria. Furthermore, a velocity β larger than 0.9 is required and the squareroot of the sum of the squared angular divergences in azimuthal and polar direction between their trajectory and the center of the

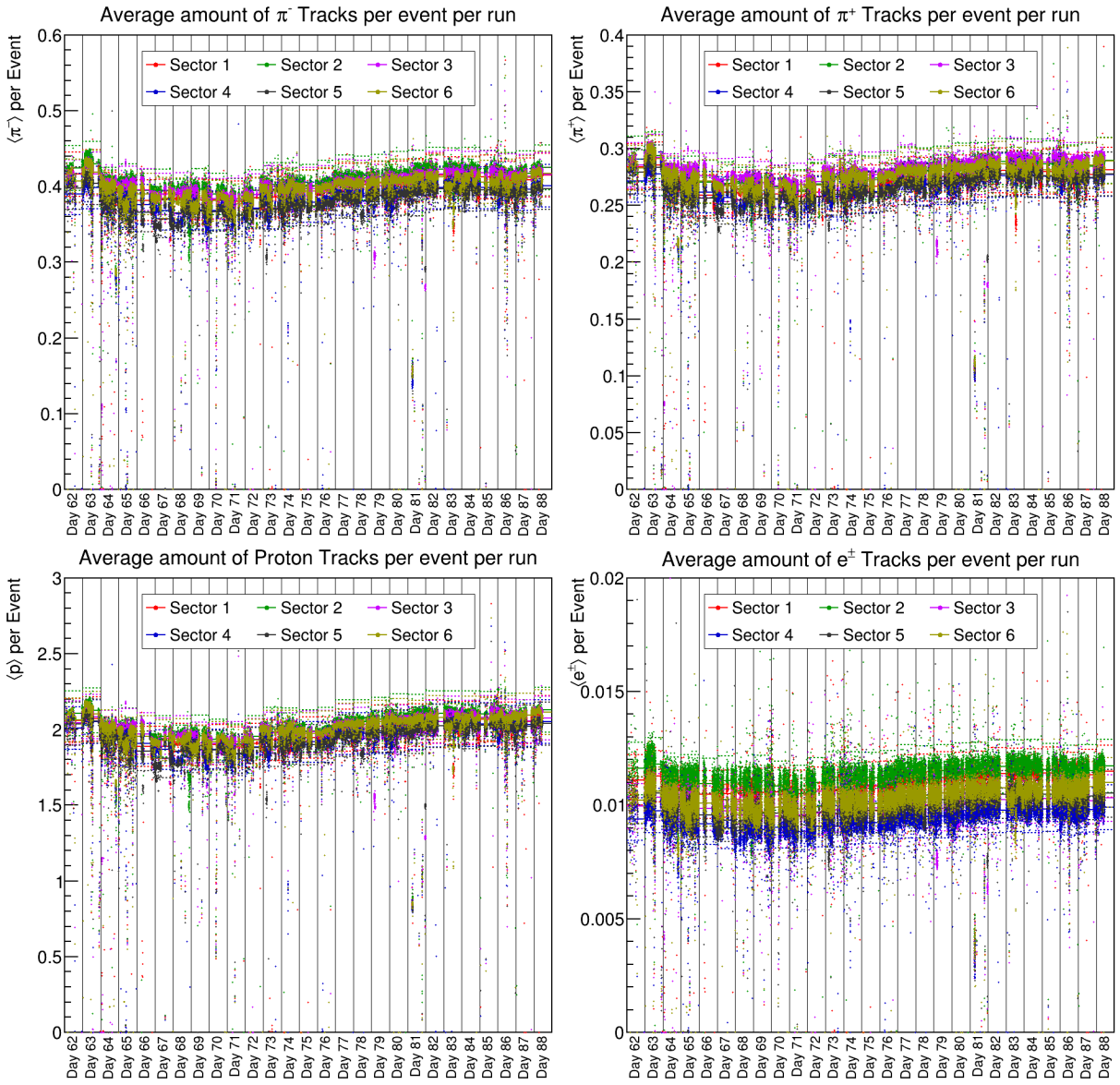

Figure 3.4.: Average amount of π^- (upper left), π^+ (upper right), Protons (lower left) and e^+e^- (lower right) per event, run and sector. Every dot represents one run and the different colors represent the six sectors. The full lines correspond the daily averages and the dotted lines correspond to the borders used to select/discard the sectors in the corresponding runs.

matched RICH ring must not exceed 2°. Using these identification criteria, the average amount of the four particle species per event is calculated for each run as well as each day of the beam time for each of the six sectors individually.

The panels of Figure 3.4 show these averages for the different sectors (colors) over the beam time (x-axis). For all particle species the second half of the beam time shows slightly larger averages than the first half. This can be related to an observed improvement in beam quality [100] combined with an improvement of the stability of the detector system. In the simulations these changes are averaged out. Next, the decision whether a sector

performed well in a run is taken by comparison of the averages of the individual runs with the corresponding daily averages. To account for statistical fluctuations as well as small performance changes which can be averaged out by the simulations, the averages of protons, π^+ and π^- tracks are allowed to have relative divergences of ± 7 %. Due to their lower absolute rates, the e^+ and e^- tracks show larger statistical fluctuations. Therefore, relative divergences of up to ± 10 % are accepted. In the subfigures of Figure 3.4 the dotted lines indicate the allowed divergences from the daily averages.

If none of the four particle species exceeds their allowed relative divergence per run, data from this sector are accepted and taken into account in the physics analyses. However, in the reconstruction of short-lived particles via their decay products, the performance in a region of space corresponding to one sector is also influenced by the performances of the adjacent sectors. As a consequence of that all runs in which one or more sectors are rated not performing well are excluded from physics analyses to preclude any bias on the performance of the analyses. Using this condition on top of the nine event selection criteria described previously, another 6.9 % of all events are discarded.

3.3. Track Selection Criteria

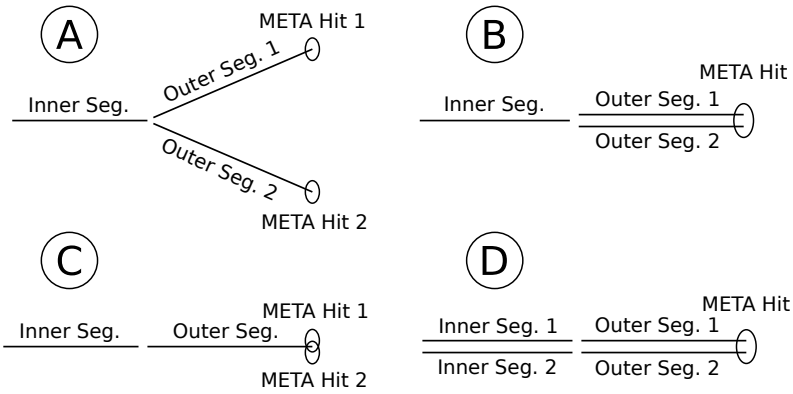

Figure 3.5.: Four possible situations in which two track candidates share either the inner track segment, the outer track segment or the META hit.

During the track reconstruction procedure, described in Section 2.3.3, only loose requirements on the quality of the created track candidates are applied. Furthermore, since a track candidate is created for any feasible combination of an inner track segment, an outer track segment and a META hit, many of the preliminary track candidates share at least one of these components. Four examples on how two track candidates with at least one common component can be created are displayed in Figure 3.5. In case A the two track candidates share a common inner track segment but are built from individual outer track segments and META hits. This case appears not only randomly as a result of the limited spacial resolutions, but also for e^+e^- pairs created in the conversion of a high energy γ. Those pairs have small opening angles in the laboratory system, but get separated by traversing the magnetic field due to their opposite charge. In case B the track candidates share their inner track segment and their META hit but are build from different outer track segments. In case C a single combination of an inner and an outer track segment is matched to two META hits. This case appears mostly due to the limited spacial resolution of the META detectors. It is an exceptional case as the two candidates can only be separated by their META matching quality but not by their tracking quality parameters. Case D represents the opposite of case C, here two completely independent combinations of an inner and outer track segment are matched to the same META hit. Note that besides these four exemplarily cases there are further possibilities of how track candidates might share one or more of their components.

Since in most cases at least one of the track candidates with one or more common components is unphysical, a procedure to identify and reject them is required. First, all track candidates for which a step of the track reconstruction procedure (cf. Section 2.3.3), namely inner track segment reconstruction, outer track segment reconstruction, META hit matching or Runge-Kutta momentum reconstruction, failed or that fulfill a (fake) rejection criterion, are removed. Next, the track candidates are required to have a Runge-Kutta tracking quality χ^2_{RK} of less than 1000 and a MMQ value of less than 3. Besides that all track candidates with a time of flight of more than 60 ns, which corresponds to a velocity $\beta \approx 0.11$ for the shortest tracks in the HADES detector, are rejected. Finally, a further criterion on the matching between the META hit and the track is applied. This criterion accounts for the fact that the META detectors have no spacial resolution besides the sizes of the RPC cells or widths of the TOF rods in y-direction of their coordinate system, which roughly corresponds to the polar direction of the laboratory system.

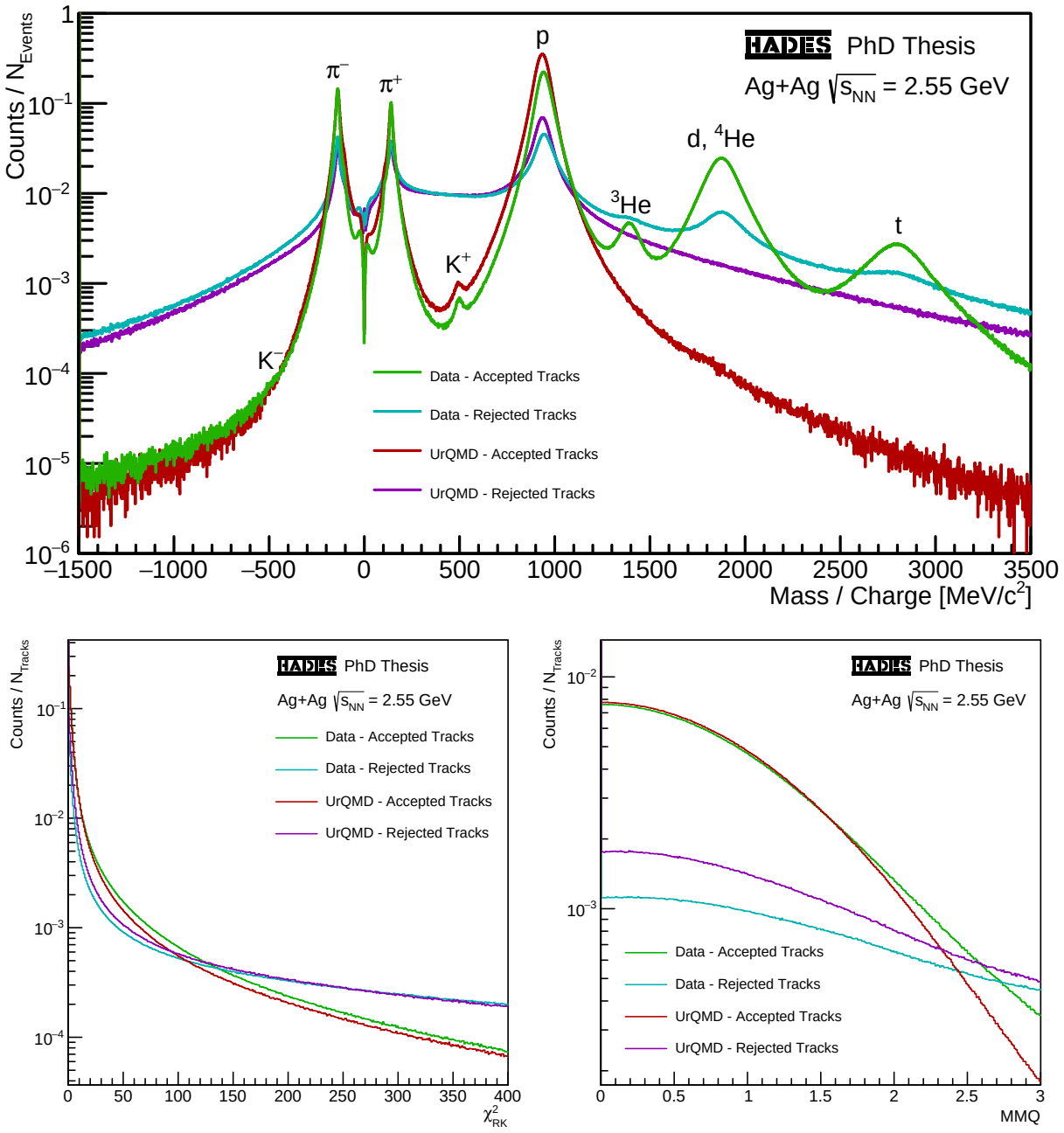

Figure 3.6.: Mass (upper panel), χ^2_{RK} (lower left) and MMQ (lower right) spectra from experimental data after all event selection criteria (cf. Section 3.2) and UrQMD simulations separately for all tracks accepted and all tracks rejected by the track selection procedure described in Section 3.3. The mass spectra are normalized to the amount of events and the track quality parameter spectra to the corresponding amounts of tracks. The experimental spectra show a subset of all events which is representative for the beam time.

For this criterion, the distance in y-direction of the META detector coordinate system between the border of the cell of the META hit and the intersection point of the extrapolated Runge-Kutta trajectory and the META detector plane is calculated. If this distance exceeds a maximum value, the track candidate is rejected. To account for the stronger deflection of low momenta particles in the magnetic field, which renders the extrapolation

using the Runge-Kutta trajectory less precise, the maximum is calculated for each track candidate individually. It ranges from ≈ 6 cm for tracks with very low momenta to 4 mm for tracks with high momenta.

After these preselection criteria are applied, the remaining track candidates are sorted by increasing ${\chi^2}_{\mathrm{RK}}$ value. Iteratively, the track candidate with the lowest ${\chi^2}_{\mathrm{RK}}$ value is selected and all track candidates which share one or more components with this selected candidate are rejected. This is repeated until all track candidates have been either selected or rejected assuring that among the selected track candidates each track component is only used once. Finally, the minimum tracking quality is increased by rejecting all remaining track candidates with a ${\chi^2}_{\mathrm{RK}}$ value larger than 400.

Figure 3.6 shows the distributions of the particle masses calculated according to Equation 3.1 in the upper panel, the distributions of the track quality parameter ${\chi^2}_{\mathrm{RK}}$ in the lower left and of the parameter MMQ in the lower right. The distributions of tracks passing the track selection procedure are shown in green for real data and red for UrQMD simulations. The cyan distributions corresponds to tracks from real data rejected by the track selection procedure and the violet distribution to according tracks from UrQMD simulations.

The mass distribution of accepted tracks from real data shows clear peaks at the nominal mass of the charged hadrons π^-, π^+, K^+ and protons as well as the nominal mass over charge ratios of the light nuclei ^{3}He, Deuterons, ^{4}He and Tritons. At the K^- mass no peak is visible because it is overshooted by the background of low quality π^- tracks. The Helium nuclei are measured at the half of their nominal mass since they are double charged and only the momentum over charge and thereby the mass over charge ratios can be measured. In the according distribution from UrQMD simulations, the charged hadron peaks are visible at the same positions and with similar magnitudes. However, the distribution shows no peaks for the light nuclei since the UrQMD model does not simulate the clustering of protons and neutrons which is also why the proton peak from UrQMD simulations overshoots the one from real data. Besides that, a high accordance between real data and UrQMD simulations is observed. Looking at the mass distributions of the rejected tracks, one observes similar peaks as for accepted tracks, however, with lower magnitudes and much more track laying in the unphysical mass regions between them. This proves that although the track selection procedure rejects a proportion of correct tracks, it significantly reduces the amount of unphysical tracks which cannot be assigned to one particle species. Comparing the distribution from real data with the one obtained from UrQMD simulations again shows a high accordance.

Concerning the distributions of the track quality parameters ${\chi^2}_{\mathrm{RK}}$ and MMQ it is shown that the rejected tracks are of significantly worse quality than the accepted ones. Furthermore, the distributions of both parameters show a strong accordance between real data and UrQMD simulations after the selection is performed although on average the quality of real data tracks is slightly lower than in case of UrQMD simulation tracks. This needs to be taken into account in the following analyses, however, it can be concluded that the UrQMD simulations reproduce the measured spectra after applying the track selection procedure fairly well.

3.4. Particle Identification

The Particle IDentification (PID) is primarily performed via two independent methods which will be described in the following. The first method, described in Section 3.4.1, utilizes the measured momentum over charge ratios as well as the measured times of flight to calculate the mass over charge ratios of the particles and thereby identify them. This method is sufficient for particles with a unique mass over charge ratio and whose signals are negligibly contaminated by background. For all other particles the measured specific energy loss in the detector materials needs to be considered additionally as described in Section 3.4.2.

3.4.1. Particle Identification via Time of Flight

Equation 3.1 allows to calculate the rest mass of a particle from its momentum and its velocity. The momenta of the measured particles are deduced using the Runge-Kutta method, as described in Section 2.3.3.4 and the velocities are calculated from the lengths of the trajectories in combination with the times of flight measured by the RPC or TOF detector. Since the deduced momenta are actually the momentum over charge ratios of the particles, also the calculated masses are actually the mass over charge ratios.

$$m_0 = p \cdot \sqrt{\frac{1}{\beta^2} - 1} \tag{3.1}$$

If the measured velocity exceeds the speed of light due to measurement uncertainties, Equation 3.1 yields an imaginary mass. In these cases, the absolute value of the calculated mass is taken. This corresponds to replacing the measured velocity faster than the speed of light $\beta_{>1}$ by a velocity slower than the speed of light $\beta_{<1}$ calculated according to Equation 3.2.

$$\beta_{<1} = \sqrt{\frac{1}{2 - \frac{1}{\beta_{>1}^2}}} \tag{3.2}$$

Figure 3.7 shows the distribution of the measured momentum over charge ratios and velocities for all reconstructed charged particles that passed the track selection procedure described in Section 3.3. The solid lines correspond to the nominal mass over charge ratios of all charged particles directly measured in the HADES detector. Besides the K^- which is rarely produced and thereby exceeded by background, the distributions of all plotted particles species are visible.

The primary aim of this method is to determine the standard deviation of the distributions in the momentum-velocity-plane corresponding to the different particle species using a Gaussian function. All tracks withing $\pm n\sigma$ are then identified as the respective particle species. The standard deviations correspond to the resolution of the mass measurement as a consequence of the resolutions of the momentum- and velocity measurement. These resolutions are strongly correlated to the absolute momentum and velocity of the tracks since both the momentum and velocity measurements are more accurate for slow particles

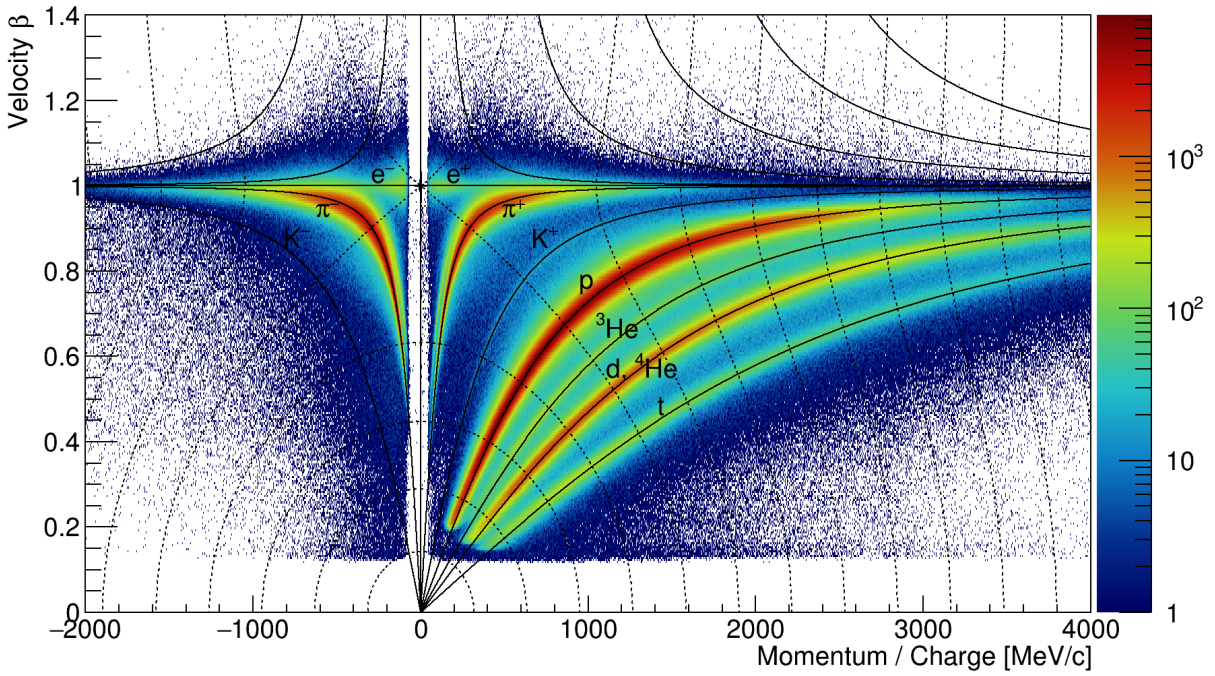

Figure 3.7.: Momentum over charge versus velocity distribution of reconstructed charged particles. The solid lines correspond to the nominal mass over charge ratios of various particle species taken from [184] and the dotted lines correspond to a various values of the newly introduced quantity a. The plot shows a subset of all events which is representative for the beam time.

than they are for fast ones. Furthermore, the resolution of the velocity measurement depends on whether the time of flight was measured by the RPC or the TOF detector since they have different time resolutions. Therefore, the determination of the standard deviations in the momentum-velocity-plane has to be performed differentially over the full range and independently for tracks measured in the RPC and the TOF detector.

Unfortunately, neither the momentum nor the velocity dimension are suited to perform the required differential projection onto the mass dimension along with. This is a consequence of the measured mass being primarily determined by the measured momentum for slow particles while at the same time being primarily determined by the measured velocity for fast particles. To overcome this problem, in this work a new method to perform the determination of the standard deviations of the distributions in the momentum-velocity-plane has been developed.

The momentum-velocity-plane can be understood as a two dimensional Cartesian coordinate system since momenta and velocities are measured independently. Ideally, the projections onto the mass dimension are performed in a different two dimensional Cartesian coordinate system with the mass defining one of the two axes implying an independence against the quantity defining the second axis. This additional quantity, called a in the following, is defined by Equation 3.3. The constant s^2 is required to compensate the magnitude differences between momenta and velocities and is fixed to 4×10^{-7}. The dotted lines in Figure 3.7 correspond to constant values of the quantity a. In the physical region $\beta < 1$ they are always perpendicular to the solid lines corresponding to constant masses

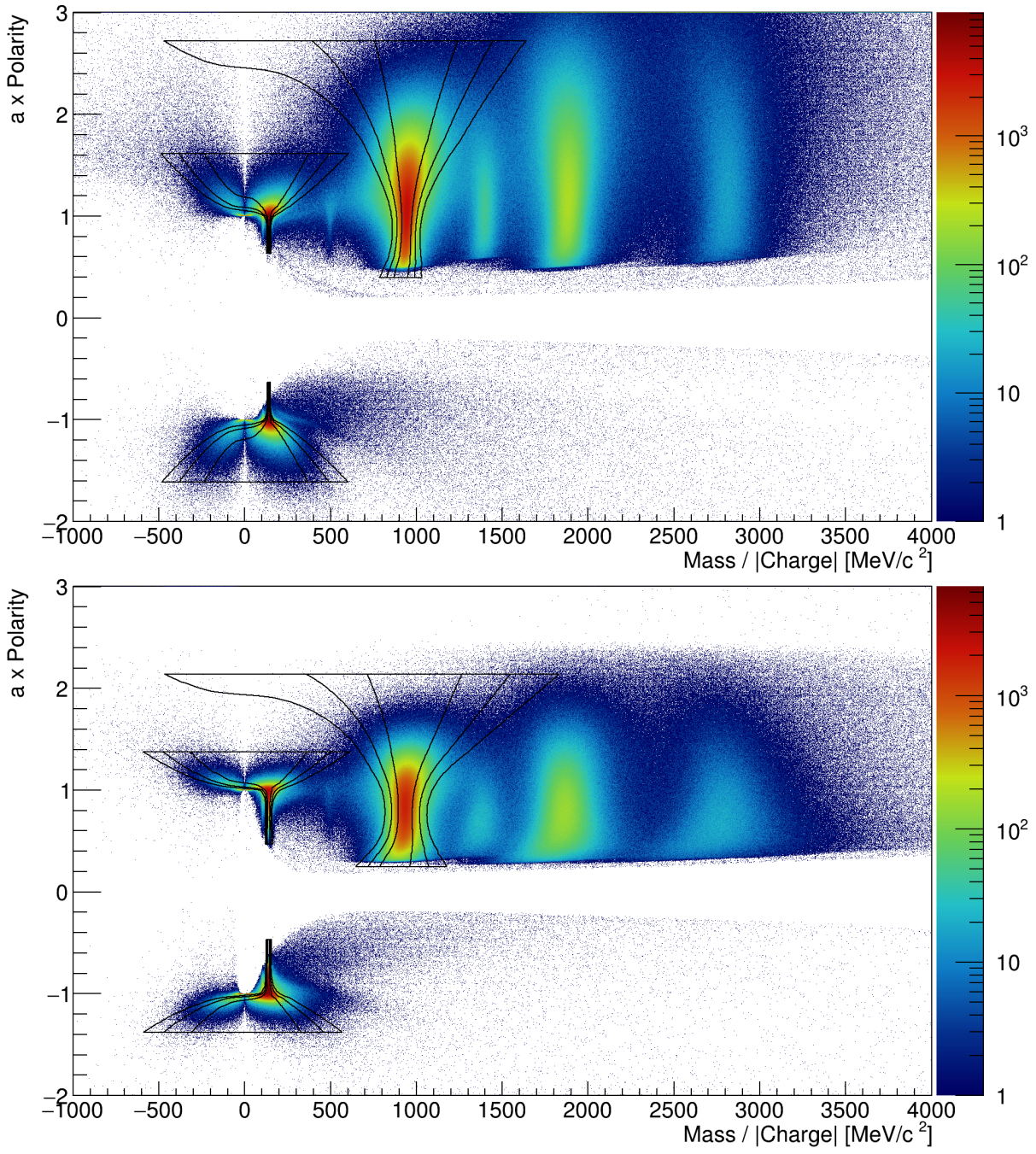

Figure 3.8.: Mass over absolute charge versus polarity (sign of charge) times a distributions of reconstructed charged particles measured by the RPC detector (upper plot) and the TOF detector (lower plot). Negative masses correspond to particles with a measured velocity faster than the speed of light. The solid lines show the ± 1, 2 and 3σ selection regions for charged pions and protons. The plots show a subset of all events which is representative for the beam time.

which demonstrates the definition of the quantity a. Together, Equations 3.1 and 3.3 define the non-linear transformation from the momentum-velocity into the mass-a coordinate system, in which the solid and dotted lines from Figure 3.7 would be parallel to the x- or y-axis by definition.

$$a = \sqrt{1 + s^2 p^2 - (1 - \beta^2)^2} \tag{3.3}$$

Figure 3.8 shows the distribution of reconstructed charged particles that passed the track selection procedure described in Section 3.3 in the mass-a coordinate system separately for the RPC (upper plot) and TOF detector (lower plot). On the x-axis, the mass over absolute charge ratio is shown with negative values corresponding to particles with a measured velocity faster than the speed of light. On the y-axis, the quantity a multiplied with the polarity (sign of charge) of the particles is drawn.

The $\pm$nσ selection regions for the various particles are now determined by projecting the distributions shown in Figure 3.8 onto the mass axis for multiple slices of the a-axis. For each of these projections, the peaks corresponding to the different particle species are fitted with a Gaussian function. The parameters μ (mean) and σ (standard deviation) of these Gaussian functions determine the selection region by connecting the results from all a-slices. In the regions where the statistics of the distributions drop too low, the fits become instable and less precise. Therefore, in these regions, the parameters μ and σ are extrapolated from the adjacent regions assuming a linear trend between a and the parameters. Yet another modification of the method has to be applied in the transition region from $\beta < 1$ to $\beta > 1$, because the dependence between mass and velocity is reversing there. Since the masses are primarily determined by the measured velocities in these region, the resolution of the velocity measurement can be used to approximate the resolution of the mass measurement. In other words, the actually non-Cartesian velocity-a coordinate system becomes approximately Cartesian in the transition region. This allows to use projections onto the velocity axis instead of the mass axis to determine the standard deviations of the distributions. The resulting parameters μ and σ are then transformed from the velocity-a into the mass-a coordinate system using Equations 3.1 and 3.3. The final $\pm$1, 2 and 3σ selection regions for charged pions and protons in the mass-a coordinate system are shown by solid lines in Figure 3.8.

Finally, the selection regions have to be transformed back into the standard momentum-velocity coordinate system. Therefore, the non-linear transformation defined by Equations 3.1 and 3.3 has to be reversed. Using the Wolfram-Alpha computation engine [180] the reverse transformation from the mass-a into the momentum-velocity coordinate system was found to be described by Equations 3.4 and 3.5. These equations involve the parameters v and w which are cubic roots of potentially complex numbers. Since cubic roots have three equivalent solutions on the complex plane, the parameter c, which itself has three possible values given by Equation 3.6, needs to be introduced. Only the appropriate combinations of one of the three possible values for the cubic roots in v and w and one of the three possible values for c yield correct results.

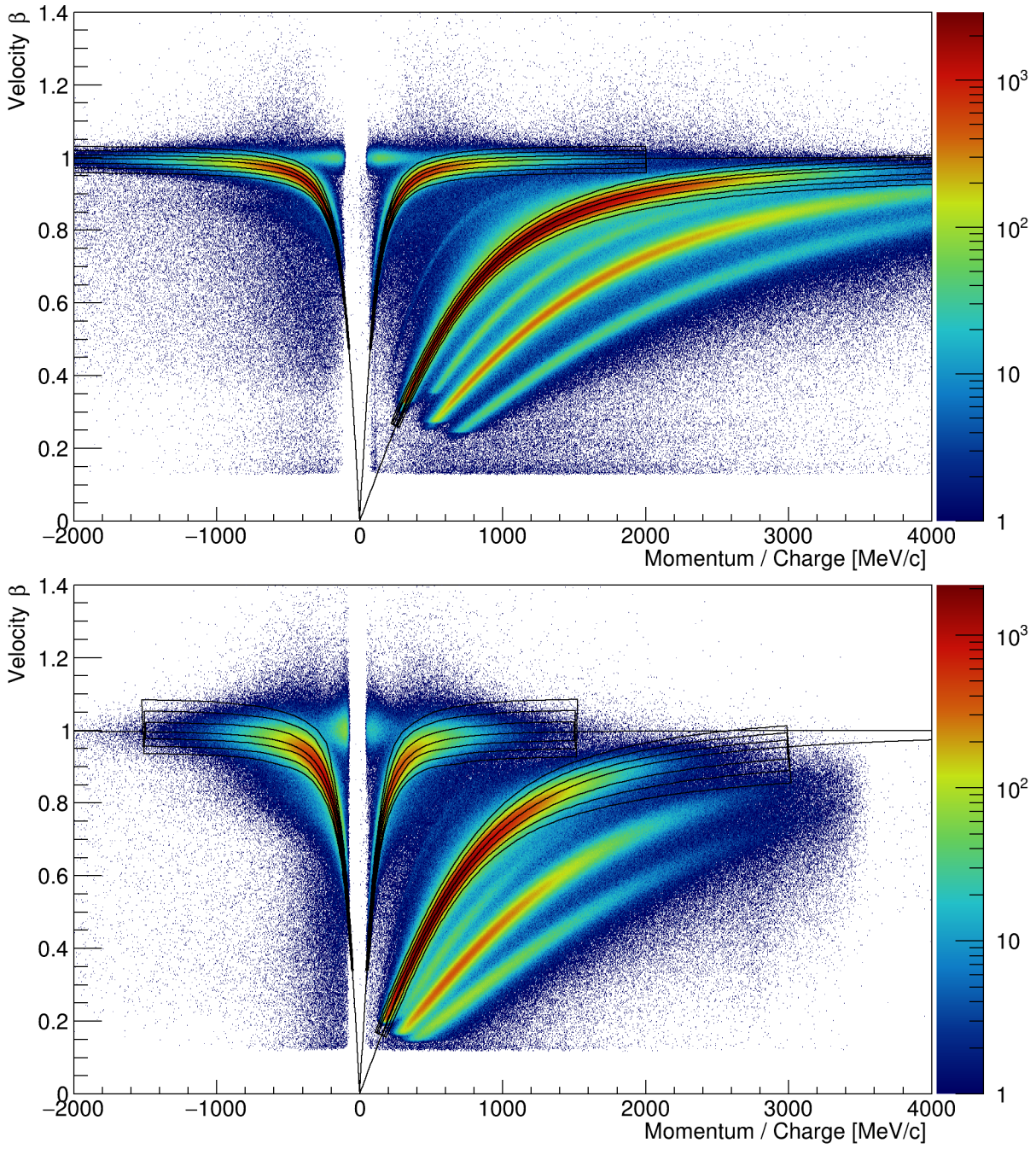

Figure 3.9.: Momentum over charge versus velocity distributions of reconstructed charged particles measured by the RPC detector (upper plot) and the TOF detector (lower plot). The solid lines show the ± 1, 2 and 3σ selection regions for charged pions and protons as well as their nominal masses taken from [184]. The plots show a subset of all events which is representative for the beam time.

$$p = \sqrt{-c_{1-3}\frac{\left(a^2+s^2m^2-1\right)^2}{3\sqrt[3]{4}s^2v} - \overline{c_{1-3}}\frac{v}{6\sqrt[3]{2}s^2} + \frac{a^2-2s^2m^2-1}{3s^2}} \quad \text{with } v = \sqrt[3]{2\left(a^2+s^2m^2-1\right)^3 + 27s^4m^4 + 3s^2m^2\sqrt{12\left(a^2+s^2m^2-1\right)^3 + 81s^4m^4}} \tag{3.4}$$

$$\beta = \sqrt{c_{1-3}\frac{a^2+s^2m^2-1}{\sqrt[3]{4}w} - \overline{c_{1-3}}\frac{w}{6\sqrt[3]{2}} + 1} \quad \text{with } w = \sqrt[3]{-27s^2m^2 + 3\sqrt{12\left(a^2+s^2m^2-1\right)^3 + 81s^4m^4}} \tag{3.5}$$

$$\text{with } c_{1-3} = \left\{-2\ ;\ \left(1+i\sqrt{3}\right)\ ;\ \left(1-i\sqrt{3}\right)\right\} \text{ and its complex conjugate } \overline{c_{1-3}} \tag{3.6}$$

Figure 3.9 sows the data and selection regions from Figure 3.8 transformed back into the momentum-velocity coordinate system again separately for the RPC (upper plot) and TOF (lower plot). Again the solid lines correspond to the ± 1, 2 and 3σ selection regions for charged pions and protons. Furthermore, the lines corresponding to the nominal masses of these particles are drawn. One can see that the distributions are almost ideally described by the selection regions. Finally, the procedure is applied onto simulated data conversely to account for slight differences between real and simulated data and allow for realistic efficiency corrections.

Concerning the selection of particles originating from weak decays another effect needs to be considered: Since the daughter particles travel the non-negligible decay lengths "confined" in their heavier and therefore usually slower mother particles, their measured times of flight are systematically shifted upwards. As a result, the calculated masses of their tracks are also shifted up. In previous analyses of weakly decaying particles [161, 170] it turned out that this effect is not fully described in simulations which results in systematic acceptance and efficiency errors when the daughter particles are selected via their $\pm 3\sigma$ selection regions. To overcome this, daughter particles from weak decays were identified using wide ranges of calculated masses at the cost of an increased proportion of background tracks in the selection regions. Furthermore, these selections did not properly take tracks with measured speeds above the speed of light and the changing momentum resolution into account.

In this work the selection method for particles originating from weak decays has been reinvestigated with the aim of obtaining a method that fulfills the following criteria:

- No systematic acceptance and efficiency errors due to the shifted times of flight.
- As low as possible background track contaminations in the selection regions.
- Differences between RPC and TOF taken into account.
- Changing momentum resolution with absolute momentum taken into account.
- Proper selection of tracks with measured speeds above the speed of light.

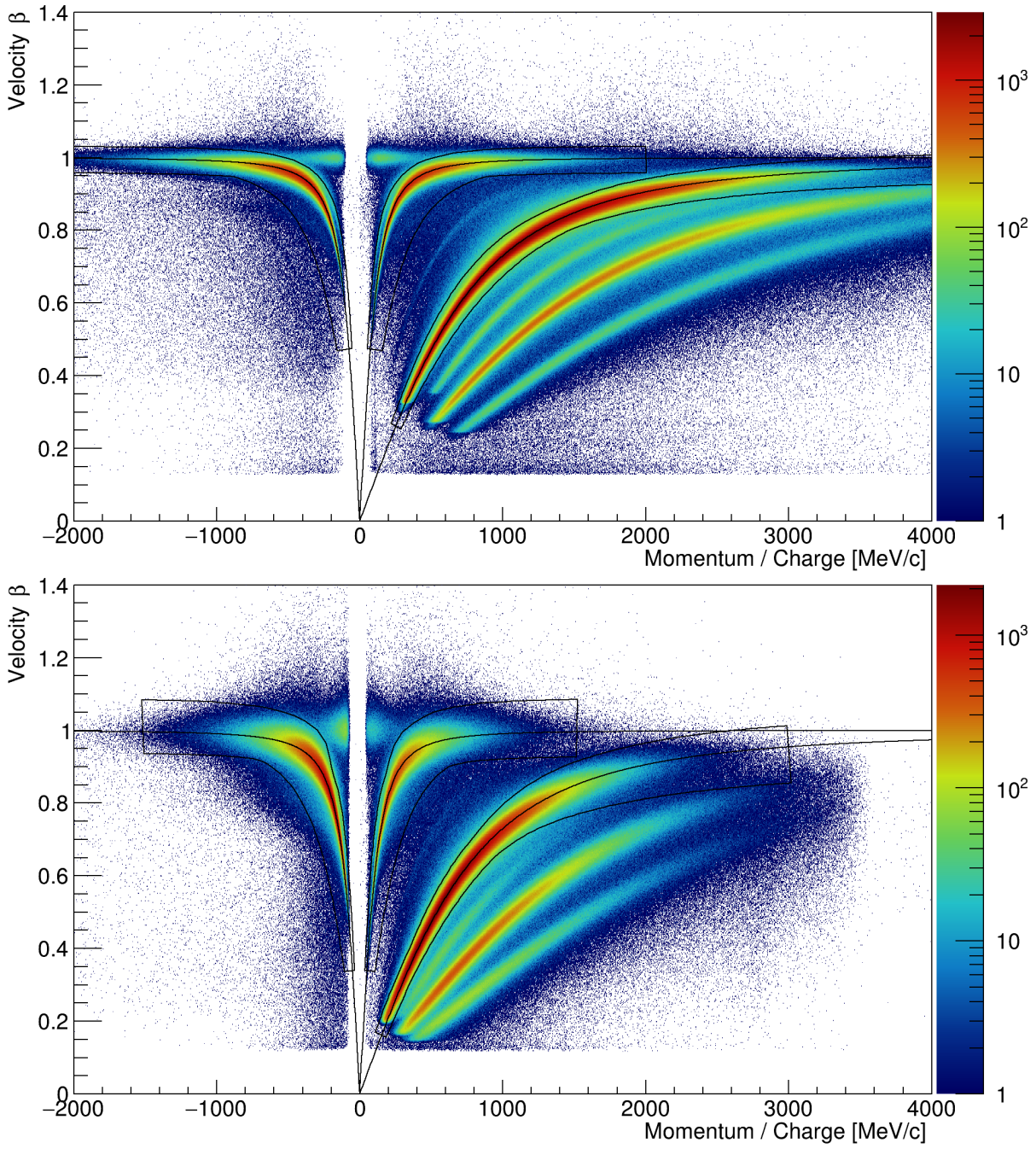

Figure 3.10.: Momentum over charge versus velocity distributions of reconstructed charged particles measured by the RPC detector (upper plot) and the TOF detector (lower plot). The solid lines show the selection regions for charged pions and protons originating from weak decays as well as their nominal masses taken from [184]. The plots show a subset of all events which is representative for the beam time.

The last four criteria are all fulfilled by the $\pm n\sigma$ selection regions obtained by the previously described method. In order to take the time of flight shift into account, the following characteristics need to be considered: The shift grows with the speed difference between the mother and the daughter particle. Therefore, it is on average stronger for daughter particles with larger mass difference to their mother particle. Concerning the decays analyzed in this thesis, the pions are affected the most while for protons from Λ decays, ^{3}He from $^3_\Lambda$H decays and Λs from Ξ^- decays, the effect is almost negligible. Furthermore, the shift usually results in higher measured masses since it is unlikely that the lighter daughter particle is slower than the heavier mother particle. Finally, the effect is most pronounced at intermediate momenta of the daughter particles.

It turned out that a selection obtained by extending the $\pm 3\sigma$ selection regions by fixed mass selection ranges, fulfills all the anticipated criteria. For charged pions the $\pm 3\sigma$ selection regions were extended by calculated masses between 100 and 300 MeV/c^2 and for protons, the $\pm 3\sigma$ selection regions were extended by calculated masses between 800 and 1100 MeV/c^2. The resulting combined selection regions are depicted in Figure 3.10 for tracks in the RPC region (upper plot) and tracks in the TOF region (lower plot). One observes that like previously mentioned the effect is much stronger for pions than for protons and primarily affects the intermediate and low momentum regions while at high momenta, the selection regions are identical to the ones shown in Figure 3.9. Finally, the method is also applied onto the $\pm 3\sigma$ selection regions obtained for simulated data to allow for realistic efficiency corrections.

3.4.2. Particle Identification via Specific Energy Loss

The identification of particles via the measured times of flight, as described in Section 3.4.1, already allows for a clean selection of most particle species. However, in some cases the identification needs to be improved further by additionally taking the measured specific energy losses of the particles into account. This is especially important for particle species with the same mass over charge ratio like for example deuterons and ^{4}He nuclei since they cannot be distinguished from each other using the method described in Section 3.4.1. Furthermore, in the analyses described in Chapter 4, it is used to improve the selection of protons and ^{3}He nuclei as they have similar mass over charge ratios.

The specific energy losses of the particles are measured independently by the MDC and the TOF detectors. Since only particles in the backward hemisphere of the collision are in the acceptance of the TOF detector, particle identification using the energy losses measured in the TOF detector will not be further discussed in this section. However, it can be performed conversely to the particle identification using the energy losses measured in the MDC detectors which will be described in the following.

When charged particles traverse matter, they interact electromagnetically with the electrons of the atoms and thereby deposit energy. For particles with $0.1 \lesssim \beta\gamma \lesssim 1000$ the amount of energy deposited per length normalized to the macroscopic density ρ of the traversed material is described with an accuracy of few percent by the Bethe-Bloch-Equation 3.7 [184]:

$$\left\langle -\frac{dE}{dx} \right\rangle = Kz^2 \frac{Z}{A} \frac{1}{\beta^2} \left[\frac{1}{2} \ln \left(\frac{2m_e c^2 \beta^2 \gamma^2 W_{max}}{I^2} \right) - \beta^2 - \frac{\delta(\beta\gamma)}{2} \right] \tag{3.7}$$

$$W_{max} = \frac{2m_e c^2 \beta^2 \gamma^2}{1 + 2\gamma m_e / M + (m_e/M)^2} \tag{3.8}$$

In this equation K is a constant factor of 0.307075 $\frac{MeVcm^2}{mol}$. z is the charge number, β the velocity, γ the Lorentz factor and M the mass of the charged particle. Z is the charge number of the traversed material, A its mass number and I its mean excitation energy. m_e is the electron mass and W_{max}, which is given by Equation 3.8, is the maximum energy transferred in a collision with a single electron [184]. Finally, $\delta(\beta\gamma)$ is a function to take into account density effects for highly relativistic particles. At typical particle energies in the HADES experiment these density effects are negligible small which is why this term is not taken into account in the following.

As already stated in Section 2.2.4, an volumetric admixture of 70 % Argon and 30 % Carbon dioxide was used as detector gas in the MDC detectors. At a macroscopic density of 1.784 $\frac{kg}{m^3}$ and a molar mass of 40 $\frac{g}{mol}$, the molar density of Argon amounts to 44.5 $\frac{mol}{m^3}$. The macroscopic density of Carbon dioxide amounts to 1.98 $\frac{kg}{m^3}$, its molar mass to 44 $\frac{g}{mol}$ and thereby its molar density to 45.0 $\frac{mol}{m^3}$. Because of the almost equal molar densities, the volumetric proportions of the constituents can be considered equal to the molar proportions. Finally, the mass proportions of the three elements in the admixture are calculated to be 68 % Argon, 23 % Oxygen and 9 % Carbon.

According to the Bragg rule of additivity [71], the energy loss of a charged particle traversing a compound material or an admixture can be approximated by the sum of the energy losses in the constituent materials weighted with their mass proportions. Using this approximation, given by Equation 3.9 in which the different constituent materials are indexed by j, effects of the molecular bindings are neglected. Finally, the energy losses are calculated using the mean excitation energies of the materials taken from [110] which amount to 188 eV for Argon, 95 eV for Oxygen and 78 eV for Carbon.

$$\left\langle -\frac{dE}{dx} \right\rangle = \sum_j w_j \left\langle -\frac{dE}{dx} \right\rangle_j \tag{3.9}$$

Figure 3.11 shows the distribution of the measured momentum over charge ratios and energy losses in the MDC detectors for all reconstructed charged particles that passed the track selection procedure described in Section 3.3. The solid lines correspond to the theoretical energy losses of several particles calculated with the Bethe-Bloch-Equation 3.7 using the approximations described previously. One observes a good accordance between the measured distributions of charged pions and protons and their theoretical predictions. However, at low momenta where the energy loss rises exponentially, the theoretical predictions are overshooted by the measurements. The distribution of measured deuterons is mostly overlaid by protons, although, around 900 MeV/c a separation is visible. The distributions of tritons and helium nuclei are not visible since they occur rare compared to protons and are thereby exceeded by background. Nevertheless, the calculated lines

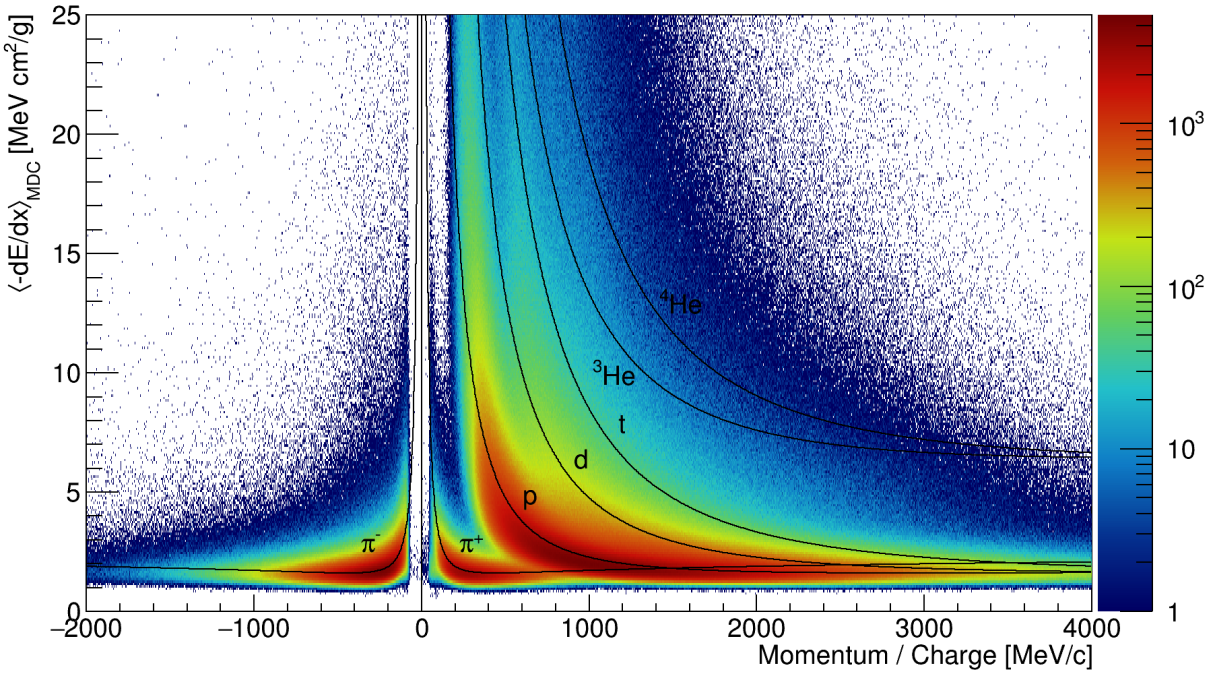

Figure 3.11.: Momentum over charge versus specific energy loss measured by the MDCs distribution of reconstructed charged particles. The solid lines correspond to the theoretical energy losses of various particle species calculated by Equation 3.7 as described in the text. The plot shows a subset of all events which is representative for the beam time.

show significantly higher energy losses for helium nuclei due to its z^2 dependence. This allows for a precise selection of helium nuclei if combined with the reconstructed masses calculated according to Equation 3.1 as it will be described later on.

Again, the primary aim of the method is to determine the standard deviation of the distributions corresponding to the various particles and then identifying them using $\pm n\sigma$ selection regions. However, since the energy loss follows an exponential trend, its logarithm is used for the calculations instead. Unlike in case of the particle identification via time of flight, the mass of a particle cannot be easily calculated from the measured momentum and energy loss. Therefore, a coordinate system transformation like it was described in Section 3.4.1 is not possible. As a result, the standard deviations are determined directly in the momentum-energy-loss-plane again separately for the RPC and the TOF detector.

First, a preselection of particles is performed using their calculated mass according to Equation 3.1. Next, the resulting distribution in the momentum-energy-loss-plane is projected onto the energy loss axis for multiple momentum slices spanning the entire range. The standard deviations of these projections are determined using a logarithmic asymmetric Gaussian fit function which is expressed by Equation 3.10 using the Heaviside function Θ and a lower σ_L and upper σ_U standard deviation. At low momenta, the energy loss rises strongly which prevents determining the standard deviations using the fitted functions. At high momenta, the statistics drop resulting in increasing relative statistical fluctuations. In both cases, the standard deviations from the adjacent momentum regions are extrapolated assuming an exponential trend. Finally, the $\pm n\sigma$ selection regions are created by connecting all momentum slices using the parameters μ, σ_L and σ_U.

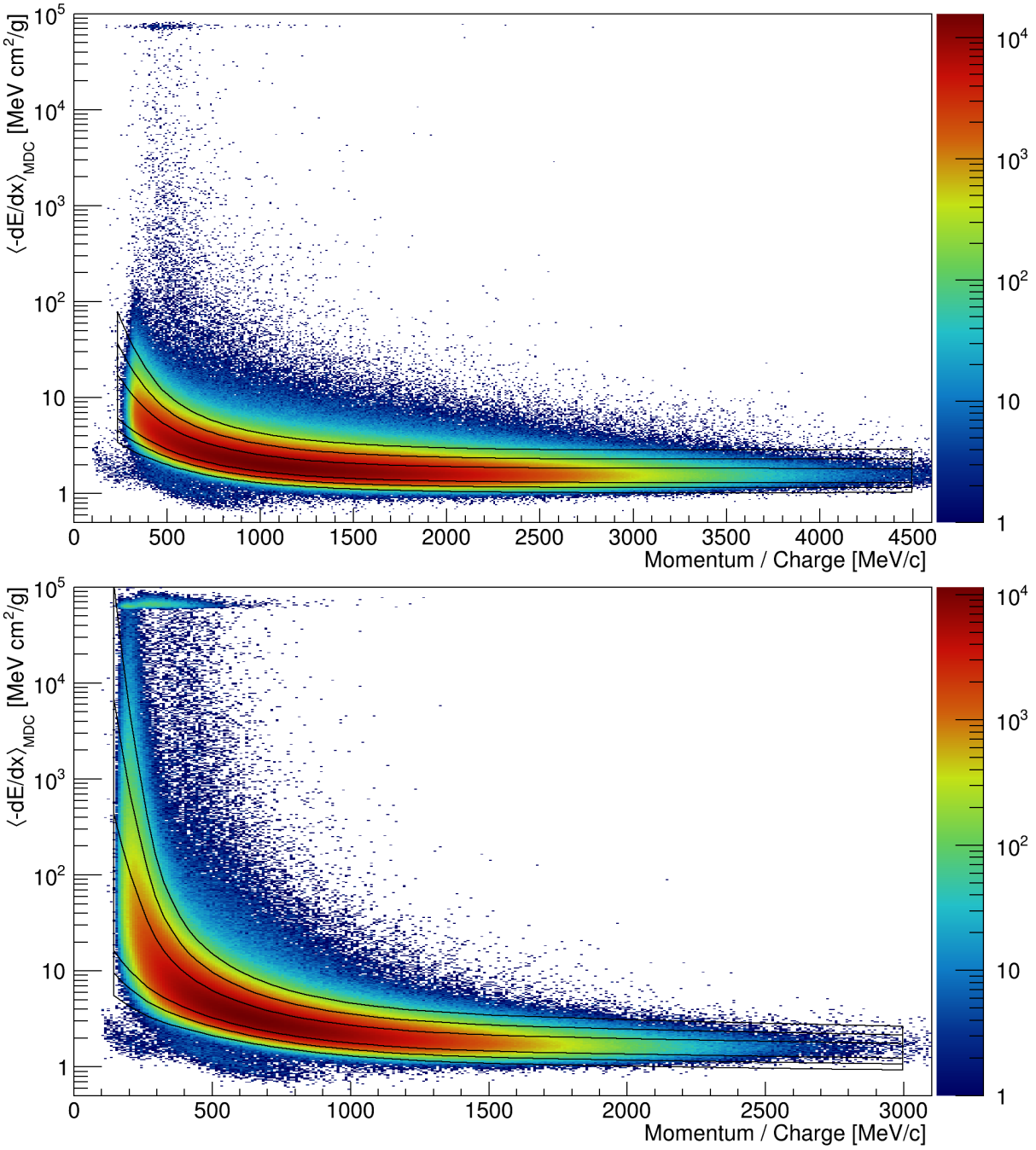

Figure 3.12.: Momentum over charge versus energy loss measured by the MDCs distributions of reconstructed charged particles in the proton mass region between 740 and 1140 MeV/c^2. The upper plots shows particles measured in the RPC detector and the lower plot particles measured in the TOF detector. The solid lines show the ± 1, 2 and 3σ selection regions for protons determined by the method described in the text. The plots show a subset of all events which is representative for the beam time.

$$f(x) = C \cdot \exp\left(\frac{(\log(x) - \mu)^2}{2\left(\Theta_1\left(\mu - \log(x)\right)\sigma_L + \Theta_0\left(\log(x) - \mu\right)\sigma_U\right)^2}\right) \tag{3.10}$$

To create the selection regions for protons only tracks in the corresponding mass region between 740 and 1140 MeV/c^2 are considered. The momentum over charge versus energy loss distributions are shown in the upper panel of Figure 3.12 for tracks from the RPC region and in the lower panel for tracks from the TOF region. The solid lines show the finally obtained ± 1, 2 and 3σ selection regions. A strong accordance between the measured distributions and the obtained selection regions is observed for tracks from the RPC as well as the TOF region. In the TOF region an accumulation of tracks at high measured energy losses between 50,000 and 100,000 $\frac{MeVcm^2}{g}$ is visible. This is an artifact of the procedure used to calculate the energy loss from the actual measurements in the event reconstruction during which an upper limit of 100,000 is applied.

To create the selection regions for ^{3}He again only tracks in the corresponding mass region, in this case between 1270 and 1520 MeV/c^2, are considered. Again, the momentum over charge versus energy loss distributions are shown in the upper panel of Figure 3.13 for tracks from the RPC region and in the lower panel for tracks from the TOF region. In these distributions two distinct distributions are observed. The one at higher energy losses corresponds to the double charged Helium nuclei while the one at lower energy losses is caused by single charged particles, namely protons and deuterons, contaminating the ^{3}He mass region. The selection region for ^{3}He in the RPC region, displayed by the solid lines, corresponds to the $\pm 3\sigma$ selection region obtained via the described method. However, to prevent the selection region from reaching into the lower band of background particles, the upper bound of the $\pm 3\sigma$ proton selection region was used as a lower limit for the lower bound of the ^{3}He selection region. The artifact caused by the energy loss calculation procedure at highest energy losses is more abundant than for the protons since Helium nuclei loose more energy than protons due to the z^2 dependence.

In the TOF region the ^{3}He selection region cannot be determined by the described method since it contains only ^{3}He nuclei from the low momentum region due to its geometrical acceptance where the energy loss rises strongly. As already stated before, the fit functions fail to describe the projected distributions under these conditions. Furthermore, a large proportion of ^{3}He in the TOF region are affected by the upper limit applied in the energy loss calculation procedure and thereby populate the artifact at high energy losses. For these reasons, the ^{3}He selection region for the TOF region was created manually.

Summing up, it has been shown that the selection regions obtained by the described method succeed to describe the measured distributions in almost all cases. Finally, the procedure is applied for simulated data conversely to account for slight differences between real and simulated data in order to allow for realistic efficiency corrections.

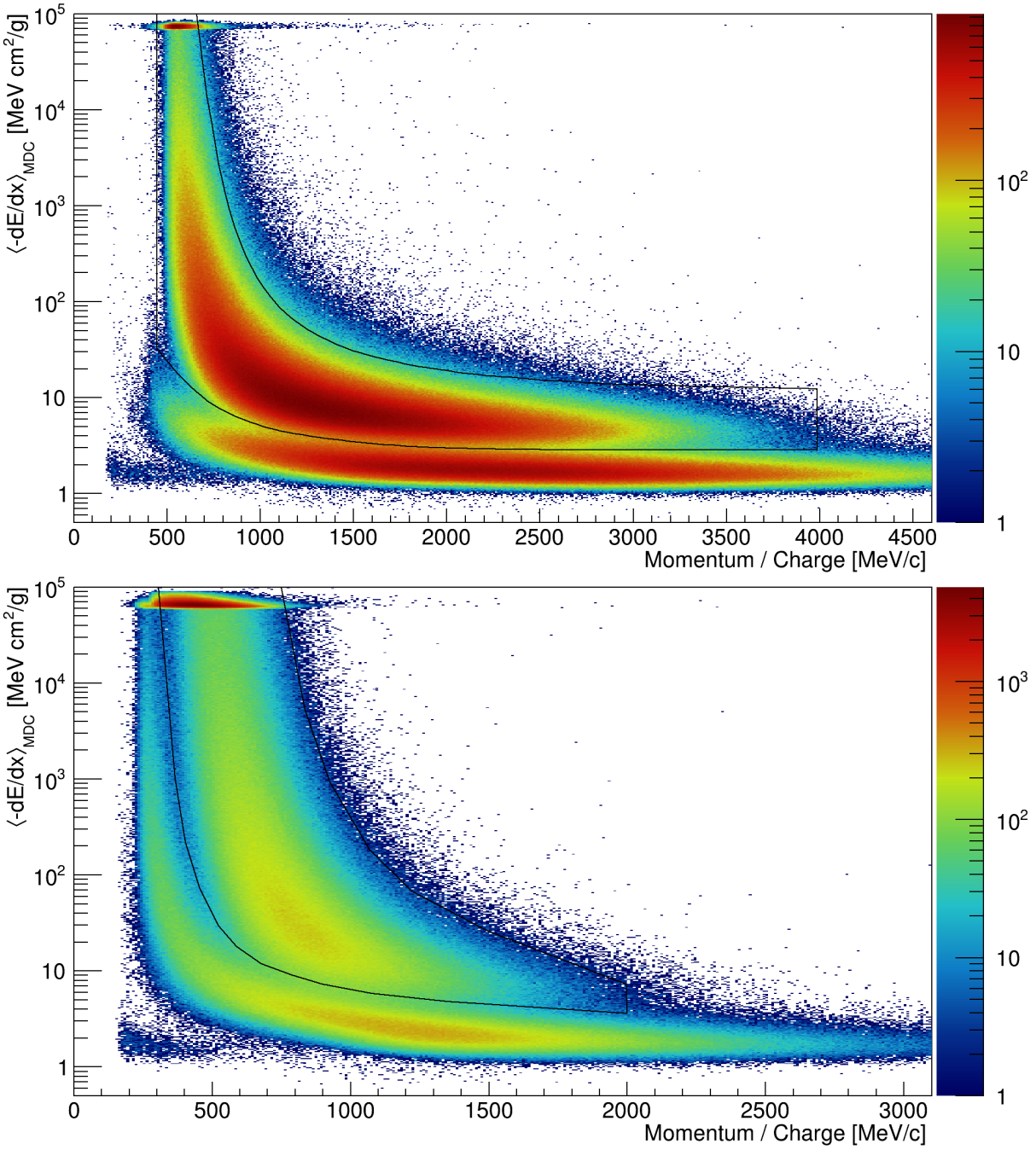

Figure 3.13.: Momentum over charge versus energy loss measured by the MDCs distributions of reconstructed charged particles in the ^{3}He mass over charge region between 1270 and 1520 MeV/c^2. The upper plots shows particles measured in the RPC detector and the lower plot particles measured in the TOF detector. The solid lines show the selection regions for ^{3}He determined by the method described in the text. The plots show a subset of all events which is representative for the beam time.

3.5. Centrality Estimation

As stated in Section 1.3.4, the centrality of a heavy ion collision is an important property since it defines the size of the created fireball and thereby strongly influences the amount and kinematic distributions of particles emerging from it. Since neither the centrality nor the impact parameter are direct observables, both are estimated based on an geometric model proposed by Glauber like described in [16, 116] for Au+Au collisions at $\sqrt{s_{NN}} = 2.42$A GeV. This section describes the same procedure but for Ag+Ag collisions at $\sqrt{s_{NN}} = 2.55$A GeV.

First, the dependence between a given impact parameter and the amount of nucleons participating in the reaction N_{Part} needs to be calculated. For this purpose, a geometric Glauber model is used in combination with a Monte-Carlo approach [134] to simulate the elementary nucleon-nucleon reactions in the collision of the two nuclei. In a first step, the positions of the nucleons inside the colliding nuclei are randomized assuming a uniform distribution in azimuthal and polar direction as well as a radial density distribution described by a two-parameter Fermi distribution 3.11.

$$\rho(r) = \frac{1 + w\,(r/R)^2}{1 + \exp\left((r - R)/a\right)} \tag{3.11}$$

The required parameter values for Ag nuclei are taken from [89] and amount to $R = 5.301$ fm, $a = 0.523$ fm and $w = 0$. To account for the non negligible sizes of the nucleons and the repulsive part of the strong interaction at small distances, two nucleons are not allowed to be positioned closer than 0.9 fm within the nuclei. In the next step, the impact parameter of the collision is randomized and the centers of gravity of the two nuclei are spaced accordingly. Finally, the collision is simulated assuming the nucleons to traverse the nuclei on straight trajectories in longitudinal direction. For each nucleon from the projectile nucleus, the distance of closest approach to each nucleon from the target nucleus is calculated. If this distance falls below a threshold based on the inelastic nucleon-nucleon cross-section according to $\sqrt{\sigma_{inel}/\pi}$, the nucleon is counted as a participant. This is repeated for the nucleons from the target nucleus accordingly. The inelastic nucleon-nucleon cross-sections are taken from [75] and amount for the beam energy of 1.58A GeV to $\sigma_{inel} = 27.23$ mb in case of symmetric (pp or nn) collisions and $\sigma_{inel} = 24.26$ mb in case of asymmetric (pn or np) collisions.

Figure 3.14 shows the differential cross-section of Ag+Ag collisions, simulated using the described Glauber model, as function of the impact parameter of the collision. According to the simple black-disk approximation, the differential cross-section should rise linear with the impact parameter until dropping instantly to 0 at the sum of the radii of the colliding nuclei. Up to an impact parameter of ≈ 10 fm a linear rise of the differential cross-section is observed since in this range every collision of the two nuclei results in at least one nucleon-nucleon reaction in the Glauber model. At impact parameters between 10 and 16 fm the Glauber model differential cross-section drops strongly however not instantly since, the simulated nuclei have diffuse surfaces unlike in the black-disk approximation. This is why nucleon-nucleon reactions can occur at impact parameters larger than the sum of the mean radii of the colliding nuclei. In the

region where the differential cross-section is rising linear, the total cross-section of Ag+Ag reactions can be calculated according to Equation 3.12 using the black-disk approximation:

$$\sigma_{tot} = \pi \cdot {b_{max}}^2 \cdot 10 \frac{mb}{fm^2} \tag{3.12}$$

Using this cross-section, the differential cross-sections beyond the linear region can be extrapolated with an appropriate scaling factor. Finally, the total cross-section of Ag+Ag collisions at $\sqrt{s_{NN}} = 2.55$A GeV amounts to 4575 mb in the described Glauber model. This total cross-section is now divided into multiple centrality classes corresponding to fixed proportions. The impact parameter borders of the centrality classes corresponding to 10 % of the total cross-section are depicted by the dotted lines in Figure 3.14.

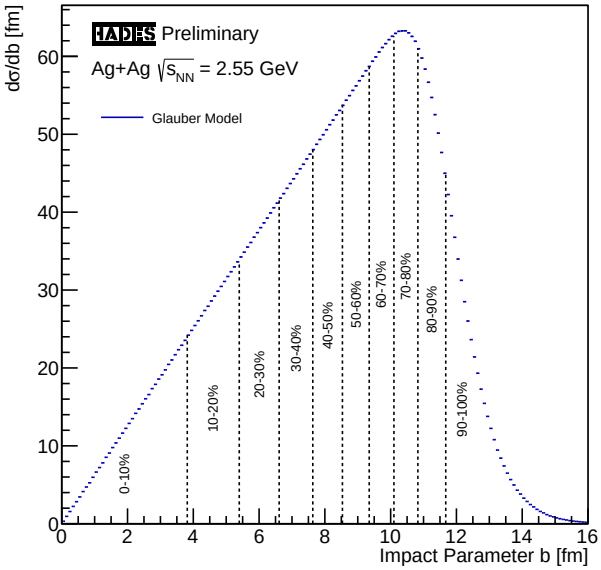

Figure 3.14.: Differential cross-section of Ag+Ag collisions simulated using the Glauber model described in the text. The dotted lines divide the total cross-section equally in 10 centrality classes.

In the next step, the actual experimental observables are simulated. Typically, centrality is determined by the amount of RPC and TOF detector hits. According to the "wounded nucleon" model [67] such quantities scale on average proportionally with N_{Part}. To take event-by-event fluctuations of the observables into account, they are sampled from N_{Part} using a Negative Binomial Distribution (NBD) described by its Probability Mass Function (PMF) 3.13:

$$P_{\mu,k}(n) = \frac{\Gamma(n+k)}{\Gamma(n+1)\,\Gamma(k)} \cdot \frac{(\mu/k)^n}{(\mu/k+1)^{n+k}} \tag{3.13}$$

The parameter μ is the mean of the distribution and the parameter k can be calculated from the mean μ and the standard deviation σ of the distribution by Equation 3.14:

$$k = \frac{\mu^2}{\sigma^2 - \mu} \tag{3.14}$$

Using this equation, the negative binomial distribution can be described by its mean μ and standard deviation σ. The parameter values can be understood to describe the distribution produced by a single participating nucleon. Therefore, the distribution produced by N_{Part} participating nucleons is described by a mean of $N_{Part} \cdot \mu$ and a standard deviation of $\sqrt{N_{Part}} \cdot \sigma$. Using the simulated N_{Part}, the amount of RPC and TOF detector hits are sampled independently. The effects of the production of particles as well as the acceptance and efficiency of the detectors are contained in the values of the parameters μ and σ. Since the detector efficiencies drop slightly at high multiplicities, N_{Part} is scaled down by an empirical correction factor ϵ expressed by Equation 3.15 in advance to the sampling:

$$\epsilon(\alpha) = 1 - \alpha \cdot {N_{Part}}^2 \tag{3.15}$$

The values of the parameters μ, σ and α are determined independently for the amount of RPC and TOF detector hits by an iterative fitting procedure aiming at minimizing the difference between the distribution sampled from the Glauber model simulation and the actually measured distribution quantified by a χ^2 value. The parameter values found to reproduce the measured distributions best are given by the following Table 3.1:

Estimator	$\boldsymbol{\mu}$	$\boldsymbol{\sigma}$	$\boldsymbol{\alpha}$
$\mathbf{N_{RPC}}$ **Hits**	0.590	0.839	5.20×10^{-6}
$\mathbf{N_{TOF}}$ **Hits**	0.252	0.520	7.20×10^{-6}

Table 3.1.: Parameter values for μ, σ and α used to sample the amount of RPC and TOF detector hits from N_{Part}.

Figure 3.15 shows the differential cross-sections in dependence of the amount of RPC detector hits (upper left), TOF detector hits (upper right) and the sum of RPC and TOF detector hits (lower left). The blue data points correspond to the Glauber model simulations calculated by the previously described method. They have been scaled using the scaling factor from the impact parameter distribution in combination with the black-disk approximation cross-section. The red data points correspond to experimentally measured events filtered by the event selection criteria described in Section 3.2 and normalized to the Glauber model results approximately in the region of the 0-30 % most central events.

In all three cases a significant drop of the distributions from experimental data at low amounts of hits is observed. This is a result of the centrality pre-selection conducted by the PT3 trigger which requires at least 20 raw RPC and TOF detector hits. However, due to further selection criteria applied onto the RPC and TOF detector hits during the event reconstruction procedure, also lower values than 20 are observed. Above this drop-off region in the range of the 30-50 % most central events the distributions from experimental data overshoot the Glauber model results in case of the amount of RPC detector hist as well as the sum of RPC and TOF detector hits. These overshoots are a result of Ag+C events contaminating the anticipated Ag+Ag events that are not rejected by the dedicated event selection criteria described in Section 3.2. Due to the asymmetry of the Ag+C collision system, particles emerging from it are strongly boosted in forward direction and thereby primarily measured in the RPC detector. Because of this contamination in this work the focus is put on the 0-30 % most central events where a strong accordance between experimental data and the Glauber model simulation is observed.

Using the differential cross-section distributions, the total cross-section is again divided into centrality classes corresponding to fixed proportions. Since, unlike the continuous impact parameter, amounts of hits can only have integer values, an infinitely precise selection of an anticipated proportion of the total cross-section is impossible. Furthermore, each border influences the two adjacent centrality classes. To overcome these problems, a

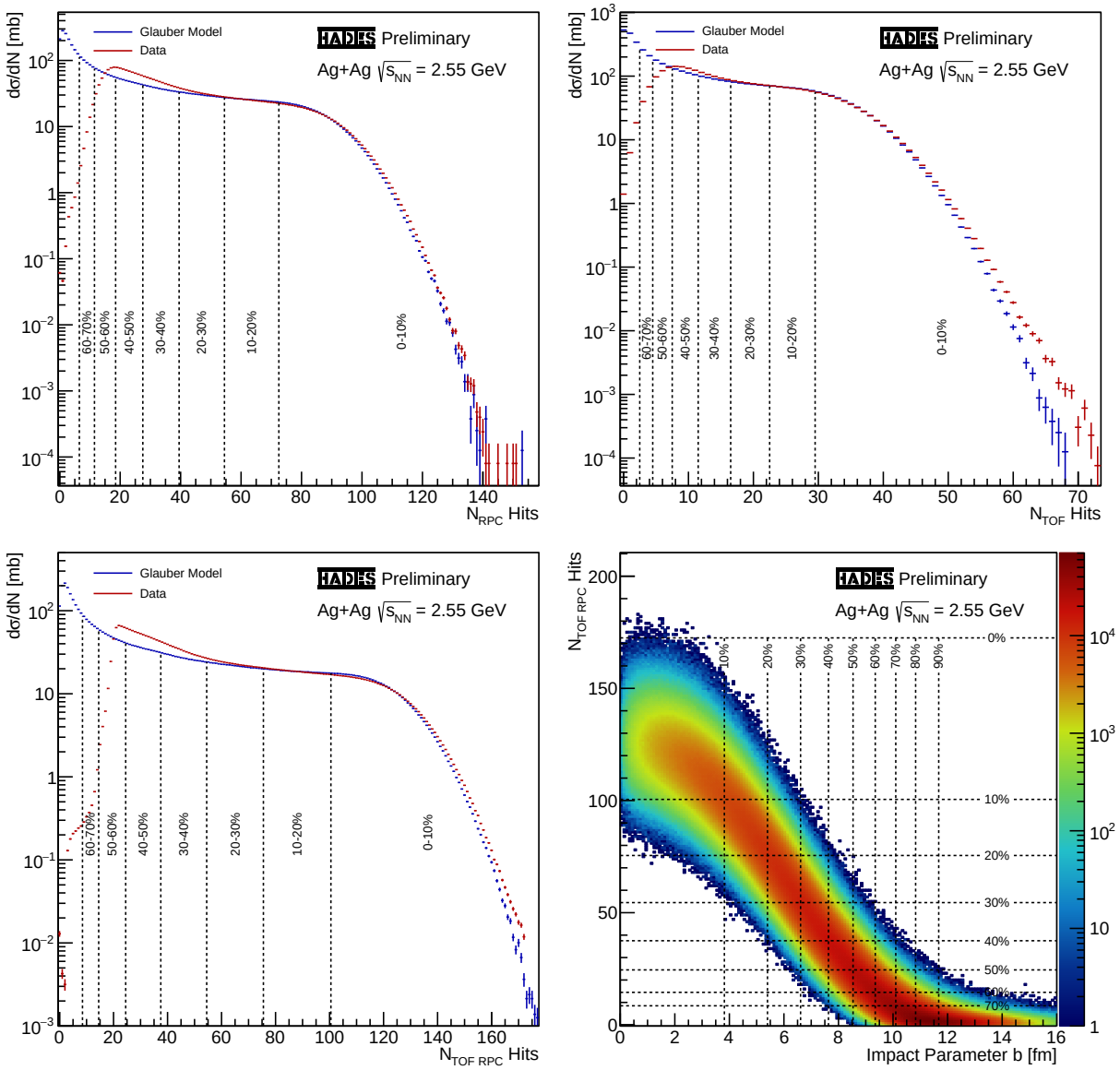

Figure 3.15.: Differential cross-sections in dependence of the amount of RPC detector hits (upper left), TOF detector hits (upper right) and the sum of RPC and TOF detector hits (lower left) for the Glauber model simulations (blue) and experimental data (red). The lower right plot shows the correlation between the impact parameter and the amount of RPC and TOF detector hits for the applied Glauber model. The dotted lines divide the total cross-section into centrality classes comprising 10 % each according to the corresponding quantity.

χ^2 technique is applied to quantify the accordance between the actual proportion of the total cross-section contained in each centrality class and the anticipated proportions. All combinations of feasible border positions are tested and finally the combination with the smallest overall χ^2 value is selected. These borders are shown in Figure 3.15 by the dotted lines for centrality classes corresponding to approximately 10 % of the total cross-section.

The lower right plot of Figure 3.15 shows the correlation between the impact parameter and the amount of RPC and TOF detector hits simulated by the Glauber model in combination

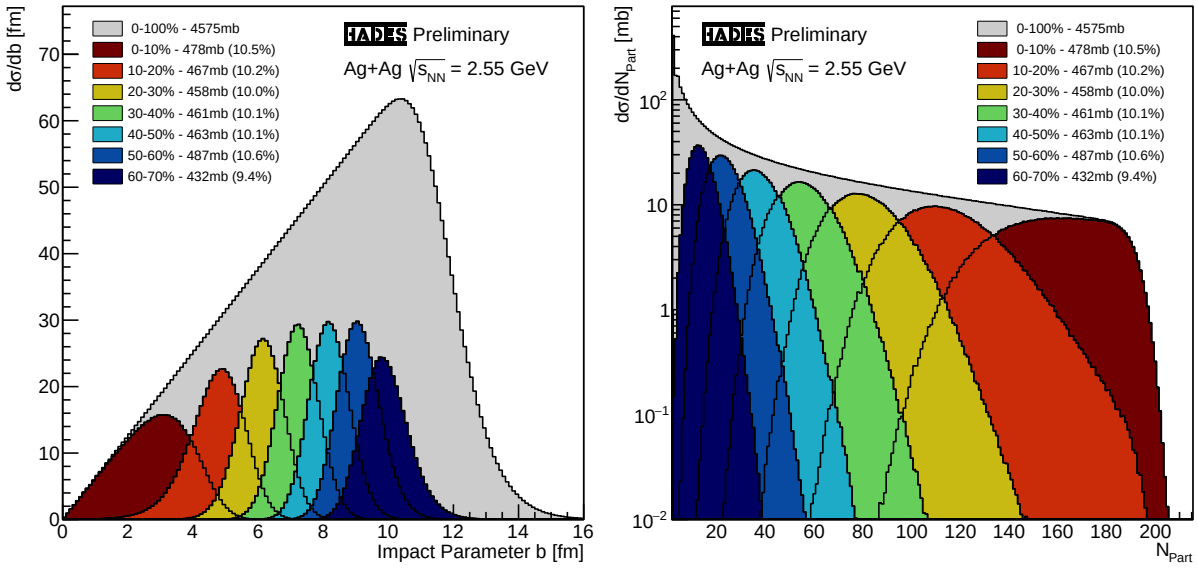

Figure 3.16.: Differential cross-sections in dependence of the impact parameter (left) and the amount of nucleons participating in the reaction (right). The colored distributions correspond to the differential cross-section distributions of events from centrality classes comprising approximately 10 % of the total cross-section that are selected using the amount of RPC and TOF detector hits. Furthermore, the actual proportions of the total cross-section contained by the different centrality classes are given in the legend.

with the technique described previously. The vertical dotted lines divide the total cross-section in 10 equal centrality classes using the impact parameter and the horizontal dotted lines using the amount of RPC and TOF detector hits. Although most events are distribute to the correct centrality class using the amount of RPC and TOF detector hits, the spread of the amount of nucleons participating in the reaction and the amounts of RPC and TOF detector hits sampled from it around their means leads to a non negligible amount of events distributed to a wrong centrality class when using the amount of RPC and TOF detector hits for the classification.

The same effect can also be observed in Figure 3.16. The left part of it shows the differential cross-sections in dependence of the impact parameter and the right plot in dependence of N_{Part} from the Glauber model simulation. The gray distribution corresponds to the total cross-section and the colored distributions correspond to centrality classes comprising approximately 10 % of the total cross-section selected using the amount of RPC and TOF detector hits. While in both cases a clear separation between the centrality classes is observed, the distributions significantly overlap with the adjacent centrality classes and, especially in the more peripheral region, even with the next to adjacent centrality classes. This effect needs to be considered when comparing experimental results with theoretical simulations where the impact parameter and thereby the actual centrality is known. The legends of the plots, furthermore, show the actual proportions of the total cross-section comprised by the centrality classes which are all close to the anticipated 10 %. The divergences are due to the fact that, as already stated, an infinitely precise selection of a proportion of the total cross-section using the amount of RPC and TOF detector hits is impossible due to their integer character.

Centrality Class	**Impact Parameter**	$\mathbf{N_{RPC} + N_{TOF}}$ **Hits**	$\langle N_{Part} \rangle$	$\Delta \langle N_{Part} \rangle$
0 - 25 %	0.00 - 6.04 fm	65 - 172	127.7	±6.4
0 - 10 %	0.00 - 3.82 fm	101 - 172	160.9	±6.9
10 - 20 %	3.82 - 5.40 fm	76 - 100	114.5	±6.2
20 - 30 %	5.40 - 6.62 fm	55 - 75	81.1	±5.1
30 - 40 %	6.62 - 7.64 fm	38 - 54	56.5	±5.4
40 - 50 %	7.64 - 8.54 fm	25 - 37	38.1	±4.7

Table 3.2.: Centrality class selection ranges and $\langle N_{Part} \rangle$ values finally used in the analyses. Please note that the given values are not yet published and therefore have to be understood as preliminary values.

In the analyses described in Chapter 4 experimental events as well as experimental events with embedded simulated particles are distributed to the various centrality classes according to their amount of RPC and TOF detector hits while entirely simulated events are distributed according to their impact parameter. Table 3.2 summarizes the impact parameter as well as amounts of RPC and TOF hit ranges consistently used throughout this thesis. Furthermore, the average amount of nucleons participating in reactions from the various centrality classes $\langle N_{Part} \rangle$, determined using the Glauber model simulation, are given. In the analyses later on these are used to study the dependence between measured observables and the size of the system created in the collision.

3.6. Off-Vertex-Decay Topology

As stated before, particles containing strangeness are produced very rarely in heavy-ion collisions at typical HADES energies. Even in the most central Ag(1.58A GeV)+Ag collisions a Λ hyperon is produced only in approximately every 10^{th} collision. On the other side, the decay products of its primary decay channel $\Lambda \rightarrow p + \pi^-$ are much more abundant. With approximately 60 protons, primarily coming from the colliding nuclei, and approximately 15 π^- [138], primarily produced as pairs or by hadronic resonances, in the most central Ag(1.58A GeV)+Ag collisions, out of 9,000 p-π^--pairs only one corresponds to the decay of a Λ hyperon. Similar ratios between expected signal rates and combinatorial pairs are found for the $K^0_S \rightarrow \pi^+ + \pi^-$ decay and the $^3_\Lambda H \rightarrow {}^3He + \pi^-$ decay. In case of the Ξ^- hyperon, which is expected to be produced only once in approximately 10,000 Ag(1.58A GeV)+Ag collisions and which decays primarily via the two-step decay process $\Xi^- \rightarrow \Lambda + \pi^- \rightarrow p + \pi^- + \pi^-$, the combinatorial background exceeds the expected signal by a factor of 135,000,000 in the most central collisions.

Obviously, a method to strongly reduce the combinatorial background is required. The decay of strangeness is mediated by the weak interaction leading to rather long mean lifetimes of the corresponding hadrons. Multiplied with the speed of light, one estimates the mean flight length $c\tau$, which amounts to several centimeters in case of the discussed decays. Therefore, the daughter particles of these decays originate from a secondary vertex which can be located several centimeters away from the primary collision vertex.

Based on this displaced secondary vertex a so called off-vertex-decay or V0 topology quantified by the parameters depicted in Figure 3.17a can be defined. The first parameter is called VDX and corresponds to the distance between the event vertex and the decay vertex which is the center point of the vector connecting the daughter particle trajectories at their points of closest approach. The next two parameters define the Distances of Closest Approach (DCA) between the daughter particle trajectories and the event vertex also called Vertex Distances (VDs). Conventionally, in this thesis the heavier daughter particle is referred to as daughter 1 (Dau1) and the lighter daughter particles as daughter 2 (Dau2). These three parameters quantify how far away from the primary event vertex the hypothetical decay occurred and therefore have larger values in case of actual weak decays than in case of combinatorial background.

The next parameter is called MotVD and is defined as the DCA between the hypothetical mother particle trajectory and the event vertex. Since the daughter particle trajectories do not necessarily have an intersection point in the three dimensional space, their DCA is quantified by another parameter called Minimum Track Distance (MTD). Ideally, those last two parameters are 0 in case of actual weak decays, however, the limited resolution of the reconstructed trajectories as well as a potential displacement between the estimated event vertex and the actual collision vertex lead to in non-zero values.

The final parameter is the opening angle between the two daughter particle trajectories which is called A. Its primary purpose is to discard constellations with very low opening angles in which the trajectories of the two daughter particles would be indistinguishable close in the first two MDC detector planes. This is necessary to achieve a realistic description of the remaining combinatorial background using the method which will be described

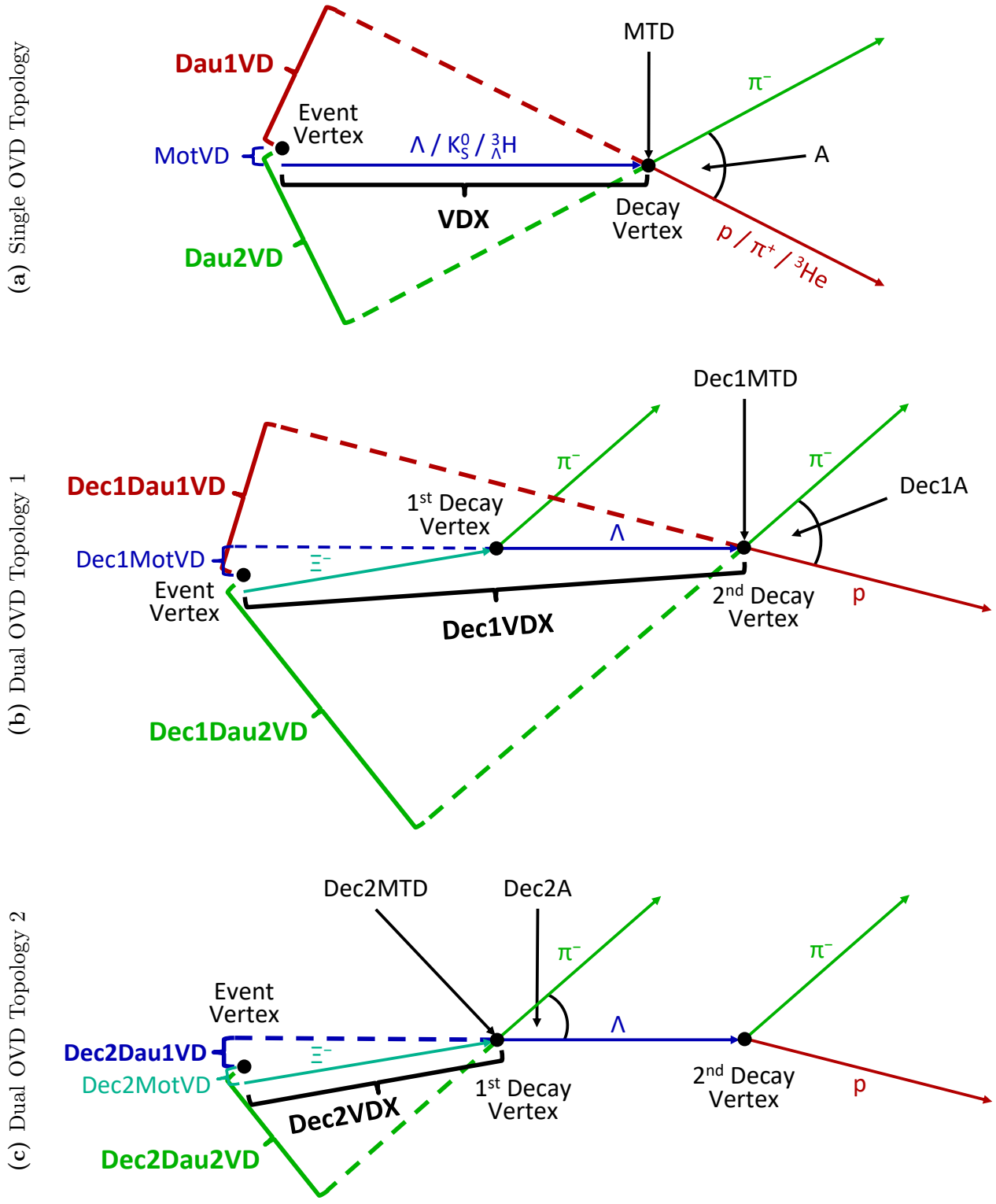

Figure 3.17.: Schematic depictions of the Off-Vertex-Decay (OVD) topologies and the corresponding parameters in case of a single decay (a) as well as the second (b) and the first (c) sub-decay of a two-step cascade decay.

in Section 3.9. Finally, to account for the forward boost of the particle emerging from the collision due to the fixed target setup, the decay vertex is required to be located after the event vertex in longitudinal direction ($Z_{\mathrm{EventVertex}} < Z_{\mathrm{DecayVertex}}$).

Particles containing two strange quarks like for example the Ξ^- hyperon usually decay via two consecutive weak decays. In these cases two sets of off-vertex-topology parameters are defined as depicted in Figures 3.17b and 3.17c. Conventionally, in this thesis the decays are numbered in the order they are reconstructed which is reverse to the order they actually occur. Note that the mother particle of the second decay is at the same time a daughter particle of the first decay and therefore the parameters Dec1MotVD and Dec2Dau1VD are identical. This needs to be taken into account when selection criteria are applied to these parameters as it is further discussed in Section 4.5. The forward boost is again accounted for by requiring the consecutive vertices to be positioned in longitudinal direction in the same order they occur in time ($Z_{\mathrm{EventVertex}} < Z_{1^{\mathrm{st}}\mathrm{DecayVertex}} < Z_{2^{\mathrm{nd}}\mathrm{DecayVertex}}$).

3.7. Event Vertex Determination

The event vertex is used as an estimate for the collision vertex in the definition of the off-vertex-topology parameters described in the previous Section 3.6. Since most of the parameters are determined using the event vertex, the precision of its determination is of extraordinary importance. In Section 2.3.2 three ways of estimating the collision vertex are described, however, the determination can be further improved using the method described in the following.

Figure 3.18 shows the distribution of the position of the Track-Candidate-Vertex, which is the most precisely determined vertex described in Section 2.3.2. The left plot shows the distributions of the transverse x- and y-position. The actual transverse position of the collision vertex is limited by the diameter of the target material disks of 2.2 mm (cf. Section 2.2.2) and the diameter of the heavy-ion beam. Using the START detector the spacial distribution of the beam-ions was monitored during the entire beam time (cf. Section 2.2.1). Consistently, the beam-ions were primarily observed in 3-4 x- and y-strips of the START detector which corresponds roughly to a Full Width at Half Maximum (FWHM) of 1 mm in x- and y-direction. The transverse distributions of the event vertex however have FWHMs $\gtrsim$ 2 mm. Therefore, in the transverse directions the most probable positions determined by Gaussian fit functions are used for the event vertex. In the analyzed beam time these most probable positions are –0.578 mm in x- and –0.299 mm in y-direction depicted by the black lines in Figure 3.18.

The right plot of Figure 3.18 shows the distribution of the Track-Candidate-Vertex in z-direction. Here the feasible collision vertex positions are the discrete positions of the 15 target segments since their thickness of 40 µm is negligible. These positions as well as the borders used to distribute the events over the 15 target segments are determined by a 15-fold Gaussian fit function with a common standard deviation σ which is depicted red in Figure 3.18. The means of the Gaussians are taken as the positions of the vertex segments and are depicted by black lines. The borders used to separate the target segments are determined by Equation 3.16 between two segments with c_i and μ_i being the scale and mean of the Gaussians corresponding

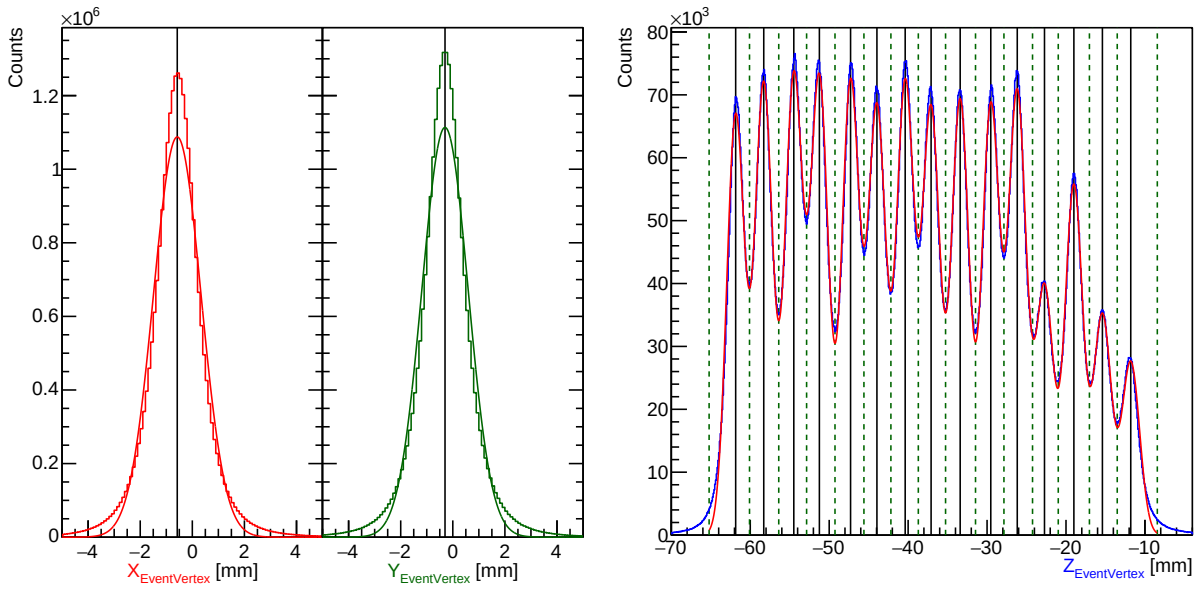

Figure 3.18.: Distribution of the event vertex reconstructed via the methods described in Section 2.3.2 of events fulfilling the event selection criteria described in Section 3.2. The left plot shows the x- and y-direction distribution as well as the corresponding Gaussian fit functions. The right plot shows the distribution in z-direction as well as the corresponding 15-fold Gaussian fit function. The lines indicate the values determined by the method described in the text to improve the collision vertex estimation. The plots show a subset of all events which is representative for the beam time.

to the two adjacent segments and σ being the common standard deviation:

$$z = \frac{\sigma^2 \ln\left(\frac{c_1}{c_2}\right) + \frac{\mu_2^2 - \mu_1^2}{2}}{\mu_2 - \mu_1} \quad (3.16)$$

The lower border of the first target segment is set to the position of the first target segment minus 3σ and the upper border of the last target segment is set to the position of last target segment plus 3σ. In the right plot of Figure 3.18 the borders are depicted as green dotted lines. Finally, the positions and ranges consistently used in the analyses described in Chapter 4 to determine the z-position of the event vertex are summarized in Table 3.3.

Target Segment	Position	Range
1	–61.848 mm	–65.212 - –60.094 mm
2	–58.290 mm	–60.094 - –56.391 mm
3	–54.483 mm	–56.391 - –52.862 mm
4	–51.243 mm	–52.862 - –49.265 mm
5	–47.292 mm	–49.265 - –45.600 mm
6	–43.953 mm	–45.600 - –42.182 mm
7	–40.373 mm	–42.182 - –38.709 mm
8	–37.090 mm	–38.709 - –35.257 mm
9	–33.406 mm	–35.257 - –31.463 mm
10	–29.529 mm	–31.463 - –27.863 mm
11	–26.175 mm	–27.863 - –24.240 mm
12	–22.725 mm	–24.240 - –20.980 mm
13	–19.002 mm	–20.980 - –17.033 mm
14	–15.388 mm	–17.033 - –13.509 mm
15	–11.797 mm	–13.509 - –8.432 mm

Table 3.3.: z-Positions and ranges of the 15 target segments used for the event vertex determination, see text for details.

3.8. Armenteros-Podolanski Method

The Armenteros-Podolanski (AP) method was first proposed 1954 by J. Podolanski and R. Armenteros [147]. It has been invented to reconstruct particles decaying into two daughter particles. First, the transverse and parallel components of the momentum vectors of the daughter particles, with respect to the hypothetical mother particle, are calculated in the laboratory system as it is shown by Figure 3.19 and defined by Equations 3.17 and 3.18:

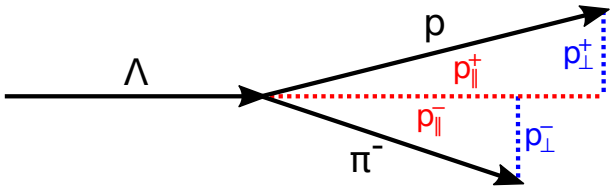

Figure 3.19.: Schematic geometric definition of the Armenteros-Podolanski variables $p_{\perp}^{\pm}$ (blue) and $p_{\parallel}^{\pm}$ (red) taking the $\Lambda \rightarrow \mathrm{p} + \pi^{-}$ decay as example.

$$p_{\perp}^{+} = \frac{|(\vec{p}_{+} + \vec{p}_{-}) \times \vec{p}_{+}|}{|\vec{p}_{+} + \vec{p}_{-}|} \quad \text{and} \quad p_{\perp}^{-} = \frac{|(\vec{p}_{+} + \vec{p}_{-}) \times \vec{p}_{-}|}{|\vec{p}_{+} + \vec{p}_{-}|} \tag{3.17}$$

$$p_{\parallel}^{+} = \frac{(\vec{p}_{+} + \vec{p}_{-}) \cdot \vec{p}_{+}}{|\vec{p}_{+} + \vec{p}_{-}|} \quad \text{and} \quad p_{\parallel}^{-} = \frac{(\vec{p}_{+} + \vec{p}_{-}) \cdot \vec{p}_{-}}{|\vec{p}_{+} + \vec{p}_{-}|} \tag{3.18}$$

In the equations + conventionally refers to the daughter particle with positive and – with negative electrical charge. However, since the charges of the daughter particles do not influence the kinematics, the method can also be applied to decays involving neutrally charged particles. The positions of the polarity signs differ in the equations just for better readability. Due to momentum conservation, the transverse components of the momentum vectors of the daughter particles are of equal size ($p_{\perp}^{+} = p_{\perp}^{-} = p_{\perp}$). They constitute the first Armenteros-Podolanski variable. The second variable α is defined by Equation 3.19 and can be understood as the asymmetry between the parallel momentum components.

$$\alpha = \frac{p_{\parallel}^{+} - p_{\parallel}^{-}}{p_{\parallel}^{+} + p_{\parallel}^{-}} \tag{3.19}$$

Using these parameters, the kinematic constraints can be described by the decay dependent constants p_{cms}, α_0 and r_{α}. The constant p_{cms} is defined by Equation 3.20 using the masses of the two daughter particles $m_{\pm}$ as well as the mass of the mother particle M. In case the entire energy released in the decay is converted into transverse momentum of the daughter particles, $p_{\perp}$ reaches its maximum possible value p_{cms} ($\Rightarrow p_{\perp} \leq p_{cms}$).

$$p_{cms} = p_{cms}^{\pm} = \sqrt{\left(\frac{M^2 + m_{\pm}^2 - m_{\mp}^2}{2M}\right)^2 - m_{\pm}^2} \tag{3.20}$$

Furthermore, in this special case, the value of the asymmetry between the longitudinal momenta α is equal to the constant α_0, defined by Equation 3.21. If the mother particle of the decay is ultra-relativistic ($\beta \rightarrow 1$) and the entire energy released in the decay is converted into longitudinal momentum of the daughter particles, $p_{\perp}$ amounts to 0 and α

can be $\alpha_0 \pm r_\alpha$, with r_α being defined by Equation 3.21 too.

$$\alpha_0 = \frac{m_+^2 - m_-^2}{M^2} \quad \text{and} \quad r_\alpha = \frac{2p_{cms}}{M} \tag{3.21}$$

At typical HADES collision energies $\sqrt{s_{NN}}$ of few GeV, most hadrons are produced with momenta comparable to their mass ($p \approx m$) hence they do not reach the ultra-relativistic limit which requires much larger momenta ($p \gg m$). Furthermore, the boost of the CM system with respect to the laboratory system amounts to approximately two third ($\beta_{cms} \approx 2/3$) which is also not sufficient to consider the mother particles ultra-relativistic in the laboratory system. Therefore, in the following the Armenteros-Podolanski variables are calculated after an additional artificial boost of $\beta = 0.99$ has been applied on the Lorentz vectors of the daughter particles.

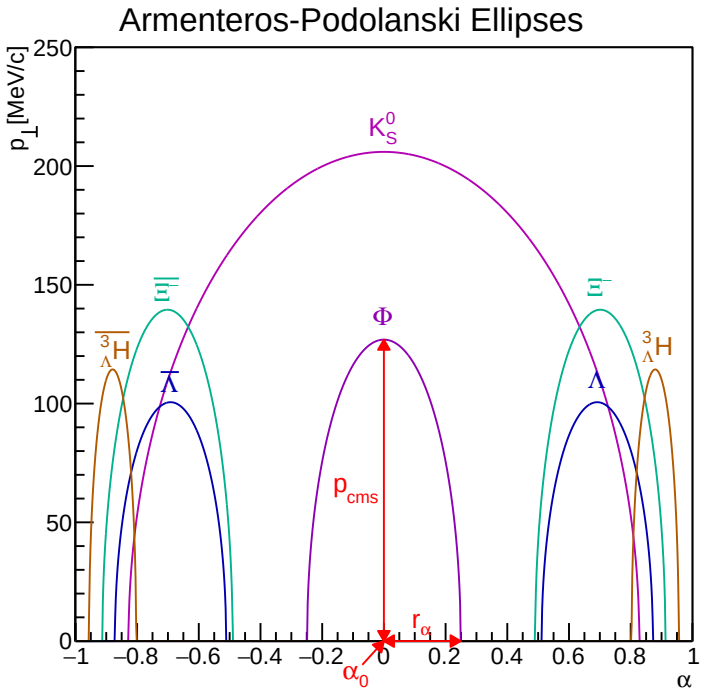

Figure 3.20.: Theoretical Armenteros-Podolanski ellipses for the most abundant two-body-decay channels of multiple particles: $K_S^0 \to \pi^+ + \pi^-$, $\phi \to K^+ + K^-$, $\Lambda \to p + \pi^-$, ${}^3_\Lambda H \to {}^3He + \pi^-$ and $\Xi^- \to \Lambda + \pi^-$. The red arrows demonstrate the meaning of the constants p_{cms}, α_0 and r_α taking the ϕ decay as example.

Using these prerequisites, the kinematic constraints of the two-body-decay can now be expressed by (half) ellipses in the α-$p_\perp$-plane ranging from $(\alpha_0 - r_\alpha,\ 0)$ over $(\alpha_0,\ p_{cms})$ to $(\alpha_0 + r_\alpha,\ 0)$. These ellipses are described by Equation 3.22 and depicted in Figure 3.20 for multiple different particle decays.

$$\left(\frac{\alpha - \alpha_0}{r_\alpha}\right)^2 + \frac{p_\perp^2}{p_{cms}^2} = 1 \tag{3.22}$$

In this work, a new way of using the Armenteros-Podolanski parameters has been developed. Therefore, the characteristic ellipses are interpreted in polar coordinates normalized to the semi-major and semi-minor axes of the ellipses. The corresponding radial coordinate as well as the azimuthal angle are given by the following Equation 3.23 and are illustrated in Figure 3.21.

$$r_{\alpha p_\perp} = \sqrt{\left(\frac{\alpha - \alpha_0}{r_\alpha}\right)^2 + \frac{p_\perp^2}{p_{cms}^2}} \quad \text{and} \quad \phi_{\alpha p_\perp} = \arctan\left(\frac{p_\perp}{p_{cms}} \cdot \frac{r_\alpha}{\alpha_0 - \alpha}\right) \tag{3.23}$$

Figure 3.21 shows the distribution of simulated K^0_S over the α-$p_\perp$-plane. These kind of plots are commonly referred to as "Armenteros-Podolanski plots". The K^0_S have been reconstructed from their π^+ and π^- decay daughters which themselves have been selected according to the criteria described in Section 3.4. Besides that no further selection criteria have been applied. One observes that the measured distribution matches the theoretical distribution given by Equation 3.22 and depicted by the red curve almost perfectly. The remaining smearing around the theoretical curve is due to the limited invariant mass resolution of the measurement.

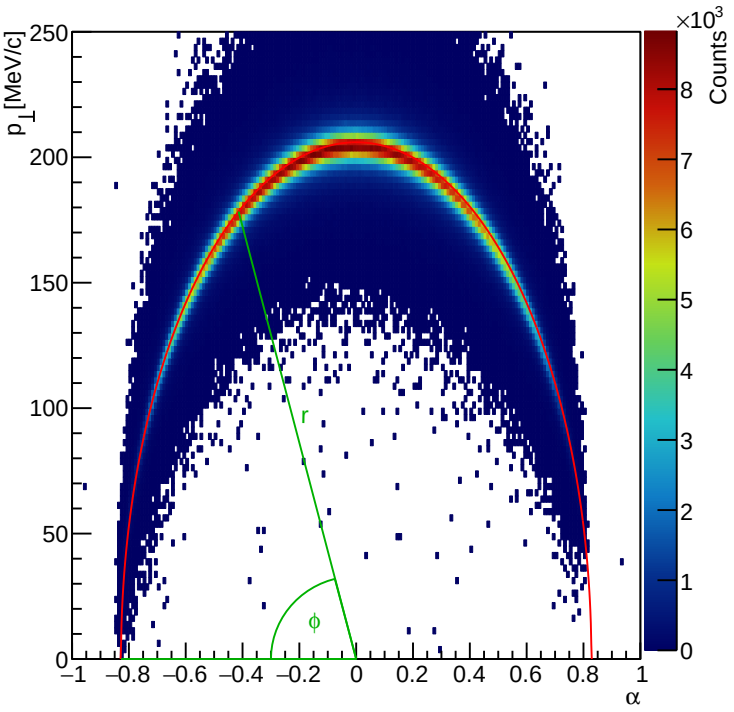

Figure 3.21.: Distribution of simulated K^0_S in the α-$p_\perp$-plane (Armenteros-Podolanski plot). The red ellipse shows the theoretical distribution according to Equation 3.22. Furthermore, the interpretation of the ellipse using polar coordinates is illustrated in green.

As already stated before, the semi-major and semi-minor axes of the ellipses, p_{cms} and r_α, correspond to the extreme cases in which the entire energy released in the decay due to the mass difference between the mother particle and the masses of the daughter particles is converted into either transverse or longitudinal momentum. Therefore, for fixed masses of the daughter particles, both ellipse axes are strongly correlated to the mass of the mother particle which can also be related to the radial component of the ellipses. However, to not bias the invariant mass distribution, independent parameters are required.

According to the definition of a polar coordinate system, the radial and azimuthal components are completely independent. Hence, the azimuthal angle in the α-$p_\perp$-plane is at most weakly correlated to the invariant mass. Furthermore, as it can be seen in Figure 3.21, actual K^0_S decays appear most abundantly around azimuthal angles of 90°, whereas the combinatorial background is located around $\approx$ 45° and 135°, as it will be shown in Section 4.3. Summing up, the azimuthal angle in the α-$p_\perp$-plane is almost independent from the invariant mass of the mother particle but shows significantly different distributions for actual decays and combinatorial background, making it an ideal parameter to be evaluated by a neural network, which will be described in Section 3.10.

3.9. Background Estimation

Although all methods described in this chapter aim at increasing the purity of the extracted signals, significant contaminations, called background in the following, always remain. The residual background needs to be properly described and subtracted to extract the true signal counts. The method applied depends on wether the anticipated signal corresponds to a particle directly measured in the detector like protons, or a decaying particle reconstructed from its daughter particles like Λs. In the following, the basic principles of the background estimation procedures for both cases are described.

In case a charged particle is measured in the detectors, the background beneath its peak in the mass spectrum consists of tracks from the tails of neighboring particle peaks, as well as tracks build from wrong combinations of inner track segments, outer track segments and META hits. These background tracks are suppressed by the track selection procedure described in Section 3.3 an the particle identification procedures described in Section 3.4. The residual background needs to be described sufficiently precise. First, two regions on both sides of the anticipated peak in the mass spectrum are defined in which pure background is assumed. Using the shape of the mass spectrum in these two regions, the background beneath the signal peak is interpolated using a cubic spline interpolation function together with the interpolation methods of the GNU Scientific Library (GSL) [92]. In Section 4.1 this approach is described in more detail and used to estimate the background contaminating the proton mass peak.

If a particle is reconstructed from its decay daughters, the background in the corresponding invariant mass spectrum is dominated by random combinations of uncorrelated particles pairs, called combinatorial background. This type of background can be reproduced by combining particles of the respective species from different events as they are necessarily uncorrelated, which is commonly referred to as the mixed-event technique. However, restrictions on the event classes, from which particles are combined, need to be taken to ensure a realistic description of the combinatorial background.

Since most of the off-vertex-decay topology parameters, described in Section 3.6, depend on the position of the collision vertex, only particles from events with the same primary event vertex should be combined. Using the event vertex estimation procedure described in Section 3.7, the events can be distributed among the 15 possible target segments each having its own discrete event vertex position, which is why only particles from events originating from the same target segment should be combined.

Furthermore, since the efficiencies of the detectors and the event reconstruction depend on the amount of particles created in the collision, due to occupancy effects, the average track quality decreases with rising multiplicity of particles. To assure that the quality of the mixed-event combinations reflects the quality of the same-event combinations, only particles from events with similar multiplicities may be combined. This is achieved by distributing the events to 20 equal multiplicity classes according to their amount of RPC and TOF detector hits, which is used as a measure for the event multiplicity, and only combining particles from events with the same multiplicity class.

Additionally, since the performance of the detector system and thereby also the quality of the tracks fluctuates over time, as it was shown in Section 3.2.1, only particles from events from the same day of the beam time are combined. Finally, a lower limit on the opening angle between the two daughter particle trajectories, which was introduced as parameter A in Section 3.6, needs to be applied. The reason therefore is to preclude further occupancy effects because in case of very low opening angles the probability that the two daughter particle tracks become indistinguishable close in the inner MDCs rises in the same-event case but not in the mixed-event case. As it will be shown in the sections of Chapter 4, the mixed-event technique describes the combinatorial background in the invariant mass spectra well. Furthermore, as it will be described in Section 3.10, the mixed-event combinations are used as a background sample for the training of the neural networks which improve the separation of actual weak decay daughter combinations and combinatorial background.

3.10. Neural Network Analysis

In references [18, 170] for the first time an Artificial Neural Network (ANN) was used to enhance the separation of weak decays and combinatorial background in HADES. In this work the approach further improved as described in the following.

The main principle is to perform a MultiVariate Analysis (MVA) taking the strong non-linear correlations between the off-vertex-decay topology parameters, described in Section 3.6, into account and thereby derive an additional response parameter with which the separation of actual signals and combinatorial background can be enhanced. All functionalities required and utilized in this work are contained in the Toolkit for MultiVariate Data Analysis with ROOT (TMVA) [109] which is fully integrated into the ROOT framework [150] and utilizes the same data structure.

As it was shown in Section 3.8, the azimuthal angle of the Armenteros-Podolanski ellipses, which is called APAngle in the following, is ideally suited as an input parameter for such kinds of analyses. Together with the off-vertex-decay topology parameters Dau1VD, Dau2VD, MotVD, VDX and MTD, which are defined in Section 3.6, a set of six input parameters is formed. Using simulated weak decays embedded into experimental data a signal sample of these six parameters with a high amount of entries is generated. Furthermore, an equally large background sample is generated using the mixed-event technique described in Section 3.9. Both samples are split into two equally large sub-samples. The first sub-samples are called training-samples and are used to train the MVA method on yielding 1 for the entries of the signal sample and 0 for the entries of the background sample. In the literature, this approach is called supervised learning since both the signal and the background sample are pure and clearly defined. The second independent sub-samples are called testing-samples and are utilized to evaluate the performance of the method in selecting signal and rejecting background after the training was finished.

In the previous analysis [170] it turned out that in order to use the off-vertex-decay topology parameters as input parameters for MVA analyses, hard selection criteria need to be applied on the signal and background sample in advance to the training. These criteria, in the following called pre-cuts, are required since due to the exponential nature

Criteria		MVA Method									
		Cuts	Likeli-hood	PDE-RS / k-NN	PDE-Foam	H-Matrix	Fisher / LD	MLP	BDT	Rule-Fit	SVM
Perfor-mance	No or linear correlations	○	+	○	○	○	+	+	○	+	○
	Nonlinear correlations	–	–	+	+	–	–	+	+	+	+
Speed	Training	–	+	+	+	+	+	○	○	○	–
	Response	+	+	–	○	+	+	+	○	+	○
Robust-ness	Overtraining	+	○	○	○	+	+	○	○	○	+
	Weak variables	+	○	–	–	+	+	○	+	○	○
Curse of dimensionality		–	+	–	–	+	+	○	○	○	
Transparency		+	+	○	○	+	+	–	–	–	–

Table 3.4.: Capabilities of the MVA approaches contained in the TMVA toolkit: Rectangular cut optimization (Cuts), Projective likelihood estimator (Likelihood), Multidimensional likelihood estimator (PDE-RS), k-Nearest Neighbour classifier (k-NN), Likelihood estimator using self-adapting phase-space binning (PDE-Foam), H-Matrix discriminant, Fisher discriminant, Linear Discriminant analysis (LD), Multi Layer Perceptron (MLP), Boosted Decision Tree (BDT), Predictive learning via rule ensembles (Rule-Fit) and Support Vector Machine (SVM). The different criteria are rated either "good" (+), "fair" (○) or "bad" (–). "Curse of dimensionality" refers to the amount of additional training samples required when further input variables are added. Table taken from [109].

of particle decays, they occur most abundantly close to the primary event vertex besides their rather long decay times. In these cases the off-vertex-decay topology parameters have almost no discrimination power and are thereby not suited to distinguish between actual decays and combinatorial background. The pre-cuts are adjusted individually for each decay and are described in more detail in the sections of Chapter 4.

In a first step, multiple different MVA approaches are tested to identify the ideal one to use. In Table 3.4 from the TMVA users guide [109], the various MVA approaches contained in the TMVA toolkit are listed and their capabilities are rated according to multiple criteria. For the reconstruction of weak decays only approaches which perform "good" concerning nonlinear correlations are considered since the input parameters used are by definition strongly nonlinearly correlated. Furthermore, since due to the large amount of combinatorial background the method needs to be evaluated a lot of times in the final analysis, at least a "fair" response speed is required. All setup variants of the remaining eligible approaches, as suggested by the TMVA developers, as well as the TensorFlow (TF) [5] ANN with default structure and with the same structure like the Multi Layer Perceptron (MLP) ANN are trained with a sample of 50,000 simulated $\Lambda \to \mathrm{p} + \pi^-$ decays and an according mixed-event background sample. Afterwards, their performances are evaluated using the independent testing samples which contain 50,000 decays and background combinations as well.

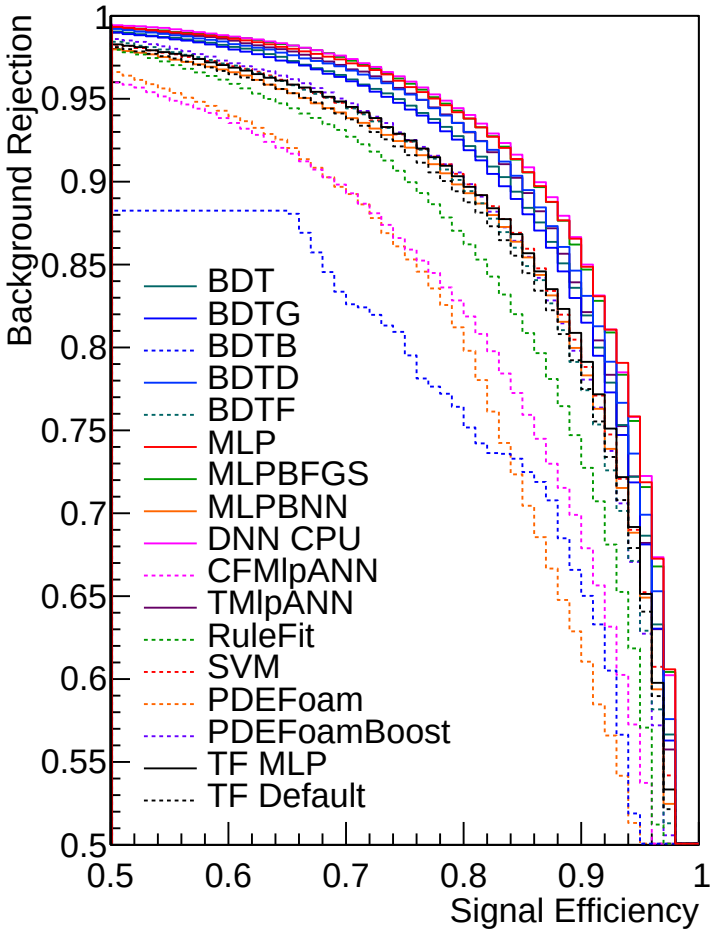

Figure 3.22.: Signal efficiency (true positive proportion) versus background rejection (true negative proportion), also called ROC-curves, for the reconstruction of Λs of various MVA approaches contained in the TMVA toolkit: Boosted Decision Tree (BDT), Multi Layer Perceptron (MLP), Deep Neural Network (DNN), Artificial Neural Network (ANN), Predictive learning via rule ensembles (Rule-Fit), Support Vector Machine (SVM) and Likelihood estimator using self-adapting phase-space binning (PDE-Foam). For each approach all setups suggested by the TMVA developers in [109] are tested. More details on the individual setups can be found there. Furthermore, the TensorFlow (TF) [5] ANN is tested with default setup and with a similar setup like the MLP ANN.

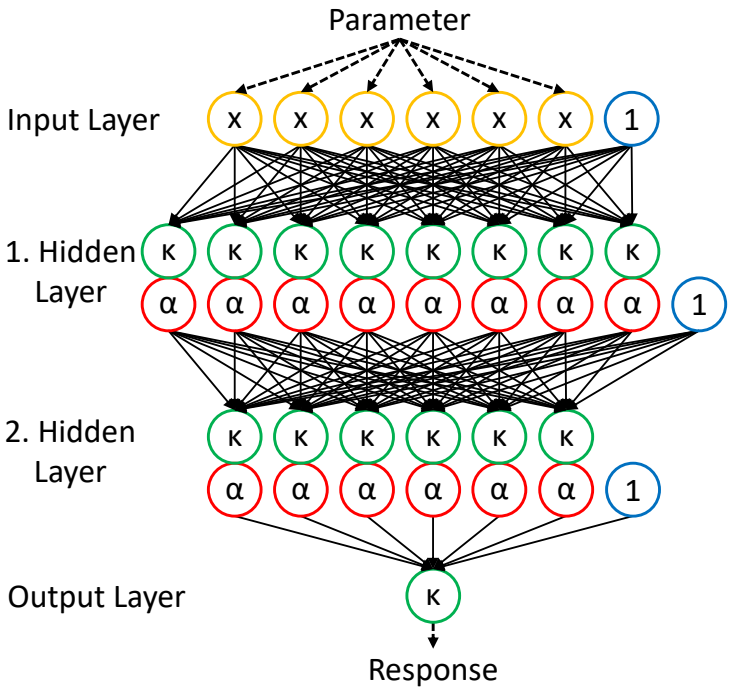

Figure 3.23.: Schematic structure of a MLP ANN with six input parameters, eight neurons in a first hidden layer, six neurons in a second hidden layer and one output parameter, like it is used in this work. The neurons of the input layer are depicted by yellow circles which represent linear functions x. The bias neurons are depicted by blue circles which represent constants of value 1. The neurons in the hidden layers are depicted by a green circle which represents their synapse function κ and a red circle which represents their activation function α. The neuron of the output layer is depicted solely by its synapse function κ (green circle). All neurons are interconnected by 117 synapses depicted by black arrows. The functionality of the network is explained in the text in more detail.

The results of these evaluations are shown in Figure 3.22. For a given signal efficiency on the x-axis, which is defined as the proportion of events from the signal sample actually classified as signal, an according selection value on the MVA response is determined. Next, the background rejection, which is defined as the proportion of events from the background sample not classified as signal, is evaluated using this selection value and depicted on the y-axis. The resulting curves are also called Receiver Operating Characteristic (ROC) curves which is an umbrella term for these kinds of plots. In this representation an approach generating an entirely random response (worst case scenario) would generate a straight curve from (0,1) to (1,0) while an ideal approach would show a 100 % background rejection for any signal efficiency. Since all tested approaches clearly diverge from the "worst case" it can be concluded that all MVA approaches were successfully trained. Furthermore, significant performance differences between the various models are observed. Although TF ANNs are commonly used in many areas the show only an average performance compared to all other approaches in this special case. The MLP ANN approach (red curve) which was already used in the previous analyses shows one of the best performances of all approaches and was therefore selected as the approach to be finally used. Its functionality is explained in the following in more detail.

The schematic structure of a MLP ANN, like it is used in this analysis, is shown in Figure 3.23. The six input parameters of the MVA analysis are stored in six input neurons depicted by yellow circles. They correspond to a linear transmission function x since they simply pass on the stored value. Additionally, the input layer as well as the two hidden layers include bias neurons depicted by blue circles which always pass on a value of 1. The neurons of the input layer are connected to the eight neurons of the first hidden layer by 56 synapses depicted by black arrows. Every synapse passes the value of its input neuron multiplied by its intrinsic weight onto its output neuron. Therefore, every neuron in the first hidden layer has seven input values that are summed according to the synapse functions κ which are depicted by green circles. Next, the summed value is transformed by the activation function α, depicted as red circles and the result is passed on. Another 54 synapses connect the neurons from the first hidden layer to the six neurons of the second hidden layer which follow the same principle but have nine input values each. Finally, seven further synapses connect the neurons from the second hidden layer to the output neuron which solely sums its seven input values using again the synapse function κ. The summed value of the output neuron now corresponds to the response value of the ANN.

Besides the weights of the 117 synapses, which are adjusted during training, the setup of the ANN is fixed. Therefore, its Number of Degrees of Freedom (NDF) also corresponds to 117. The setup with eight neurons in the first and six neurons in the second hidden layer is chosen as it was found to provide a fair compromise between the capability of the ANN to adjust to any given training sample while remaining a low risk of training the neural network on statistical fluctuations, also called overtraining, due to too many free parameters. Within the TMVA toolkit three possible synapse functions κ, defined by Equation 3.24, are provided. In these functions j is the index of the neuron executing the function and i indexes the neurons from the previous layer l. y_i^l is the output value of neuron i from the layer l and w_{ij}^l is the weight of the synapse connecting neuron i from layer l with neuron j from layer $l+1$. The weights w_{0j}^l correspond to the weights of the synapses coming from the bias neurons. By default the "Sum" synapse function is used.

The functions "Sum of Squares" and "Sum of Absolutes" have also been tested, again using Λ decays, however the training does not converge when using them.

$$\kappa : \mathbb{R}^n \to \mathbb{R} = \begin{cases} w_{0j}^{(l)} + \sum_{i=1}^{n-1} y_i^{(l)} w_{ij}^{(l)} & \text{Sum} \\ w_{0j}^{(l)} + \sum_{i=1}^{n-1} \left(y_i^{(l)} w_{ij}^{(l)} \right)^2 & \text{Sum of Squares} \\ w_{0j}^{(l)} + \sum_{i=1}^{n-1} \left| y_i^{(l)} w_{ij}^{(l)} \right| & \text{Sum of Absolutes} \end{cases} \tag{3.24}$$

For the activation function α the four alternatives defined by Equation 3.25 are provided by the TMVA toolkit. In these functions x corresponds to the result of the synapse function of the neuron. By default the "Sigmoid" activation function is used. Again the other possibilities "Linear", "TanH" and "Radial" have been tested using Λ decays. In case of the "Linear" activation function the training does not converge. In case of the "TanH" and the "Radial" activation function very similar performances as compared to the default "Sigmoid" activation function are found. Therefore, the "Sum" synapse function in combination with the "Sigmoid" activation function is used for the final analyses.

$$\alpha : \mathbb{R} \to \mathbb{R} = \begin{cases} x & \text{Linear} \\ \frac{1}{1+e^{-x}} & \text{Sigmoid} \\ \frac{e^x - e^{-x}}{e^x + e^{-x}} & \text{TanH} \\ e^{-x^2/2} & \text{Radial} \end{cases} \tag{3.25}$$

The full response function of a MLP ANN with the described setup is finally expressed by Equation 3.26 with $\text{sig}(x)$ standing for the "Sigmoid" activation function. The response value y_{ANN} is calculated based on the values of the neurons in the input layer $y_i^{(1)}$ which correspond to the values of the input parameters $\vec{x}$. The synapse weights $w_{ij}^{(l)}$ can be interpreted as free parameters of the response function.

$$y_{ANN}(\vec{x}) = w_{01}^{(3)} + \sum_{k=1}^{6} w_{k1}^{(3)} \cdot \text{sig}\left(w_{0k}^{(2)} + \sum_{j=1}^{8} w_{jk}^{(2)} \cdot \text{sig}\left(w_{0j}^{(1)} + \sum_{i=1}^{6} w_{ij}^{(1)} y_i^{(1)} \right) \right) \tag{3.26}$$

In general the aim of the training is to find values for the synapse weights so that the response function yields 1 for signal and 0 for background events. Therefore, the so called Back Propagation (BP) method is used. At the beginning, the synapse weights are initialized with random values. The accordance between the actual and anticipated responses for the full training sample $\vec{x}_{1\ldots N}$ is quantified according to Equation 3.27, called error function, which follows the same principles like the χ^2 technique. $\hat{y}$ represents the anticipated result and therefore amounts to 1 for signal and 0 for background events.

$$E = \sum_{i=1}^{N} \frac{1}{2} \left(y_{ANN}(\vec{x}_i) - \hat{y} \right)^2 \tag{3.27}$$

Next, the gradient with respect to the synapse weights of the error function is calculated and the current weights are adjusted by subtracting the gradient multiplied with a positive value η called learning rate. This approach is also referred to as method of steepest gradient descent. In the BP implementation of the TMVA toolkit the weights are adjusted individually for each event from the training sample. Additionally, the entire training sample is processed multiple times iteratively in so called training cycles. The effect of a different amount of training cycles on the performance of the ANN has been investigated again using Λ decays. It has been found that 1500 training cycles provide a good compromise between performance of the ANN and the time required for the training.

In addition to the default BP training algorithm, the TMVA toolkit also provides more complex algorithms like for example the Broyden-Fletcher-Goldfarb-Shannon (BFGS) method. It follows the same base principle like the BP method, however, it also takes into account the second derivatives of the error function and therefore leads to a quicker convergence of the training at the cost of a higher computation time per training cycle. Concerning the Λ decays, the use of the BFGS training method provides no significant advantage compared to the standard BP method.

Finally, after the training is finished, a so called overtraining check is performed to assure that the ANN response is not influenced by statistical fluctuations of the training sample. This check is performed by calculating the signal efficiency and background rejection of the ANN for both the training and testing sample for three different selections on the ANN response. In case a strong difference between the training and the testing sample is found, the overtraining check and the entire training are considered unsuccessful.

Since high amounts of simulated decays are used to generate the signal sample and the background sample is generated using the mixed-event technique, statistical fluctuations are no problem to any of the analyses using the described MLP ANN. The individual analyses utilizing the described MLP ANN as well as their results are described in detail in the sections of Chapter 4. More details on the TMVA toolkit, its different MVA approaches and specific implementations can be found in [109].

4. Analysis Results

In this chapter the different particle analyses are described and their results are presented. Section 4.1 concerns the analysis of protons, Section 4.2 the reconstruction and analysis of Λs, Section 4.3 the reconstruction and analysis of K^0_S, Section 4.4 the reconstruction and analysis of ${}^3_\Lambda H$ and Section 4.5 the reconstruction and production rate estimation of Ξ^-. Each of these sections follows the same structure: First, the criteria used to identify the required particle tracks are described. In case of decaying particles, the method used to reconstruct and identify them is discussed next. Afterwards, the different sets of selection criteria used to perform the analysis and estimate the corresponding systematic uncertainties are defined. Finally, the actual analysis of the particle species including corrections for acceptance and efficiency effects is described. The proton, the Λ, the K^0_S and the ${}^3_\Lambda H$ are analyzed multi-differentially in transverse momentum, rapidity and centrality. The measured data points are extrapolated to the full phase-space using either an analytic model described in Section 1.4 or an effective model. Furthermore, different sources of systematic uncertainties are determined. For the Λ, the K^0_S and the ${}^3_\Lambda H$ the lifetime is measured in addition. For the Ξ^- a signal below the threshold of 5σ is found which is why both a production rate and an upper production limit estimation are performed.

Particle	**Color**	**Section / Reference**
Proton	Red	4.1
Λ	Blue	4.2
K^0_S	Magenta	4.3
${}^3_\Lambda H$	Orange	4.4
Ξ^-	Teal	4.5
K^+	Pink	[122]
K^-	Green	
ϕ	Violet	
Σ^+	Yellow	5.1
Σ^0	Azure	
Σ^-	Spring	
Background	Black	3.9

Table 4.1.: Color-code used for the various particles analyzed or shown in this thesis.

Throughout this thesis the color-scheme defined in Table 4.1 is used to ease the readability. For the interpretation of the analysis results in Chapter 5 also particles analyzed in the scope of other projects are necessary. The color-scheme is defined such that positive charged particles have reddish, neutral charged particles blueish and negative charged particles greenish colors. Background is always depicted black.

4.1. Proton Analysis

Protons consist of two up- and one down-quark $|uud\rangle$, carry an electrical charge of $+1$ and are the lightest existing baryons with a mass of ≈ 938 MeV/c^2. Thus, free protons are stable particles. In fixed-target heavy-ion collisions at beam energies of few GeV, protons are the most abundant charged particle emitted from the fireball. Only neutrons are emitted with higher abundances due to the isospin-asymmetry of the colliding nuclei. Both protons and neutrons are not produced in the collision as the production channel of a nucleon-antinucleon-pair in an elementary NN collision, given by Equation 4.1, is strongly suppressed due to its high threshold around 3.75 GeV.

$$N + N \rightarrow N + N + N + \overline{N} \tag{4.1}$$

Instead, the protons and neutrons emitted from heavy-ion collisions at this energy are either recombinations of the quarks contained in the constituent nucleons of the initially colliding nuclei or constituent nucleons themselves. As protons dominate the detectable part of particles emitted from the fireball and do not decay, their kinematic distributions provide direct access to the properties of the hot and dense matter at kinetic freeze-out. A large proportion of up to 50 % of the protons and neutrons emitted from heavy-ion collisions in the low energy regime are bound in light nuclei, primarily deuterons, tritons, ^{3}He and ^{4}He [177]. Combining free and bound proton multiplicities the amount of nucleons participating in the collision can be accessed as the production of nucleons is strongly suppressed and the multiplicity of neutrons can be estimated using the proton-neutron-ratio of the initially colliding nuclei. However, in this work only the measurement of free protons, which is described in the following, is considered.

4.1.1. Signal Extraction

Because of their properties, protons are directly measured in the detectors and thereby appear as a peak in the measured mass spectrum shown for example in Figure 3.6. In addition to the track selection criteria described in Section 3.3, proton candidates are identified based on their polarity, requiring a positive charge, their specific energy loss measured by the MDCs using the 3σ selection regions obtained via the method described in Section 3.4.2 as well as the track quality parameters $\chi^2{}_{\mathrm{RK}}$, MMQ and the total amount of MDC sense wire layers contributing to the track ($\mathrm{N_{MDC}}$). For the track quality parameters three different sets of selection criteria given by Table 4.2 are estimated by an educated guess. By default the minimal criteria set called “Standard” is used. The stronger sets of

Parameter	**Standard**	**Medium**	**Tight**
$\boldsymbol{\chi^2{}_{\mathrm{RK}}}$	< 400	< 300	< 200
MMQ	< 3.0	< 2.5	< 2.0
$\mathbf{N_{MDC}}$	—	> 17	> 19

Table 4.2.: The three sets of selection criteria used in the analysis of protons.

selection criteria called "Medium" and "Tight" are used to estimate the systematic effects of the performed selection by comparing their results with those of the default set of criteria.

The proton candidate sample selected by the described criteria is already almost free of background. Using the estimation procedure described in the following, its contribution integrated over the entire phase-space covered by the measurement amounts to $\lesssim 1$ %. However, a sophisticated method to estimate the remaining background beneath the signal is still required since in the high momentum region of the phase-space, the proportion of background tracks rises strongly. The primary contributions to the background tracks are deuteron tracks with calculated masses in the proton region that come from the tails of the deuteron peak. They are particularly important as they populate the high momentum region of the phase-space where the mass peaks are broad. ^{3}He-tracks contribute to the background in a similar phase-space region, however, due to their double charge they are strongly suppressed by the selection based on the measured specific energy loss. Especially in the lower momentum region of the phase-space also π^+-tracks contribute to the background. However, their contribution is less critical as in this region of the phase-space the mass peaks are narrow. The contribution of K^+-tracks is always negligible due to their low abundance.

The method used to perform the estimation of the background was developed and tuned specifically for the extraction of proton signals from the HADES Ag(1.58A GeV)+Ag beam time within this project. However, it is successfully applied to proton-, deuteron-, triton- and ^{3}He-signals from the HADES Au(1.23A GeV)+Au beam time with only minor modifications [112]. In the following, the method is described in detail.

The extraction of the proton signal counts is performed on the mass spectrum in the range between 100 and 2200 MeV/c^2 for particle candidates that passed the previously described selection criteria. Within the procedure, multiple quality checks are performed to reject phase-space cells for which the background estimation has either high statistical or systematic uncertainties. The method only considers cells with at least 1000 entries as otherwise the statistical uncertainties would render a precise estimation of the background almost impossible. In the first step, the peak finding method implemented in the ROOT class `TSpectrum`, which is described in [135], is used to determine the positions of all peaks in the spectrum. To prevent the identification of statistically fluctuating bins as peaks, a peak is required to exceed its surroundings by at least 1 % of the highest bin in the spectrum. The highest peak found in the range between 100 and 450 MeV/c^2 is assumed to be the π^+-peak, the highest peak between 450 and 1000 MeV/c^2 is assumed to be the proton peak and the highest peak between 1500 and 2200 MeV/c^2 is assumed to be the deuteron peak. As already stated before, the contribution of K^+ and ^{3}He which have rest masses in the considered range too, are negligible. In case no peak is identified in the proton region, the spectrum is discarded. In case neither a π^+ nor a deuteron peak is identified, the spectrum is considered free of background and the remaining steps of the background estimation procedure are skipped.

In the next step, it is ensured that the identified peak positions correspond to a local maximum of the spectrum. If not already the case, the positions are shifted accordingly. The final peak positions are depicted by red triangles in Figure 4.1. In case the local maximum of the proton peak deceeds 10 % of the global maximum, the spectrum is discarded

as well. Next, the minimum between the π^+ and proton peak as well as the proton and deuteron peak is determined. Using five equally spaced points positioned on the spectrum based on the determined minima, the shape of the spectrum around the minima is approximated using the cubic spline interpolation method from the GSL library. These interpolation points are depicted in Figure 4.1 by purple markers. If no π^+ or no deuteron peak is found, no interpolation is performed and the respective minimum is positioned beneath the proton peak at zero. Depending on the relation between the height of the opposite peak and the proton peak, the minimum is shifted outwards to take the long tail of a high background peak into account.

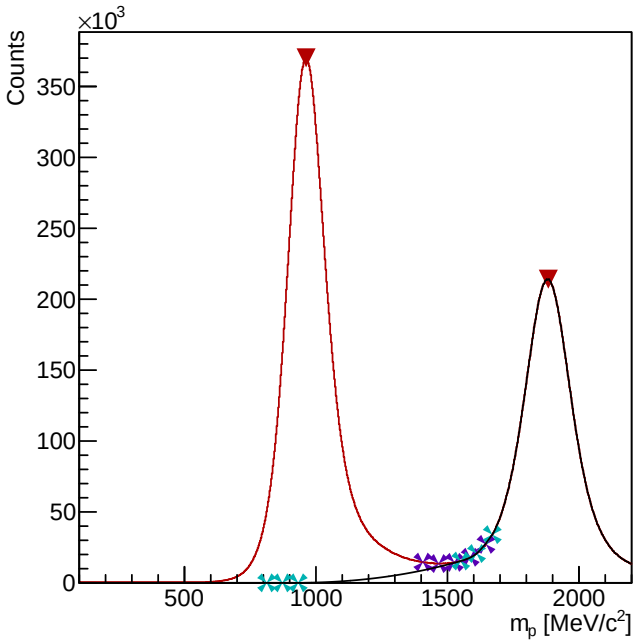

Figure 4.1.: Exemplary mass spectrum of the range relevant for the proton signal extraction, as described in the text. The red markers depict the identified peaks and the purple and cyan markers the used interpolation points.

In the next step, first the slope between the positions of the minima on both sides of the proton peak is calculated. Using the interpolations of the spectrum around the minima, the positions at which the slope of the interpolations equals the previously calculated slope are determined. Obviously, this is only done if the according interpolation has been performed, otherwise, the position of the minimum is taken. Based on these positions, three further interpolation points, which are depicted as cyan markers in Figure 4.1, are positioned on both sides of the proton peak. Finally, these six points are interpolated again using the cubic spline interpolation method from the GSL library. This final interpolation gives the estimated shape of the background beneath the proton peak depicted black in Figure 4.1.

To extract the amount of signal counts, the background is subtracted from the spectrum. Outside of the interpolation region the spectrum is assumed to consist of background only. The shape of the proton peak in the subtracted spectrum is approximated by an asymmetric[1] Gaussian function to determine its width. Finally, the subtracted spectrum is integrated in the $\pm 2\sigma$ range of the fit function which yields the anticipated proton signal counts. As a final check, the signal counts have to exceed at least 10 % of the total entries of the spectrum as it is discarded otherwise.

Over the entire Ag(1.58A GeV)+Ag beam time in the 0-25 % most central events about 28 billion protons in the RPC region and about 15 billion in the TOF region are measured. In the following section the emission of protons is analyzed multi-differentially.

[1]The independent treatment of RPC and TOF detector region can result in asymmetric peaks.

4.1.2. Multi-Differential Analysis

For the purpose of the multi-differential proton analysis, the entire phase-space is divided into 39 transverse momentum intervals with a width of 40 MeV/c from 160 to 1720 MeV/c and 16 rapidity intervals with a width of 0.1 from –0.85 to 0.75 in the CM system of the collision. The rapidity interval centered around 0, also called mid-rapidity, is analyzed additionally using 73 transverse momentum intervals with a width of 20 MeV/c from 260 to 1720 MeV/c. Furthermore, the analysis is performed independently for the three 10 % centrality intervals of the 0-30 % most central events resulting in a grand total of 2091 individual intervals. For each of these intervals, the proton signal counts are extracted using the method described in Section 4.1.1 independently for tracks measured in the RPC and TOF detector since they differ in the achieved mass resolution. However, as a fixed mass, transverse momentum and rapidity interval can be transformed to a polar angle interval, only in few phase-space intervals tracks in both RPC and TOF detector are measured. In these intervals, the extracted signal counts are summed up. If an interval is discarded by one of the quality criteria during the signal extraction, it is treated as if it were outside of the phase-space region covered by HADES.

Next, the extracted signal counts are corrected for losses due to acceptance and efficiency effects. In this work, acceptance a refers to the geometrical coverage of the active detector areas as particles not traversing an active detector part cannot be detected. Efficiency ϵ refers to the proportion of particles that traversed the active areas of the detector system but still do not contribute to the final signals extracted due to one of the following reasons:

- **The efficiencies of the detectors and the electronics ϵ_{det}:** Not every particle traversing the active area of a detector is actually recorded as the induced signal might e.g. be rejected by a threshold, overlay with the signal of another particle or hit the detector during its dead-time due to a previously recorded particle.
- **The efficiency of the track reconstruction method ϵ_{rec}:** To contribute to the actual analyses the track of a particle needs to be successfully reconstructed from the recorded detector hits. For this purpose the method described in Section 2.3.3 is used. As stated there, the reconstruction of tracks is in particular challenging and error-prone if a high amount of particles is measured close to each other in space and time resulting in not all tracks being properly reconstructed.
- **The efficiency of the track selection criteria ϵ_{sel}:** To reduce the amount of background contamination in advance to the signal extraction, the criteria described in Section 4.1.1 are applied. For the protons these criteria correspond to the standard track selection criteria described in Section 3.3, the 3σ MDC specific energy loss selection regions and the track quality criteria on ${\chi^2}_{\mathrm{RK}}$, MMQ and $\mathrm{N_{MDC}}$.

The total efficiency ϵ is equal to the product of the individual efficiencies. Both acceptance and efficiency are estimated using simulated UrQMD events with one proton simulated with Pluto embedded into each. The detector response and the reconstructed tracks corresponding to the simulated particles are generated as described in Section 2.3.4. The differential analysis of protons is applied to the simulated data conversely as to real data, taking only the embedded protons into account, yielding $N^{sim}_{rec,p}(p_t, y)$. Together with

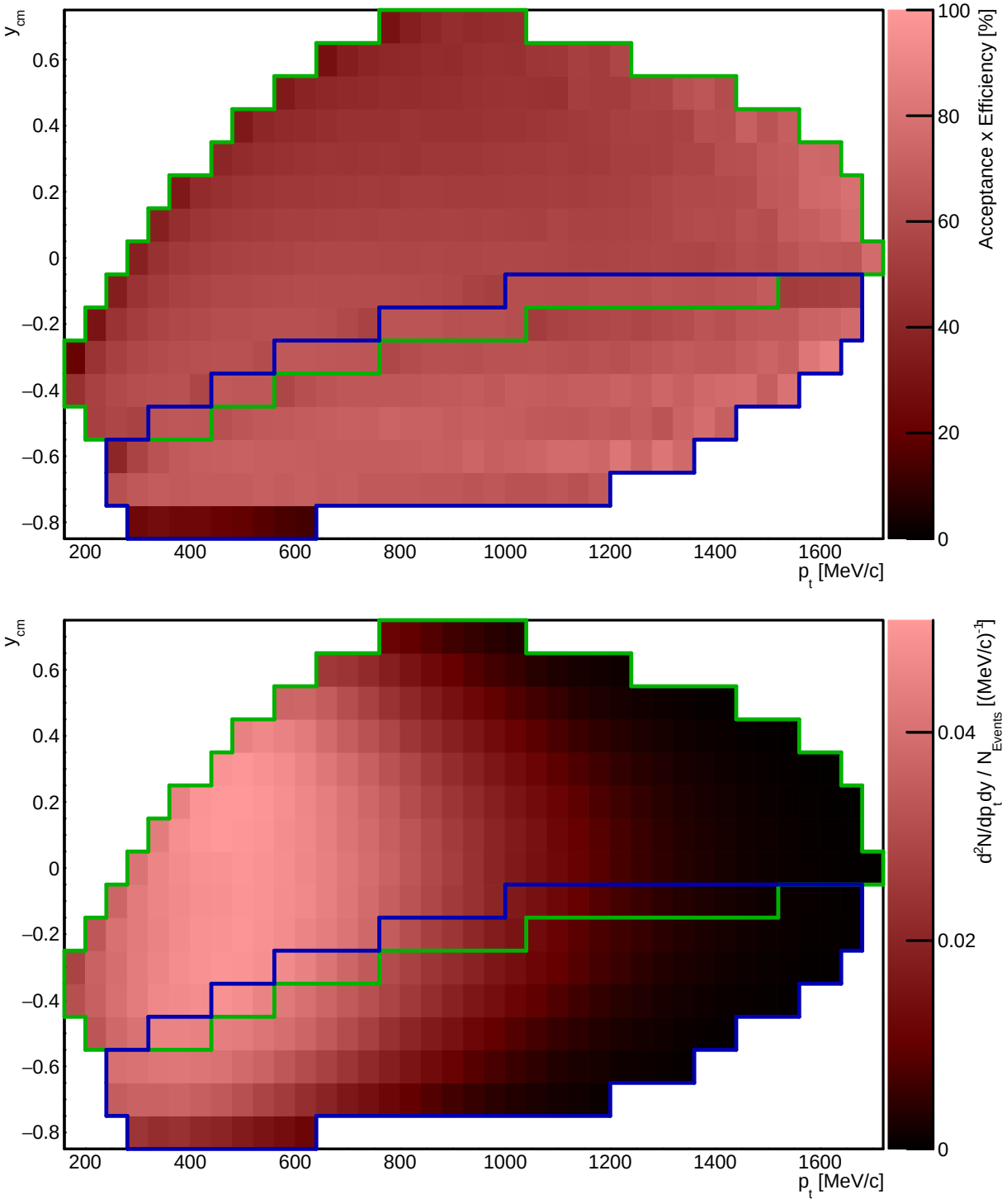

Figure 4.2.: Acceptance × Efficiency values (upper panel) as well as corrected and normalized proton emission rates (lower panel) from the 0-10 % most central Ag(1.58A GeV)+Ag events. The green-framed part of the phase-space is covered by the RPC and the blue-framed part by the TOF detector.

the amount of initially generated protons in the simulation input $N^{sim}_{gen,p}(p_t, y)$, the total correction quotients are calculated according to Equation 4.2. Their calculation and application to the amounts of extracted proton counts is done individually for each phase-space interval, since they depend strongly on the location where a particles traverses the detectors as well as its properties. To avoid high uncertainties, intervals with a correction quotient deceeding 10 % or a relative statistical uncertainty exceeding 20 % are discarded in addition. Furthermore, a manual selection is performed to discard intervals in which the signal extraction method failed for example because a peak was not properly identified. The determined Acceptance × Efficiency values are displayed in the upper panel of Figure 4.2. Finally, the corrected counts are normalized to the number of analyzed events as well as the transverse momentum and rapidity interval widths.

$$a_p \cdot \epsilon_{det,p} \cdot \epsilon_{rec,p} \cdot \epsilon_{sel,p} = \frac{N^{sim}_{rec,p}(p_t, y)}{N^{sim}_{gen,p}(p_t, y)} \tag{4.2}$$

The thereby obtained emission rates of protons over the entire phase-space are depicted in the lower panel of Figure 4.2 for the 0-10 % most central Ag(1.58A GeV)+Ag events. One observes that a large proportion of the phase-space to which protons are emitted is covered by the measurement and a smooth trend is observed both in transverse and longitudinal direction. This also holds true for the transition region between the part covered by the RPC detector (green frame) and the part covered by the TOF detector (blue frame) which indicates a reasonable description of the acceptance and efficiency by the simulations.

The next step of the multi-differential analysis is the extrapolation of the data in transverse momentum and rapidity to the complete phase-space. For this purpose, either analytical models as described in Section 1.4 or effective models are used to estimate the shape of the spectra in the uncovered regions. The extrapolation is performed independently in transverse and longitudinal direction. Because the measurement covers a larger proportion of the total phase-space in transverse direction than it does in longitudinal direction, the systematic uncertainties of the extrapolation in transverse direction are smaller. For this reason it is performed before the extrapolation in longitudinal direction.

Similar as the lower plot of Figure 4.2, the left plot of Figure 4.3 shows the corrected and normalized proton emission rates from the 0-10 % most central Ag(1.58A GeV)+Ag events, however, in a different representation. In [175] it was found that further constraints on the model parameters are required to obtain stable and reliable fits of the model functions. Therefore, the model parameters T_{Eff} and β are shared globally among the spectra. Furthermore, due to the mass symmetry of the Ag+Ag collision system the scaling parameter C is shared among corresponding spectra in backward and forward direction.

The ratios between the data and the fit functions used for extrapolation are depicted in the right plot of Figure 4.3. For better visibility the ratios are shifted by ±x. Quantitatively, a good accordance between the data and the fit functions can be observed.

The integration in transverse direction is performed by summing the measured yields and adding the integrals of the SR fit functions in the regions not covered by data. The resulting yields of the rapidity intervals are depicted in the upper part of Figure 4.4 by the full circles. The open circles correspond to data reflected at mid-rapidity showing that the

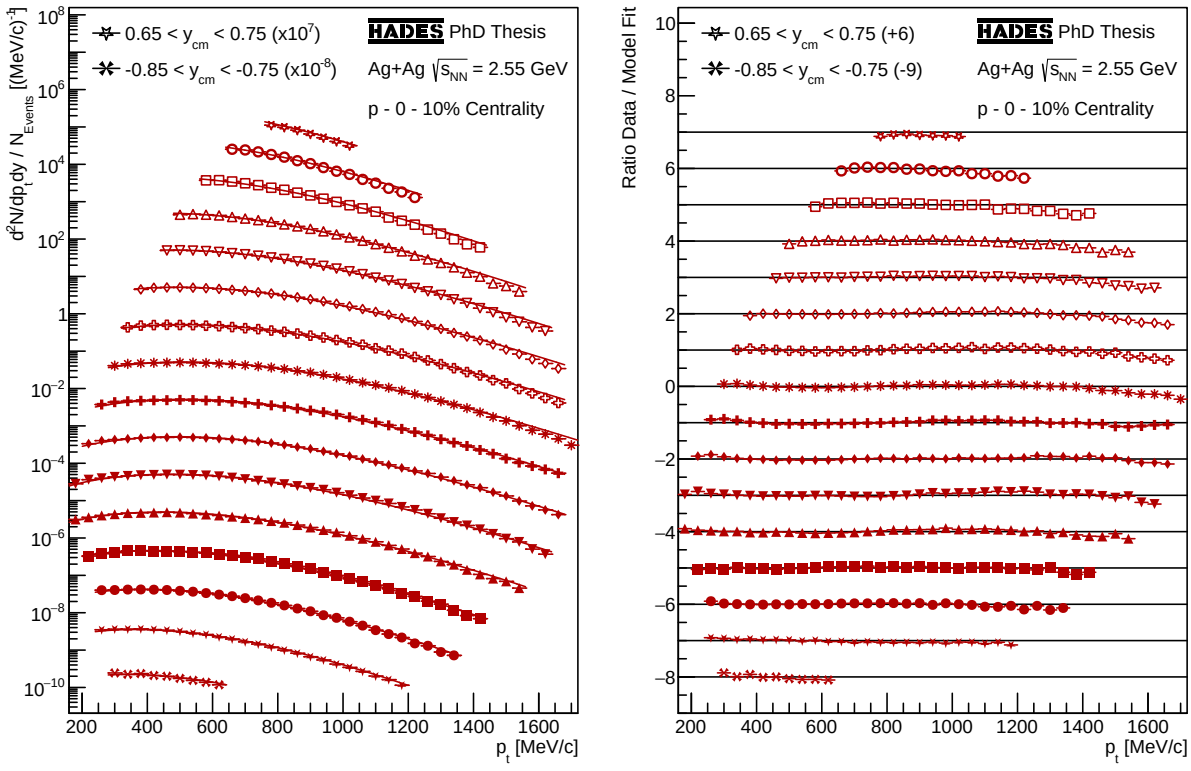

Figure 4.3.: Transverse momentum spectra of protons from the 0-10 % most central Ag(1.58A GeV)+Ag events for the multiple rapidity intervals scaled by 10^x for better visibility (left). The spectra of the various rapidity intervals are depicted by different marker styles with full markers corresponding to the backward hemisphere and open markers to the forward hemisphere. The mid-rapidity interval, is depicted by the symbol ✳. The spectra are fitted with SR model-functions (cf. Section 1.4) with a common effective temperature T_{Eff} and a common blast β. Furthermore, the ratios between the data points and the fit functions shifted by ±x for better visibility are displayed (right).

measured proton yields reflect the mass symmetry of the collision system well. The lower part of Figure 4.4 shows the proportion of the total yield obtained by extrapolation using the corresponding SR model function for each rapidity interval. Around CM rapidity –0.3 less than 10 % of the yield are obtained via extrapolation. This proportion rises to almost 95 % in the most forward rapidity interval pointing out the importance of the fits of the transverse spectra.

The estimated systematic uncertainties of the measurement are depicted as boxes around the data points, determined via three different methods out of which always the largest uncertainty is taken. The first method aims at estimating the uncertainties of the acceptance and efficiency correction as a result of the selection criteria described in Section 4.1.1. Therefore, the entire multi-differential analysis is repeated conversely for the alternative sets of selection criteria namely “Medium” and “Tight”. The differences between the results for the multiple selection criteria sets outside their ±1σ statistical uncertainties are the first estimated systematic uncertainties. The second method utilizes the mass symmetry of the Ag+Ag collision system. Because of it, any differences between corresponding forward and backward data points outside of their statistical uncertainties must be a result of

the systematic uncertainties of the method. Again, the differences outside their $\pm 1\sigma$ statistical uncertainties are taken as estimated systematic uncertainties. The third method is also based on the collision symmetry, with the aim to obtain a globally averaged relative systematic uncertainty estimate. Therefore, the corrected and normalized yields before extrapolation, shown in the lower panel of Figure 4.2, are compared to their corresponding measured yield in the other hemisphere of the collision.[1] For all intervals, the relative difference outside the $\pm 1\sigma$ statistical uncertainties are averaged yielding a global relative systematic uncertainty of ≈ 3 %.

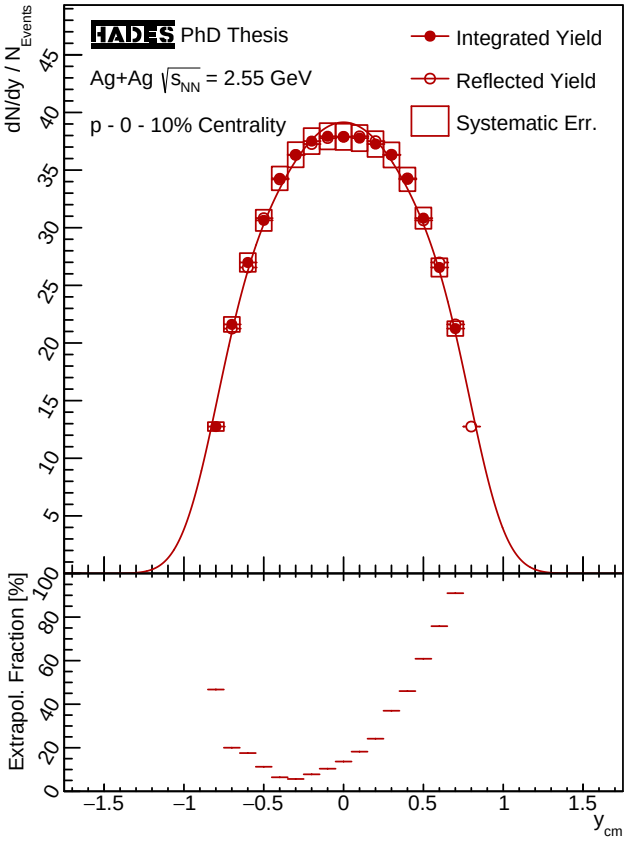

Figure 4.4.: Rapidity spectrum of protons from the 0-10 % most central Ag(1.58A GeV)+Ag events after transverse integration (upper part). The open symbols correspond to the data mirrored at mid-rapidity. The lower part shows fraction of the yields obtained by the extrapolation in transverse direction.

In order to obtain the integrated yield over the entire phase-space (4π), the rapidity distribution is fitted with a function based on the SR model in order to perform the extrapolation to phase-space regions not covered by the measurement like it is done for the transverse spectra. The corresponding fit function is depicted in Figure 4.4 and again it is observed that the shape of the measured distribution is well described. Next, the measured yields are summed and the integrals of the model function in the regions not covered by the measurement are added. This results in the total yield of protons from the 0-10 % most central Ag(1.58A GeV)+Ag events of $54.08 \pm 0.04 \pm 1.50 \pm 4.42$ protons per event with the first uncertainty being statistical and the second and third one systematic. The first systematic uncertainty is estimated by propagating the systematic uncertainties of the yields in the rapidity spectrum to the integrated yield. The second systematic uncertainty is an estimate for the uncertainty arising from the selection of the SR model for the extrapolation. It is estimated by performing the entire multi-differential analysis using the UrQMD model for the extrapolations and determining the differences between the fully integrated yields outside their $\pm 1\sigma$ statistical uncertainties not covered by the first systematic uncertainty.

[1] In most intervals the relative systematic difference between forward- and background-hemisphere is below 5 %. In some intervals however it ranges up to ≈ 20 %.

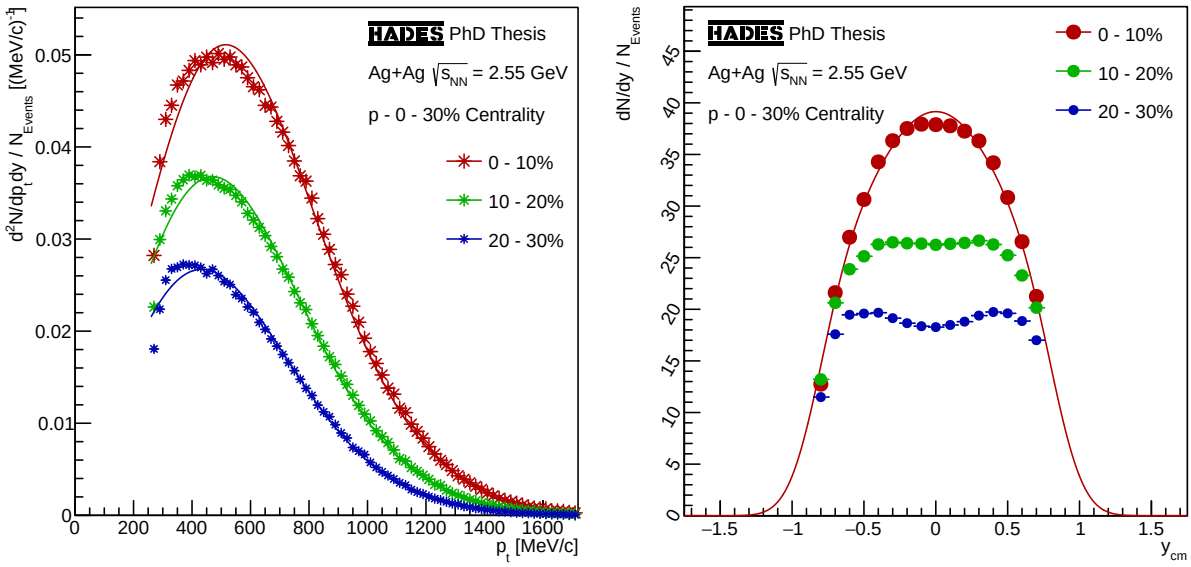

Figure 4.5.: Mid-rapidity transverse momentum spectra (left) and rapidity spectra (right) of protons from the three most central 10 % Ag(1.58A GeV)+Ag centrality classes and the according SR fit functions.

In the next step, the multi-differential analysis is performed for the semi-central centrality classes of the 10-20 % and 20-30 % most central Ag(1.58A GeV)+Ag events. The results are displayed in Appendix A.8 as well as Figure 4.5 which shows the mid-rapidity transverse momentum spectra in the left and the rapidity spectra after integration and extrapolation over transverse momentum in the right. Again, SR model functions are used to fit and extrapolate the measured data.

For the mid-rapidity transverse momentum spectra, one observes that in particular in the semi-central events, the measured distribution seems to drop significantly steeper than the SR model function at low transverse momenta. This effect applies to the first 5 to 10 intervals and might be a systematic effect of the acceptance and efficiency correction close to the border of the accessible phase-space region. The vast majority of the measured data points are well described by the SR model.

A strong difference of the rapidity distributions between the most central and the semi-central collisions is observed. While the rapidity spectrum of the most central events is well described by the SR model function, the rapidity spectra from the semi-central events show a very different shape with two maxima at ± 0.3 (10-20 %) and ± 0.5 (20-30 %) around mid-rapidity. The reason for this is, that in semi-central collisions a large fraction of protons from the colliding nuclei only sparsely interact with the fireball. Initially, protons from the colliding nuclei are located at projectile- and target-rapidity which correspond to $\approx \pm 0.82$ around mid-rapidity in case of Ag(1.58A GeV)+Ag collisions. By the interactions with the fireball, their distributions are shifted towards mid-rapidity which results in the shape of the rapidity spectra in Figure 4.5. As such effects are not included in the SR model, the corresponding functions do not describe these shapes which is why for the semi-central centrality classes no total yield is determined in this work. Alternative approaches utilizing effective models are investigated in [112].

The parameter values obtained by the SR model fits to the transverse momentum spectra using the method described previously describe the state of the fireball at kinetic freeze-out of the protons. Their values as well as the 4π integrated yield are summarized in Table 4.3 with the first uncertainty being again of statistical nature and all following of systematic nature. The systematic uncertainties of the model parameters are derived from the differences between the analyses conducted with different selection criteria sets. As the previously describe effects in the semi-central collisions also apply less pronounced to the 0-10 % most central events and the SR model does not include them, all values have to be understood as rough estimates. In Chapter 5 the obtained results are used for further in-depth analyses.

Centrality	**4π Yield / Event**	T_{Eff} **[MeV]**	β
0-10 %	54.32 ± 0.02 ± 1.63 ± 4.05	69 ± 1 ± 3	0.48 ± 0.01 ± 0.02
10-20 %	—	70 ± 1 ± 3	0.44 ± 0.01 ± 0.02
20-30 %	—	69 ± 1 ± 3	0.41 ± 0.01 ± 0.02

Table 4.3.: Integrated 4π yields and SR model parameter values obtained in the analysis of protons from the 0-30 % most central Ag(1.58A GeV)+Ag events.

4.2. Λ Analysis

Λ hyperons consist of one up-, down- and strange-quark $|uds\rangle$, carry no electric charge and are the lightest existing hyperons with a mass of $\approx$ 1115 MeV/c^2. Thus, they can only decay via the weak interaction to non-strange particles which results in a rather long decay length cτ of 7.89 cm. Their most probable decay channel is $\Lambda \rightarrow p + \pi^-$ with a Branching Ratio (BR) of $\approx$ 63.9 %. Their second most probable decay channel is $\Lambda \rightarrow n + \pi^0$ with a BR of $\approx$ 35.8 % and the remaining decay channels have negligible BRs [184]. In fixed-target heavy-ion collisions at beam energies of few GeV, Λ hyperons are the most abundantly produced strange baryons due to the energetically favored Kaon-Hyperon production channel, given by Equation 1.7, which was discussed in Section 1.3.2.

Besides the isospin, the heavier Σ^0 hyperons have the same quantum-numbers like Λ hyperons. Because of that, they decay electromagnetically with a decay length cτ of only 2.22×10^{-9} cm via the decay channel $\Sigma^0 \rightarrow \Lambda + \gamma$ with a BR of almost 100 %. The analysis method described in the following does not allow to distinguish between directly produced Λ hyperons and Λ hyperons from Σ^0 decays. Therefore, all yields determined in the following for Λ hyperons have to be understood as combined yields of Λ and Σ^0 hyperons.

Furthermore, the reconstruction of the charged Σ hyperons is challenging since their primary decay channels $\Sigma^+ \rightarrow p + \pi^0$, $\Sigma^+ \rightarrow n + \pi^+$ (BRs $\approx$ 50 %) and $\Sigma^- \rightarrow n + \pi^-$ (BR $\approx$ 100 %) all involve an electrically neutral particle. As a result, the Λ hyperons provide the easiest experimental access to ground-state hyperons produced in low energy heavy-ion collisions. Their long decay length allows to identify their decays using the OVD topology parameters introduced in Section 3.6 which are analyzed in this work using an ANN like described in Section 3.10. The details of their reconstruction and analysis are described in the following sections.

4.2.1. Artificial Neutral Network Training

Due to their decay-length of a few cm, Λ hyperons have to be reconstructed from their daughter particles, in this work a proton (Dau1) and a π^- (Dau2). The tracks of the daughter particles are identified using the standard track selection described in Section 3.3, combined with the momentum-velocity selection regions generated specifically for the daughter particles of weak decays as explained in Section 3.4.1. Furthermore, since the protons and π^- from weak decays have different momentum and velocity distributions than free protons and π^-, the range of the value a defined in Section 3.4.1 is limited. The protons are required to have a-values between 0.4 and 2.1 which roughly corresponds to velocities above 0.26 c and momenta below 2900 MeV/c and the π^- are required to have a-values between 0.65 and 1.05 which roughly corresponds to velocities above 0.49 c and momenta below 500 MeV/c. The values are determined using simulated Λ hyperons embedded into experimental data using the method described in Section 2.3.4 such that at least $\pm 3\sigma$ of the distributions are covered and the phase-space of the reconstructed Λ hyperons is not reduced. To counter the possible offsets on the times of flight of the daughter particle tracks, discussed in Section 3.4.1, their energies are adjusted such that their reconstructed masses are equal to their nominal masses.

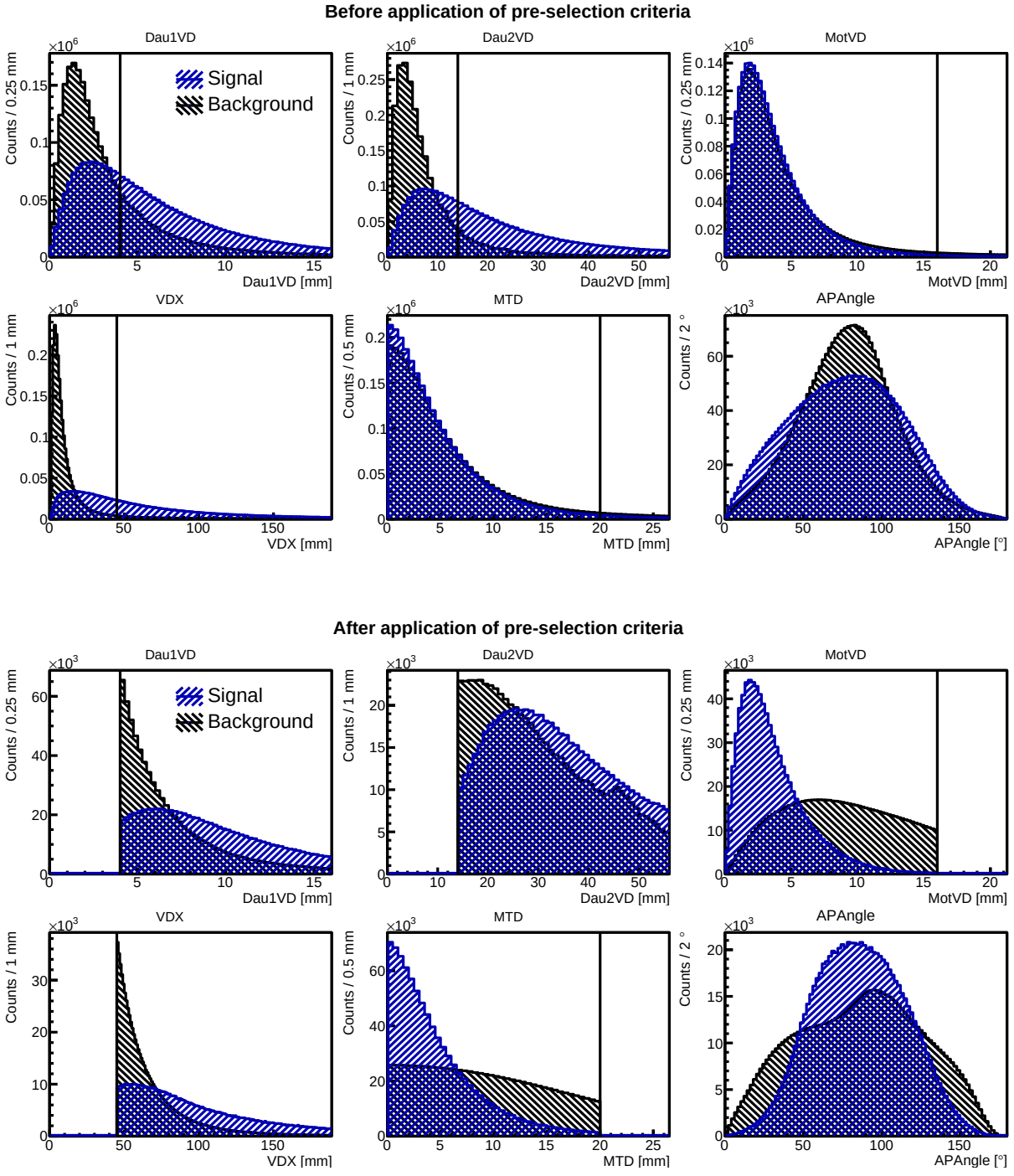

Figure 4.6.: Signal and background distributions of the parameters used for training the ANN to reconstruct Λs before (upper panel) and after (lower panel) all of the pre-selection criteria, which are indicated by lines - See the text for details.

The basic principle of the identification and reconstruction of weakly decaying particles is described in Sections 3.6, 3.8 and 3.10. To enhance the discrimination power between actual signals and combinatorial background, the decay parameters, summarized in Appendix A.6, are evaluated by an ANN in addition to the standard hard selection criteria. The training of the ANN is performed using a signal sample obtained from simulated Λs embedded into experimental data and a background sample obtained via the mixed-event method described in Section 3.9. Figure 4.6 shows in the upper panel the distributions of the training samples. The parameters Dau1VD, Dau2VD and VDX show significant discrimination power in contrast to the parameters MotVD, MTD and APAngle.

Parameter	**Set 1**	**Set 2**	**Set 3**	**Set 4**	**Set 5**	**Set 6**
Dau1VD [mm]	> 3	> 3	> 4	> 4	$\mathbf{> 4}$	> 5
Dau2VD [mm]	> 10	> 12	> 12	> 13	$\mathbf{> 14}$	> 15
MotVD [mm]	< 20	< 18	< 20	< 18	$\mathbf{< 16}$	< 15
VDX [mm]	> 30	> 35	> 40	$\mathbf{> 45}$	> 50	> 50
MTD [mm]	< 20	< 18	$\mathbf{< 20}$	< 18	< 16	< 15

Table 4.4.: The six pre-selection criteria sets tested for the reconstruction of Λ hyperons. The bold selection criteria are finally used - See the text for details.

As already explained in Section 3.10, hard pre-selection criteria on the parameters in advance to the ANN training are required. To determine the optimal pre-selection criteria, the six candidate sets given by Table 4.4 are estimated based on the pre-selection criteria used in [170] and for each of them the ANN is trained. Afterwards, an optimization of the obtained signal is performed using the method described later on and the results are compared. It is found that the chosen set of pre-selection criteria barely influences the obtained signal. Furthermore, since in the previous work [170] the momentum of the Λ candidate was used instead of the APAngle these two possibilities are tested. Both variants result in similar amounts of reconstructed Λs, but since the use of the momentum strongly biases the shape of the combinatorial background in the invariant mass spectrum, the APAngle is used as sixth parameter. The final pre-selection criteria which are emphasized in Table 4.4 are determined such that they are close to the optimized selection criteria but leave some room for variations.

The lower panel of Figure 4.6 shows the distributions of the training samples after the final pre-selection criteria are applied. It is observed that the parameters MotVD and MTD now show a pretty strong discrimination power which further emphasizes the need for the pre-selection. Examining the background distribution of the parameter Dau2VD an excess around 45 mm is observed. It is a result of the strong correlations between the parameters and reflects the criterion VDX > 45 mm. The same effect is observed for Dau1VD if the range is extended, however, much weaker than for Dau2VD since the proton is much heavier than the π^- which is why the proton is most probably emitted in direction of the decaying Λ while the π^- can also be emitted under a much smaller angle.

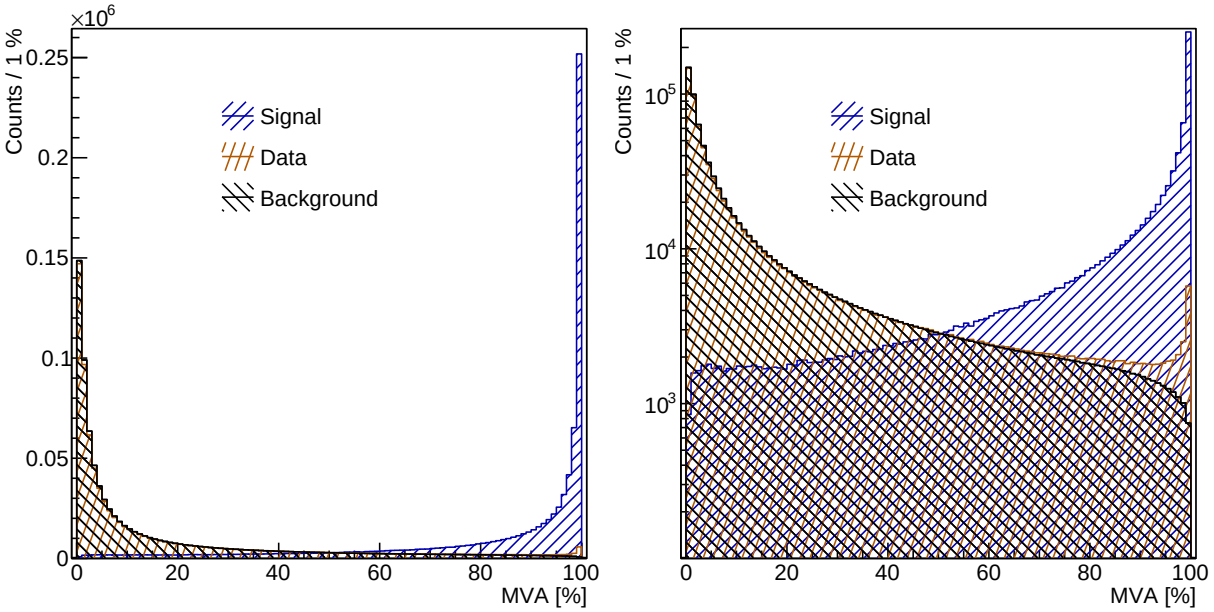

Figure 4.7.: ANN response distribution for the signal- (blue) and background (black) samples used for training and testing of the ANN as well p-π^- combinations from real events (orange) in linear (left) and logarithmic (right) representation.

Figure 4.7 sows the distributions of the ANN response parameter (MVA) for the two training samples as well as experimental p-π^- pairs. The linear depiction in the left clearly shows how strong the response parameter separates the background sample with values close to 0 from the signal sample with values close to 1 as intended by the training. Therefore, the response parameter can be interpreted as the probability of a given set of input parameter values being signal. The logarithmic depiction in the right shows that the distribution obtained from experimental data has a very similar shape like the background sample but with a very clear excess at values close to 1. The excess comes from actual Λ decays in experimental data which constitute only a very small proportion of the entire sample since the combinatorial background is much more abundant. Furthermore, the accordance between the background and experimental data sample demonstrates that the mixed-event technique is well suited to describe the combinatorial background.

Next, the distributions of invariant masses of p-π^- pairs from experimental data and mixed-event-pairs are generated. The mixed-event distribution is normalized to the data distribution using their integrals in regions left and right to the Λ peak, so called side-bands. These side-bands are positioned at least $\pm 6\sigma$ outside of the signal region as determined by a Gaussian function fitted to the data distribution after subtraction of the normalized mixed-event background in order to exclude the tails of the Λ peak. The quality of the obtained Λ peak is quantified by its significance calculated according to Equation 4.3 with signal S and background B counts from $\pm 2\sigma$ around the peak.

$$\text{Significance} := \frac{S}{\sqrt{S+B}} \tag{4.3}$$

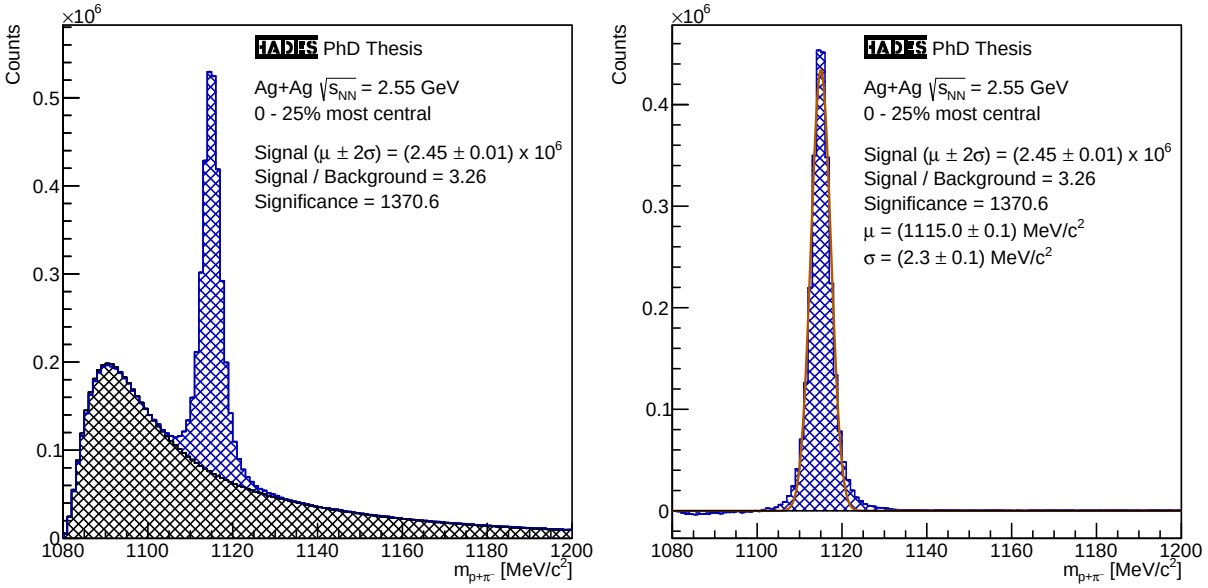

Figure 4.8.: Invariant mass distribution of p-π^- pairs from the 0-25 % most central Ag(1.58A GeV)+Ag events after application of the full Λ reconstruction method before (left) and after (right) subtraction of the mixed-event combinatorial background.

The significance defines by how many σ the signal exceeds the statistical fluctuations calculated by $\sqrt{N}$. The selection criteria used for the following analyses are determined by an iterative optimization procedure aimed at maximizing the significance of the Λ peak. Figure 4.8 shows the invariant mass distributions of the 0-25 % most central Ag(1.58A GeV)+Ag events and mixed-event background in the left and after subtraction of the normalized background in the right using the selection criteria obtained via the optimization procedure denoted in Table 4.5 under the name "Standard". The spectra show again a very strong accordance between the combinatorial background from data and the mixed-event technique. In the subtracted spectrum the Gaussian fit function used to determine the position and width of the peak is depicted orange. The mean lies with a value of 1115 MeV/c^2 very close to the nominal mass of Λ hyperons and the width of 2.3 MeV/c^2 is slightly lower than in the analysis of Au(1.23A GeV)+Au events described in [170].

In total, 2.45 million Λ hyperons within $\pm 2\sigma$ around the Λ peak are reconstructed which is more than ever measured by HADES in a single beam time before. The use of an ANN strongly suppresses the combinatorial background resulting in a very high signal to background ratio of 3.26 compared to similar analyses. In the following sections, the lifetime of the Λ hyperons is determined and their production is analyzed multi-differentially. The different selection criteria sets used in the following analyses are summarized in Table 4.5. Unfortunately, since an ANN does not allow to clearly track how the response is calculated based on the input parameters due to the complicated correlations between its layers, there is a risk for high systematic uncertainties. To preclude this problem, the ANN is only used for the "Standard" selection criteria set but not for the selection criteria sets "Loose", "Medium" and "Tight" that are used to estimate the systematic effects of selection criteria variations.

Parameter	Pre-Selection	Standard	Loose	Medium	Tight
Dau1VD	$>$ 4 mm	$>$ 4 mm	$>$ 6 mm	$>$ 7 mm	$>$ 8 mm
Dau2VD	$>$ 14 mm	$>$ 15 mm	$>$ 20 mm	$>$ 23 mm	$>$ 26 mm
MotVD	$<$ 16 mm	$<$ 15 mm	$<$ 14 mm	$<$ 11 mm	$<$ 8 mm
VDX	$>$ 45 mm	$>$ 45 mm	$>$ 55 mm	$>$ 60 mm	$>$ 65 mm
MTD	$<$ 20 mm	$<$ 20 mm	$<$ 16 mm	$<$ 13 mm	$<$ 10 mm
A	$>$ 15°				
MVA	—	$>$ 76 %	—		

Table 4.5.: The five final selection criteria sets used for the reconstruction and analysis of Λ hyperons.

4.2.2. Lifetime Measurement

The lifetime of Λ hyperons is a well established property that is measured with high precision and independent from the collision system. It can be used to assess how well the acceptance and efficiency corrections work. For this purpose, first the decay-time t_{decay} is calculated from the decay-length l_{decay}, which is identical to the OVD topology parameter VDX, using Equation 4.4:

$$t_{decay} = \frac{l_{decay}}{\beta\gamma c} \qquad (4.4)$$

c is the speed of light, β represents the velocity of the decaying particle and γ its Lorentz-factor to take the time dilation into account. The decay-time range from 120 to 1600 ps is divided into 37 equally sized intervals of 40 ps width. For each of these intervals the invariant mass spectrum of p-π^- pairs is created and the amount of Λ signal counts is extracted within $\pm 2\sigma$ like described in the previous section. Next, the obtained signal counts are corrected for acceptance and efficiency effects using Λ hyperons generated according to the DIS model with the parameter values obtained in Section 4.2.3 and embedded into experimental data. The reasons for acceptance and efficiency losses are basically identical to those listed for protons in Section 4.1.2 with some differences as it will de discussed in more detail in

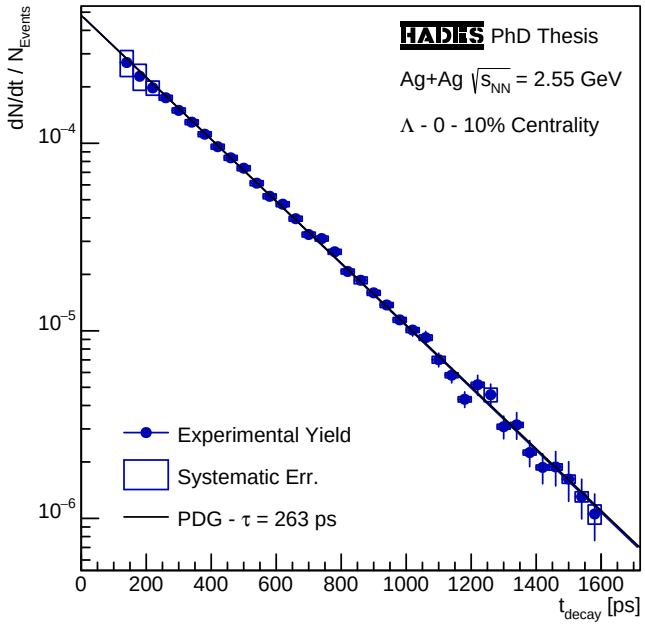

Figure 4.9.: Decay-time spectrum of Λs from the 0-10 % most central Ag(1.58A GeV)+Ag events. The blue exponential decay curve corresponds to the data and the black to the Λ literature lifetime [184].

the following Section 4.2.3. The resulting decay-time spectrum normalized to the interval widths is shown in Figure 4.9. Again, the systematic uncertainties are estimated from the differences between the yields obtained using the four selection criteria sets defined in Section 4.2.1 and are depicted as boxes around the data points.

The functions depicted in Figure 4.9 correspond to the decay law given by Equation 4.5:

$$N(t) = N_0 \cdot \exp\left(-\frac{t}{\tau}\right) \Rightarrow \frac{dN}{dt} = -\frac{N_0}{\tau} \cdot \exp\left(-\frac{t}{\tau}\right) \tag{4.5}$$

Therefore, their slopes in logarithmic representation are directly related to the mean lifetime τ. The black function corresponds to the literature value of the lifetime of 263 ps [184] and the blue function is fitted to the data points. The thereby obtained lifetime is $(262 \pm 2 \pm 3)$ ps with the first uncertainty being of statistical and the second of systematic nature. The systematic uncertainty was determined by averaging the relative uncertainties of the multiple intervals and applying the average to the determined lifetime. The measured mean lifetime is consistent with its literature value, which proves that the selection criteria applied to the OVD topology parameters and the use of the ANN do not bias the acceptance and efficiency corrections critically.

4.2.3. Multi-Differential Analysis

The multi-differential analysis of the Λ hyperon production is conducted in analogy to the one of protons. The entire phase-space of the Λ hyperons is divided into 20 transverse momentum intervals with a width of 80 MeV/c from 160 to 1760 MeV/c and 13 rapidity intervals with a width of 0.1 from –0.75 to 0.55 in the CM system of collision. The mid-rapidity region from –0.15 to 0.15 is analyzed additionally using 27 transverse momentum intervals with a width of 60 MeV/c from 180 to 1800 MeV/c. Furthermore, the analysis is performed independently for the three 10 % centrality intervals of the 0-30 % most central events as well resulting in a grand total of 861 individual intervals. For each of these intervals, the Λ signal counts are extracted using the method described in Section 4.2.1. In case of the Λs, no distinction between RPC and TOF detector is made, since the daughter particles might also be measured in different detectors due to their opposite polarity. Figure 4.10 shows the invariant mass distributions from four different regions of the total phase-space. The amounts of signal counts for each interval are depicted in the upper panel of Figure 4.11, while its lower panel shows the corresponding significances.

The next step is again the correction for acceptance and efficiency effects. The successful reconstruction of a Λ hyperon requires that it decays to charged decay products and that the daughter particles traverse the active areas of the detectors. Therefore, the total acceptance consists of the BR of the relevant decay channel as well as the individual acceptances of the daughter particles: $a_\Lambda = BR_\Lambda \cdot a_p a_{\pi^-}$. This results in significantly lower total acceptances than in case of the proton analysis.

The reasons for efficiency losses of the protons also hold true for the Λs, however, the detection efficiency ϵ_{det}, the track reconstruction efficiency ϵ_{rec} and the track selection efficiency ϵ_{sel} have to be taken into account for both daughter particles again. A further efficiency arises from the selection criteria on the OVD topology parameters:

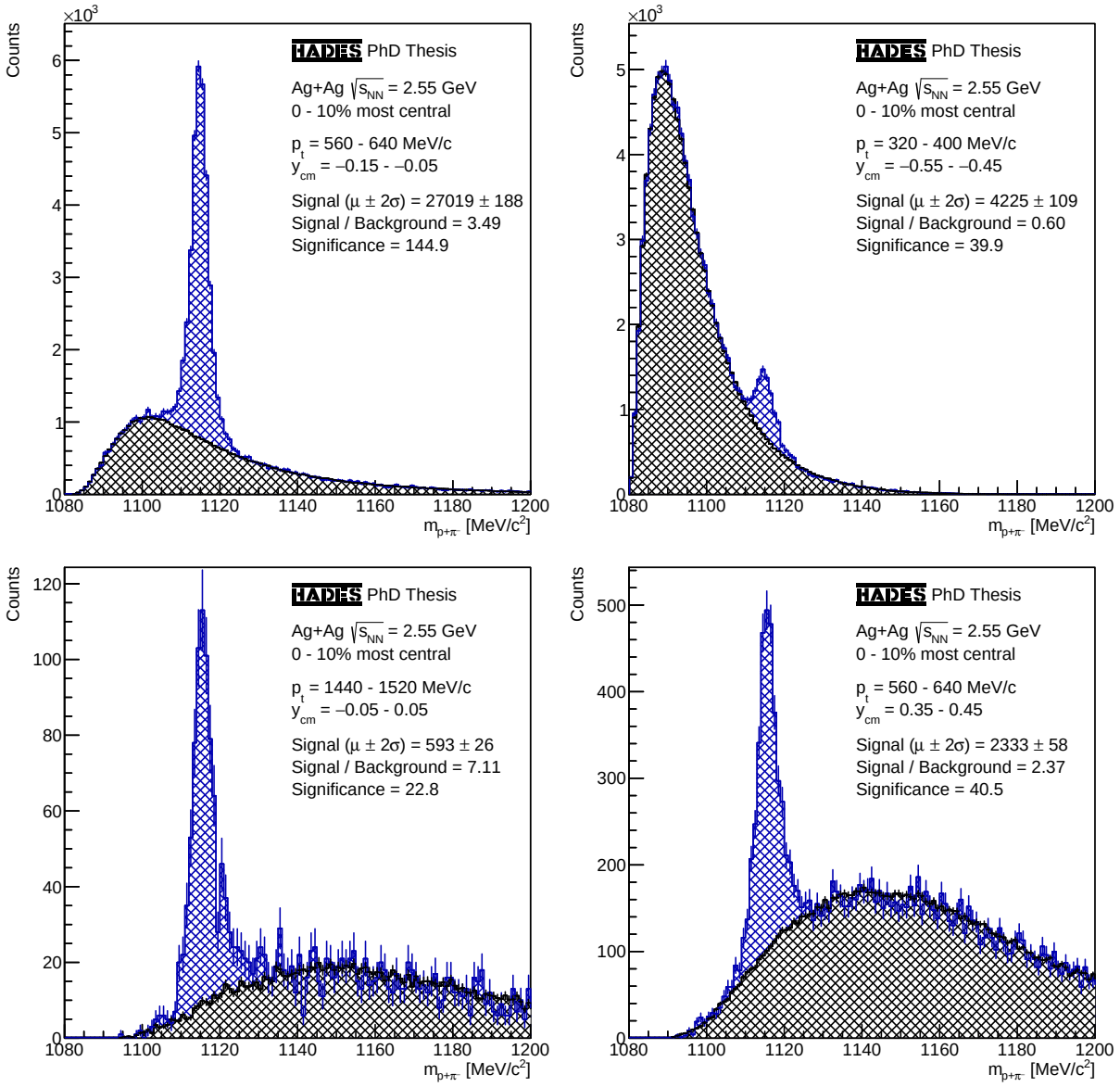

Figure 4.10.: Invariant mass distributions of p-π^- pairs from the 0-10 % most central Ag(1.58A GeV)+Ag events at the center of the total phase-space (upper left), the low-p_t backward-rapidity region (upper right), the high-p_t mid-rapidity region (lower left) and the medium-p_t forward-rapidity region (lower right).

- **The efficiency of the OVD topology criteria ϵ_{OVD}:** Due to the large amount of combinatorial background compared to the anticipated signals strong selection criteria as discussed in Section 4.2.1 are required. These result in large efficiency losses, however otherwise no signal could be reconstructed at all.

The total efficiency of the reconstruction of Λ hyperons therefore results in: $\epsilon_\Lambda = \epsilon_{det,p}\epsilon_{det,\pi^-} \cdot \epsilon_{rec,p}\epsilon_{rec,\pi^-} \cdot \epsilon_{sel,p}\epsilon_{sel,\pi^-} \cdot \epsilon_{OVD,\Lambda}$ and is again significantly lower than the one of protons. Both acceptance and efficiency are estimated using simulated Λ hyperons embedded into experimental data according to the method described in Section 2.3.4. The reconstruction and analysis procedure is applied conversely to the simulated data

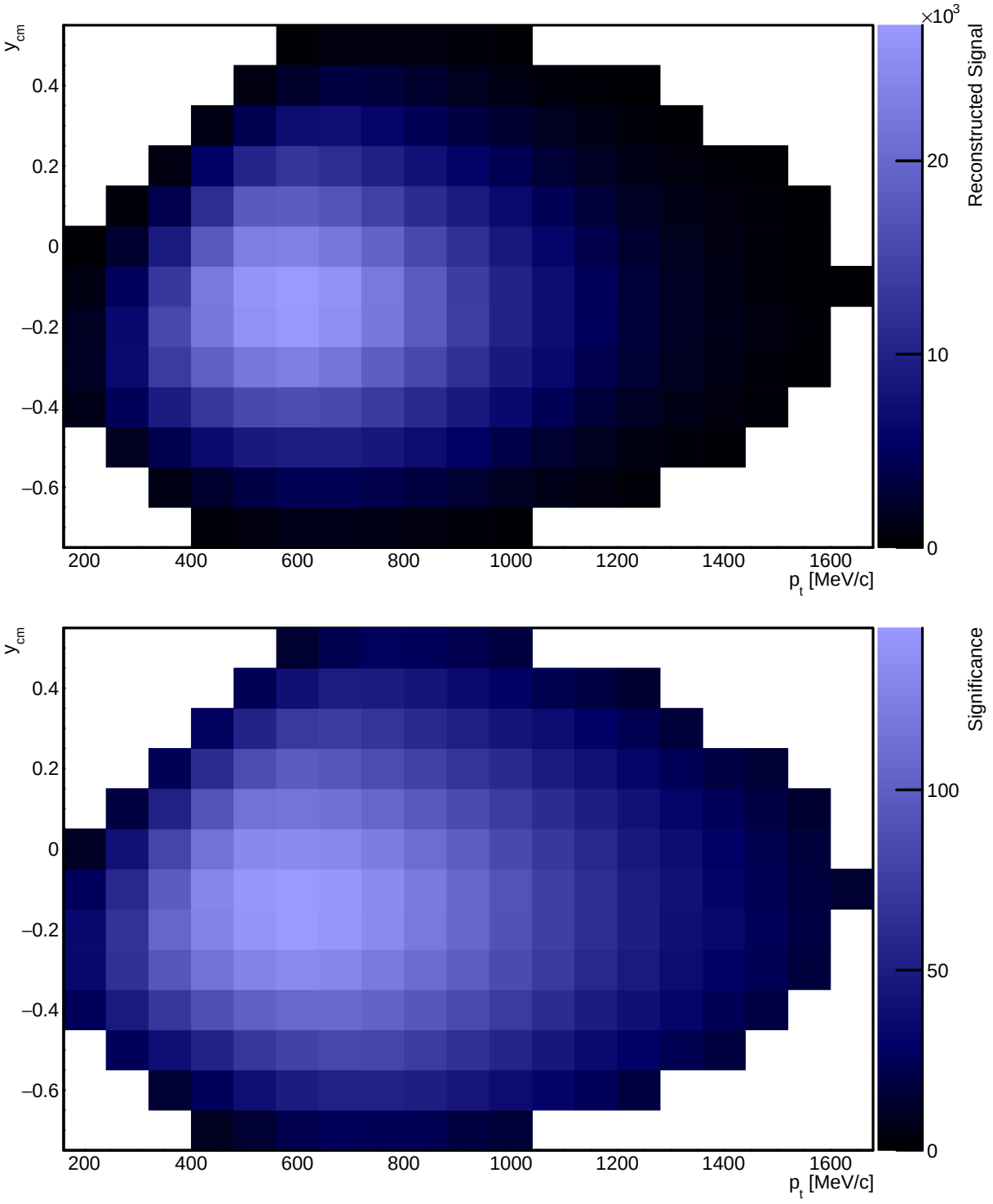

Figure 4.11.: Extracted Λ signal counts (upper panel) and their significances (lower panel) from the 0-10 % most central Ag(1.58A GeV)+Ag events.

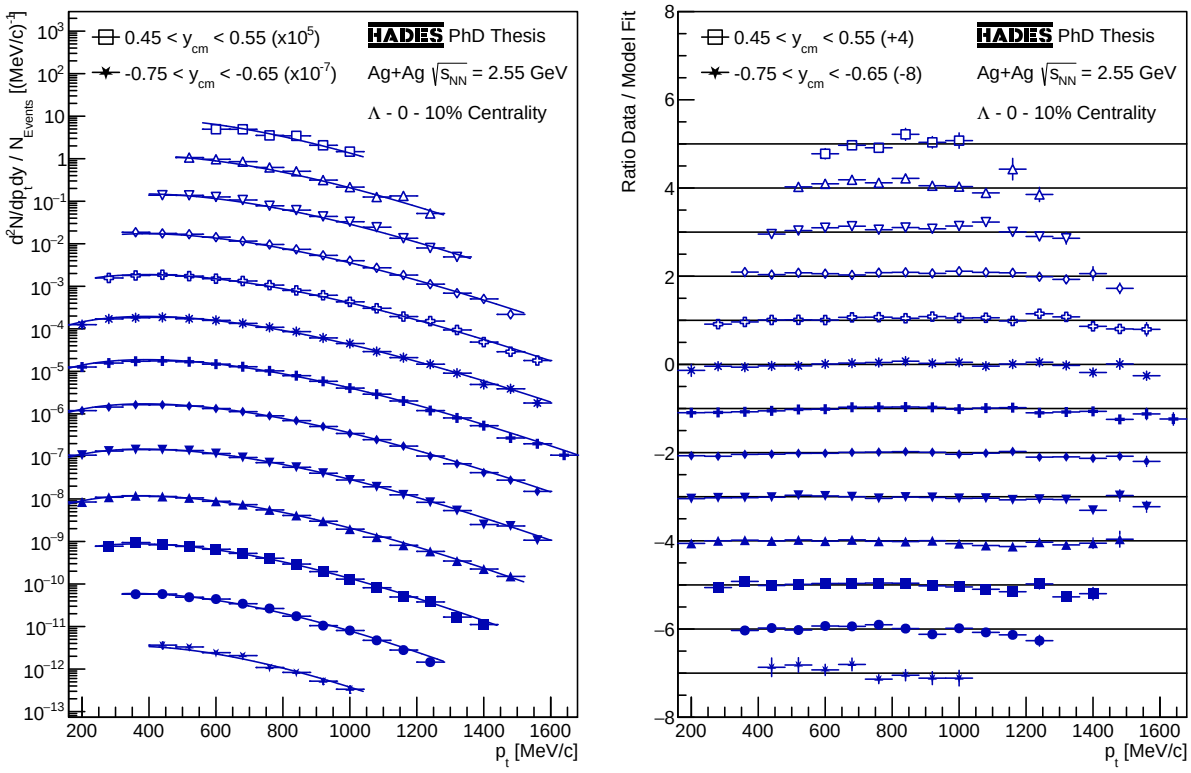

Figure 4.12.: Transverse momentum spectra of Λs from the 0-10 % most central Ag(1.58A GeV)+Ag events for the multiple rapidity intervals scaled by 10^{x} for better visibility (left). The spectra of the various rapidity intervals are depicted by different marker styles with full markers corresponding to the backward hemisphere and open markers to the forward hemisphere. The mid-rapidity interval, is depicted by the symbol ✳. The spectra are fitted with DIS model-functions with a common effective temperature T_{Eff} and a common η. Furthermore, the ratios between the data points and the fit functions shifted by ±x for better visibility are displayed (right).

yielding $N^{sim}_{rec,\Lambda}(p_t, y)$. The ratio to the amount of initially generated Λ hyperons in the simulation input $N^{sim}_{gen,\Lambda}(p_t, y)$ yields the total correction quotients according to Equation 4.6. These correction quotients are calculated and applied to each of the individual phase-space intervals. High uncertainties on the corrected yields are avoided by rejecting any interval for which either the acceptance or the efficiency quotient deceeds 1 % or the relative statistical uncertainty exceeds 20 %. The determined Acceptance × Efficiency values are displayed in the upper panel of Figure 4.13. As for the protons a manual selection is applied in addition and the resulting corrected yields are normalized to the number of analyzed events as well as the transverse momentum and rapidity interval widths.

$$BR_\Lambda \cdot a_p a_{\pi^-} \cdot \epsilon_{det,p}\epsilon_{det,\pi^-} \cdot \epsilon_{rec,p}\epsilon_{rec,\pi^-} \cdot \epsilon_{sel,p}\epsilon_{sel,\pi^-} \cdot \epsilon_{OVD,\Lambda} = \frac{N^{sim}_{rec,\Lambda}(p_t, y)}{N^{sim}_{gen,\Lambda}(p_t, y)} \tag{4.6}$$

The fully corrected and normalized Λ production rates over the entire phase-space are depicted in the lower panel of Figure 4.13 for the 0-10 % most central Ag(1.58A GeV)+Ag events. As for the protons a large proportion of the phase-space is covered by the

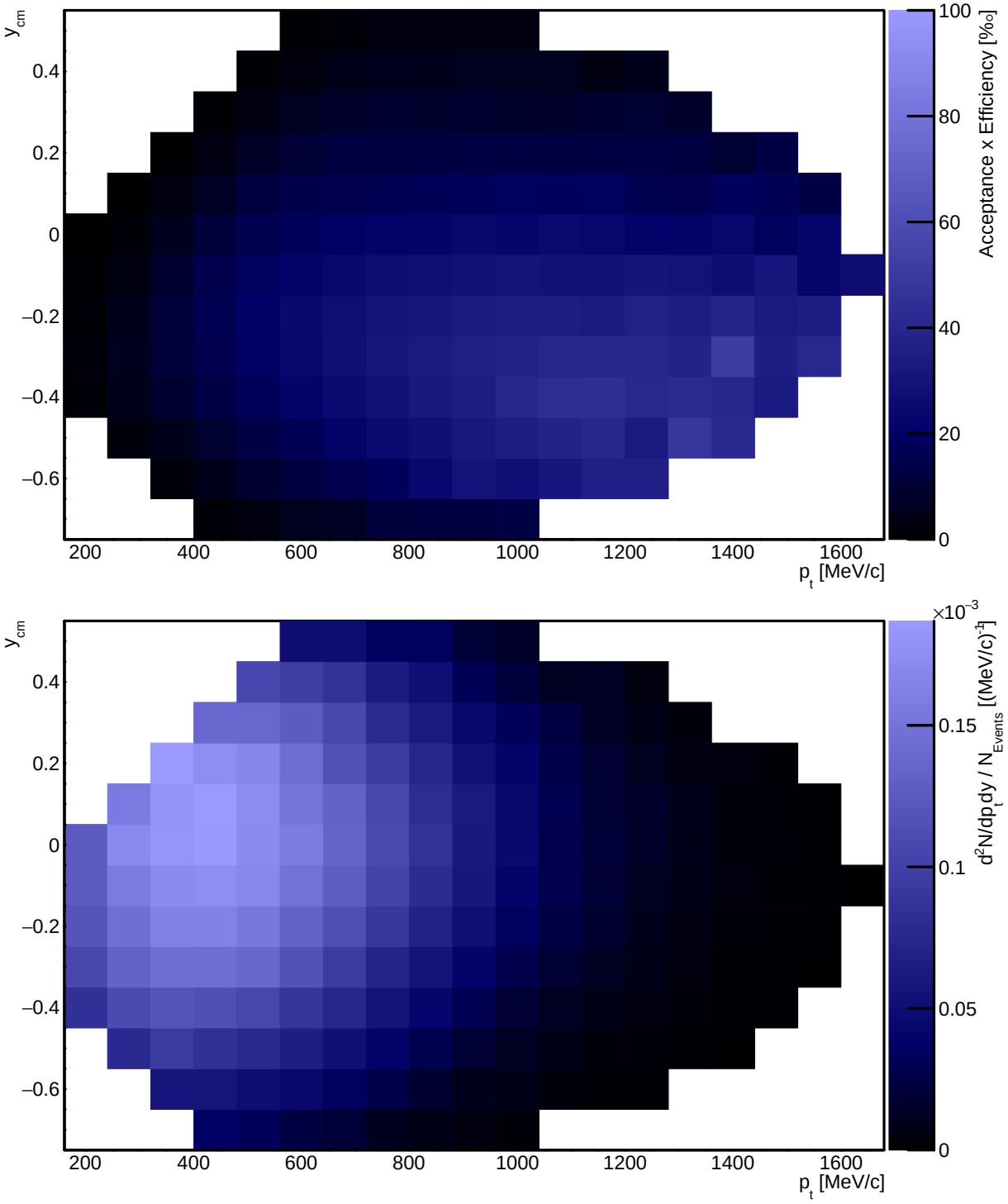

Figure 4.13.: Acceptance × Efficiency values (upper panel) as well as corrected and normalized Λ production rates (lower panel) from the 0-10 % most central Ag(1.58A GeV)+Ag events.

measurement with a common smooth shape. The next step is the extrapolation from the phase-space region covered by the measurement to the total phase-space which is again performed first in transverse and afterwards in longitudinal direction.

The left plot of Figure 4.12 shows the corrected and normalized Λ production rates already shown in the lower plot of Figure 4.13 using individual transverse momentum spectra for each rapidity interval. In contrast to the protons, the transverse spectra of the Λ hyperons are extrapolated using DIS model functions (cf. Section 1.4) which are depicted in Figure 4.12 as well. The fit method however remains the same meaning that the functions for the individual spectra are fitted with a common T_{Eff} parameter value and symmetric scaling parameters C to account for the mass symmetry of the collision system. Since the parameter η is only required to add a longitudinal anisotropy to the model, it is fixed to 0 for the transverse fits. One observes that the shapes of the spectra are well described by the model functions which is supported by the ratios between the model functions and the data points depicted in the right plot of Figure 4.12. For better visualization the rations are shifted by ±x.

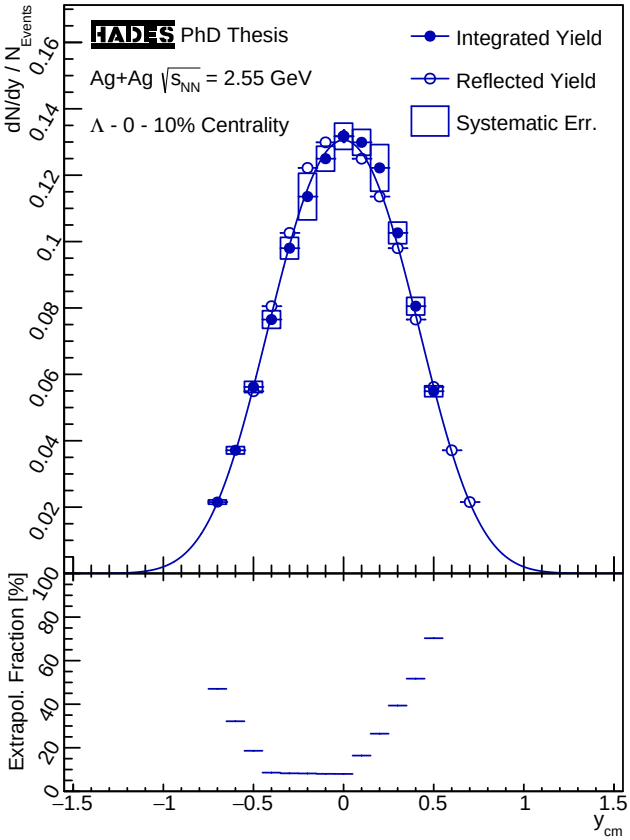

Figure 4.14.: Rapidity spectrum of Λs from the 0-10 % most central Ag(1.58A GeV)+Ag events after transverse integration (upper part). The open symbols correspond to the data mirrored at mid-rapidity. The lower part shows fraction of the yields obtained by the extrapolation in transverse direction.

The rapidity spectrum displayed in Figure 4.14 is obtained by integrating the transverse spectra and adding the extrapolation to the full phase-space by integrating the fit functions in the uncovered regions. Again, the full circles represent the integrated yields and the open circles the yields reflected at mid-rapidity. Close examination reveals a slight excess of the yields at forward rapidity over those at backward rapidity. The proportions of the yields obtained by extrapolation, displayed in the lower part of Figure 4.14, show low proportions of less than 10 % at mid-rapidity and some backward rapidity intervals as well as rising proportions towards the outer rapidities. Therefore, the excess of the yields in forward direction might be a result of the model functions used for the transverse extrapolation.

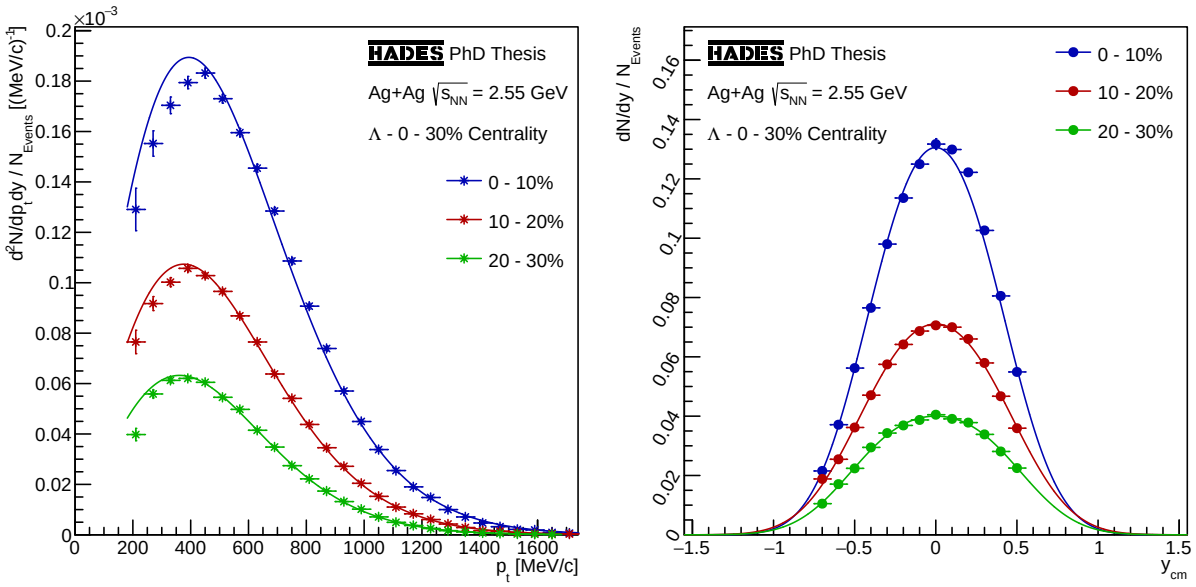

Figure 4.15.: Mid-rapidity transverse momentum spectra (left) and rapidity spectra (right) of Λs from the three most central 10 % Ag(1.58A GeV)+Ag centrality classes and the according DIS fit functions.

The systematic uncertainties depicted by boxes around the data points in Figure 4.14 are estimated via the exact same method as for the protons. Again, the systematic differences between the analyses using the different selection criteria sets defined in Section 4.2.1, the differences between corresponding forward and backward rapidity intervals as well as the globally averaged relative difference between corresponding forward and backward rapidity intervals, which amounts to ≈ 3 % as well, are calculated and the largest uncertainty is taken. The extrapolation to the full 4π yield is performed using the DIS model function fitted to the rapidity spectrum which is depicted in Figure 4.14. The resulting yield for the 0-10 % most central Ag(1.58A GeV)+Ag events amounts to $(12.58 \pm 0.05 \pm 0.41) \times 10^{-2}$ Λ hyperons per event. The first uncertainty is statistical and the second one systematic estimated by propagating the systematic uncertainties of the yields in the rapidity spectrum to the integrated yield. Like for the protons, the UrQMD model is applied to determine the systematic uncertainty arising from the selection of the DIS model for the extrapolation, however, no difference exceeding the first systematic uncertainty is found.

Finally, the multi-differential analysis is again performed for the semi-central centrality classes of the 10-20 % and 20-30 % most central Ag(1.58A GeV)+Ag events. The results are displayed in Appendix A.8 as well as Figure 4.15 showing the mid-rapidity transverse momentum spectra in the left and the rapidity spectra after integration and extrapolation over transverse momentum in the right. The DIS fit functions used for the extrapolations are depicted too.

Concerning the mid-rapidity transverse momentum spectra, as with the protons, the model functions describe the measured yields over most of the transverse momentum range. Only at low transverse momenta around 200 MeV/c slight discrepancies that are almost entirely covered by the uncertainties of the data are observed. Also concerning the rapidity spectra after integration and extrapolation over transverse momentum, a strong accordance

between the model functions and the data points can be observed for all centrality classes. In contrast to the protons, the Λ hyperons are newly produced inside the fireball, which is why their kinematic distributions are not contaminated.

Table 4.6 summarizes the integrated 4π yields as well as the DIS model parameters obtained in the multi-differential analysis of Λ hyperons. The parameter values for T_{Eff} are determined by the transverse momentum spectra fits and the values for η by the rapidity spectrum fits. Like before, the first uncertainty is statistical and the second one systematic. The systematic uncertainties of the model parameters are derived from the differences between the analyses conducted with different selection criteria sets. In Chapter 5 the obtained results will be put in context and analyzed further.

Centrality	**4π Yield / Event**	$\boldsymbol{T_{Eff}}$ **[MeV]**	$\boldsymbol{\eta}$
0-10 %	$(12.48 \pm 0.05 \pm 0.41) \times 10^{-2}$	$117 \pm 1 \pm 4$	$0.21 \pm 0.01 \pm 0.03$
10-20 %	$(7.48 \pm 0.04 \pm 0.23) \times 10^{-2}$	$109 \pm 1 \pm 4$	$0.24 \pm 0.01 \pm 0.03$
20-30 %	$(4.45 \pm 0.03 \pm 0.14) \times 10^{-2}$	$101 \pm 1 \pm 4$	$0.26 \pm 0.01 \pm 0.03$

Table 4.6.: Integrated 4π yields and DIS model parameter values obtained in the analysis of Λs from the 0-30 % most central Ag(1.58A GeV)+Ag events.

4.3. K^0_S Analysis

The kaons are the lightest existing strange mesons with masses close to 495 MeV/c^2 and like the Λ hyperons they can only decay via the weak interaction to non-strange particles which results in a rather long decay lengths $c\tau$. They exist in four different quark-content-states from which two are electrically neutral (K^0 $|d\overline{s}\rangle$ and $\overline{K^0}$ $|\overline{d}s\rangle$) and two are electrically charged (K^+ $|u\overline{s}\rangle$ and K^- $|\overline{u}s\rangle$).

Experimentally it is observed that neutral kaons either decay into two pions ($\pi^+ + \pi^-$ or $\pi^0 + \pi^0$) which are both CP+1 eigenstates or into three pions ($\pi^+ + \pi^- + \pi^0$ or $\pi^0 + \pi^0 + \pi^0$) which are both CP–1 eigenstates. Neglecting the very little CP-symmetry violation, the CP-quantum-number is conserved by the weak interaction, however, none of the kaon quark-content-states is a CP-eigenstate. Therefore, the weakly decaying neural kaon states have to be combined states of the neutral quark-content-states. The CP+1 neural kaon state which decays into two pions has a significantly lower decay length than the CP–1 neutral kaon state which decays into three pions since the phasespace-factor of the two pion decay is much larger than the one of the three pion decay. Therefore, the CP+1 neutral kaon state is called K^0short (K^0_S ($|d\overline{s}\rangle - |\overline{d}s\rangle$) / $\sqrt{2}$) and the CP–1 neutral kaon state is called K^0long (K^0_L ($|d\overline{s}\rangle + |\overline{d}s\rangle$) / $\sqrt{2}$).

The K^0_S has a decay length $c\tau$ of 2.68 cm and decays primarily via two decay channels: $K^0_S \rightarrow \pi^+ + \pi^-$ (BR $\approx$ 69.2 %) and $K^0_S \rightarrow \pi^0 + \pi^0$ (BR $\approx$ 30.7 %) with all remaining decay channels having negligible BRs [184]. In fixed-target heavy-ion collisions at beam energies of few GeV, K^0_S mesons are primarily produced as K^0 mesons by the Kaon-Hyperon production channel, given by Equation 1.7. Neglecting the CP-symmetry violation the produced K^0 mesons decay equally probable as K^0_S or K^0_L mesons which is why all results obtained for K^0_S mesons can also be assigned to the K^0_L mesons.

In combination with the K^+ mesons which are analyzed in [122] all ground-state particles involving an anti-strange quark are measured. Together with the Λ hyperons, this allows to estimate the amount of the unmeasured Σ^+ and Σ^- hyperons via the strangeness-balance equation 1.5 as described in Section 5.1. Like for the Λ hyperons, the long decay length of K^0_S mesons allows to identify their decays using the OVD topology parameters introduced in Section 3.6 which are analyzed in this work using an ANN like described in Section 3.10. The details of their reconstruction and analysis are described in this section.

4.3.1. Artificial Neutral Network Training

Like Λ hyperons, K^0_S mesons mostly decay in front of the first detectors and have to be reconstructed from their daughter particles, in this work a π^+ (Dau1) and a π^- (Dau2). The tracks of the daughter particles are identified in close analogy to the ones of Λ hyperons again using the standard track selection combined with the momentum-velocity selection regions generated specifically for the daughter particles of weak decays. Furthermore, the range of the value a defined in Section 3.4.1 is limited too. Both π^+ and π^- are required to have a-values between 0.7 and 1.4 which roughly corresponds to velocities above 0.53 c and momenta below 1500 MeV/c. The values are determined using simulated K^0_S mesons embedded into experimental data using the method described in Section 2.3.4 such that

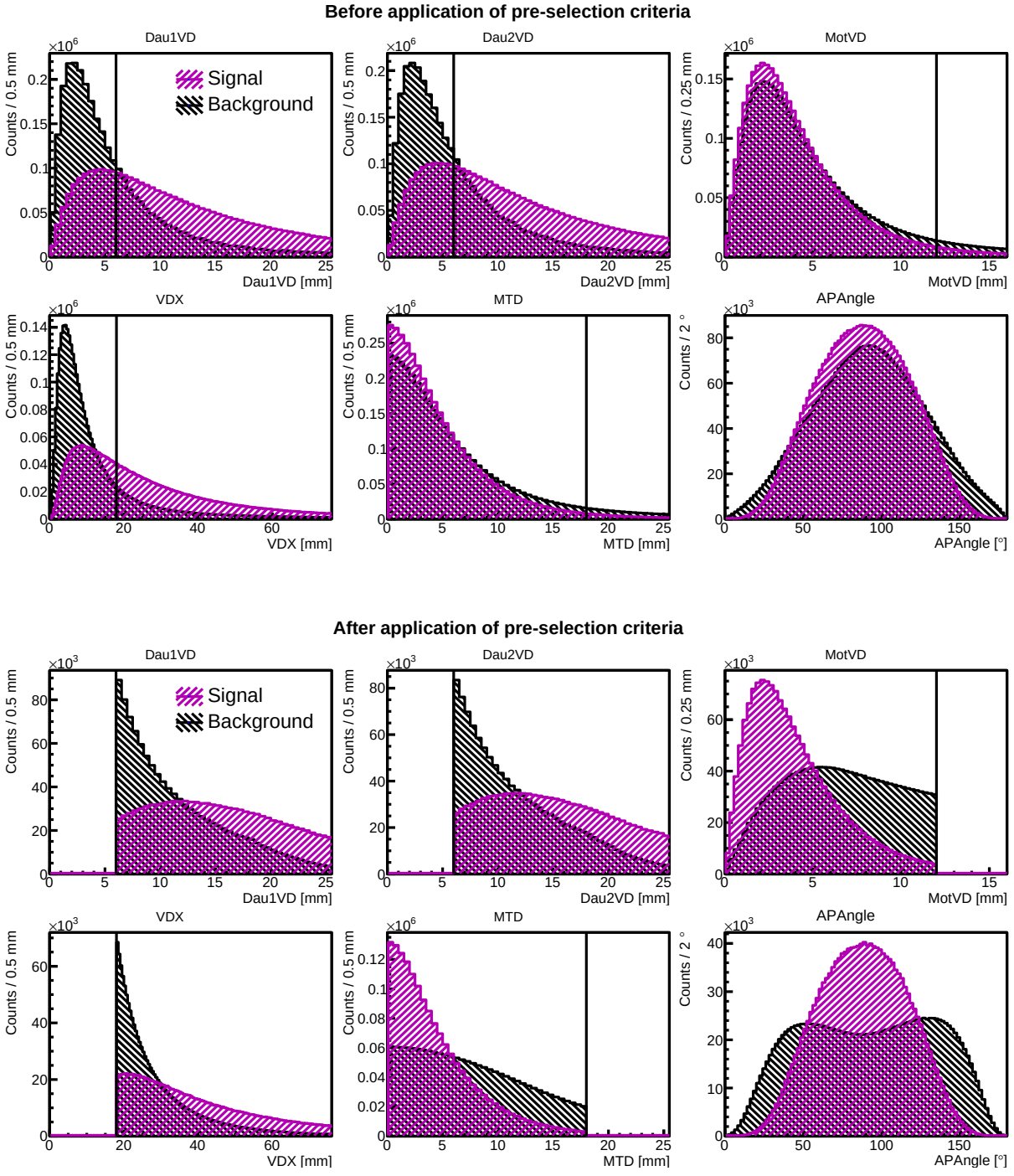

Figure 4.16.: Signal and background distributions of the parameters used for training the ANN to reconstruct K^0_S before (upper panel) and after (lower panel) all of the the pre-selection criteria, which are indicated by lines - See the text for details.

at least $\pm 3\sigma$ of the distributions are covered and the phase-space of the reconstructed K^0_S mesons is not reduced. Again, the energies of the identified tracks are adjusted such that their reconstructed masses are equal to their nominal masses.

The reconstruction of K^0_S mesons follows the same structure as the reconstruction of any weakly decaying particle described in Sections 3.6, 3.8 and 3.10. Again, the discrimination power between actual signals and combinatorial background is enhanced by evaluating the decay parameters, summarized in Appendix A.6, by an ANN in addition to the standard hard selection criteria. The training of the ANN is performed using a signal sample obtained from simulated K^0_S embedded into experimental data and a background sample obtained via the mixed-event method described in Section 3.9. Figure 4.16 shows in the upper panel the distributions of the training samples for K^0_S mesons. As for the Λs, only the parameters Dau1VD, Dau2VD and VDX show significant discrimination power in contrast to the parameters MotVD, MTD and APAngle.

Parameter	**Set 1**	**Set 2**	**Set 3**	**Set 4**	**Final**
Dau1VD [mm]	> 5	$\mathbf{> 6}$	> 7	> 8	$\mathbf{> 6}$
Dau2VD [mm]	> 5	$\mathbf{> 6}$	> 7	> 8	$\mathbf{> 6}$
MotVD [mm]	< 20	< 18	$\mathbf{< 16}$	< 15	$\mathbf{< 12}$
VDX [mm]	> 10	$\mathbf{> 15}$	> 20	> 20	$\mathbf{> 18}$
MTD [mm]	$\mathbf{< 20}$	< 18	< 16	< 15	$\mathbf{< 18}$

Table 4.7.: The four pre-selection criteria sets tested for the reconstruction of K^0_S mesons. The bold selection criteria are finally used - See the text for details.

As before, hard pre-selection criteria are required in advance to the ANN training. To determine the optimal pre-selection criteria, the four candidate sets given by Table 4.7 are estimated based on the pre-selection criteria used in [170] and each of them is tested. Again, it is found that the chosen set of pre-selection criteria barely influences the obtained signal. Furthermore, the momentum of the K^0_S candidate was tested instead of the APAngle as it was done in [170]. Both possibilities result in similar amounts of reconstructed K^0_S, and since the use of the momentum strongly biases the shape of combinatorial background in the invariant mass spectrum, the APAngle is chosen as sixth parameter. Based on the tests the pre-selection criteria which are emphasized in Table 4.7 are determined, however, later it was found that the pre-selection criteria from the rightmost column are better suited to reconstruct K^0_S mesons which is why they are finally used.

The lower panel of Figure 4.16 shows the distributions of the training samples after the final pre-selection criteria are applied. It is observed that the parameters MotVD, MTD and APAngle now show a pretty strong discrimination power which further emphasizes the need for the pre-selection. In contrast to the Λ hyperons, the parameters Dau1VD and Dau2VD show a similar distribution since the π^+ and the π^- have the same mass. Furthermore, they barely reflect the VDX criterion since the amount of energy released in the K^0_S decay is significantly higher than in the Λ decay.

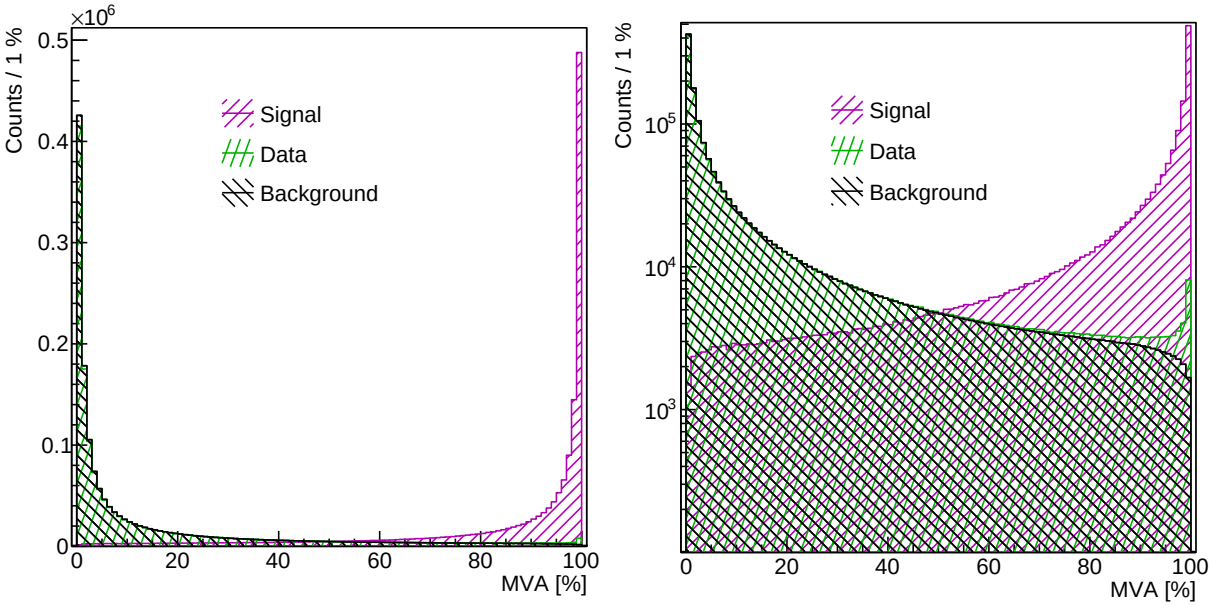

Figure 4.17.: ANN response distribution for the signal- (magenta) and background (black) samples used for training and testing of the ANN as well π^+-π^- combinations from real events (green) in linear (left) and logarithmic (right) representation.

The distributions of the ANN response parameter (MVA) for the two training samples as well as experimental π^+-π^- pairs are shown in Figure 4.17. They show strong similarities compared to the corresponding distributions of Λ hyperons since again a strong separation between the background sample with values close to 0 and the signal sample with values close to 1 is observed. Furthermore, in particular the logarithmic depiction in the right shows that the experimental distribution is consistent with the background distribution over a wide range, but due to actual K^0_S decays in the data, a clear excess around values of 1 can be observed. It can be concluded that the mixed-event technique describes the combinatorial background in the reconstruction of K^0_S mesons well.

In the nest step, the π^+-π^- invariant mass distributions are generated for experimental data and mixed-event background. Since the K^0_S peak is significantly broader than the Λ peak as a result from the higher amount of energy released in the decay and the lighter daughters, the side-bands used to normalize the mixed-event background are positioned $\pm 4\sigma$ outside the signal region as determined by a Gaussian function fitted to the data distribution after subtraction of the normalized mixed-event background. As for the Λ hyperons the selection criteria are optimized in an iterative procedure aimed at maximizing the significance of the signal calculated according to Equation 4.3.

The resulting optimized selection criteria are denoted in Table 4.8 as "Standard" and the corresponding invariant mass spectra of the 0-25 % most central Ag(1.58A GeV)+Ag events are depicted in Figure 4.18 before (left) and after (right) subtraction of background. As for the Λ hyperons a well description of the combinatorial background is observed although it tends to overshoot the experimental distribution slightly at invariant masses below 450 MeV/c^2. The subtracted spectrum in the right also shows the Gaussian fit function with a mean close to the nominal mass of K^0_S mesons and a significantly lower

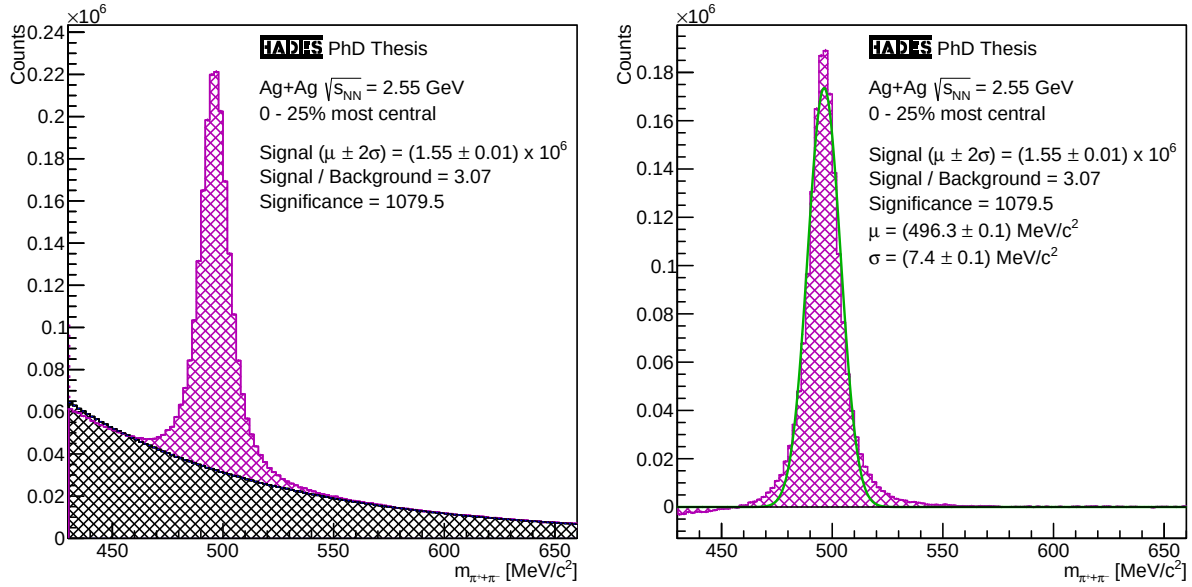

Figure 4.18.: Invariant mass distribution of π^+-π^- pairs from the 0-25 % most central Ag(1.58A GeV)+Ag events after application of the full K^0_S reconstruction method before (left) and after (right) subtraction of the mixed-event combinatorial background.

width than in the analysis of Au(1.23A GeV)+Au events described in [170].

In total, 1.55 million K^0_S mesons within $\pm 2\sigma$ around the K^0_S peak are reconstructed which is again more than ever measured by HADES in a single beam time before. The use of an ANN results in a strong suppression of the combinatorial background and a very high signal to background ratio of 3.07. In the following sections, the lifetime of the K^0_S hyperons is determined and their production is analyzed multi-differentially. The different selection criteria sets used in the following analyses are summarized in Table 4.8, again using the ANN response only for the "Standard" selection criteria set but not for the sets "Loose", "Medium" and "Tight" that are used to estimate the systematic effects of selection criteria variations.

Parameter	Pre-Selection	Standard	Loose	Medium	Tight
Dau1VD	$>$ 6 mm	$>$ 6 mm	$>$ 9 mm	$>$ 10 mm	$>$ 11 mm
Dau2VD	$>$ 6 mm	$>$ 6 mm	$>$ 9 mm	$>$ 10 mm	$>$ 11 mm
MotVD	$<$ 12 mm	$<$ 11 mm	$<$ 12 mm	$<$ 10 mm	$<$ 8 mm
VDX	$>$ 18 mm	$>$ 19 mm	$>$ 20 mm	$>$ 22 mm	$>$ 24 mm
MTD	$<$ 18 mm	$<$ 17 mm	$<$ 16 mm	$<$ 13 mm	$<$ 10 mm
A	$>$ 15°				
MVA	—	$>$ 77 %	—		

Table 4.8.: The five final selection criteria sets used for the reconstruction and analysis of K^0_S mesons.

4.3.2. Lifetime Measurement

Just like the lifetime of Λ hyperons, the lifetime of K^0_S mesons is well established, measured with high precision and independent from the collision system and can therefore be used to assess the quality of the acceptance and efficiency corrections. The measurement is performed in the same way like for the Λ hyperons starting with the calculation of the decay-times from the decay-lengths via Equation 4.4. Due to the shorter lifetime of K^0_S mesons, the decay-time range from 40 to 500 ps is divided into 46 equally sized intervals of 10 ps width. For each of these intervals the invariant mass spectrum of π^+-π^- pairs is created and the amount of K^0_S signal counts is extracted within $\pm 2\sigma$ like described in the previous section. Using K^0_S mesons generated according to the DIS model with the parameter values obtained in Section 4.3.3 and embedded into experimental data, the counts are corrected for acceptance and efficiency effects which are identical to the ones for Λ hyperons discussed in Section 4.2.3. The corrected counts are then normalized to the decay-time interval widths and depicted in Figure 4.19. As before, the systematic uncertainties, depicted as boxes, are estimated based on the differences between the four selection criteria sets defined in Section 4.3.1.

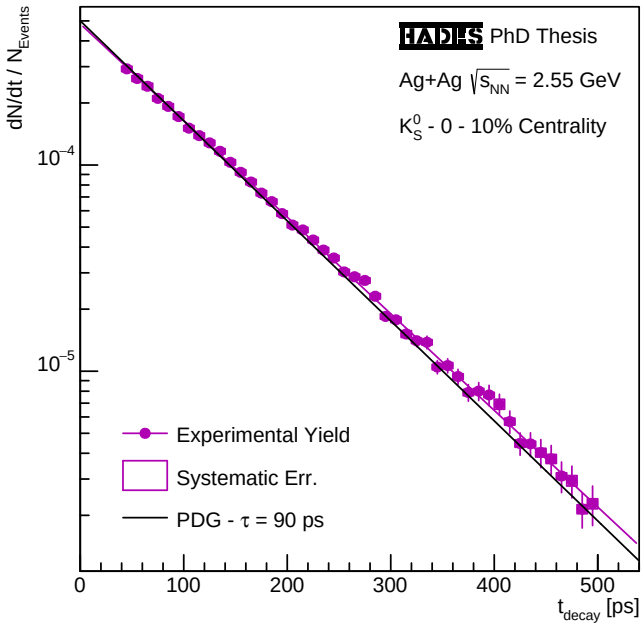

Figure 4.19.: Lifetime spectrum of K^0_S from the 0-10 % most central Ag(1.58A GeV)+Ag events. The magenta exponential decay curve corresponds to the data and the black to the K^0_S literature lifetime [184].

Again, the exponential decay curve functions, defined by Equation 4.5, are depicted in Figure 4.19 too. The black one corresponds to the literature value of the K^0_S lifetime of 90 ps [184]. The magenta function is fitted to the data points and yields the measured K^0_S lifetime of $(92 \pm 1 \pm 1)$ ps. As usual, the first uncertainty denotes the statistical one and the second uncertainty the systematic one which is determined by averaging the relative uncertainties of the multiple intervals and applying the average to the determined lifetime. In this measurement a slightly higher lifetime, about 2.2 % above the nominal lifetime, is determined. However, the values are consistent within the uncertainties of the measurement. This further supports the observation from the Λ hyperons that the simulated particles embedded into experimental data are suited to describe acceptance and efficiency losses without being critically biased by the use of the OVD topology parameters or the ANN.

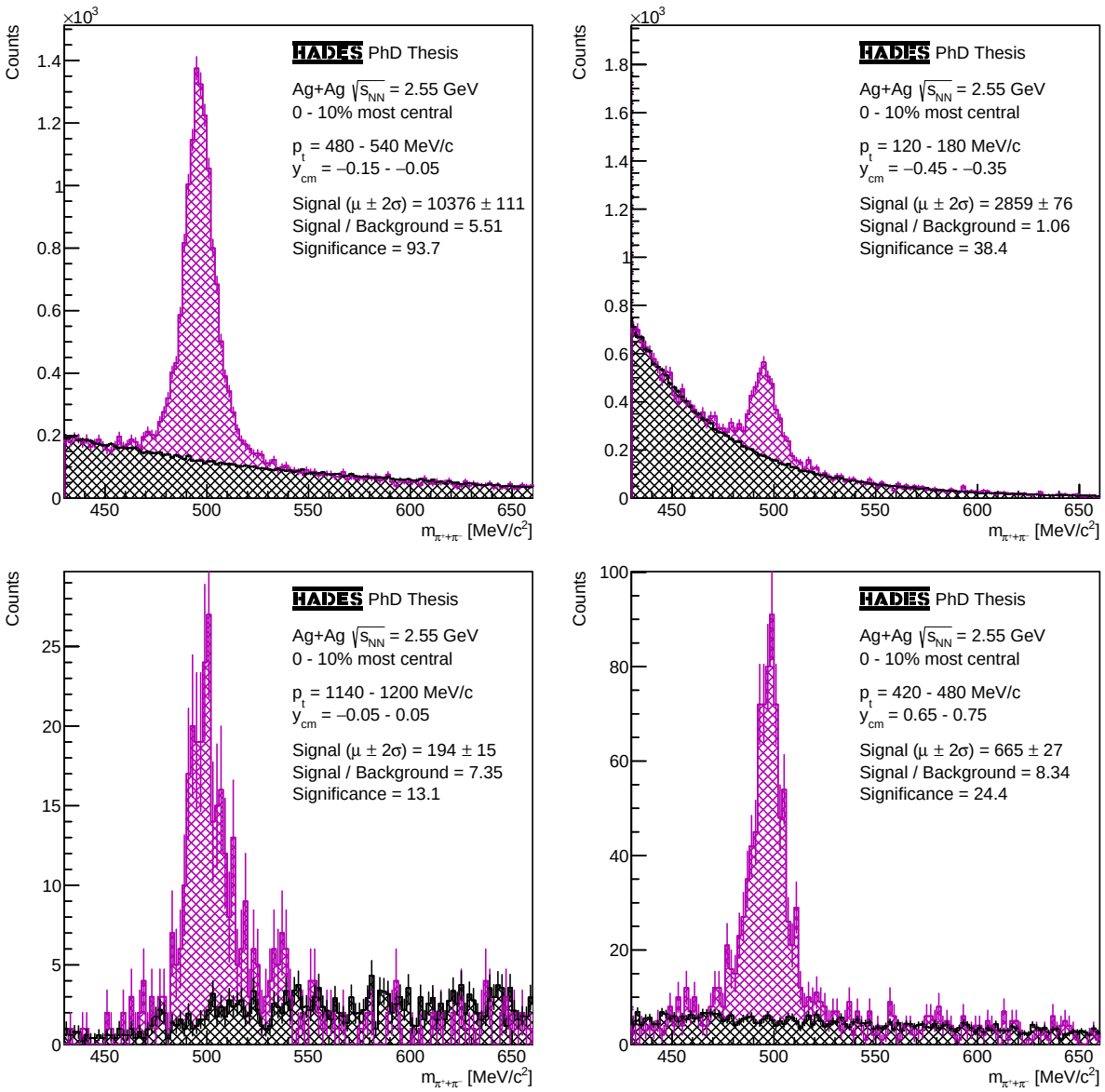

Figure 4.20.: Invariant mass distributions of π^+-π^- pairs from the 0-10 % most central Ag(1.58A GeV)+Ag events at the center of the total phase-space (upper left), the low-p_t backward-rapidity region (upper right), the high-p_t mid-rapidity region (lower left) and the medium-p_t forward-rapidity region (lower right).

4.3.3. Multi-Differential Analysis

The method used to perform the multi-differential analysis of the production of K^0_S mesons is basically identical to the one of Λ hyperons which is why in the following only the important steps and differences are discussed in detail. The entire phase-space of the K^0_S mesons is divided into 22 transverse momentum intervals with a width of 60 MeV/c from 0 to 1320 MeV/c and 15 rapidity intervals with a width of 0.1 from –0.65 to 0.85 in the CM system of collision. The mid-rapidity region from –0.15 to 0.15 is analyzed additionally using 34 transverse momentum intervals with a width of 40 MeV/c from 0 to 1360 MeV/c. Again, the analysis is performed independently for the three 10 % centrality intervals of the 0-30 % most central events resulting in a grand total of 1092 individual intervals. For each of these intervals, the K^0_S signal counts are extracted using the method described in Section 4.3.1 without distinguishing between RPC and TOF detector region. Figure 4.20 shows the invariant mass distributions from four different regions of the total phase-space. The amounts of signal counts for each interval are depicted in the upper panel of Figure 4.21, while its lower panel shows the corresponding significances.

Next, the correction for acceptance and efficiency effects is performed using Equation 4.7 and simulated K^0_S mesons embedded into experimental data by the method described in Section 2.3.4. As for the Λ hyperons, the total acceptance consists of the acceptances of the π^+ and the π^- as well as the BR of the decay channel and the total efficiency consists of the detection, reconstruction and selection efficiencies of the π^+ and the π^- as well as the efficiency of the OVD selection criteria. Again, in the application of the correction quotients to the signal counts of the multiple intervals, intervals with an acceptance or efficiency quotient deceeding 1 % or a relative statistical uncertainty exceeding 20 % are rejected. The determined Acceptance × Efficiency values are displayed in the upper panel of Figure 4.22. Finally a normalization to the number of analyzed events as well as the transverse momentum and rapidity interval widths is performed.

$$BR_{K^0_S} \cdot a_{\pi^+} a_{\pi^-} \cdot \epsilon_{det,\pi^+} \epsilon_{det,\pi^-} \cdot \epsilon_{rec,\pi^+} \epsilon_{rec,\pi^-} \cdot \epsilon_{sel,\pi^+} \epsilon_{sel,\pi^-} \cdot \epsilon_{OVD,K^0_S} = \frac{N^{sim}_{rec,K^0_S}(p_t, y)}{N^{sim}_{gen,K^0_S}(p_t, y)} \quad (4.7)$$

The fully corrected and normalized K^0_S production rates over the entire phase-space are depicted in the lower panel of Figure 4.22 for the 0-10 % most central Ag(1.58A GeV)+Ag events. The measurement covers a large proportion of the phase-space down to vanishing transverse momenta with smooth shapes. In the next step, the extrapolation in transverse direction is performed. The individual corrected and normalize K^0_S transverse momentum spectra for each rapidity interval are shown in the left plot of Figure 4.23. Like for the Λ hyperons, DIS model functions (cf. Section 1.4), depicted in Figure 4.23 as well, are used for the extrapolation. The fit method remains identical too meaning that the functions for the individual spectra are fitted with a common value for the parameter T_{Eff}, symmetric scaling parameters C and the parameter η fixed to 0. Over the entire phase-space from lowest to highest momenta the spectra are well described by the model functions. This is also reflected by the right plot of Figure 4.23 which shows the ratios between the model functions and the data points, again shifted by ±x for better visibility.

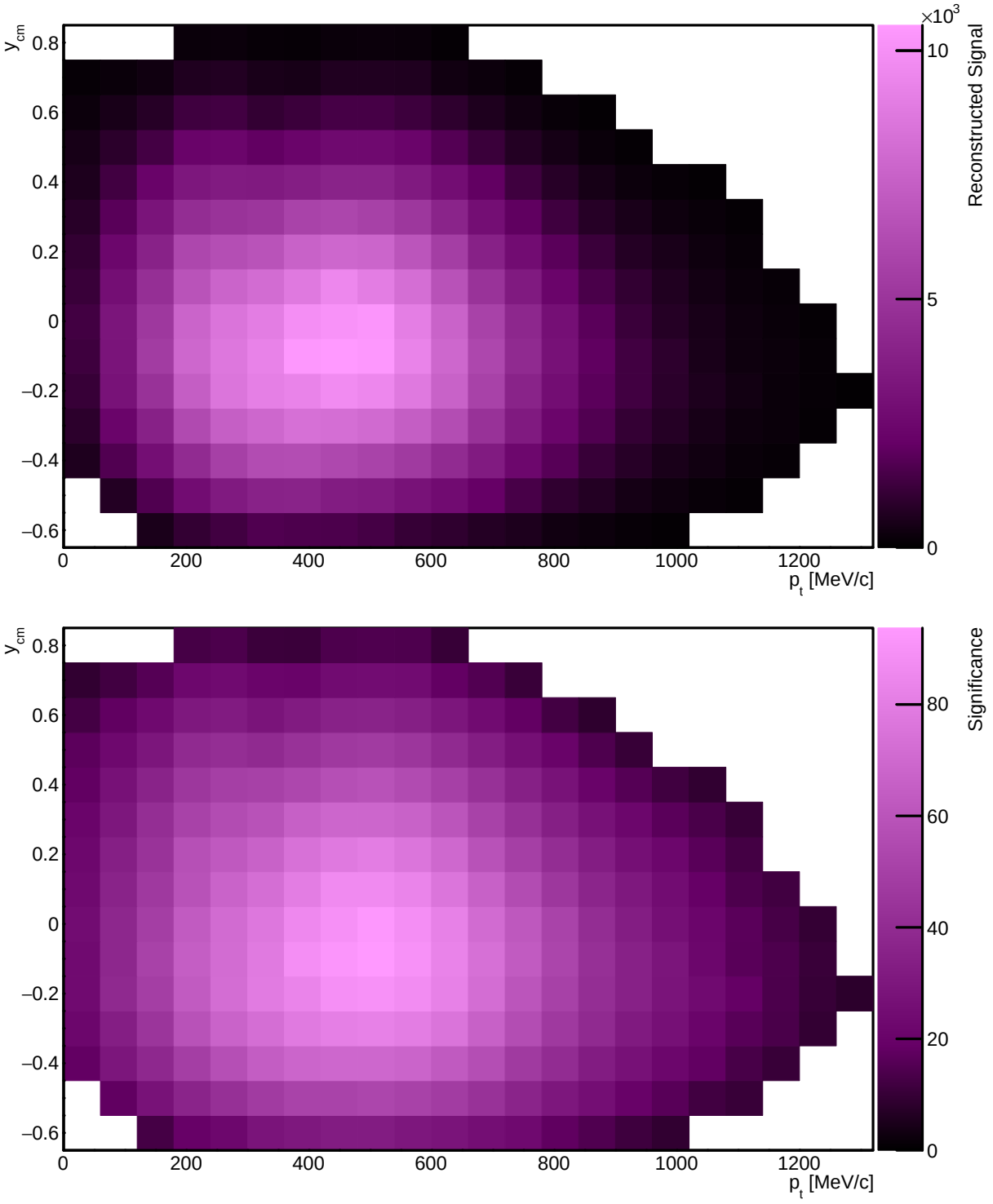

Figure 4.21.: Extracted K^0_S signal counts (upper panel) and their significances (lower panel) from the 0-10 % most central Ag(1.58A GeV)+Ag events.

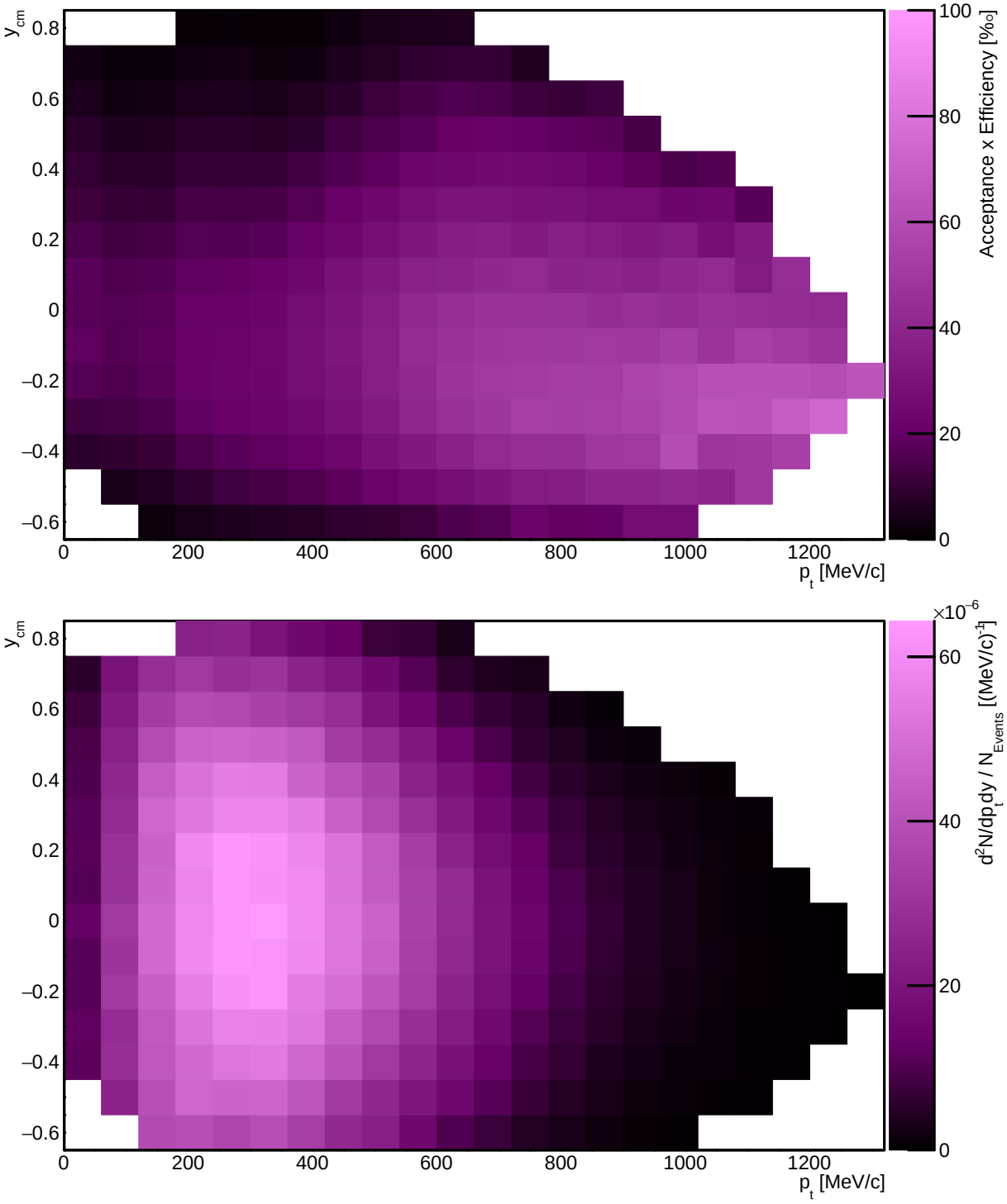

Figure 4.22.: Acceptance × Efficiency values (upper panel) as well as corrected and normalized K^0_S production rates (lower panel) from the 0-10 % most central Ag(1.58A GeV)+Ag events.

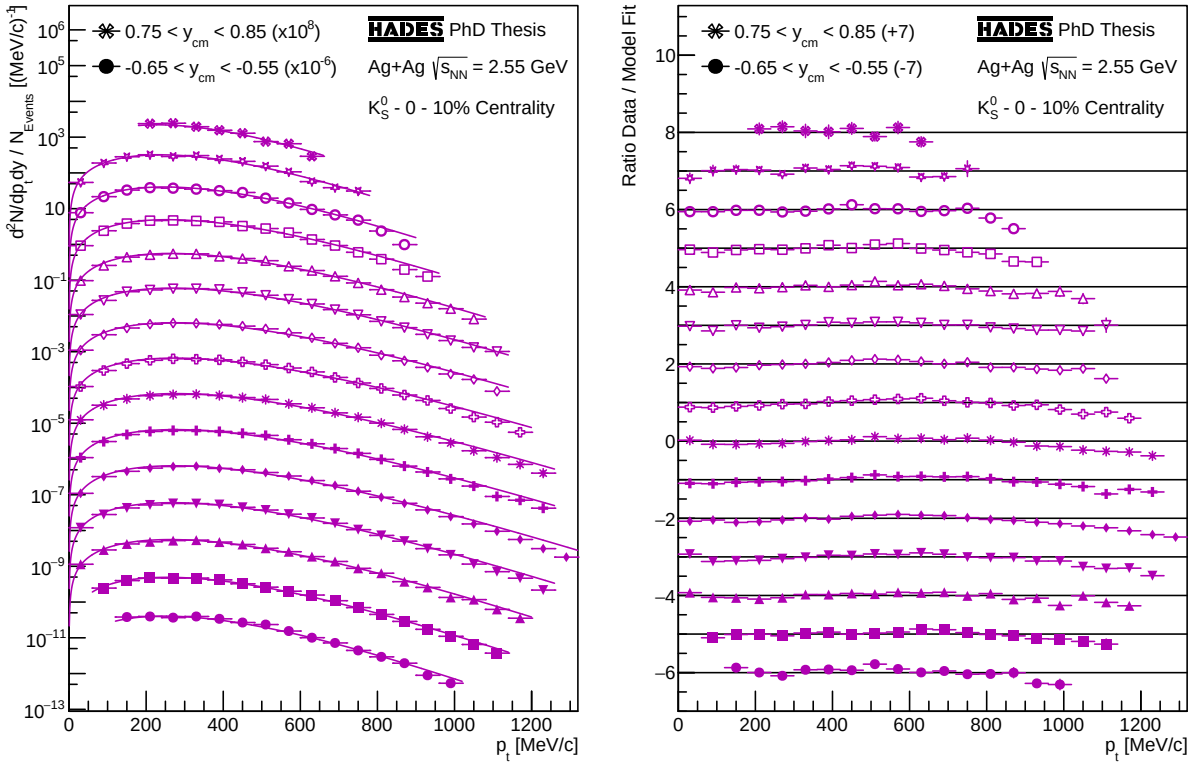

Figure 4.23.: Transverse momentum spectra of K^0_S from the 0-10 % most central Ag(1.58A GeV)+Ag events for the multiple rapidity intervals scaled by 10^x for better visibility (left). The spectra of the various rapidity intervals are depicted by different marker styles with full markers corresponding to the backward hemisphere and open markers to the forward hemisphere. The mid-rapidity interval, is depicted by the symbol ✳. The spectra are fitted with DIS model-functions with a common effective temperature T_{Eff} and a common η. Furthermore, the ratios between the data points and the fit functions shifted by ±x for better visibility are displayed (right).

After integration of the transverse momentum spectra as well as the model functions for extrapolation, the rapidity spectrum displayed in Figure 4.24 is obtained. Here a strong symmetry between the yields depicted by full circles and the yields reflected at mid-rapidity depicted by open circles is observed. Furthermore, the proportions of the yields obtained by extrapolation, which are displayed in the lower part of Figure 4.24, reveal that thanks to the large proportion of the phase-space covered by the measurement in most rapidity intervals less than 1 % of the total yield are obtained by extrapolations. Even in the most forward rapidity interval less than 40 % of the yield are obtained via extrapolation.

The systematic uncertainties depicted by boxes around the data points in Figure 4.24 are determined via the same method as for the protons and the Λ hyperons. The systematic differences between the analyses using the different selection criteria sets defined in Section 4.3.1, the differences between corresponding forward and backward rapidity intervals as well as the globally averaged relative difference between corresponding forward and backward rapidity intervals, which amounts to ≈ 3 % as well are calculated and the largest uncertainty is taken. The extrapolation to the full 4π yield is performed using the DIS model function fitted to the rapidity spectrum and depicted in Figure 4.24 and

results in $(4.50 \pm 0.02 \pm 0.15) \times 10^{-2}$ K^0_S mesons per event for the 0-10 % most central Ag(1.58A GeV)+Ag events. The systematic uncertainty is estimated by propagating the uncertainties of the yields in the rapidity spectrum to the integrated yield. Again, the UrQMD model was tested as alternative to the DIS model but no difference outside the previous uncertainties is found.

Finally, the multi-differential analysis is performed for the 10-20 % and 20-30 % most central Ag(1.58A GeV)+Ag events. The results are displayed in Appendix A.8 as well as Figure 4.25 showing the mid-rapidity transverse momentum spectra in the left and the rapidity spectra after integration and extrapolation in the right. Furthermore, the DIS fit functions used for the extrapolations are depicted.

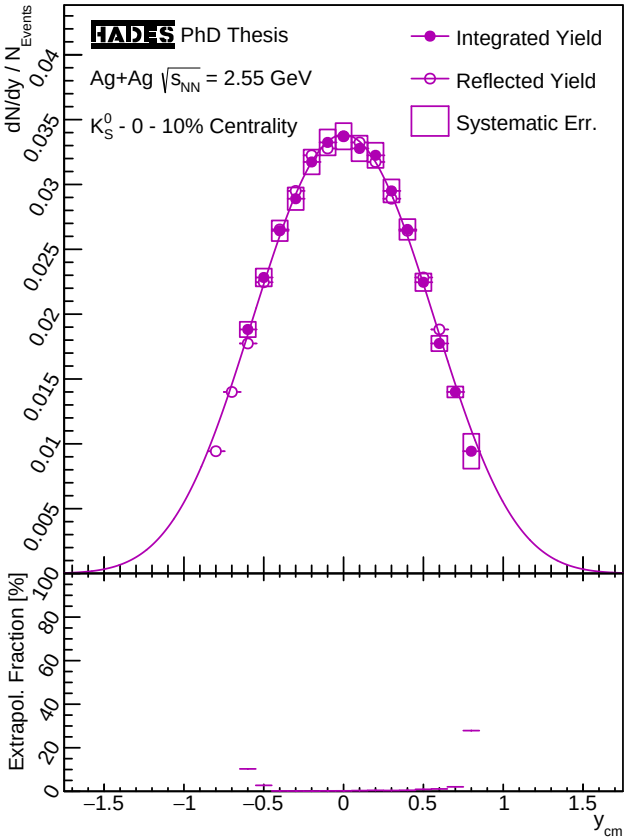

Figure 4.24.: Rapidity spectrum of K^0_S from the 0-10 % most central Ag(1.58A GeV)+Ag events after transverse integration (upper part). The open symbols correspond to the data mirrored at mid-rapidity. The lower part shows fraction of the yields obtained by the extrapolation in transverse direction.

Concerning the mid-rapidity transverse momentum spectra, a strong accordance between the model functions and the measured yields over the entire transverse momentum range is observed. Only around transverse momenta of 200 MeV/c slight discrepancies can be observed. Also concerning the rapidity spectra after integration and extrapolation, a strong accordance between the model functions and the data points is observed for all centrality classes. Like the Λ hyperons, the K^0_S mesons are newly produced inside the fireball, which is why their kinematic distributions are not contaminated.

Table 4.9 summarizes the integrated 4π yields as well as the DIS model parameters obtained in the multi-differential analysis of K^0_S mesons. Like for the Λ hyperons, the values of T_{Eff} are determined by the transverse momentum spectra fits and the values for η by the rapidity spectrum fits. The systematic uncertainties of the model parameters are again derived from the differences between the analyses conducted with different selection criteria sets. In Chapter 5 the obtained results will be put in context and analyzed further.

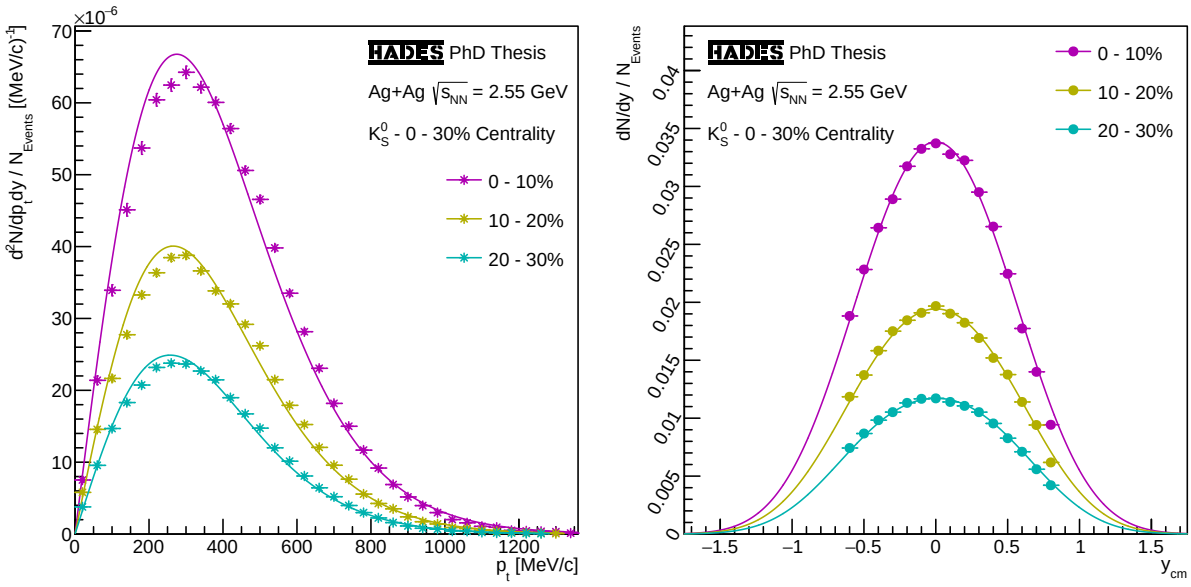

Figure 4.25.: Mid-rapidity transverse momentum spectra (left) and rapidity spectra (right) of K^0_S from the three most central 10 % Ag(1.58A GeV)+Ag centrality classes and the according DIS fit functions.

Centrality	4π Yield / Event	T_{Eff} [MeV]	η
0-10 %	$(4.50 \pm 0.02 \pm 0.15) \times 10^{-2}$	$108 \pm 1 \pm 4$	$0.27 \pm 0.01 \pm 0.01$
10-20 %	$(2.72 \pm 0.01 \pm 0.09) \times 10^{-2}$	$103 \pm 1 \pm 4$	$0.31 \pm 0.01 \pm 0.01$
20-30 %	$(1.67 \pm 0.01 \pm 0.06) \times 10^{-2}$	$98 \pm 1 \pm 3$	$0.33 \pm 0.01 \pm 0.01$

Table 4.9.: Integrated 4π yields and DIS model parameter values obtained in the analysis of K^0_S from the 0-30 % most central Ag(1.58A GeV)+Ag events.

4.4. $^{3}_{\Lambda}$H Analysis

The $^{3}_{\Lambda}$H is a hypernucleus and consists of one proton, neutron and Λ. With a mass of ≈ 2991 MeV/c^2 it is the lightest known hypernucleus and has a nuclear binding energy of only ≈ 0.8 MeV per nucleon which is even lower than the one of the deuteron which has the lowest among the regular nuclei with ≈ 1.1 MeV per nucleon [113]. Due to the low binding energy, the decay of the $^{3}_{\Lambda}$H is expected to have similar properties like the decay of free Λ hyperons, however, multiple measurements of the $^{3}_{\Lambda}$H lifetime yielded values significantly below the free Λ lifetime, which resulted in the so called $^{3}_{\Lambda}$H lifetime puzzle. More recent measurements however, yield lifetimes only slightly below or compatible with the the free Λ lifetime. A very recent review of the $^{3}_{\Lambda}$H lifetime and other properties is performed in [108].

The $^{3}_{\Lambda}$H has six mesonic decay channels. They correspond to the two primary decay channels of the Λ hyperon and the possibility of no, partial or full nuclear breakup in the final state. Most abundantly a partial nuclear breakup occurs: $^{3}_{\Lambda}\mathrm{H} \rightarrow \mathrm{d} + \mathrm{p} + \pi^-$ (BR ≈ 40 %) and $^{3}_{\Lambda}\mathrm{H} \rightarrow \mathrm{d} + \mathrm{n} + \pi^0$ (BR ≈ 20 %). Second most abundantly no nuclear breakup occurs: $^{3}_{\Lambda}\mathrm{H} \rightarrow {}^{3}\mathrm{He} + \pi^-$ (BR ≈ 27 %) and $^{3}_{\Lambda}\mathrm{H} \rightarrow \mathrm{t} + \pi^0$ (BR ≈ 13 %). The decay channels in which a full nuclear breakup occurs ($^{3}_{\Lambda}\mathrm{H} \rightarrow \mathrm{p} + \mathrm{p} + \mathrm{n} + \pi^-$ and $^{3}_{\Lambda}\mathrm{H} \rightarrow \mathrm{p} + \mathrm{n} + \mathrm{n} + \pi^0$) as well as all non-mesonic decay channels have negligible BRs. A theoretical review of the $^{3}_{\Lambda}$H decay channels and their BRs can be found in [114].

In fixed-target heavy-ion collisions at beam energies of few GeV, $^{3}_{\Lambda}$H are produced by clustering of a previously produced Λ hyperon (cf. Section 4.2) with nucleons from the bulk. The exact clustering mechanism is still unknown even for regular nuclei and therefore topic of current studies like for example [175]. The $^{3}_{\Lambda}$H was already investigated by HADES in Ar(1.76A GeV)+KCl collisions via its two-body decay channel with only charged products, however, no clear signal could be reconstructed [34, 160]. In Au(1.23A GeV)+Au collisions, the reconstruction was attempted via the same decay channel [54] and via its three-body decay channel with only charged products [111], however, again no clear signal could be reconstructed. In this work, the reconstruction via the two-body decay channel is investigated for Ag(1.58A GeV)+Ag collisions which are advantageous due to their higher energy and smaller system size compared to Au(1.23A GeV)+Au collisions. Like for the Λs and the K^0_S, the OVD topology parameters are evaluated in this work using an ANN. The details of their reconstruction and analysis are described in the following sections.

4.4.1. Artificial Neutral Network Training

Like the Λs and the K^0_S also the majority of the $^{3}_{\Lambda}$H decay in front of the first detectors and need to be reconstructed from their decay daughters, in this work ^{3}He (Dau1) and π^- (Dau2). For the π^- exactly the same selection criteria as for π^- from Λ decays are used. The ^{3}He is identified in a mass range from 1270 to 1520 MeV/c^2 and an a-range from 0.5 to 2 which roughly corresponds to a velocity above 0.3 c and a measured momentum below 2800 MeV/c. Furthermore, the ^{3}He-candidates have to have velocities below the speed of light and fulfill the MDC specific energy loss selection regions determined in Section 3.4.2. Like already before the a-range selections are obtained from simulated $^{3}_{\Lambda}$H embedded into experimental data using the method described in Section 2.3.4.

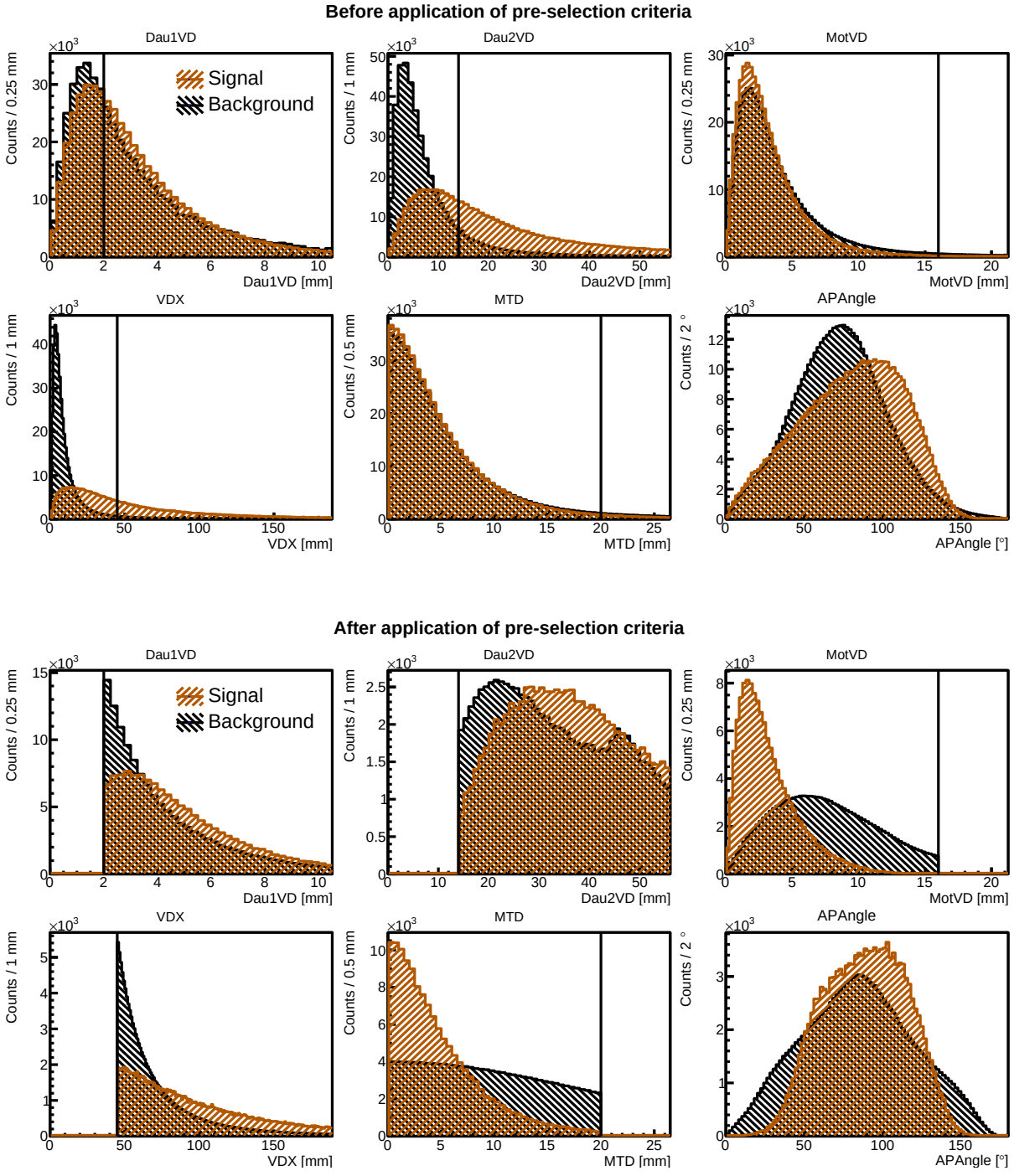

Figure 4.26.: Signal and background distributions of the parameters used for training the ANN to reconstruct ${}^{3}_{\Lambda}\mathrm{H}$ before (upper panel) and after (lower panel) all of the pre-selection criteria, which are indicated by lines - See the text for details.

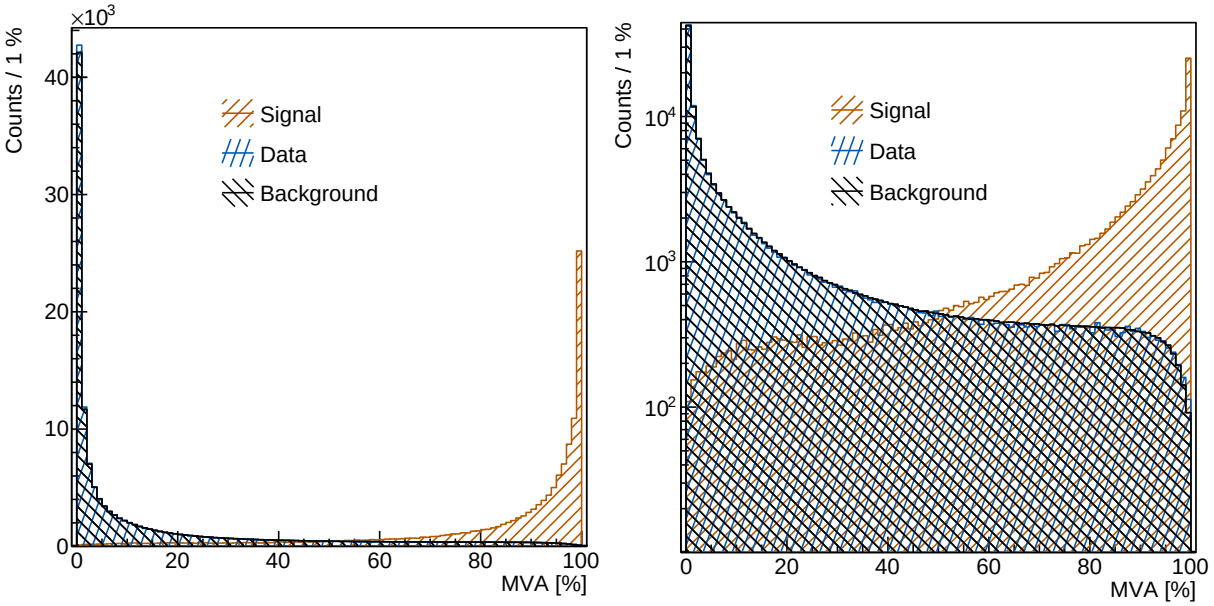

Figure 4.27.: ANN response distribution for the signal- (orange) and background (black) samples used for training and testing of the ANN as well ^{3}He-π^{-} combinations from real events (azure) in linear (left) and logarithmic (right) representation.

The methods described in Sections 3.6, 3.8 and 3.10 are used for the reconstruction of $^{3}_{\Lambda}$H as well, beginning with the training of an ANN to evaluate the decay parameters summarized in Appendix A.6. The corresponding distributions from the signal sample obtained from simulated $^{3}_{\Lambda}$H as well as from the background sample obtained via the mixed event method is shown in the upper part of Figure 4.26. At this stage, only the parameters Dau2VD, VDX and APAngle show a significant discrimination power. The parameters MotVD and MTD again show basically no discrimination power, however, this time the same holds true also for Dau1VD, because of the large mass difference between the ^{3}He and the π^{-} in combination with the low amount of energy released in the decay which results in the ^{3}He being barely deflected.

Due to the low binding energy of the $^{3}_{\Lambda}$H, many calculations predict a similar lifetime as for free Λ hyperons and measurements confirm at least a similar order of magnitude. For this reason, the same pre-selection criteria already used for the Λ hyperons are also used for the $^{3}_{\Lambda}$H. Only the lower limit on the parameter Dau1VD is halved to account for the much higher mass of the ^{3}He compared to the proton. The used pre-selection criteria are denoted in Table 4.10 and the parameter distributions after their application are depicted in the lower panel of Figure 4.26.

The pre-selection criteria again result in a significant discrimination power of the parameters MotVD and MTD and also the discrimination power of the parameter Dau1VD is slightly raised. The background distribution of the parameter Dau2VD shows a very pronounced peak-like structure at 45 mm resulting from the criterion VDX $>$ 45 mm. In case of the $^{3}_{\Lambda}$H the effect is much stronger than for Λ hyperons or K^{0}_{S} mesons again because of the large mass difference between the ^{3}He and the π^{-} in combination with the low amount of energy released in the decay.

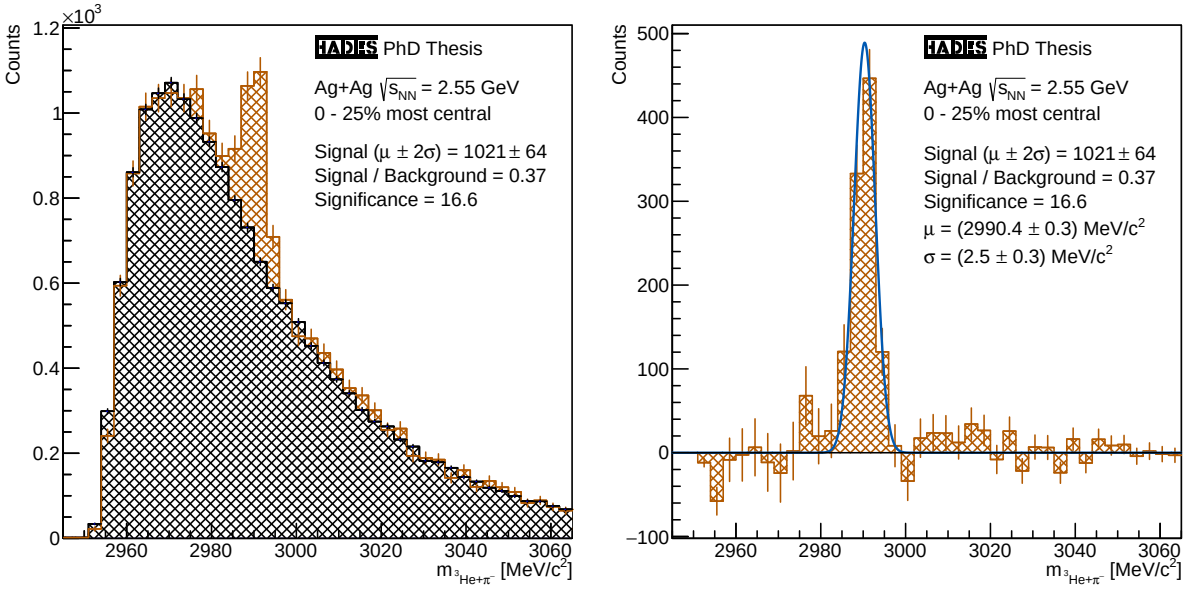

Figure 4.28.: Invariant mass distribution of ^{3}He-π^- pairs from the 0-25 % most central Ag(1.58A GeV)+Ag events after application of the full $^3_\Lambda$H reconstruction method before (left) and after (right) subtraction of the mixed-event combinatorial background.

Figure 4.27 shows the ANN response parameter (MVA) distributions obtained for the two training samples as well as experimental ^{3}He-π^- pairs. As for the Λ hyperons and K^0_S mesons, a very strong separation between the two training samples is observed. As in particular visible in the logarithmic depiction in the right, the distributions of the background sample and experimental data match perfectly. Unlike for the Λs and K^0_S no strong excess of the data distribution around 1 can be observed since the $^3_\Lambda$H is produced much less abundant than Λ hyperons or K^0_S mesons. Under close examination, however, a slight excess in the last two intervals of the data distribution is observed which might be due to actual $^3_\Lambda$H decays.

As for the Λ hyperons and K^0_S, in the next step, the ^{3}He-π^- invariant mass distributions for experimental data and mixed-event background are generated and the selection criteria are optimized for a maximum significance (Equation 4.3) in an iterative procedure. To obtain sufficient signal counts to perform a differential analysis, in the optimization procedure at least 1000 signal counts and a signal to background ratio of 1/3 are required. Kinematically, the analyzed $^3_\Lambda$H decay channel has many similarities with the primary decay channel of free Λ hyperons due to the low binding energy of the $^3_\Lambda$H. Furthermore, due to its double charge the ^{3}He are measured in the detectors at panel of its nominal mass $\approx$ 1404 MeV/c^2 which is why its momentum resolution is comparable to the one of protons which have a mass of $\approx$ 938 MeV/c^2. For these reasons, the peak widths of Λs and $^3_\Lambda$H are similar and therefore the side-bands used for the normalization of the mixed-event background are positioned again at least $\pm 6\sigma$ outside the signal region.

The final optimized selection criteria are denoted in Table 4.10 in the column "Standard" and the corresponding invariant mass distributions are shown in Figure 4.28 before (left) and after (right) subtraction of the mixed-event background. Around the nominal mass of the $^3_\Lambda$H of $\approx$ 2991 MeV/c^2 a clear peak with $\approx$ 1000 counts within $\pm 2\sigma$ a significance

of 16.6 and signal to background ratio of 0.37 is observed. Outside the signal region, the background of the data distribution is described well by the mixed-event background. The Gaussian function fitted to the subtracted invariant mass spectrum in the right of Figure 4.28 has a mean very close to the nominal $^{3}_{\Lambda}$H mass and a width of 2.5 MeV/c^2 which is close to the width of the Λ peak shown in Figure 4.8. Thereby it confirms the kinematic similarities between the $^{3}_{\Lambda}$H and Λ decay.

In the following section, the production rates of $^{3}_{\Lambda}$H are estimated and a lifetime measurement is performed. Table 4.10 summarizes the selection criteria sets used in these analyses again with only the "Standard" using the ANN response and the sets "Loose", "Medium" and "Tight" to estimate the systematical uncertainties not. However, not using the ANN response results in very strong criteria on the remaining parameters to achieve the required suppression of the combinatorial background. Unfortunately, this results in low signal counts and large statistical uncertainties using these selection criteria.

Parameter	**Pre-Selection**	**Standard**	**Loose**	**Medium**	**Tight**
Dau1VD	$>$ 2 mm	$>$ 3 mm	$>$ 4 mm	$>$ 6 mm	$>$ 8 mm
Dau2VD	$>$ 14 mm	$>$ 14 mm	$>$ 30 mm	$>$ 35 mm	$>$ 40 mm
MotVD	$<$ 16 mm	$<$ 16 mm	$<$ 8 mm	$<$ 6 mm	$<$ 4 mm
VDX	$>$ 45 mm	$>$ 45 mm	$>$ 90 mm	$>$ 100 mm	$>$ 110 mm
MTD	$<$ 20 mm	$<$ 12 mm	$<$ 10 mm	$<$ 8 mm	$<$ 6 mm
A	$>$ 15°				
MVA	—	$>$ 98.1 %	—		

Table 4.10.: The five final selection criteria sets used for the reconstruction and analysis of $^{3}_{\Lambda}$H hypernuclei.

4.4.2. Lifetime Measurement

The $^{3}_{\Lambda}$H lifetime was an unsolved riddle for several years since theories predicted lifetimes close to the free Λ lifetime while measurements resulted in significantly lower lifetimes [10, 13, 24, 152]. The measurement is conducted in analogy to the lifetime measurement of Λ hyperons and K^0_S mesons. As it yields the correct lifetimes for these particles, the method is verified to be working correctly. First, the decay-times are calculated from the measured decay-lengths using Equation 4.4 and their range from 300 to 1000 ps is divided into 7 equally sized intervals with a width of 100 ps. For each of these intervals the amounts of reconstructed $^{3}_{\Lambda}$H within $\pm 2\sigma$ is extracted and corrected for acceptance and efficiency effect using $^{3}_{\Lambda}$H embedded into experimental data as described in Section 2.3.4. By normalizing the corrected counts for the decay-time interval widths and the amounts of analyzed events, the decay-time spectrum displayed in Figure 4.29 is obtained. As before, the systematic uncertainties, depicted as boxes, are estimated based on the differences between the four selection criteria sets defined in Section 4.4.1. The low amounts of

reconstructed ${}^{3}_{\Lambda}\mathrm{H}$ decays results in large statistical uncertainties of the measurement.

The orange function depicted in Figure 4.29 corresponds to the exponential decay law defined by Equation 4.5, is fitted to the data points and yields the measured lifetime of $(253 \pm 24 \pm 42)$ ps. The systematic uncertainty is again determined by applying the averaged relative uncertainty of the data points to the obtained value. The result is pretty close to the lifetime of free Λ hyperons of 263 ps [184] which is depicted black in Figure 4.29. As for the Λ hyperons and K^0_S mesons, the measured lifetime is compatible to its expectation value, however unfortunately the large statistical and systematic uncertainties significantly reduce the relevance of this measurement. Nevertheless, it falls in line with further recent measurements of the lifetime of ${}^{3}_{\Lambda}\mathrm{H}$ which resulted in lifetimes compatible with the free Λ lifetime too [6, 12, 108] and thereby enforces the according theoretical predictions.

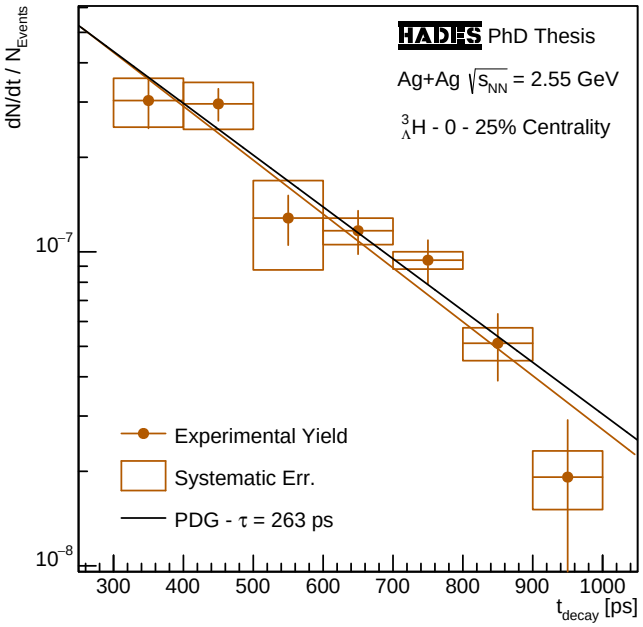

Figure 4.29.: Lifetime spectrum of ${}^{3}_{\Lambda}\mathrm{H}$ from the 0-25 % most central Ag(1.58A GeV)+Ag events. The orange exponential decay curve corresponds to the data and the black to the free Λ lifetime [184].

4.4.3. Differential and Multi-Differential Analysis

Unfortunately, the low amount of only $\approx$ 1000 signal counts makes precise multi-differential analysis of the production of ${}^{3}_{\Lambda}\mathrm{H}$ for all centrality classes like conducted for Λ hyperons and K^0_S mesons very challenging. In this section, the multi-differential analysis is therefore conducted only for the 0-25 % most central events. However, acceptance and efficiency values averaged over the entire phase-space, still allow to obtain centrality-differential production rates. Therefore, ${}^{3}_{\Lambda}\mathrm{H}$ generated with an effective temperature of 200 MeV around mid-rapidity by the Pluto event generator and embedded into experimental data by the method described in Section 2.3.4, are used. The obtained rates are listed in Table 4.11 for the three 0-30 % most central classes of Ag(1.58A GeV)+Ag events. The low amount of reconstructed ${}^{3}_{\Lambda}\mathrm{H}$ results in large relative statistical uncertainties of up to 16 % and

Centrality	**4π Yield / Event**
0-25 %	$(3.30 \pm 0.21 \pm 0.54) \times 10^{-4}$
0-10 %	$(6.13 \pm 0.52 \pm 1.01) \times 10^{-4}$
10-20 %	$(2.31 \pm 0.27 \pm 0.38) \times 10^{-4}$
20-30 %	$(0.88 \pm 0.14 \pm 0.15) \times 10^{-4}$

Table 4.11.: 4π yields obtained in the analysis of ${}^{3}_{\Lambda}\mathrm{H}$ for the 0-30 % most central Ag(1.58A GeV)+Ag events.

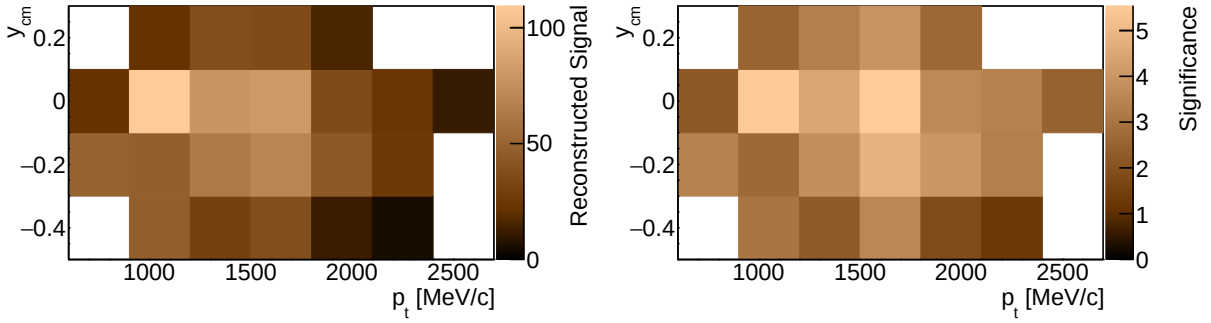

Figure 4.30.: Extracted $^{3}_{\Lambda}$H signal counts (left) and their significances (right) from the 0-25 % most central Ag(1.58A GeV)+Ag events.

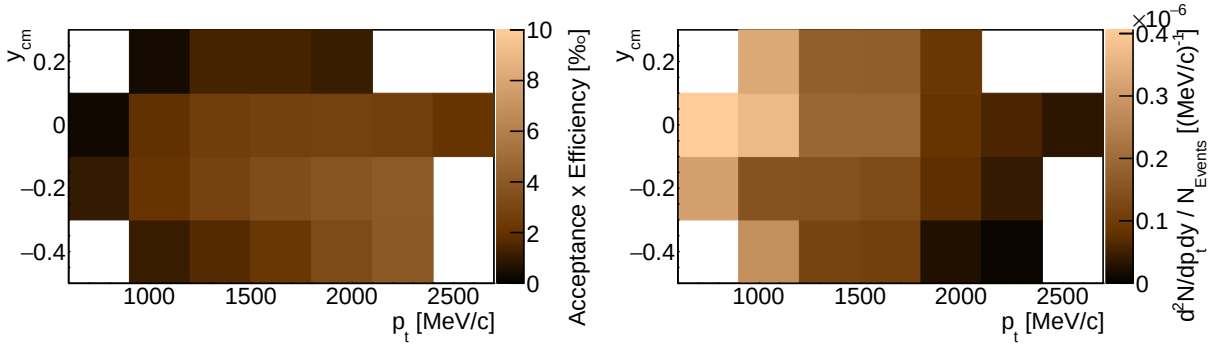

Figure 4.31.: Acceptance × Efficiency values (left) as well as corrected and normalized $^{3}_{\Lambda}$H production rates (right) from the 0-25 % most central Ag(1.58A GeV)+Ag events.

even higher ones for the selection criteria sets not using the ANN response. Therefore, the systematic uncertainties of the production rates cannot be determined by cut variations, as they would be exceeded by the statistical uncertainties. Instead, the relative systematic uncertainties from the $^{3}_{\Lambda}$H lifetime measurement in the previous section which amount to $\approx$ 16.5 % are used.

The method used for the multi-differential transverse momentum and rapidity analysis of the $^{3}_{\Lambda}$H production is again almost identical to the one used for Λ hyperons and K^{0}_{S} mesons which is why in the following only the important steps and differences are discussed. In case of the $^{3}_{\Lambda}$H, the low amount of signal counts requires significantly larger phase-space intervals. The entire phase-space is divided into 7 transverse momentum intervals with a width of 300 MeV/c from 600 to 2700 MeV/c and 4 rapidity intervals with a width of 0.2 from –0.5 to 0.3 in the CM system of collision resulting in a grand total of 28 individual intervals. For each of these intervals, the $^{3}_{\Lambda}$H signal counts are extracted using the method described in Section 4.4.1 without distinguishing between RPC and TOF detector region. Figure 4.32 shows the invariant mass distributions from four different regions of the total phase-space. The amounts of signal counts for each interval are depicted in the left of Figure 4.30, while its right shows the corresponding significances.

Next, the correction for acceptance and efficiency effects is performed using the same simulated $^{3}_{\Lambda}$H as before and Equation 4.8. Like for Λs and K^{0}_{S}, the total acceptance consists of the acceptances of the ^{3}He and the π^{-} as well as the BR of the decay channel

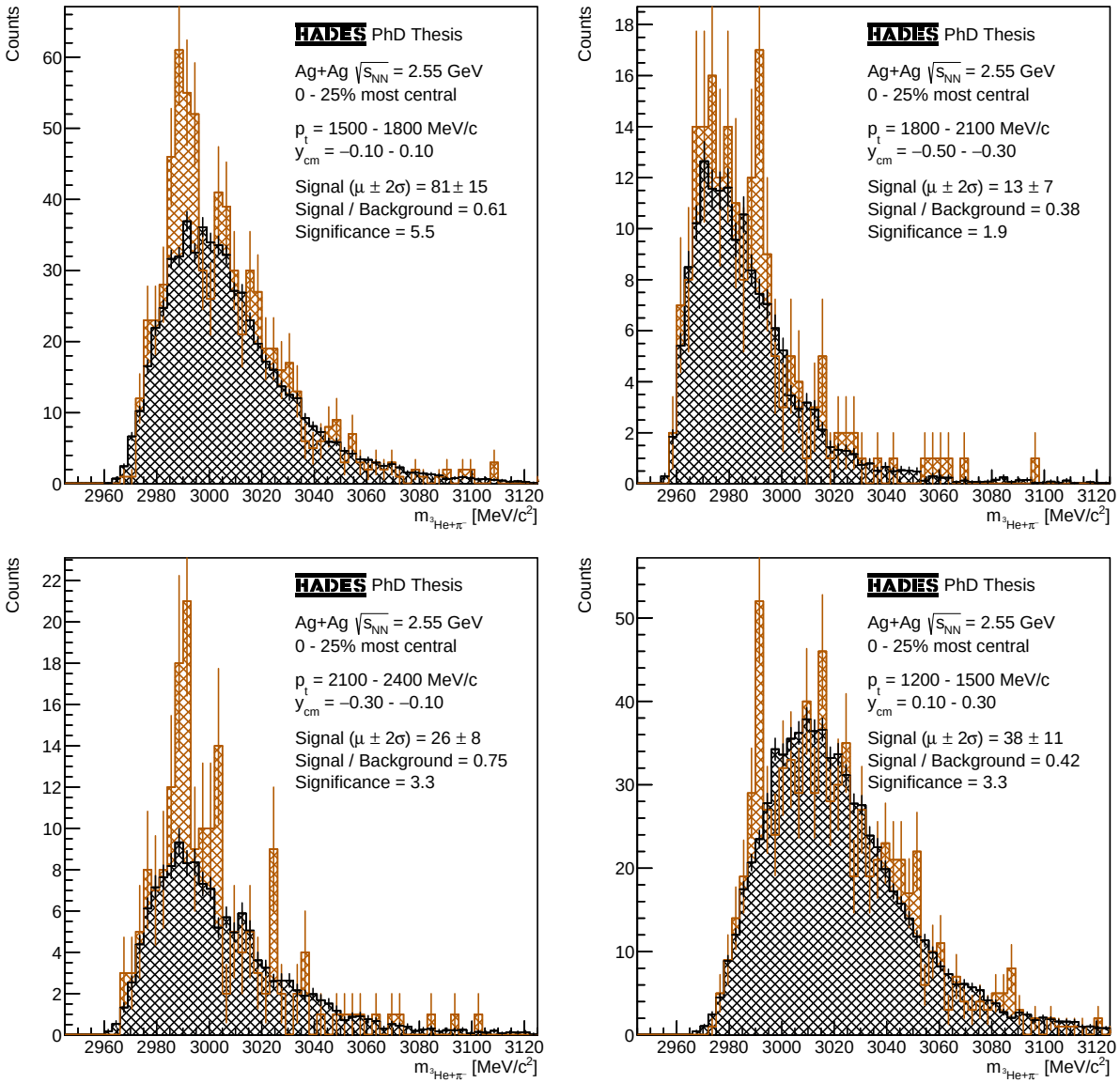

Figure 4.32.: Invariant mass distributions of ^{3}He-π^- pairs from the 0-25 % most central Ag(1.58A GeV)+Ag events at the center of the total phase-space (upper left), the medium-p_t backward-rapidity region (upper right), the high-p_t mid-rapidity region (lower left) and the medium-p_t forward-rapidity region (lower right).

$$BR_{^3_\Lambda H} \cdot a_{^3He} a_{\pi^-} \cdot \epsilon_{det,^3He} \epsilon_{det,\pi^-} \cdot \epsilon_{rec,^3He} \epsilon_{rec,\pi^-} \cdot \epsilon_{sel,^3He} \epsilon_{sel,\pi^-} \cdot \epsilon_{OVD,^3_\Lambda H} = \frac{N^{sim}_{rec,^3_\Lambda H}(p_t, y)}{N^{sim}_{gen,^3_\Lambda H}(p_t, y)} \quad (4.8)$$

and the total efficiency consists of the detection, reconstruction and selection efficiencies of the ^{3}He and the π^- as well as the efficiency of the OVD selection criteria. Intervals with an acceptance or efficiency quotient deceeding 1 % are again rejected. To allow larger statistical fluctuations due to the low amounts of signal counts, relative statistical uncertainties up to 100 % are allowed. The determined Acceptance × Efficiency values are displayed in the left of Figure 4.31. Finally, a normalization to the number of analyzed events as well as the transverse momentum and rapidity interval widths is performed.

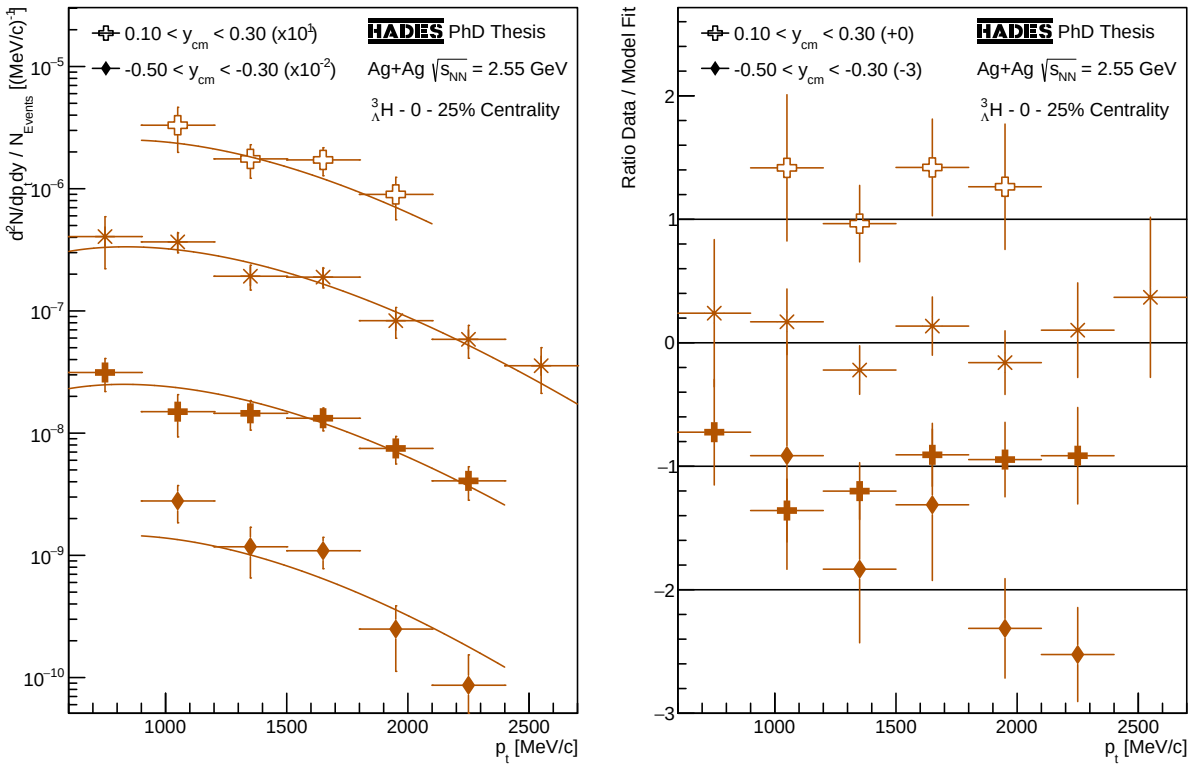

Figure 4.33.: Transverse momentum spectra of $^{3}_{\Lambda}$H from the 0-25 % most central Ag(1.58A GeV)+Ag events for the multiple rapidity intervals scaled by 10^{x} for better visibility (left). Again, full markers correspond to the backward hemisphere and open markers to the forward hemisphere. The mid-rapidity interval, is depicted by the symbol ✳. The spectra are fitted with DIS model-functions with a common effective temperature T_{Eff} and a common η. Furthermore, the ratios between the data points and the fit functions shifted by ±x for better visibility are displayed (right).

The fully corrected and normalized $^{3}_{\Lambda}$H production rates over the entire phase-space are depicted in the right of Figure 4.31 for the 0-25 % most central Ag(1.58A GeV)+Ag events. Due to the large intervals, the measurement covers a large part of the phase-space including one rapidity interval from the forward hemisphere. In the next step, the extrapolation in transverse direction is performed. The individual corrected and normalize $^{3}_{\Lambda}$H transverse momentum spectra for each rapidity interval are shown in the left of Figure 4.33. For better visibility, the spectra are scaled by factors 10^{x}. Like for the Λ hyperons and K^{0}_{S} mesons, DIS model functions (cf. Section 1.4), depicted in Figure 4.33 as well, are used for the extrapolation. The fit method remains identical too meaning that the functions for the individual spectra are fitted with a common value for the parameter T_{Eff}, symmetric scaling parameters C and the parameter η fixed to 0 for the transverse fits. All measured data points are well described by the fit functions within their statistical uncertainties. This is also reflected by the right plot of Figure 4.33 which shows the ratios between the model functions and and the data points, again shifted by ±x for better visibility. The effective temperature T_{Eff} obtained by the combined transverse fit amounts to (210 ± 19 ± 35) MeV with the systematic uncertainty corresponding to a relative uncertainty of 16.5 % as motivated before.

After integration of the transverse momentum spectra as well as the model functions for extrapolation, the rapidity spectrum displayed in Figure 4.34 is obtained. The integrated yields are depicted by full circles and the yields reflected at mid-rapidity, which are symmetric within the statistical uncertainties, by open circles. Furthermore, the proportions of the yields obtained by extrapolation, which are displayed in the lower part of Figure 4.34, show that due to the low amounts of signal counts even in the best intervals $\gtrsim$ 20 % of the total yield is obtained by the extrapolations. The systematic uncertainties depicted by boxes around the data points in Figure 4.34 are again estimated based on the relative systematic uncertainty of the ${}^{3}_{\Lambda}$H lifetime measurement of $\approx$ 16.5 %. This is done since unfortunately, the low amounts of signal counts, in particular when using the selection criteria sets without the ANN response parameter, as well as the low amount of intervals with both a forward- and backward-hemisphere yield hinder the method used for protons, Λ hyperons and K^0_S mesons. Besides the large uncertainties, the full 4π production rate obtained by integration and extrapolation of $(3.96 \pm 0.21 \pm 0.66) \times 10^{-4}$ ${}^{3}_{\Lambda}$H per event is consistent within uncertainties with the previously determined value using averaged acceptances and efficiencies.

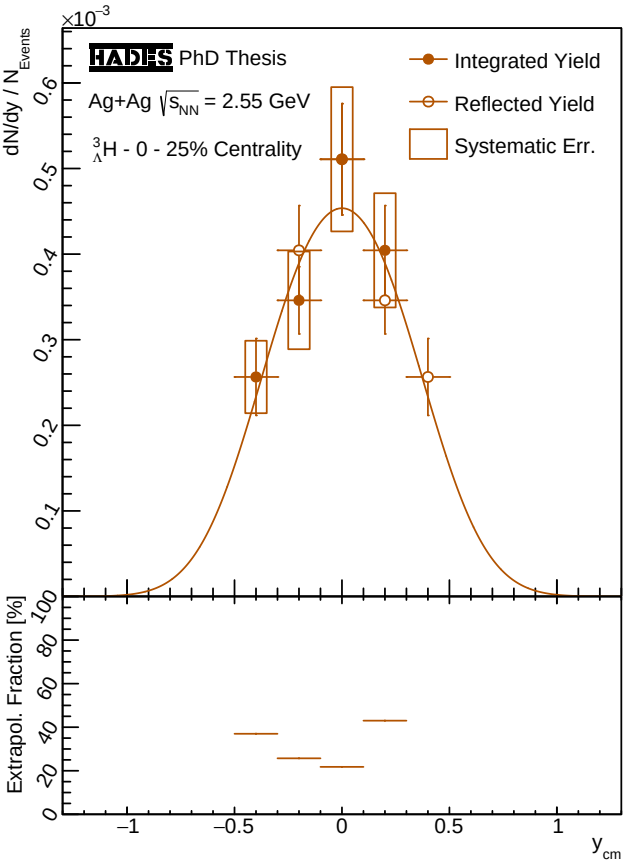

Figure 4.34.: Rapidity spectrum of ${}^{3}_{\Lambda}$H from the 0-25 % most central Ag(1.58A GeV)+Ag events after transverse integration (upper part). The open symbols correspond to the data mirrored at mid-rapidity. The lower part shows fraction of the yields obtained by the extrapolation in transverse direction.

The rapidity spectrum shown in Figure 4.34 clearly shows that the measured ${}^{3}_{\Lambda}$H are dominantly produced and emitted from the fireball by a source at mid-rapidity. The same emission pattern, which is well described by an IS phase-space distribution model (cf. Section 1.4), was already observed for Λ hyperons and K^0_S mesons. On the other side, for example the HypHI collaboration proposed the production of hypernuclei in projectile fragmentation reactions [152]. In these reactions, a hyperon produced in the fireball forms a hypernuclei with a fragment of the colliding nuclei. Such hypernuclei are therefore emitted from two sources at target- and projectile-rapidity which are not covered by the HADES spectrometer. Concerning the total production rates, the HypHI collaboration measured a ${}^{3}_{\Lambda}$H / Λ ratio of $(2.2 \pm 1.3) \times 10^{-3}$ [153]. In this work, a ratio of $(3.8 \pm 0.4) \times 10^{-3}$ is measured for the 0-30 % most central events. For the interpretation one needs to consider that the HypHI collaboration measured smaller collision systems at

higher energies, namely He(3.7A GeV)+C and Li(3.0A GeV)+C collisions. In this work, Ag(1.58A GeV)+Ag collisions with a significantly lower energy and larger system size, are analyzed so different hypernuclei production mechanisms might be predominant.

4.5. Ξ^- Analysis

Ξ^- hyperons consist of one down- and two strange-quarks $|dss\rangle$, carry an electrical charge of –1 and are besides the Ξ^0 hyperons the lightest existing double strange hyperons with a mass of $\approx$ 1322 MeV/c^2. They decay via the weak interaction to single strange hyperons with a decay length cτ of 4.91 cm. Since the single strange hyperons decay further via the weak interaction, their decay topology develops a multi-step structure which is why the Ξ hyperons are historically called "cascade". the most probable decay channel of Ξ^- hyperons is $\Xi^- \rightarrow \Lambda + \pi^-$ with a BR of almost 100 %. If the Λ hyperon decays further into a p-π^- pair, their total decay reads $\Xi^- \rightarrow p + \pi^- + \pi^-$ and has an overall BR of 63.8 % [184]. In fixed-target heavy-ion collisions at beam energies of few GeV, the production of Ξ hyperons is suppressed due to the rather high energetic threshold - See Equation 1.8.

Due to the low production rates in combination with the high abundances of the decay products, the combinatorial background overshoots the anticipated signal by a factor of about 135,000,000 like already stated in Section 3.6. Therefore, the reconstruction of the Ξ^- hyperon is particular challenging and never succeeded in heavy-ion collisions at such low beam energies. However, the double OVD topology of its decay allows for a stronger suppression of the combinatorial background than for the particles discussed so far. Thus, in combination with analyzing the OVD topology parameters with an ANN, a successful reconstruction might be possible.

The same was already attempted in [161, 170] for Au(1.23A GeV)+Au collisions, however, no clear signal could be reconstructed. In comparison the Ag(1.58A GeV)+Ag collisions have two advantages: The slightly increased energy leads to a significantly increased production rate since the excitation function of the production is expected to be very steep below the free NN threshold energy. Furthermore, the smaller size of the Ag nuclei compared to the Au nuclei results in lower amounts of protons and π^- from other sources which decreases the combinatorial background. For these reasons, the reconstruction of the Ξ^- hyperons is reattempted in this work using an ANN to evaluate the OVD topology parameters like for the Λs, the K^0_S and the $^3_\Lambda$H as described in the following sections.

4.5.1. Artificial Neutral Network Training

Both the Ξ^- hyperons and the Λ hyperons produced in its decays decay in front of the first detectors and need to be reconstructed from their daughter particles. First, the Λ hyperon is reconstructed using the same method as for free Λs, however, with different ranges on the parameter a for the proton (Dec1Dau1) and the π^-(Dec1Dau2), namely between 0.72 and 1.51 for protons which roughly corresponds to velocities above 0.48 c and momenta below 1800 MeV/c and values between 0.84 and 1.04 for π^- which roughly corresponds to velocities above 0.67 c and momenta below 500 MeV/c. Next, the reconstructed Λ hyperons (Dec2Dau1) are combined with another π^- (Dec2Dau2) resulting in

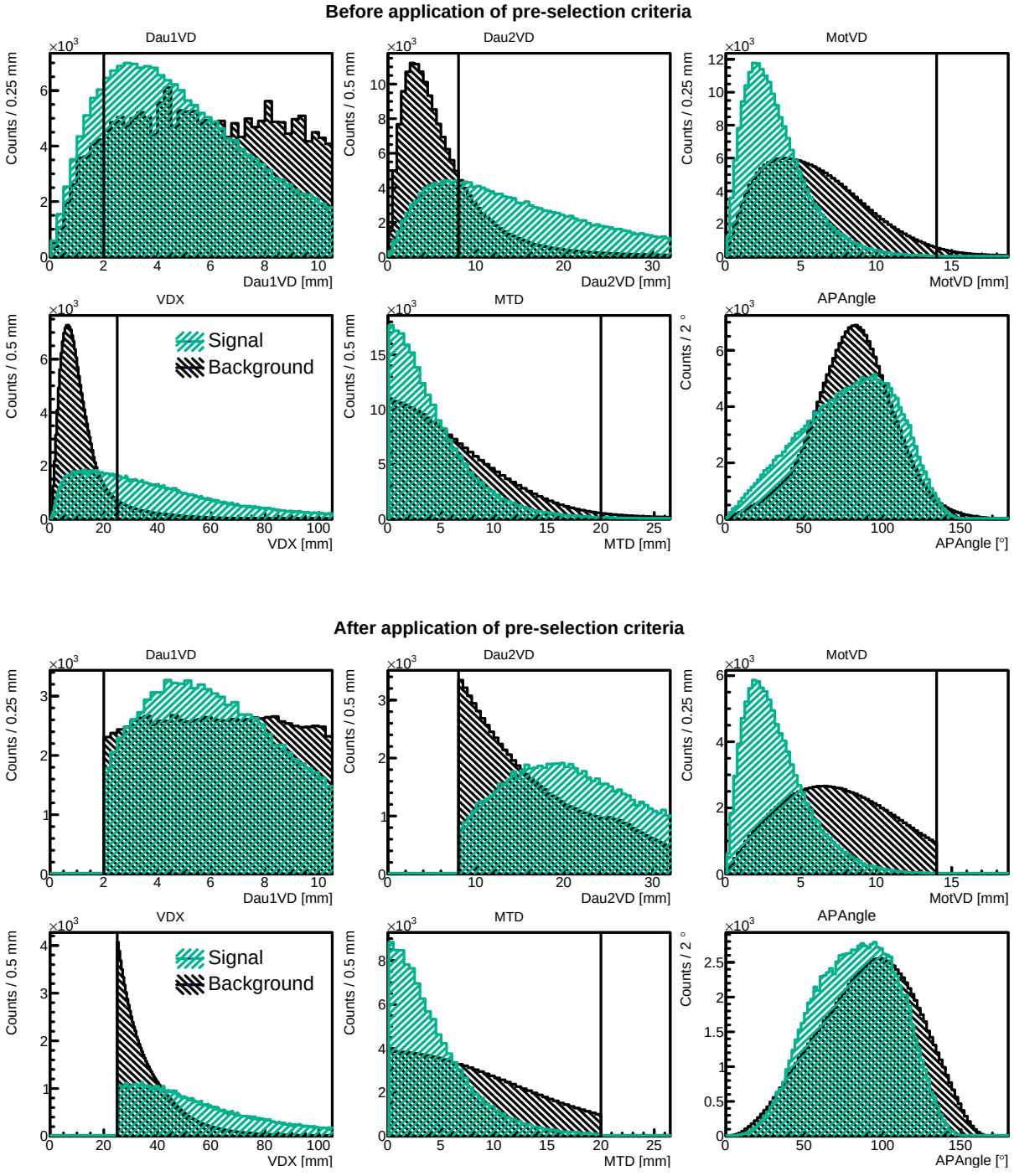

Figure 4.35.: Signal and background distributions of the parameters used for training the ANN to reconstruct Ξ^- before (upper panel) and after (lower panel) all of the pre-selection criteria, which are indicated by lines.

the Ξ^- candidates. The Λ hyperons are required to have an invariant mass within a defined range which will be discussed in the following paragraph as well as an a-value between 0.78 and 1.65 which roughly corresponds to velocities above 0.5 c and momenta below 2100 MeV/c. For the π^- from the Ξ^- decay a slightly different a-range than for the π^- from the Λ decay, namely from 0.87 to 1.05 which roughly corresponds to velocities above 0.71 c and momenta below 500 MeV/c, is used. This is to account for the different mass relation and the different amount of energy released in the Ξ^- decay. As for the Λs, the K^0_S and the ${}^3_\Lambda H$ the ranges are determined using Ξ^- hyperons embedded into experimental data using the method described in Section 2.3.4. However, this time the primary aim is to reduce the combinatorial background of the Ξ^- candidates which is why about $\pm 2\sigma$ of the distributions are used as ranges. As before, the energies of the identified tracks are adjusted such that their reconstructed masses are equal to their nominal masses.

The reconstruction of Ξ^- hyperons is performed by applying the basic principle for the identification and reconstruction of weakly decaying particles, as described in Sections 3.6, 3.8 and 3.10, twice: First to reconstruct Λ hyperons and afterwards to reconstruct Ξ^- hyperons. The training of the ANN used to identify the Λ hyperons required to reconstruct Ξ^- hyperons can be performed using either simulated free Λ hyperons or Λ hyperons from the decays of simulated Ξ^- hyperons. On first sight it might seem obvious to use the Λ hyperons from Ξ^- decays, however, they pose a problem: The additional displacement of the Λ decay due to the random decay-length of the Ξ^- hyperon strongly influences the OVD topology parameters of the Λ which confuses the ANN. This effect results in a significantly reduced performance of the Λ identification if the ANN is trained using Λ hyperons from simulated Ξ^- hyperons compared to using simulated free Λ hyperons and was shown in [170]. Therefore, in this work, the Λ hyperons are identified using the exact same method as free Λ hyperons described in Section 4.2.1.

Λ hyperons are selected from a mass range around its nominal mass of 1115 MeV/c^2. This range is set to ± 7.5 MeV/c^2 which roughly corresponds to $\pm 3\sigma$ for the training of the ANN used to identify Ξ^- decays, but is varied in the optimization procedure later on. Afterwards, the energy of the Λ hyperon is adjusted such that it has its nominal mass too. The distributions of the OVD topology parameters, summarized in Appendix A.6, of the signal sample obtained from simulated Ξ^- hyperons and the background sample obtained via the mixed-event method are shown in the upper panel of Figure 4.35. Unlike for Λs, K^0_S or ${}^3_\Lambda H$ all parameters already show some discrimination power. This is because of the additional background coming from p-π^- pairs falsely identified as Λ hyperons.

The pre-selection criteria for the training of the Ξ^- ANN cannot be determined by an optimization procedure as for the Λ hyperons or K^0_S mesons, because that would require a signal with high significance to guarantee a stable criteria optimization. However, they can be estimated from the pre-selection criteria of the Λ hyperons since both decays have to some extend comparable amounts of energy released and mass relations between the daughter particles. Special care has to be taken concerning the parameters Dec1MotVD and Dec2Dau1VD as their definition is identical and both an upper limit as well as a lower limit is applied to them. The pre-selection criteria used for the reconstruction of Ξ^- hyperons are listed in Table 4.12 in the column "Pre".

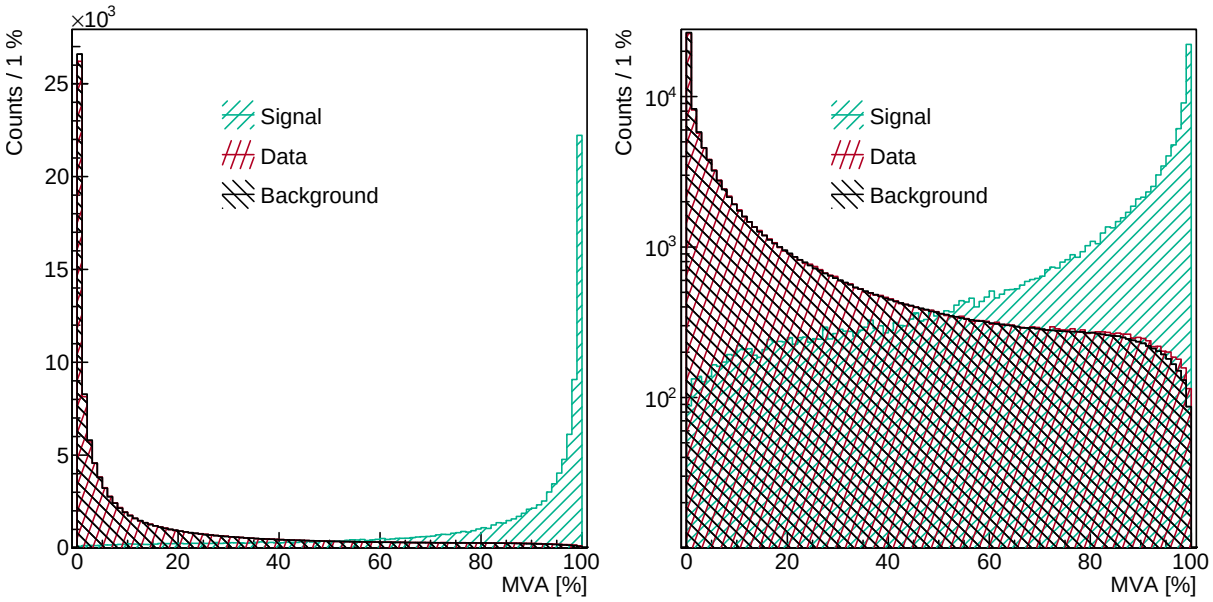

Figure 4.36.: ANN response distribution for the signal- (teal) and background (black) samples used for training and testing of the ANN as well Λ-π^- combinations from real events (red) in linear (left) and logarithmic (right) representation.

The lower panel of Figure 4.35 shows the distributions of the training samples after the pre-selection criteria are applied. It is observed that the discrimination power of the parameters MotVD and MTD is significantly increased while it remains rather similar for the remaining parameters. On the other side the background distribution of the parameter Dau2VD shows again a peak-like structure resulting from the strong correlations between the parameters and the criterion VDX $>$ 25 mm. Due to the higher amount of energy released in the decay of Ξ^- hyperons, it is however less pronounced than in case of the Λ hyperons.

Using the trained ANN, the response parameter (MVA) distributions shown in Figure 4.36 are obtained for the two training samples as well as experimental Λ-π^- pairs. As for the Λs, the K^0_S and the ${}^3_\Lambda H$ a very strong separation of the signal and background sample is observed which indicated a successful training of the ANN. Furthermore, again a strong accordance between the background and data distribution can be observed. At values close to 1 the data distribution shows even a slight excess over the background distribution, however, unlike as for the Λ hyperons or K^0_S mesons this excess does not peak at 1 which is why it is questionable wether it comes from actual Ξ^- hyperon decays.

Concerning the reconstruction of Ξ^- hyperons the so called Look-Elsewhere-Effect [99] needs to be considered. It is a consequence of statistical fluctuations that if only enough variations are tested, a significant fluctuation can be found at any position. The total amount of 15 variable selection criteria makes the reconstruction of Ξ^- hyperons especially vulnerable to this effect. Therefore, in the following section constraints on some criteria are used to reduce the amount of accessible variations. Furthermore, only signals exceeding a significance, defined by Equation 4.3, of 5 are assumed to be real. This reduces the probability of falsely identifying a statistical fluctuation as signal to about 1:1,750,000.

4.5.2. Production Rate Estimation

In the scope of this project, numerous attempts to reconstruct a Ξ^- signal using multiple different approaches have been taken. These approaches include for example variations of the OVD (pre-)selection criteria for both the Λ as well as the Ξ^- decay, tagging of events including at least one Kaon and variations of the analyzed centrality range. Unfortunately, none of them resulted in a signal exceeding the significance threshold of 5. Therefore, it is concluded that no Ξ^- hyperon signal could be reconstructed and an estimation of the upper limit of its production rate is performed as described in the following.

In the first step, the selection criteria sets to be used for the upper production limit estimation need to be determined. Unlike for Λs, K^0_S or ${}^3_\Lambda H$, these cannot be determined by optimizing the significance of the reconstructed signal. Instead, simulated Ξ^- hyperons embedded into experimental data are used. From previous iterations of the upper limit estimation it is known that its order of magnitude amounts to 8×10^{-5} Ξ^- hyperons per event. Using this rate in combination with the acceptance and efficiency correction factors obtained from simulated Ξ^- hyperons and the amount of analyzed events, the expected amount of signal counts is calculated. An according amount of reconstructed simulated

Parameter	**Pre**	**Set1**	**Set2**	**Set3**	**Set4**	**Set5**	**Set6**	**Set7**	**Set8**
Dec1Dau1VD [mm]	> 4	> 4				> 6	> 7	> 7	> 7
Dec1Dau2VD [mm]	> 14	> 15				> 16	> 16	> 16	> 17
Dec1MotVD[1] [mm]	< 16	< 15				< 16	< 16	< 16	< 16
Dec1VDX [mm]	> 45	> 45				> 70	> 66	> 71	> 65
Dec1MTD [mm]	< 20	< 20				< 10	< 8	< 7	< 7
Dec1A [°]	> 15								
Dec1MVA [%]	—	> 76				> 8	> 10	> 10	> 10
m_Λ [MeV/c^2]	± 7.5	1110 - 1120							
Dec2Dau1VD[1] [mm]	> 2	> 4	> 5	> 5	> 5	> 3	> 5	> 5	> 5
Dec2Dau2VD [mm]	> 8	> 11	> 16	> 15	> 12	> 13	> 15	> 15	> 11
Dec2MotVD [mm]	< 14	< 10	< 5	< 5	< 10	< 6	< 5	< 5	< 5
Dec2VDX [mm]	> 25	> 25	> 44	> 43	> 25	> 25	> 46	> 42	> 25
Dec2MTD [mm]	< 20	< 15	< 8	< 7	< 11	< 15	< 8	< 8	< 10
Dec2A [°]	> 15								
Dec2MVA [%]	—	> 97	—	> 80	> 90	> 98	—	> 80	> 90

[1]Note that the parameters Dec1MotVD and Dec2Dau1VD are identical!

Table 4.12.: The nine selection criteria sets used for the reconstruction of Ξ^- hyperons.

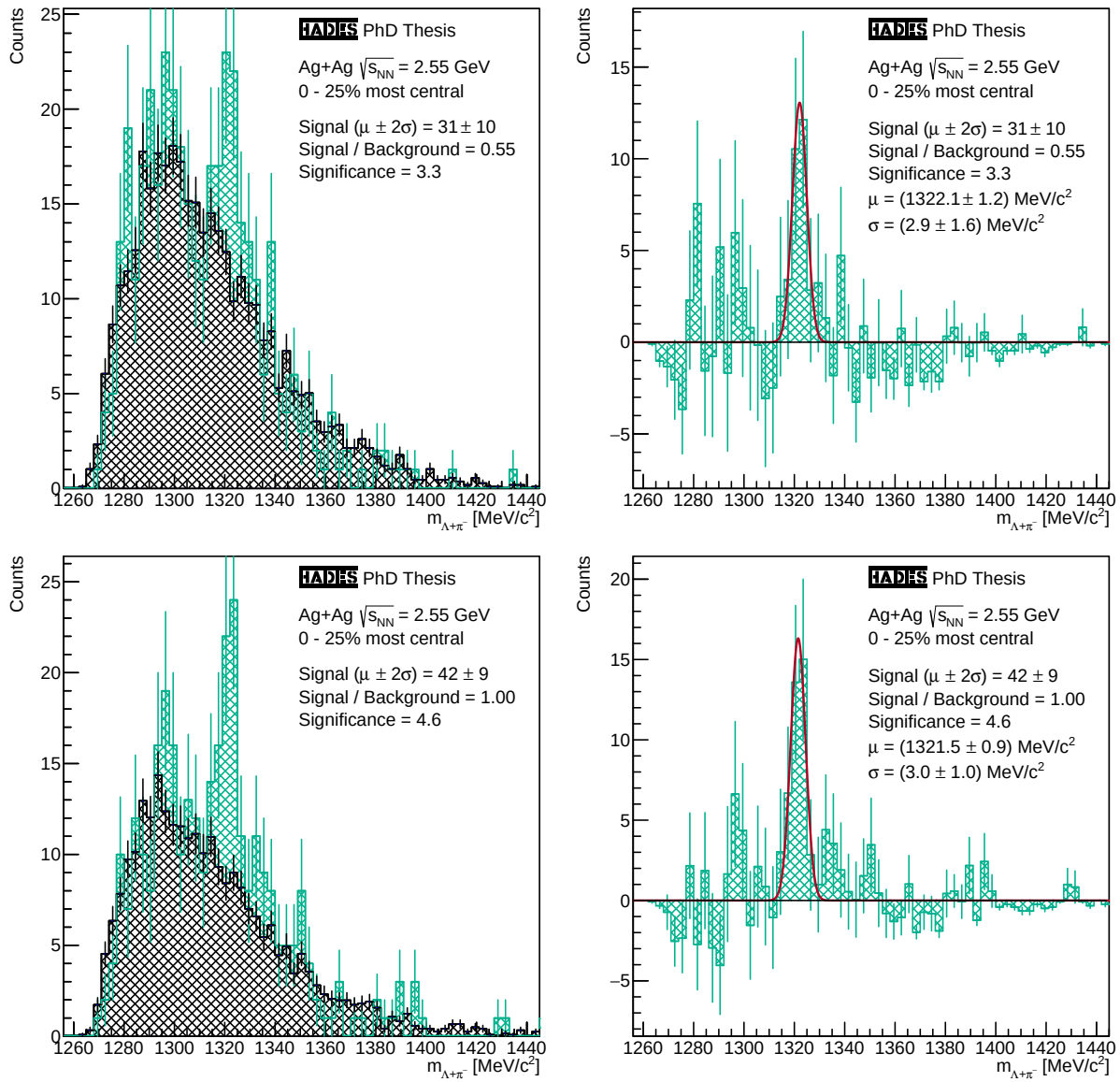

Figure 4.37.: Invariant mass distribution of Λ-π^- pairs from the 0-25 % most central Ag(1.58A GeV)+Ag events after application of the full Ξ^- reconstruction method before (left) and after (right) subtraction of the mixed-event combinatorial background for selection criteria set 1 (upper panel) and set 5 (lower panel).

Ξ^- hyperons is then added to the scaled mixed-event background spectrum to obtain an estimate for the data spectrum under the assumed production rate. The simulated Ξ^- hyperons are added to the scaled mixed-event background spectrum instead to the data spectrum to counter the large statistical fluctuations and potential Ξ^- signals below the significance threshold. Using these estimated proxy data spectra, the selection criteria optimization is performed like for the Λs, K^0_S and ${}^3_\Lambda$H in an iterative procedure maximizing the significance of the signal.

To avoid the potentially critical Look-Elsewhere-Effect discussed in the previous section and to take systematic variations into account, in total eight selection criteria sets in addition to the pre-selection criteria, all listed in Table 4.12, are determined. The first four sets use the selection criteria optimized for the reconstruction of Λ hyperons in Section 4.2.1 to identify the Λ hyperons and only optimize the criteria related to the Ξ^- decay. The first set is obtained by optimizing all selection criteria including the ANN response criterion, while the second, third and fourth one keep the ANN response criterion fixed. In the second set, the ANN response criterion is not used at all, in the third set a medium criterion of > 80 % and in the fourth set a strong criterion of > 90 % is applied. The > 80 % criterion is much weaker than the > 90 % one, since the ANN response parameter distribution of signals rises faster than exponentially towards 100 % as shown in Figure 4.36.

In case of the fifth through eighth selection criteria set, also the selection criteria used to identify Λ hyperons are optimized with respect to the obtained Ξ^- signal. Again, the fifth set is obtained by optimizing all selection criteria including the ANN response criterion, while the sixth, seventh and eighth one keep the ANN response criterion fixed. In the sixth set, the ANN response criterion is not used at all, in the seventh set a medium criterion of > 80 % and in the eighth set a strong criterion of >90 % is applied. These four optimization procedures are exceptionally vulnerable to the Look-Elsewhere-Effect as the doubled amount of optimized criteria results in a squared amount of possible variations.

Examining the optimized selection criteria, one observes that stronger criteria on the ANN response parameter of the Ξ^- decay allow for weaker criteria on the remaining parameters which further indicates that the ANN is working as intended. Surprisingly, the criteria sets for which also the Λ parameters are optimized favorite weak criteria on the ANN response parameter of the Λ decay of around 10 % which still strongly suppress the combinatorial background since Figure 4.7 shows that its distribution rises faster than exponentially towards responses of 0 %. However, this also indicates that a non-negligible amount of Λ hyperons from Ξ^- decays is rejected by the ANN of the Λ decay, which might serve as a staring point for further investigations.

Figure 4.37 shows the invariant mass distributions of Λ-π^- pairs from the 0-25 % most central Ag(1.58A GeV)+Ag events before (left) and after (right) subtraction of the normalized mixed-event background for selection criteria set 1 (upper panel) and set 5(lower panel). In both cases, the data distribution shows a peak-like structure around the nominal mass of Ξ^- hyperons of ≈ 1322 MeV/c^2 which are probably actual Ξ^- hyperons. Unfortunately, none of these structures exceeds the required confidence threshold of a significance above 5 which is why some uncertainty wether the signals are real remains. The Gaussian functions fitted to the spectra after subtraction of the background prove the correct position of the structures. Due to the high statistical uncertainties of the data points, the statistical uncertainties of the determined widths are large which significantly reduces their relevance.

$$S_{max} = \frac{Thres^2}{2} + \sqrt{\frac{Thres^4}{4} + Thres^2 B} \tag{4.9}$$

Like in [161, 170], the actual determination of the upper production limits is based on the Feldman-Cousins approach [86]. First, it is calculated how many signal counts could be present in a defined region of the invariant mass spectrum without exceeding a given threshold. In this work, as stated before, a significance of 5 is used as threshold. The corresponding maximum amount of signal counts is calculated via Equation 4.9 with the threshold $Thres$ and the amount of background counts in the relevant region B.

Selection Criteria	**Upper Production Limit / Event**	**4π Yield / Event**
Set 1	$(0.63 \pm 0.13) \times 10^{-4}$	$(0.37 \pm 0.12) \times 10^{-4}$
Set 2	$(0.67 \pm 0.14) \times 10^{-4}$	$(0.40 \pm 0.12) \times 10^{-4}$
Set 3	$(0.67 \pm 0.14) \times 10^{-4}$	$(0.38 \pm 0.12) \times 10^{-4}$
Set 4	$(0.67 \pm 0.14) \times 10^{-4}$	$(0.37 \pm 0.13) \times 10^{-4}$
Set 5	$(0.42 \pm 0.09) \times 10^{-4}$	$(0.37 \pm 0.08) \times 10^{-4}$
Set 6	$(0.46 \pm 0.09) \times 10^{-4}$	$(0.29 \pm 0.09) \times 10^{-4}$
Set 7	$(0.45 \pm 0.09) \times 10^{-4}$	$(0.35 \pm 0.09) \times 10^{-4}$
Set 8	$(0.46 \pm 0.09) \times 10^{-4}$	$(0.34 \pm 0.09) \times 10^{-4}$

Table 4.13.: Upper limits on Ξ^- production rate for the 0-25 % most central Ag(1.58A GeV)+Ag events using the different selection criteria sets and 4π yields obtained under the assumption that the peak-like structures in the invariant mass spectra are actual Ξ^- decays.

Next, the production rates corresponding to these maxima on the signal counts are calculated using the amount of analyzed events as well as acceptance and efficiency values averaged over the entire phase-space. Therefore, Equation 4.10 is used in combination with Ξ^- hyperons generated with an effective temperature of 105 MeV by the Pluto event generator and embedded into experimental data by the method described in Section 2.3.4. Finally, as a cross-check, an according amount of simulated Ξ^- hyperons is added to the normalized mixed-event background and it is checked wether the required significance threshold is actually exceeded.

$$BR_{\Xi^-} \cdot a_\Lambda \cdot a_{\pi^-} \cdot \epsilon_\Lambda \cdot \epsilon_{det,\pi^-} \cdot \epsilon_{rec,\pi^-} \cdot \epsilon_{sel,\pi^-} \cdot \epsilon_{OVD,\Xi^-} = \frac{N^{sim}_{rec,\Xi^-}}{N^{sim}_{gen,\Xi^-}} \tag{4.10}$$

The finally obtained upper limits for the Ξ^- production rate from the 0-25 % most central Ag(1.58A GeV)+Ag events are listed in Table 4.13 for the various selection criteria sets. Furthermore, the 4π yields obtained under the assumption that the structures observed in the invariant mass spectra are actual signals, are listed too. The total upper limit on the production rate of Ξ^- hyperons amounts to 0.81×10^{-4} Ξ^- hyperons per event which is significantly below the upper limit determined in [170] for Au(1.23A GeV)+Au collisions. Using only the four latter selection criteria sets it lies again significantly lower at 0.55×10^{-4} Ξ^- hyperons per event. These results are supported by the determined 4π yields which are averaged to a final value of $(0.36 \pm 0.11) \times 10^{-4}$ Ξ^- hyperons per event and thereby below the determined upper production limits. In Chapter 5 the results are put in context with theoretical predictions and previous measurements.

5. Interpretation of the Results

In this chapter, the results of the different particle analyses described in Chapter 4 are put to context and confronted with previous measurements and world data. In Section 5.1 the measured (Λ+Σ^0) and K^0_S production rates are used to estimate the production rates of the unmeasured Σ hyperons utilizing the conservation of strangeness under the strong interaction. In Section 5.2 the mid-rapidity yields of Λ hyperons and K^0_S mesons as well as the ratio between the production rates of Ξ^- and Λ+Σ^0 hyperons are put in context with world data from lowest to highest energy available in particle collisions. In Section 5.3 the universal scaling of the production rates of strange hadrons with $\langle A_{\mathrm{Part}} \rangle$ observed in [18] for Au(1.23A GeV)+Au collisions is revisited using the production rates obtained for Ag(1.58A GeV)+Ag collisions. In Section 5.4 the longitudinal anisotropy of the fireball, arising from the nucleons of the colliding nuclei not being fully stopped in the reaction zone, is investigated. In Section 5.5 the kinematic distributions of protons and Λ hyperons are compared to determine differences due to the strange-quark contained in the Λ hyperons. Finally, in Section 5.6 the ${}^3_\Lambda$H lifetime obtained in Section 4.4.2 is compared to previous measurements at various energies and collision systems.

5.1. Strangeness Balance

As already discussed in Section 1.3.2, the conservation of strangeness under the strong interaction results in the strangeness-balance equation 1.5. With only minor approximations this relation allows to estimate the production rates of Σ^+, Σ^0 and Σ^- hyperons from the measured production rates of Λ hyperons and K^0_S mesons as described in the following.

First, the production of multi-strange hyperons and anti-kaons are disregarded as their high energetic thresholds result in low production rates: $M(\Xi) \approx M(\Omega) \approx M(\overline{K}) \approx 0$. This results in the strangeness-balance equation 5.1:

$$M(\Lambda) + M\left(\Sigma^+\right) + M\left(\Sigma^0\right) + M\left(\Sigma^-\right) = M\left(K^+\right) + M\left(K^0_S\right) + M\left(K^0_L\right) \tag{5.1}$$

Since the wave functions of K^0_S and K^0_L mesons differ only in the signs of the contained quark states, their production rates are equal assuming CP-symmetry: $M(K^0_S) \approx M(K^0_L)$. The initially colliding heavy-ions contain more neutrons than protons and therefore more down- than up-quarks. This so called isospin asymmetry results in the production of hadrons involving down-quarks being more likely than the production of similar hadrons involving up-quarks. The effect on the production rates can be approximated by scaling the rates with the respective amounts of down-quarks N_d and up-quarks N_u in the collision system. However, this disregards that down- and up-quarks are also produced via pair-production and any further non-linear effects as well as fluctuations. In the analyzed collisions of ^{107}Ag ions with either ^{107}Ag or ^{109}Ag nuclei, the average amount of down-quarks in the most central collisions amounts to $N_d \approx 168$ and the average amount of up-quarks to

$N_u \approx 154.5$. For the kaons the isospin asymmetry leads to the relation $M(K^+)/N_u \approx M(K^0)/N_d$ and for the Σs to the relation $M(\Sigma^+)/N_u^2 \approx M(\Sigma^0)/N_u/N_d \approx M(\Sigma^-)/N_d^2$.

The isospin asymmetry approximation can be tested using the measurement of K^0_S mesons from Section 4.3 and the measurement of K^+ mesons from [122]. Therefore, the ratio $M(K^+)/2M(K^0_S)$ is compared to the ratio N_u/N_d. Due to their positive charge, the K^+ mesons are repulsed electromagnetically from the fireball in contrast to the neutrally charged K^0_S mesons. This results in a broader rapidity distribution which is shown in Figure 5.1. The different width results in different systematic effects in the extrapolation to the full phase-space which strongly depends on the model chosen for the extrapolation. To circumvent this problem, in Table 5.1 not the fully extrapolated 4π yields of the K^0_S and K^+ mesons, but their yields at mid-rapidity are compared. In the class of the 0-10 % most central Ag(1.58A GeV)+Ag events, the isospin asymmetry relation is perfectly fulfilled. In the more peripheral centrality classes of the 10-20 and 20-30 % most central Ag(1.58A GeV)+Ag events, the $M(K^+)/2M(K^0_S)$ rises and significantly exceeds the N_u/N_d ratio. Therefore, the production rates calculated for these centrality classes in the following have to be understood as rough estimates of the actual rates.

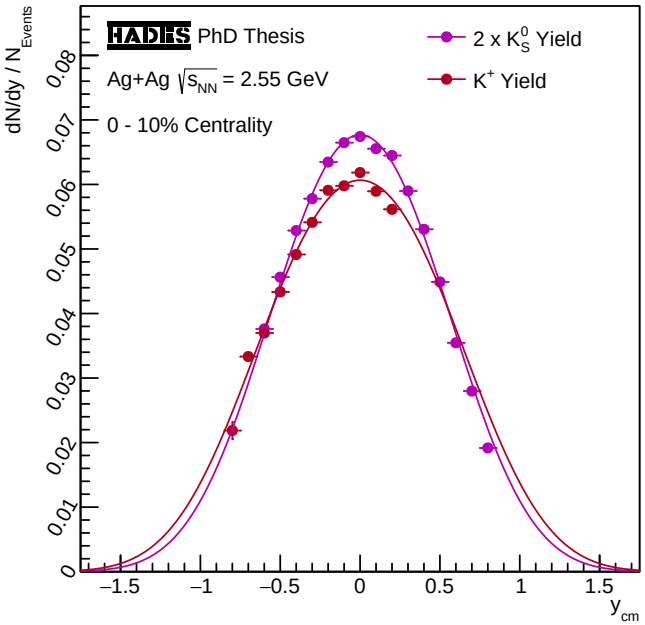

Figure 5.1.: Rapidity spectrum of K^0_S mesons scaled with 2 in comparison to the rapidity spectrum of K^+ mesons from the 0-10 % most central Ag(1.58A GeV)+Ag events. The K^0_S data are taken from Section 4.3.3 and the K^+ data are preliminary results from [122]. Only statistical uncertainties are shown.

Centrality	**Mid-Rapidity Yield / 10^{-2}**		**K^+ / 2 K^0_S**	**N_u / N_d**
	K^0_S [4.3]	**K^+ [122]**		
0-10 %	3.37 ± 0.02	6.18 ± 0.03	0.92 ± 0.01	0.92
10-20 %	1.97 ± 0.01	3.77 ± 0.02	0.96 ± 0.01	
20-30 %	1.17 ± 0.01	2.39 ± 0.01	1.02 ± 0.01	

Table 5.1.: Mid-Rapidity yields of K^0_S mesons from Section 4.3 and K^+ mesons from [122] to test the isospin asymmetry approximation used in this section.

Using the discussed relations, the production rates of Λ, Σ^+, Σ^0 and Σ^- hyperons can be calculated via Equations 5.2 to 5.5 from the combined production rate of Λ and Σ^0 hyperons $M(\Lambda+\Sigma^0)$ measured in Section 4.2 and the production rate of K^0_S mesons $M(K^0_S)$

measured in Section 4.3. Again, the full 4π production rates of K^+ mesons are not used due to the potential problems arising from the electromagnetic repulsion of the fireball. The results are summarized by Table 5.2 showing the production rates of the various hadrons as well as the ratio between Σ^0 and Λ hyperons for the three analyzed centrality classes of the 0-30 % most central Ag(1.58A GeV)+Ag collisions.

$$M(\Lambda) = \left(\frac{N_d N_u}{N_d^2 + N_u^2} + 1\right) M\left(\Lambda + \Sigma^0\right) - 2\frac{N_d N_u}{N_d^2 + N_u^2}\left(\frac{N_u}{N_d} + 1\right) M\left(K_S^0\right) \tag{5.2}$$

$$M\left(\Sigma^+\right) = \frac{N_u^2}{N_d^2 + N_u^2} \cdot \left(2\left(\frac{N_u}{N_d} + 1\right) M\left(K_S^0\right) - M\left(\Lambda + \Sigma^0\right)\right) \tag{5.3}$$

$$M\left(\Sigma^0\right) = \frac{N_d N_u}{N_d^2 + N_u^2} \cdot \left(2\left(\frac{N_u}{N_d} + 1\right) M\left(K_S^0\right) - M\left(\Lambda + \Sigma^0\right)\right) \tag{5.4}$$

$$M\left(\Sigma^-\right) = \frac{N_d^2}{N_d^2 + N_u^2} \cdot \left(2\left(\frac{N_u}{N_d} + 1\right) M\left(K_S^0\right) - M\left(\Lambda + \Sigma^0\right)\right) \tag{5.5}$$

Centrality	**Production Rates / 10^{-2}**				**Σ^0 / Λ[1]**
	Λ[1]	**Σ^+**	**Σ^0**	**Σ^-**	
0-10 %	10.09 ± 0.07	2.20 ± 0.02	2.39 ± 0.02	2.60 ± 0.02	0.24 ± 0.01
10-20 %	6.00 ± 0.04	1.36 ± 0.01	1.48 ± 0.01	1.61 ± 0.02	0.25 ± 0.01
20-30 %	3.47 ± 0.04	0.90 ± 0.01	0.98 ± 0.01	1.06 ± 0.01	0.28 ± 0.02

[1]Calculated yield of pure Λ hyperons without Σ^0 contribution.

Table 5.2.: Production rates of Λ, Σ^+, Σ^0 and Σ^- hyperons as well as the ratio between Σ^0 and Λ hyperons for the 0-30 % most central Ag(1.58A GeV)+Ag events. They are calculated using Equations 5.2 to 5.5 as well as the combined production rate of Λ and Σ^0 hyperons $M(\Lambda + \Sigma^0)$ measured in Section 4.2 and the production rate of K^0_S mesons $M(K^0_S)$ measured in Section 4.3. Statistical uncertainties are propagated according to the law of Gaus and systematic uncertainties are disregarded.

The calculated ratio between Σ^0 and Λ hyperons is rising slightly towards the more peripheral events. Using the preliminary 4π production rates of K^+ from [122] instead of the relation $M(K^+)/N_u \approx M(K^0)/N_d$ to estimate the K^+ production rate based on the K^0_S production rate even strengthens this effect since more K^+ than expected from the isospin asymmetry approximation are measured in particular in the more peripheral centrality classes. Although the systematic uncertainties of the method are quite large, there is also a physical effect to explain this observation: The strangeness-balance calculations do not take interactions between Σ hyperons and nucleons from the fireball into account. While free Σ hyperons cannot decay to Λ hyperons via the strong interaction due to the isospin conservation, Σ hyperons in a baryon-rich medium can be converted to Λ hyperons in

strong Σ + N processes. The corresponding channels are listed in Equation 5.6 for the three charge states of Σ hyperons. Because of charge conservation, the two charged Σ states have only one available channel while the neutral Σs have two. Thus, the effect is stronger for Σ^0 hyperons than for Σ^+ or Σ^- hyperons. Furthermore, the effect is stronger for central than for peripheral events as Σ hyperons produced in central events traverse a larger medium and are therefore more likely converted to Λ hyperons which would explain the rise of the ratio between Σ^0 and Λ hyperons towards peripheral events.

$$\begin{aligned} &\Sigma^+: && \Sigma^+ + n \rightarrow \Lambda + p \\ &\Sigma^0: && \Sigma^0 + n \rightarrow \Lambda + n \quad \text{and} \quad \Sigma^0 + p \rightarrow \Lambda + p \\ &\Sigma^-: && \Sigma^- + p \rightarrow \Lambda + n \end{aligned} \tag{5.6}$$

Further investigations of the production of Σ hyperons are required since the strangeness-balance calculations do not take all relevant effects into account and are therefore error-prone. Furthermore, at the moment the conducted approximation of isospin asymmetry effect is only for the 0-10 % most central events consistent with the measured yields of K^0_S and K^+ mesons. In [61], the reconstruction of the Σ^0 hyperon is attempted via its decay channel $\Sigma^0 \rightarrow \Lambda + \gamma$, using the new electromagnetic calorimeter to detect the γ. Furthermore, the Compressed Baryonic Matter (CBM) experiment, which is currently under development and will be used to study heavy-ion collisions at the FAIR facility, will allow to reconstruct Σ^+ and Σ^- hyperons via the missing-mass method.

5.2. Energy Excitation Functions

The presented excitation functions describe the dependence between an observable and the average energy available in binary NN collisions $\sqrt{s_{NN}}$ and are therefore an important tool to study the production of particles and compare the obtained results with world data. Figure 5.2 shows the yields of Λ hyperons (blue) and K^0_S mesons (magenta) at mid-rapidity measured by various experiments in central Au+Au (HADES, E895, E891, STAR and PHENIX) or Pb+Pb (NA49, NA57, WA97 and ALICE) collisions. Since the Ag+Ag collision system analyzed in this work is significantly smaller, the obtained yields are scaled using the average amount of nucleons participating in the collision $\langle A_{Part} \rangle$. For the 0-10 % most central Ag(1.58A GeV)+Ag collisions it amounts to 160.9 (cf. Section 3.5) and for the 0-10 % most central Au(1.23A GeV)+Au collisions to 303.0 [16]. Furthermore, as it will be shown in Section 5.3, the yields of strange hadrons scale stronger than linear with $\langle A_{Part} \rangle$. For both Ag(1.58A GeV)+Ag and Au(1.23A GeV)+Au the scaling is well described by $\langle A_{Part} \rangle^{1.45}$ which is why the Ag(1.58A GeV)+Ag yields in Figure 5.2 are scaled by $(303.0/160.9)^{1.45}$. However, it is to note that due to participant spectator interplays a smaller collision system does not necessarily probe the same physics like non-central events in a larger collision system. This becomes obvious if effects like for example azimuthal anisotropies (flow) are taken into account.

Unfortunately, there are no data on the production of K^0_S mesons in large collisions systems below $\sqrt{s_{NN}}$ =7.7 GeV available besides the Au(1.23A GeV)+Au data measured by HADES. The yields of the Λ hyperons however line up very well with the trend observed by other experiments conducted in the low energy region. Once published, the data from Au+Au collisions at $\sqrt{s_{NN}} = 3$ GeV measured by STAR will contribute further to this region [181].

Another effect which can be observed in Figure 5.2 is the baryon-dominance at low energies and the meson-dominance at high energies. While at low energies, the associative production of Λs and Kaons described by Equation 1.7 results in significantly more Λ hyperons than K^0_S mesons, its relative contribution decreases with increasing energy due to the vanishing amount of nucleons remaining in the collision zone. At the same time the pair production of Kaons increases which results in the K^0_S mesons becoming more abundant than Λ hyperons at $\sqrt{s_{NN}} \gtrapprox 10$ GeV.

Figure 5.3 shows the ratio between the production rate of Ξ^- hyperons and the combined rate of Λ and Σ^0 hyperons in dependence of $\sqrt{s_{NN}}$ measured by various experiments. As Ξ^- data are rare also data from smaller collision systems are taken into account this time. The full marker symbols correspond to measurements in "nucleus-nucleus" (A+A) collision systems and the open marker symbols to measurements in proton-induced (p+X) collision systems. For HADES, the yields measured in p(3.5 GeV)+Nb [35], Ar(1.76A GeV)+KCl [30] and Ag(1.58A GeV)+Ag (cf. Section 4.5) collisions are depicted. Furthermore, the upper limits on the Ξ^- production rate from Au(1.23A GeV)+Au [170] and Ag(1.58A GeV)+Ag (cf. Section 4.5) collisions are depicted too. For the STAR 3 GeV data point the (Λ+Σ^0) yield is estimated based on E895 and HADES data. The black arrows depict the production thresholds for Λ and Ξ^- hyperons in binary NN collisions.

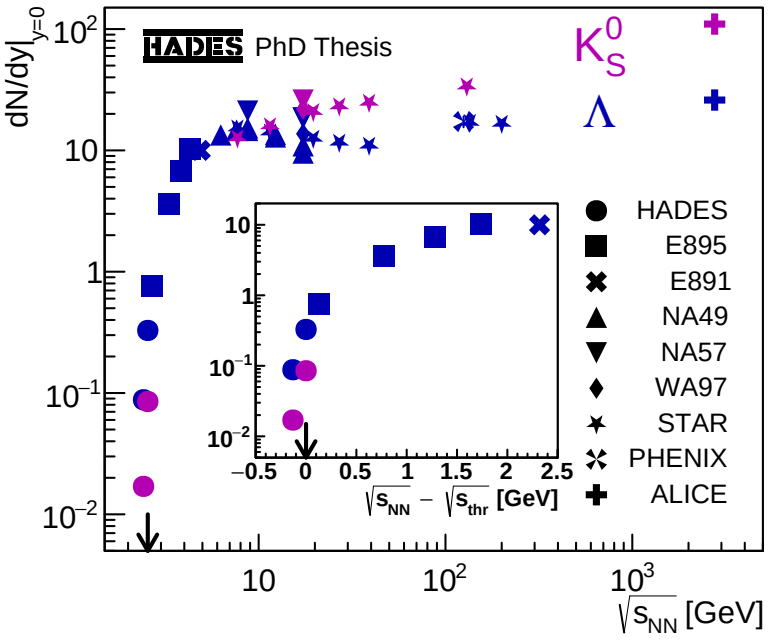

Figure 5.2.: Production rates of Λ hyperons (blue) and K^0_S mesons (magenta) at mid-rapidity in dependence of $\sqrt{s_{NN}}$ measured by various experiments in heavy-ion collisions. The original version of this plot is taken from [18] and the data are from: HADES [18], E895 [146], E891 [41], NA49 [42, 48], NA57 [50, 51, 52], WA97 [43, 49], STAR [14, 25, 28, 29], PHENIX [26] and ALICE [8]. Furthermore, the production rates measured in Sections 4.2 and 4.3 are depicted. To be comparable to the other data points from either Au+Au or Pb+Pb collisions, the Ag+Ag results are scaled to the size of Au+Au collisions - See the text for details. The arrows on the x-axes depict the threshold energy of strangeness production in binary NN collisions. All data points show only statistical uncertainties.

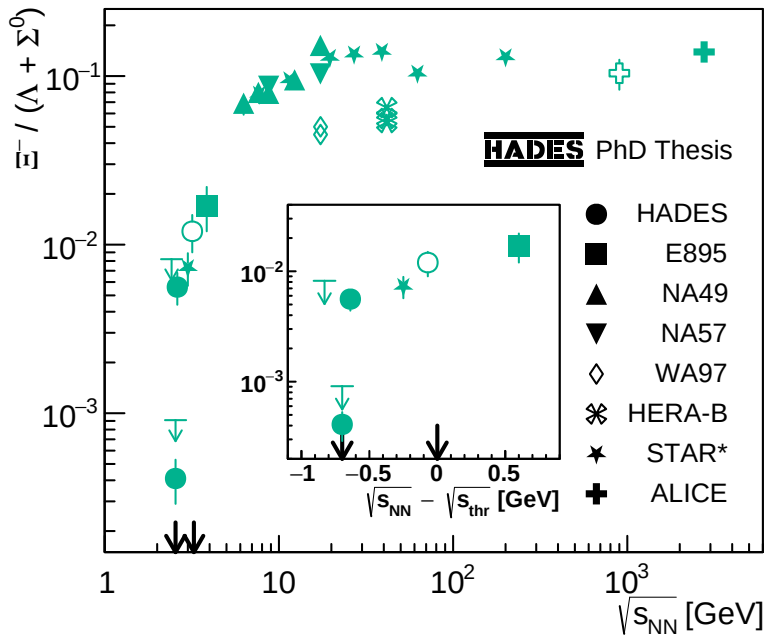

*For the STAR 3 GeV data point the (Λ+Σ^0) yield is estimated based on E895 and HADES data, thus the large uncertainty.

Figure 5.3.: Ratios between the production rates of Ξ^- and Λ+Σ^0 hyperons in dependence of $\sqrt{s_{NN}}$ measured by various experiments. The full markers correspond to "nucleus-nucleus" collision systems and the open markers to "proton-anything" collision systems. The original version of this plot is taken from [35] and the data are from: HADES [30, 35, 170], E895 [80], NA49 [42], NA57 [50], WA97 [52], HERA-B [37], STAR [7, 14, 25, 39] and ALICE [4, 8, 9]. Furthermore, the upper limit and production rate determined in Section 4.5 are depicted. The arrows on the x-axes depict the threshold energies of the production of Λ and Ξ^- hyperons in binary NN collisions. All data points show only statistical uncertainties.

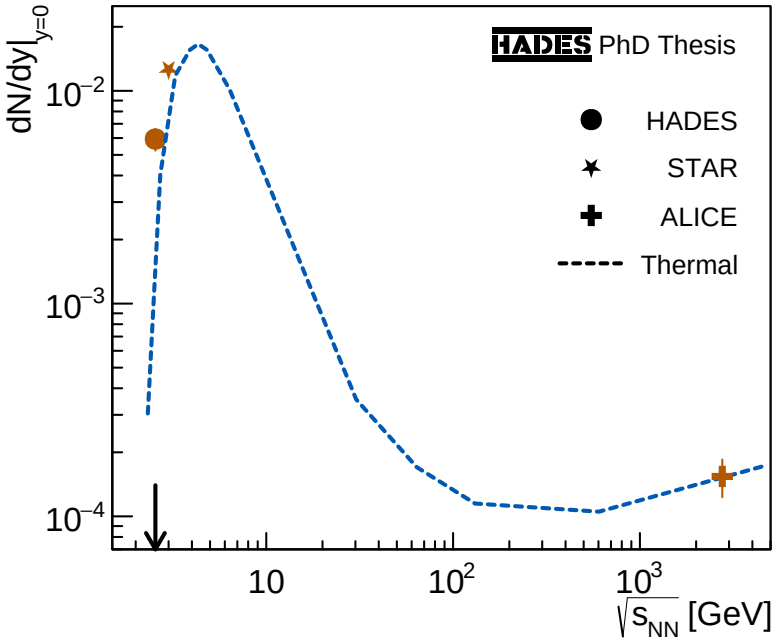

Figure 5.4.: Production rates of ${}^{3}_{\Lambda}$H at mid-rapidity in dependence of $\sqrt{s_{NN}}$ measured by STAR [6] and ALICE [12] in heavy-ion collisions. The production rate measured in Section 4.4 is depicted too. Again, they are scaled to the size of Au+Au collisions to be comparable to the other data points - See the text for details. All data points show only statistical uncertainties. The thermal model prediction is taken from [6] as well.

At the moment, below the free NN production threshold energy of Ξ^- hyperons only data measured by HADES are available and suggest a very steep rise of the excitation function. This trend is supported by the measurements of E895 [80], NA49 [42], NA57 [50] and in particular the estimated STAR 3 GeV data point [7]. The final (Λ+Σ^0) yields from Au+Au collisions at $\sqrt{s_{NN}} = 3$ GeV measured by STAR, once published, will allow for more conclusive results in this energy region.

Finally, the production rates of ${}^{3}_{\Lambda}$H at mid-rapidity measured by STAR in Au+Au and by ALICE in Pb+Pb collisions are shown in Figure 5.4. Furthermore, the production rates measured in this work are depicted scaled by the same method as for Λ hyperons and K^0_S mesons. However, as it will be shown in Section 5.3, the production of ${}^{3}_{\Lambda}$H scales much stronger with $\langle A_{Part} \rangle$. Furthermore, the ${}^{3}_{\Lambda}$H production is analyzed only for the 0-25 % most central events which is why the total scaling factor amounts to $(303.0/127.7)^{2.84}$. Furthermore, Figure 5.4 shows a thermal model prediction of the production rates taken from [6]. At low energies, the prediction slightly undershoots the measured production rates, however, the trend is well described.

Unfortunately, only very few data on the production of ${}^{3}_{\Lambda}$H in heavy-ion collisions in the fireball region are available. Thus, the excitation function of ${}^{3}_{\Lambda}$H which is of great interest as it is influenced by the production of hyperons, and the formation of light nuclei at the same time, is the least constrained one. Nevertheless, the three data points depicted in Figure 5.4 as well as the depicted thermal model prediction already reflect the most important aspects of the production of hypernuclei: Both the Λ hyperons as well as protons and neutron for it to bind with are required. At very low collision energies $\sqrt{s_{NN}}$ close to the threshold energy of hyperon production in binary NN collisions, the production rates of hypernuclei are limited by the production of Λ hyperons, since the created systems are baryon dominated and large amounts of protons and neutrons are available. Thus, in this energy region, the production rates of hypernuclei show a similar steep rise as the strange hadrons shown in Figure 5.2. At increased collision energies, the production rate of Λ hyperons rises, but the baryon dominance of the created systems ceases. Therefore, at

some point the production of hypernuclei becomes limited by the availability of protons and neutrons which is why the production rates reach a local maximum and start to drop. Once the baryochemical potential of the created system approaches 0, all baryons required for the formation of a hypernucleus are produced as baryon-antibaryon-pairs and the production rates reach a local minimum. At even higher collision energies, the increased amount of available energy boosts the production of baryon-antibaryon-pairs which results again in increasing hypernuclei production rates. All of the described effects be be observed in the thermal model prediction depicted in Figure 5.4.

Further data on the production of hypernuclei are required to determine for example the collision energy at which the maximum production rates of hypernuclei are achieved. In particular the upcoming CBM experiment at the FAIR facility will allow to study heavy-ion collisions at beam energies of up to $\approx$ 10 GeV per nucleon [172] which corresponds to $\sqrt{s_{NN}} \approx 4.7$ GeV where high production rates of hypernuclei are expected.

5.3. Universal $\langle A_{Part} \rangle$ Scaling

One of the most astonishing results of the analysis of strange hadron production in Au(1.23A GeV)+Au collisions presented in [18] was that despite their different free NN production thresholds, Λ hyperons and K^0_S, K^+, K^- and ϕ mesons scale similar with $\langle A_{Part} \rangle$. Using fit functions of the form $Mult \propto \langle A_{Part} \rangle^{\alpha}$ to describe the dependence between the production rates and $\langle A_{Part} \rangle$, it was found that the production rates of these strange hadrons are well described by a common slope parameter α of 1.45 $\pm$ 0.06 [18].

Unfortunately, in case of the Au(1.23A GeV)+Au data only two data points of K^- and ϕ mesons with significant statistical uncertainties are available. The increased energy and increased amount of recorded events in case of the Ag(1.58A GeV)+Ag data allow to significantly decrease the systematic uncertainties in the measurement of K^- and ϕ mesons and thereby reinvestigate the universal scaling of the production rates of strange hadrons with $\langle A_{Part} \rangle$ with higher precision.

Figure 5.5 shows the production rates of Λ hyperons, K^0_S K^+ mesons and ${}^3_\Lambda H$ divided by $\langle A_{Part} \rangle$ in dependence of $\langle A_{Part} \rangle$. The values for $\langle A_{Part} \rangle$ correspond to the three centrality classes of the 0-30 % most central Ag+Ag collisions as determined in Section 3.5. The production rates of Λ hyperons are taken from Section 4.2, the rates of K^0_S mesons from Section 4.3 and the rates of ${}^3_\Lambda H$ from Section 4.4. The production rates of K^+ mesons are preliminary results from [122] provided by M. Kohls. Unfortunately, the production rates of K^- and ϕ mesons which are studied in the same work still show significant uncertainties and are therefore not shown. The boxes around the data points depict their systematic uncertainties. The depicted lines correspond to fit functions of the form $Mult \propto \langle A_{Part} \rangle^{\alpha}$.

The production rates of Λ hyperons and K^0_S, K^+ mesons are well described by a common slope α of 1.44 $\pm$ 0.03 similar to the observations from the Au(1.23A GeV)+Au data. Within their uncertainties, the common slopes obtained for Au(1.23A GeV)+Au and Ag(1.58A GeV)+Ag collisions are identical even though the higher $\sqrt{s_{NN}}$ in case of the Ag+Ag collisions. This indicates the production mechanism of strange hadrons in this energy regime being almost independent from the available energy in binary NN collisions. Furthermore, it is a sign that even though strange hadrons are produced at their free NN threshold energy in Ag(1.58A GeV)+Ag collisions, the predominant proportion of strange hadrons is still produced by collective effects.

In contrast, the production rates of ${}^3_\Lambda H$ which could not be measured in Au(1.23A GeV)+Au collisions show a significantly steeper trend as the other particle species with a slope α of 2.84 $\pm$ 0.32. This can be understood in the coalescence picture of light-nuclei production: First, a free Λ hyperon is produced which later binds with a proton and a neutron forming the ${}^3_\Lambda H$. In this case, the ${}^3_\Lambda H$ production scales not only with the production of Λ hyperons but in addition with the amount of available protons and neutrons. The steep rise of the yields towards central collisions further contradicts the production of ${}^3_\Lambda H$ primarily in projectile fragmentation reactions, already discussed in Section 4.4.3, as the amount of projectile fragments ceases towards central collisions. However, it is again to note that the production of hypernuclei in projectile fragmentation reactions was proposed by the HypHI collaboration for small collision systems [152] in contrast to the larger Ag+Ag collision system analyzed in this work.

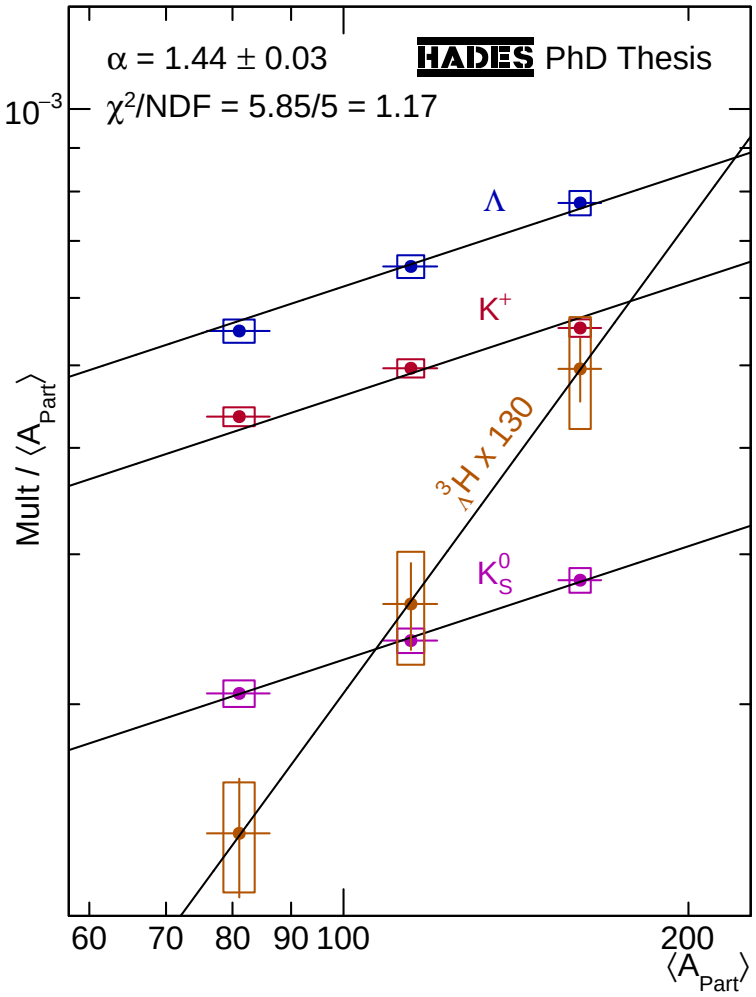

Figure 5.5.: Scaling of the production rates of Λ hyperons (cf. Section 4.2), K^0_S (cf. Section 4.3), K^+ mesons (Preliminary results from [122]) and ${}^3_\Lambda H$ (cf. Section 4.4) with $\langle A_{Part} \rangle$. The scaling of the production rates is quantified using $Mult \propto \langle A_{Part} \rangle^\alpha$ fit functions. In case of Λ hyperons, K^0_S and K^+ mesons it is well described by a common slope α of 1.44 ± 0.03. The ${}^3_\Lambda H$ production rates show a significantly steeper trend with an scaling parameter α of 2.84 ± 0.32.

To summarize, the observations fall in line with the Au(1.23A GeV)+Au measurements. However, as already discussed in Section 5.1, the production rates of Λ hyperons and K^0_S and K^+ mesons are strongly correlated due to the strangeness balance. Final data on the production of K^- and φ mesons will allow to draw more conclusions once they are available. The stronger scaling of the ${}^3_\Lambda H$ production is not unexpected but needs to be revised if production rates of further light-nuclei like deuterons, tritons or ^{3}He are measured.

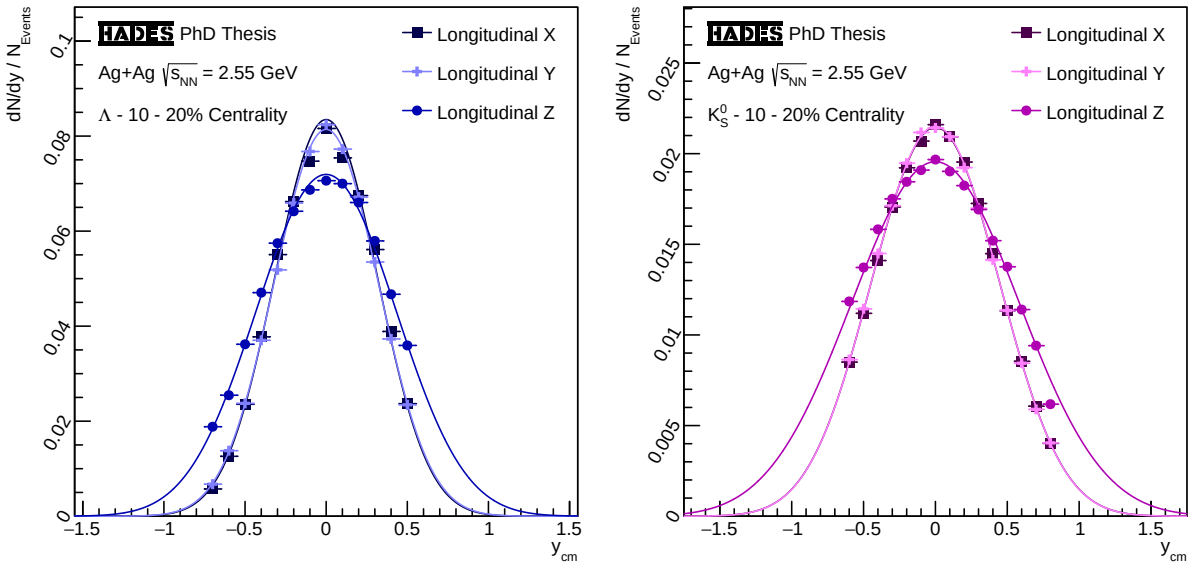

Figure 5.6.: Rapidity spectra of Λs (left) and K^0_S (right) from the 10-20 % most central Ag(1.58A GeV)+Ag events. The plots compare the obtained spectra for each of the three spacial coordinates as longitudinal one - See the text for details. For better visibility no systematic uncertainties are shown.

5.4. Longitudinal Anisotropy

In particle collisions, conventionally the z-coordinate is aligned parallel to the beam axis. Therefore the incident particles have only momentum in longitudinal (Z) but not transverse (XY) direction. Accordingly, the rapidity is conventionally defined based on the momentum of the particles in z-direction. While any momentum in transverse direction is generated by the radial expansion of the fireball, the momentum in longitudinal direction contains remnants of the initial momenta of the colliding nuclei as their nucleons are not fully stopped in the collision zone [53, 155]. This effect can be quantified by rotating the reference coordinate system. A rotation of $-\pi/2$ around the y-axis results in a coordinate system with the x-direction being the longitudinal one and a rotation of $\pi/2$ around the x-axis results in a coordinate system with the y-direction being the longitudinal one. In the following, this method is applied to the multi-differential analyses of Λ hyperons and K^0_S mesons to quantify the longitudinal anisotropy of the fireball.

Figure 5.6 shows the rapidity spectra of Λ hyperons (left) and K^0_S mesons (right) from the 10-20 % most central Ag(1.58A GeV)+Ag events obtained by running the full multi-differential analyses described in Sections 4.2.3 and 4.3.3 after rotation of the coordinate system around the y-axis ("Longitudinal X"), around the x-axis ("Longitudinal Y") and without rotation (default case - "Longitudinal Z"). In the following these three cases are referenced via their corresponding letter. Additionally, the plots show IS model functions (cf. Section 1.4) fitted to the spectra which are used to quantify their widths later on. For better visibility no systematic uncertainties are shown.

First of all, a strong accordance between the widths in x- and y-direction is observed which confirms the expected isotropy of the fireball in the transverse directions. Furthermore, for

both particles a larger width in z-direction is observed due to the additional contribution from the initial momenta of the colliding nucleons. Next, the widths σ of the rapidity spectra are quantified using the Gaussian approximation of the IS model functions defined by Equation 1.15. The resulting widths are displayed by Figure 5.7 in dependence of $\langle A_{Part} \rangle$ for x-direction (rectangles), y-direction (crosses) and z-direction (circles). The upper third shows the widths of the rapidity distributions of Λ hyperons, the middle third of K^0_S mesons and the lower third the ratios between the default longitudinal direction Z and the default transverse directions X and Y.

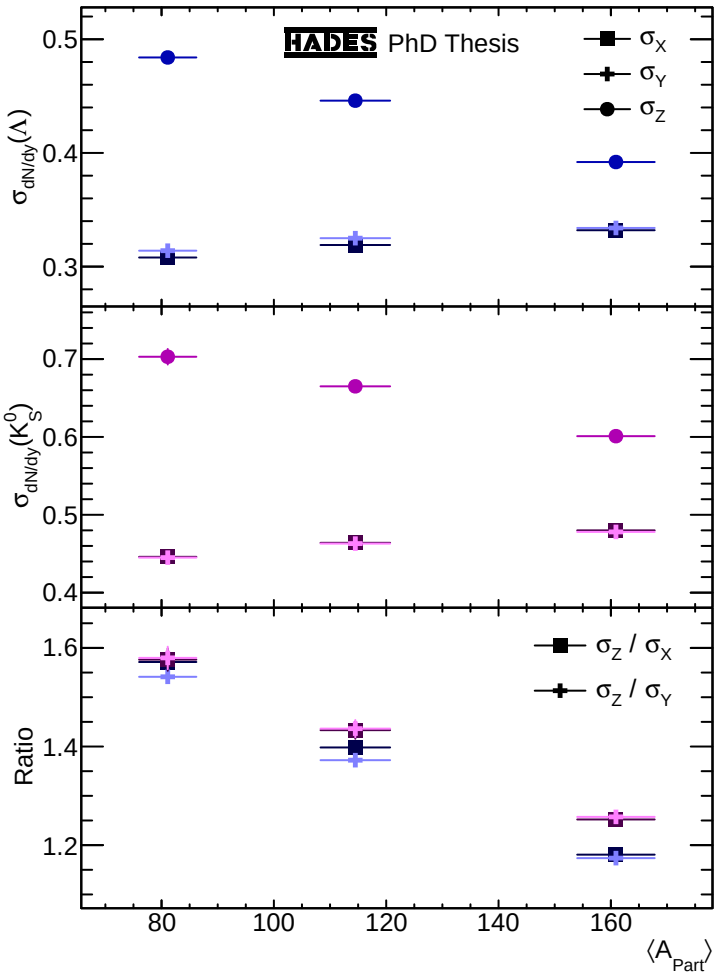

Figure 5.7.: Compilation of the widths determined for the different rapidity spectra of Λ hyperons (blue) and K^0_S mesons (magenta) in dependence of $\langle A_{Part} \rangle$ for the 0-30 % most central Ag(1.58A GeV)+Ag events.

Again, a strong accordance between the x- and y-direction is observed. Both show a slight increase with $\langle A_{Part} \rangle$ as a result from the increase of the effective temperature towards more central events which was already observed in Sections 4.2.3 and 4.3.3. On the other side, the widths in z-direction show an opposite trend significantly decreasing with increasing $\langle A_{Part} \rangle$. This is because in central events the increased amount of participating nucleons results in more NN reactions and thereby a higher degree of thermalization. Therefore, the nucleons are stopped stronger in central events which over-compensates the increase of the widths due to the effective temperature increase. The same effect is also observed in the ratios between the z-widths and x- or y-widths which show a strong decrease towards more central events.

Nevertheless, even in the 0-10 % most central collisions a full isotropic fireball with equal widths in all directions and a ratio of 1 is not reached. Linear extrapolations of the ratios reveal that theoretically at $\langle A_{Part} \rangle$ of 197 (Λ) / 223 (K^0_S) the fireball would be fully isotropic. This corresponds to the most central collisions possible which have an A_{Part} of 214. However, it is very challenging to measure such central collisions as their cross-section is very small. The observations fall in line with those made for Au(1.23A GeV)+Au collisions in [170, 171] and stress the need for phase-space distribution models including a longitudinal anisotropy like the ones described in Section 1.4.

5.5. Proton Λ Comparison

The comparison of the kinematic distributions of protons and Λ hyperons allows to gain more information on the production of strangeness. Both particles have a mass in the 1 GeV/c^2 region and both are the lightest hadron of their kind - The proton is the lightest baryon and the Λ is the lightest hyperon. Furthermore, at collision energies in the few GeV region, Λs are predominantly produced from protons or neutrons via the production channel given by Equation 1.7 as the pair-production is energetically almost impossible. Therefore, Λ hyperons can be assumed to have the same kinematic distributions like free protons besides effects due to the exchange of an up-quark by a strange-quark. In addition, the proton is affected by the coulomb repulsion of the fireball, however, this effect is only relevant at lowest transverse masses/momenta as shown for example in [139].

Figure 5.8 compares the mid-rapidity transverse mass spectra (left) and rapidity spectra (right) from the 0-10 % most central Au(1.23A GeV)+Au (upper panel) and Ag(1.58A GeV)+Ag collisions (lower panel) of Protons (red) and Λ hyperons (blue). The Au+Au Proton spectra are preliminary results from [175] and the Au+Au Λ spectra are from [18, 170] while the Ag+Ag spectra are obtained by the analyses described in Sections 4.1.2 and 4.2.3. To achieve the same orders of magnitude, the proton spectra are scaled to match the transverse integrated yield of the Λ hyperons at mid-rapidity. All spectra have an according SR model function (cf. Section 1.4) adjusted to them. The transverse spectra are adjusted using the method from [175] with a single effective temperature and blast for all spectra but in contrast to the method described in Section 4.1.2 no enforced symmetry of the scaling parameters C. The parameter values obtained by these transverse fits are listed in Table 5.3 with the first uncertainty being of statistic and the second one of systematic nature. The values listed for protons from Ag+Ag collisions differ slightly from the values listed in Table 4.3 because of the use of the transverse mass instead of the transverse momentum and the slight changes to the method. Within their uncertainties both sets of values are compatible.

In both collision systems the spectra of protons are described by very similar parameter values which are almost compatible within their uncertainties. In the Au+Au collision system, the effective temperature is slightly higher than in the Ag+Ag system while the blast is slightly lower. In Section 5.4 it showed that the effective temperature of the transverse spectra rises slightly with increasing $\langle A_{Part} \rangle$. Since $\langle A_{Part} \rangle$ of the 0-10 % most central Au(1.23A GeV)+Au collisions is almost twice as high as for the 0-10 % most central Ag(1.58A GeV)+Ag collisions (cf. [16] and Section 3.5), this might explain the effective

Au(1.23A GeV)+Au		
	T_{Eff} [MeV]	**β**
p	70 ± 1 ± 3	0.46 ± 0.01 ± 0.02
Λ	106 ± 1 ± 4	0.00 ± 0.01 ± 0.01

Ag(1.58A GeV)+Ag		
	T_{Eff} [MeV]	**β**
p	66 ± 1 ± 2	0.49 ± 0.01 ± 0.02
Λ	76 ± 1 ± 3	0.33 ± 0.01 ± 0.02

Table 5.3.: Summary of the SR model parameter values obtained in the analysis of Protons and Λ hyperons from Au(1.23A GeV)+Au and Ag(1.58A GeV)+Ag collisions.

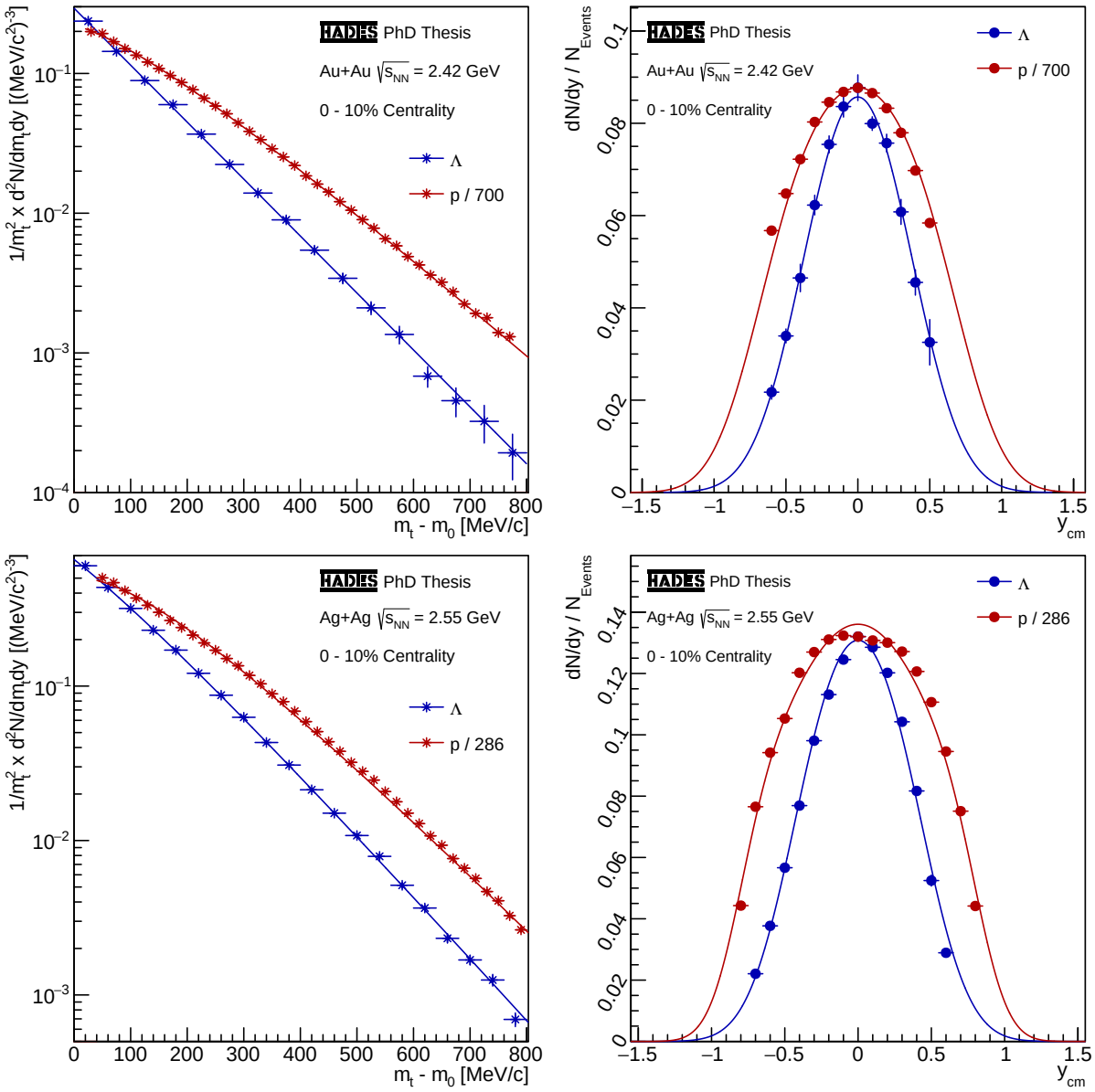

Figure 5.8.: Comparison of the mid-rapidity transverse mass spectra (left) and rapidity spectra (right) of Protons (red) and Λ hyperons (blue) from Au(1.23A GeV)+Au (upper panel) and Ag(1.58A GeV)+Ag collisions (lower panel). The Au+Au Proton spectra are preliminary results from [175] and the Au+Au Λ spectra are from [18, 170]. The Ag+Ag spectra are obtained by the analyses described in Sections 4.1.2 and 4.2.3. The Proton spectra are scaled to the transverse integrated yield of the Λ hyperons at mid-rapidity.

temperature difference. On the other side, the slightly higher collision energy in the Ag+Ag collisions might explain the increased blast as more energy for the radial expansion of the fireball is available. Unfortunately, clear conclusions are difficult since both effects interplay and the observed differences are close to the uncertainties of the measurement. Analyzing the emission of protons from Ag(1.23A GeV)+Ag collisions measured in the same campaign will allow for more conclusive interpretations.

The Λ hyperons on the other side show a much stronger difference between the two collision systems: While in Au(1.23A GeV)+Au collisions, their kinematic spectra are best described with a purely thermal model without any blast, in Ag(1.58A GeV)+Ag collisions a non negligible blast leads to the best description of the spectra. This can also be observed in Figure 5.8, where the Au+Au transverse mass spectrum at mid-rapidity of Λ hyperons shows a perfectly straight trend, while the corresponding Ag+Ag spectrum shows a clear curvature. In comparison with the proton spectra, the effective temperature of the Λ hyperons is however still significantly higher while their blast is lower. Similar observations were made at slightly higher collision energies at the AGS [79].

One possible interpretation of this observation assumes the fireball to have a non-constant density and temperature profile with a higher density and temperature in its center like for example stars. In that case, Λ hyperons, which are produced close to or even below their free NN threshold energy in the analyzed collisions, are more likely produced in the center region of the fireball. The protons on the other side are not newly produced which is why they are emitted from the entire volume of the fireball. Assuming a radial increasing blast for the fireball, which is reasonable considering that the center of the fireball has no defined radial direction, the effective temperature and blast measured for protons correspond to the entire fireball while the ones measured for Λ hyperons correspond only to a subvolume of it. This centralization of the production of strange hadrons would be stronger for Au(1.23A GeV)+Au than for Ag(1.58A GeV)+Ag collisions due to the lower amount of energy being available in average NN collisions explaining the differences in the measured effective temperature and blast.

This interpretation is also supported by the SHM model using canonical volumes to describe the conservation of strangeness at low energies. Only the intersection volume between a canonical volume and the fireball volume is relevant to the production of a further strange hadron balancing the strangeness quantum-number. As the canonical volumes are always smaller than the fireball volume, strange hadrons produced in the center of the fireball have the full canonical volume available. For strange hadrons produced in the outer regions of the fireball however, a part of the canonical volume lies outside of the fireball. Therefore, in the outer regions of the fireball the production of strange hadrons is stronger canonically suppressed than in the center region, effectively leading to the centralization of the production of strange hadrons discussed in the previous paragraph.

Again, the analysis of the production of Λ hyperons in Ag(1.23A GeV)+Ag collisions will allow to either approve or disprove the previous interpretations. Furthermore, the HADES collaboration plans to conduct a beam energy scan of Au(0.8A GeV)+Au, Au(0.6A GeV)+Au, Au(0.4A GeV)+Au and Au(0.2A GeV)+Au collisions to gain more information on the correlations between the emission/production of particles at low energies.

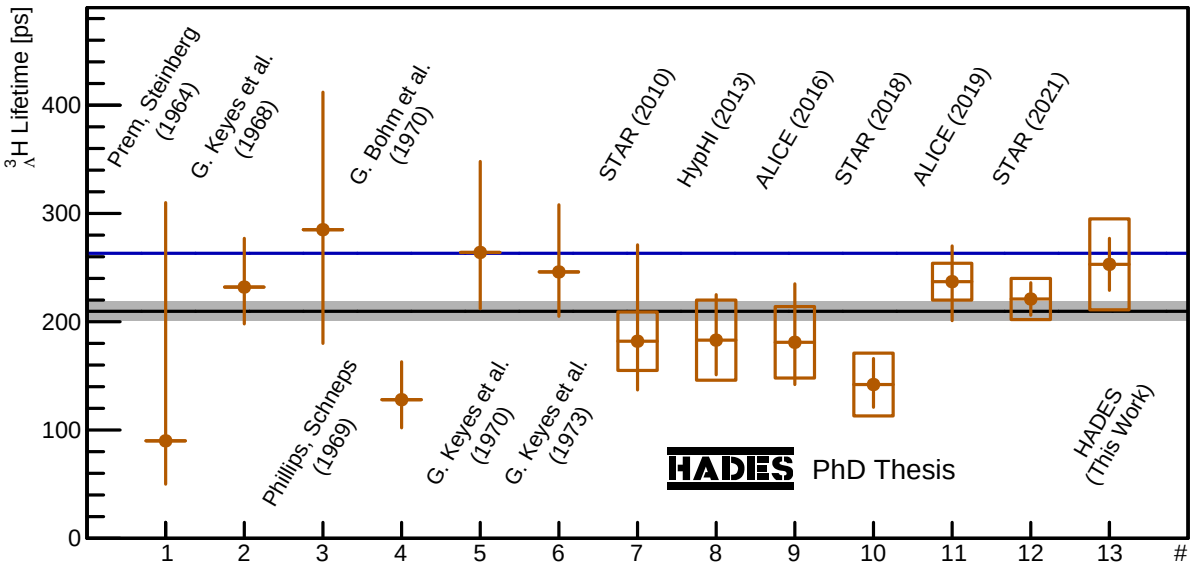

Figure 5.9.: Comparison of $^3_\Lambda$H lifetimes measured by various experiments. The measurements are listed in chronological order and the data are from (in the same order): [149, 118, 142, 70, 119, 120, 10, 152, 13, 24, 12, 6] and Section 4.4.2 of this thesis. The blue line depicts the free Λ lifetime of $\approx$ 263 ps [184] and the black line with the gray box the current average of all measurements of (210 $\pm$ 9) ps.

5.6. $^3_\Lambda$H Lifetime

Already in the 1960s, the lifetime of $^3_\Lambda$H was measured using photographic detection techniques [149, 118, 142, 70, 119, 120]. Most of these early measurements suffered from large uncertainties which is why beginning in the 2010s more precise measurements mostly at heavy-ion collision experiments were conducted [10, 152, 13, 24]. These measurements yielded significantly lower lifetimes than the lifetime of free Λ hyperons which was not expected as many theoretic calculations predict similar lifetimes due to the low binding energy of the $^3_\Lambda$H. In even more recent measurements [12, 6] lifetimes closer to the lifetime of free Λ hyperons were measured. Those measurements are now reinforced by the measurement by HADES, described in Section 4.4.2, which yielded a lifetime compatible with the one of free Λ hyperons as well.

Figure 5.9 summarizes $^3_\Lambda$H lifetimes measurements from various experiments. The blue line depicts the free Λ lifetime of $\approx$ 263 ps [184] and the black line with the gray box the current average of all measurements of (210 $\pm$ 9) ps. Although the most recent measurements are compatible with the free Λ lifetime within their uncertainties, more measurements especially with reduced uncertainties are required to gain more clarity on the lifetime of $^3_\Lambda$H, since currently the world average of measured $^3_\Lambda$H lifetimes and the free Λ lifetime are still almost 6σ away from each other. In particular, the upcoming FAIR experiment CBM, which will measure heavy-ion collisions at $\sqrt{s_{NN}} \lesssim 4.7$ GeV where a maximal $^3_\Lambda$H production rates are expected, will allow for more precise measurements.

6. Summary and Outlook

In this thesis, the emission of protons as well as the production of Λ hyperons, K^0_S mesons, ${}^3_\Lambda$H hypernuclei and Ξ^- hyperons in Ag(1.58A GeV)+Ag collisions measured by the HADES spectrometer are studied. The used dataset of 13.64 billion recorded events and more than three billion events after all cleaning criteria and selection of the 0-30 % most central events constitutes the worldwide largest heavy-ion collision dataset available at these energies. Thanks to the large amount of available events in combination with a sophisticated method involving state-of-the-art machine learning techniques to recognize weak decays, for the first time ${}^3_\Lambda$H hypernuclei and Ξ^- hyperons were successfully reconstructed and analyzed in heavy-ion collisions at such low energies. In the following, the contents of this thesis are summarized.

6.1. Introduction

In Chapter 1 the theoretic prerequisites and motivation of the conducted studies are summarized starting with an introduction to the so called standard model which forms the base of our current understanding of nuclear physics. Next, the most important aspects of the phenomenology of the strong interaction relevant for the formation of hadrons from quarks and gluons as well as the formation of nuclei from nucleons are discussed. The effects include in particular the confinement of quarks in hadrons in a low-dense "cold" environment and their asymptotic freedom in a dense or "hot" environment. As a result of these effects, QCD matter is assumed to undergo a phase transition to a QGP phase if it is either strongly compressed or heated which is depicted in the QCD phase diagram shown in Figure 6.1. In nature, the extreme conditions required for such a phase transition are only achieved in the heaviest astronomic objects, namely black holes and neutron stars. While black holes are not directly observable due to their event horizon, neutron stars can be observed and are therefore one of the few possibilities to study QCD matter under extreme conditions. In particular, the merging of two colliding neutron stars is of great interest as the properties of matter created in such events are expected to be achievable and examinable on earth in heavy-ion collisions.

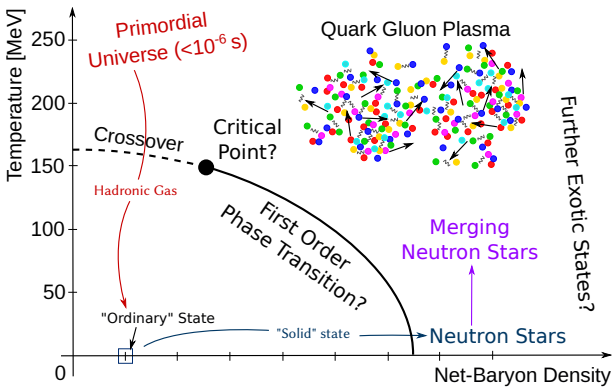

Figure 6.1.: Schematic phase diagram of QCD matter - See Figure 1.1.

The collisions of heavy-ions accelerated to relativistic energies are the only possibility to study QCD matter under extreme conditions on earth. However, as the extreme conditions last for only tiny fractions of a second, only the particles emerging from the created system

can be studied and allow to draw conclusions on the processes of interest. At low collision energies $\sqrt{s_{NN}}$ of few GeV the production of hadrons involving strange-quarks provides an important access to the properties of the created medium as the production happens close to its threshold energy in binary NN collisions making it especially sensitive to medium effects. Further important effects include for example the modification of the wave functions of hadrons by coupling to the medium which is effectively described by potentials and might have significant effects on the macroscopic properties of the created matter like its EoS and are therefore exceptionally relevant for the stability of neutron stars. Finally, in Chapter 1 the concept of centrality as well as analytical models to describe the kinematic distributions of emitted particles are described. The chapter concludes with a summary of previous measurements and results on the studied topics.

6.2. The HADES Experiment

The precise measurement of particles emitted from heavy-ion collisions requires very sophisticated detector setups spanning a large proportion of the full 4π spherical angle in the CM system of the collision. In Chapter 2 the HADES spectrometer used in this thesis is described. The chapter is splitted into two primary Sections 2.2 and 2.3. It begins with a short introduction to the current GSI and the upcoming FAIR research facility. Afterwards, in the first primary sub-section the technical setup and capabilities of the entire detector system, which is schematically depicted in Figure 6.2, as well as its individual sub-detectors are discussed. A special focus is put on the sub-detectors most relevant to the analyses described in this thesis, those being the MDCs detectors as well as the two META detectors RPC and TOF. In the second primary sub-section, the software procedures used to process the raw data recorded by the detectors are discussed. These procedures include in particular the estimation of the reaction time and the collision vertex as well as the reconstruction of particle trajectories and their properties from raw detector hits. Furthermore, the procedures used to generate artificial events based on reactions simulated by various event generators are described. These simulated events are required to deduce properties of the detector system like for example detection efficiencies that cannot be obtained from actually measured events. The chapter concludes with a summary of the key-features of the analyzed Ag(1.58A GeV)+Ag beam time.

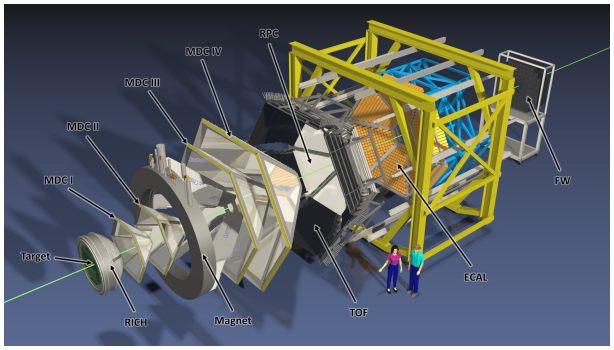

Figure 6.2.: Schematic depiction of the HADES experiment - See Figure 2.2.

6.3. Analysis Methods

In Chapter 3 various methods and procedures required to perform the physics analyses that were either developed or revised in the scope of this work are described. The first one being the calibration procedure of the START and VETO detector which is crucial to almost

all analyses conducted with HADES as the START detector determines the reaction time which is required as a reference time for all sub-sequent time measurements of various detectors. The procedure comprises two steps: First, the constant delays between all strips of the START detector and all pads of the VETO detector are compensated by individual offsets. In the second step, the offsets of the strips are adjusted for each run of the beam time individually making use of the measured times of flight and momenta of π^- tracks. After calibration, a time precision of approximately 50 ps ic achieved by the START detector.

Next, the rejection procedure for problematic events is described. It comprises two steps as well: In the first step, nine predefined criteria to identify problematic or irrelevant events are tested and all events failing at least one criterion are rejected. In the second step, the performance of the entire detector system and event reconstruction procedure is evaluated over the entire beam time for each individual run by comparing the average amount of reconstructed proton, π^+, π^- and $e^+ + e^-$ tracks per event to their corresponding daily average. All runs for which at least one number exceeds a defined relative divergence are discarded. Afterwards, selection criteria are applied to the reconstructed particle tracks contained in the selected events. These criteria aim at discarding tracks created from a wrong combination of multiple detector hits that do not correspond to actual particles.

Afterwards, the procedures to identify protons, π^+, π^- and ^{3}He tracks using the measured momentum, ToF and/or specific energy loss information are described. In both cases the standard procedures were improved in the scope of this project to achieve a higher selection precision. In case of the selection using the measured ToF, the new quantity a was introduced to construct a Cartesian coordinate system in combination with the calculated mass which allows a precise selection of the mass peaks independent from the momentum. In case of the selection using the measured specific energy loss in the MDC chambers, the extracted momentum slices are for the first time fitted with logarithmic asymmetric Gaussian fit functions to enable a precise selection even for highest specific energy losses at lowest momenta.

The next section describes the procedure used to estimate the centrality of a reaction based on the measured detector signals. The procedure is basically identical to the one used for Au(1.23A GeV)+Au collisions in [16] but was revised and tuned specifically for the Ag(1.58A GeV)+Ag collisions analyzed in this work. It utilizes a geometric Glauber model [134] in combination with the "wounded nucleon" model [67] to sample the amount of hits in the RPC and TOF detector from a given impact parameter and thereby determine criteria to distribute the 0-30 % most central events to three equal centrality classes.

The remaining sections of Chapter 3 primarily describe methods crucial to identify and reconstruct weakly decaying hadrons. They start with a description of the OVD topologies arising from the rather long lifetimes of weak decays. Based on the topologies, six geometric topology parameters are defined that allow to distinguish between random particle combinations and combinations of daughter particles of a weakly decaying hadron. Most of these topology parameters strongly depend on the position of the reaction vertex. It is approximated by the primary event vertex using a procedure which is described in Section 3.7 to achieve an even more precise estimation than on event reconstruction level. A further parameter to identify weak decays is derived from the AP method. Therefore, for

the first time, the characteristic AP ellipses are interpreted in a polar coordinate system whose azimuthal angle constitutes the parameter APAngle. Besides the strong rejection of wrong signals in case of both directly measured particles as well as reconstructed particles using the previously described methods, some background always remains and needs to be estimated and subtracted. In case of directly measured particles, it is estimated using an interpolation procedure of the relevant mass region. In case of reconstructed particles, the combinatorial background is estimated using the mixed-event technique. Finally, the procedure to enhance the identification of weakly decaying hadrons utilizing an ANN is described. It is very similar to the procedure described in [170], however, it was further improved by replacing the previously used momentum of the reconstructed mother particle as input parameter by the newly introduced APAngle. Furthermore, multiple cross-checks to determine the optimal ANN setup were performed.

6.4. Analysis Results

Chapter 4 describes the actual analyses of the emission of protons as well as the production of Λ hyperons, K^0_S mesons, $^3_\Lambda$H hypernuclei and Ξ^- hyperons using the previously described methods. Out of all analyzed particles only the protons are measured directly in the detectors. To estimate the amount of background tracks contaminating the proton mass region and thereby extract the amounts of pure proton signal counts, a very sophisticated background estimation procedure utilizing multiple cubic spline interpolations was developed. Using this procedure in combination with simulated protons generated by the Pluto event generator embedded into simulated UrQMD events to estimate acceptance and efficiency losses, a multi-differential analysis of the emission of protons in transverse momentum, rapidity and centrality is performed. The obtained spectra are fitted with SR model functions (cf. Section 1.4) to extrapolate the yields and obtain full 4π yields as well as extract the model parameters T_{Eff} and β describing the emission pattern.

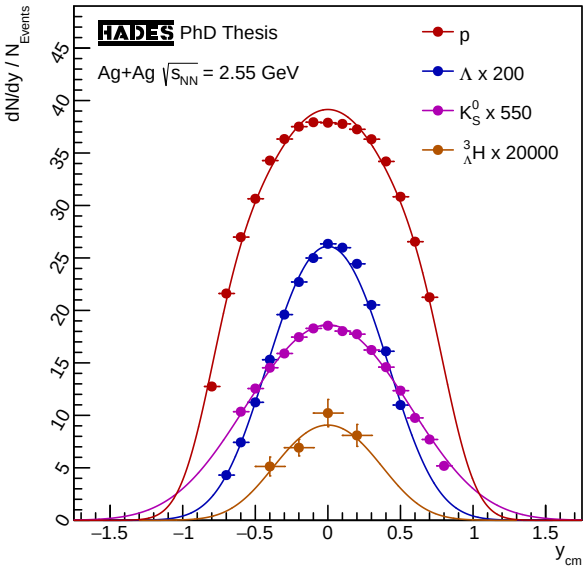

Figure 6.3.: Rapidity spectra of protons, Λs, K^0_S and $^3_\Lambda$H and their model functions - See Figures 4.4, 4.14, 4.24 and 4.34.

In case of Λ hyperons and K^0_S mesons, the conducted analyses are mostly identical. First, the training of the ANNs used to enhance the discrimination power between actual signals and combinatorial background are described. Based on that an iterative optimization procedure is applied to identify the selection criteria yielding the most significant signals. In the next step, these selection criteria are used to measure the lifetime of both particles which compared to the literature lifetimes of the particles allows to perform a consistency check of the acceptance and efficiency correction using Λ hyperons and K^0_S mesons simulated by the Pluto event generator and embedded into experimental data according to

the method described in Section 2.3.4. For both particles the measured lifetimes are compatible with the literature values within uncertainties. Finally, the production of both particles is analyzed multi-differentially as a function of transverse momentum, rapidity and centrality. The obtained spectra are fitted with DIS model functions (cf. Section 1.4) to extrapolate the yields and obtain full 4π yields as well as extract the model parameter T_{Eff} describing the emission pattern.

In this thesis, for the first time the ${}^{3}_{\Lambda}\mathrm{H}$ is successfully reconstructed via its two-body decay channel in heavy-ion collisions at $\sqrt{s_{NN}} = 2.55$ GeV. Again, first the training of the ANN and the optimization of the selection criteria are described. Unfortunately, the low amount of only ≈ 1000 reconstructed ${}^{3}_{\Lambda}\mathrm{H}$ results in large statistical uncertainties. Again, a lifetime measurement is performed and the obtained result of $(253 \pm 24 \pm 42)$ ps is compared to world data in Chapter 5 to contribute to resolving the ${}^{3}_{\Lambda}\mathrm{H}$ lifetime puzzle. The result is compatible with recent measurements by the ALICE [12] and the STAR [6] collaboration as well as the lifetime of free Λ hyperons. Finally, also the production of ${}^{3}_{\Lambda}\mathrm{H}$ is analyzed multi-differentially. Due to the low amount of reconstructed signals, the full production rates for each centrality class are determined independent from the multi-differential analysis in transverse momentum and rapidity which is only performed for the 0-25 % most central events. The results show that the measured ${}^{3}_{\Lambda}\mathrm{H}$ are produced by a source at mid-rapidity.

In addition to the ${}^{3}_{\Lambda}\mathrm{H}$, also the Ξ^- hyperons are for the first time successfully reconstructed in heavy-ion collisions at $\sqrt{s_{NN}} = 2.55$ GeV. This time, the full reconstruction procedure consists of two adjacent weak decay reconstructions since Ξ^- hyperons decay in two independent steps. After all optimization procedures, the best obtained signal does not exceed the threshold of 5σ significance. Thus, both a production rate as well as an upper production limit are estimated. The determined upper limit amounts to 0.81×10^{-4} and the total production rate to $(0.36 \pm 0.11) \times 10^{-4}$ Ξ^- hyperons per event. The order of magnitude of these rates is consistent with previous measurements is the same energy region [7, 30, 170].

6.5. Interpretation of the Results

In the final Chapter 5 the results obtained in Chapter 4 are interpreted. In the first section, the measured $(\Lambda+\Sigma^0)$ and K^0_S production rates are used to estimate the rates of pure Λ and Σ hyperons utilizing the conservation of strangeness in the strong interaction. The isospin asymmetry as as result of the different amount of up- and down-quarks in the initially colliding nuclei is taken into account by a simple approximation. Comparing the K^0_S production rates to the preliminary K^+ production rates

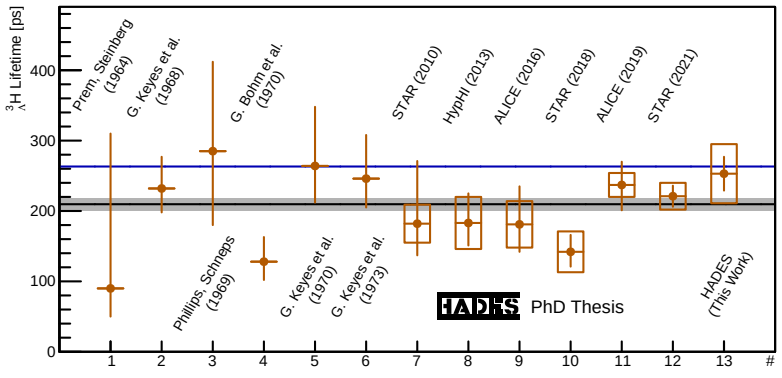

Figure 6.4.: ${}^{3}_{\Lambda}\mathrm{H}$ lifetime measurements - See Figure 5.9.

from [122] shows that this approximation works well at least for the 0-10 % most central events. Surprisingly, the resulting production rates show a rising Σ^0 to Λ ratio towards peripheral events, which might be explained by Σ + N interactions. The reconstruction of Σ^0 hyperons in [61] will provide more clearance on this topic.

In the second section, the production rates of Λ hyperons, K^0_S mesons and ${}^3_\Lambda H$ at mid-rapidity as well as the ratio of Ξ^- and Λ hyperons are compared to world data from various collision systems and energies. The production rates of Λ hyperons and K^0_S mesons line up perfectly with the world data and strongly enforce an exponential rise of their excitation function close to the strangeness production threshold energy in free NN collisions. In case of the ${}^3_\Lambda H$ unfortunately only very few measurements at mid-rapidity are available. However, the measured production rate aligns very well with the existing data and shows a fair accordance with the shown thermal model prediction. Also the new data point of the Ξ^- to Λ ratio aligns very well with the available measurements, however the limited amount of data in this energy region makes further interpretations challenging.

In the third section, the scaling of the production rates of Λ hyperons, K^0_S and K^+ mesons and ${}^3_\Lambda H$ with $\langle A_{Part} \rangle$ is investigated. For Au(1.23A GeV)+Au collisions it was found that the production rates of strange hadrons are well described proportionally to $\langle A_{Part} \rangle^\alpha$ with a common exponent $\alpha = 1.45 \pm 0.06$ [18]. Besides the different energy of the Ag(1.58A GeV)+Ag collisions the scaling of Λ hyperons and K^0_S and K^+ mesons is well described with a compatible exponent of $\alpha = 1.44 \pm 0.03$. The production rate of ${}^3_\Lambda H$ on the other side scale much stronger and are well described by $\alpha = 2.84 \pm 0.32$. This important observation is explained if the ${}^3_\Lambda H$ are formed from participant nucleons.

In the fourth section, the longitudinal anisotropy of the fireball, which is a result of the nucleons from the colliding nuclei not being fully stopped in the reaction zone, is studied in dependence of the centrality of the collision. The analysis is performed by examining the rapidity distributions of Λ hyperons and K^0_S mesons in the standard case and after rotating the coordinate system. It shows that in x- and y-direction the fireball is indeed isotropic while in z-direction significantly larger widths are observed. Furthermore, the transverse widths decrease towards more peripheral events while the longitudinal widths increase since the stopping of the nucleons is stronger in central collisions.

In the fifth section, the transverse and longitudinal kinematic distributions of protons and Λ hyperons from Au(1.23A GeV)+Au and Ag(1.58A GeV)+Ag collisions are compared. It shows that in both collision systems the protons experience a stronger blast and therefore lower effective temperature than the Λ hyperons. The difference is significantly stronger for the Au(1.23A GeV)+Au than for the Ag(1.58A GeV)+Ag collisions which can be interpreted as a consequence of the higher $\sqrt{s_{NN}}$ in the Ag+Ag collision than in the Au+Au collisions. The same observations were already made at the AGS accelerator around the year 2000 [79] but were not further analyzed and interpreted.

In the final sixth section, the obtained ${}^3_\Lambda H$ lifetime is compared to world data to contribute to resolving the ${}^3_\Lambda H$ lifetime puzzle as already discussed in Section 6.4. The corresponding comparison is shown in Figure 6.4.

6.6. Outlook

Within the scope of the FAIR Phase-0 physics program, the HADES experiment received upgrades like for example the new Multi-Anode PhotoMultiplier Tubes (MAPMTs) and FEEs for its RICH detector which will also be used for the RICH detector of the future CBM experiment. This upgrade significantly enhances the detection efficiency of electrons and positrons [20]. Furthermore, the new ECAL detector was build which allows to directly measure photons. Combined, the upgrades allow for a more precise measurement of electromagnetic probes than ever before. Recently, the HADES experiment was further upgraded with a forward tracking system consisting of four Strawtube Tracking Stations (STSs), developed for the future $\overline{\mathrm{P}}$ANDA experiment, and a forward RPC (fRPC) detector. With this upgrade the geometrical acceptance of the experiment is extended further into the forward rapidity region which enhances the measurement of exclusive channels in elementary reactions. Further upcoming upgrades of HADES include for example an exchange of the current CTS system and replacing the FEEs of the MDC detectors by electronics based on $\overline{\mathrm{P}}$ANDA STT REadout Chip (PASTTREC) chips [179].

Up to now, the HADES collaboration proposed six measurement campaigns for the FAIR Phase-0 physics program. One of them was the measurement of Ag(1.58A GeV)+Ag collisions which was conducted in March 2019. In February 2022, the HADES experiment is scheduled for a four week measurement campaign of p(4.5 GeV)+p collisions with the aims to study electromagnetic and hadronic decays of hyperons, study the production of multi-strange hyperons and ϕ mesons and to measure the production of hadrons as a reference measurement for the separately proposed measurement of p(4.5 GeV)+Ag collisions which is not scheduled yet. Besides that, the HADES collaboration plans conduct a beam energy scan of Au+Au collisions with beam energies of 800, 600, 400 and 200 GeV per nucleon. The primary aims of these measurements will be the study of the production of hyperons at $\sqrt{s_{NN}}$ far below the free NN threshold energy of strangeness production as well as the extension of the freeze-out curve in the QCD phase diagram at highest accessible baryochemical potentials. Furthermore, the measurement of d+p collisions at beam energies of 1.00, 1.13, 1.25 and 1.75 GeV per nucleon and the measurement of pion-induced π+CH_2, π+C and π+Ag collisions were proposed but not scheduled yet.

7. Zusammenfassung und Ausblick

In dieser Arbeit wurden die Emission von Protonen sowie die Produktion von Λ Hyperonen, K^0_S Mesonen, ${}^3_\Lambda$H Hyperkernen und Ξ^- Hyperonen in vom HADES Detetktor gemessenen Ag(1.58A GeV)+Ag Kollisionen untersucht. Das verwendete Datenset von 13.64 Milliarden aufgezeichneten Kollisionen und mehr als drei Milliarden selektierten und 0-30 % zentralsten Kollisionen ist das größte Datenset von Schwerionenkollisionen bei diesen Energien weltweit. Dank der großen Menge an vorhandenen Daten in Kombination mit einer spezialisierten Methode zur Rekonstruktion schwacher Zerfälle unter Verwendung künstlicher Intelligenz, konnten zum ersten Mal ${}^3_\Lambda$H Hyperkerne und Ξ^- Hyperonen in Schwerionenkollisionen bei derart niedrigen Energien erfolgreich rekonstruiert und analysiert werden. Im Folgenden werden die Inhalte dieser Arbeit zusammengefasst.

7.1. Einführung

In Kapitel 1 werden die theoretischen Grundlagen sowie die Motivation der durchgeführten Analysen zusammengefasst, beginnend mit einer Einführung in das so genannte Standardmodell welches die Grundlage unseres heutigen Verständnisses der Kernphysik darstellt. Als nächstes werden die wichtigsten Aspekte der Phänomenologie der starken Wechselwirkung, welche für die Bindung von Quarks zu Hadronen und von Nukleonen zu Kernen verantwortlich ist, diskutiert. Darunter fällt insbesondere das *Confinement* von Quarks in Hadronen bei niedrigen Dichten und Temperaturen sowie deren asymptotische Freiheit bei hohen Dichten und Temperaturen. Aus diesem Grund wird angenommen dass QCD Materie einen Phasenübergang durchläuft wenn sie entweder stark komprimiert oder erhitzt wird was im QCD Phasendiagramm 7.1 dargestellt wird. In der Natur werden die dafür notwendigen extremen Bedingungen nur in den schwersten existierenden Objekten, nämlich schwarzen Löchern und Neutronensternen, erreicht. Während sich schwarze Löcher aufgrund ihres Ereignishorizonts nicht direkt beobachten lassen, ist dies bei Neutronensterne nicht der Fall woraus sich eine einzigartige Möglichkeit zur Untersuchung von QCD Materie unter extremen Bedingungen ergibt. Insbesondere die Verschmelzung von zwei Neutronensternen in so genannten *Merger Events* ist von großem Interesse, da erwartet wird dass die Eigenschaften der Materie darin auf der Erde in Schwerionenkollisionen erzeugt und untersucht werden können.

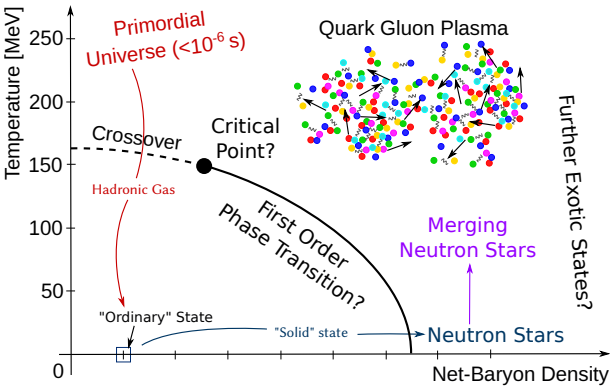

Abbildung 7.1.: Schematisches Phasendiagramm von QCD Materie - Siehe Abbildung 1.1.

Kollisionen von Schwerionen bei relativistischen Energien stellen die einzige Möglichkeit dar auf der Erde QCD Materie unter extremen Bedingungen zu erforschen. Da diese Bedingungen allerdings nur für einen winzigen Bruchteil einer Sekunde erreicht werden, lassen sich nur die daraus hervorgehenden Teilchen messen um Rückschlüsse auf die relevanten Prozesse zu treffen. Bei niedrigen Kollisionsenergien $\sqrt{s_{NN}}$ von wenigen GeV bietet die Produktion von Hadronen mit *strange*-Quarks einen wichtigen Zugang zu den Eigenschaften des Mediums, da deren Produktion nahe der Schwellenenergie in isolierten NN Kollisionen stattfindet und somit besonders sensitiv auf Mediumeffekte ist. Auch die Modifikation der Wellenfunktionen von Hadronen durch Kopplung an das Medium, welche effektiv durch Potentiale beschrieben werden, sind von großem Interesse. Diese könnten sich signifikant auf die makroskopischen Eigenschaften der Materie, wie zum Beispiel deren EoS und damit die Stabilität von Neutronensternen, auswirken. Schließlich werden in Kapitel 1 das Konzept der Zentralität und analytische Modelle zur Beschreibung kinematischer Verteilungen von Teilchen beschrieben. Das Kapitel endet mit einer Zusammenfassung bisheriger Messungen und Ergebnisse der untersuchten Themen.

7.2. Das HADES Experiment

Die präzise Messung von Teilchen aus Schwerionenkollisionen erfordert sehr spezialisierte Detektoren die einen großen Teil des 4π Raumwinkels im CM System der Kollision abdecken. In Kapitel 2 wird das HADES Spektrometer welches für diese Arbeit verwendet wird beschrieben. Das Kapitel unterteilt sich in die zwei vorrangigen Abschnitte 2.2 und 2.3. Zu Beginn werden das aktuelle GSI und das zukünftige FAIR Forschungszentrum vorgestellt. Im darauf folgenden Hauptabschnitt werden Aufbau, Funktionsweise und Eigenschaften des Spektrometers, welches in Abbildung 7.2 schematisch dargestellt ist, sowie der einzelnen Detektoren beschrieben. Dabei wird der Schwerpunkt auf die MDC und die META Detektoren RPC und TOF gelegt welche für die Analysen in diese Arbeit besonders wichtig sind. Im zweiten Hauptabschnitt werden die Softwareprozesse zur Verarbeitung der aufgezeichneten Rohdaten sowie der Generierung von künstlichen *Events*, die auf simulierten Teilchenkollisionen basieren, beschrieben. Diese simulierten *Events* werden benötigt um Eigenschaften der Detektorsysteme die sich nicht aus gemessenen *Events* ableiten lassen, wie zum Beispiel Detektionseffizienzen, zu bestimmen. Das Kapitel endet mit einer Zusammenfassung der wichtigsten Daten der analysierten Ag(1.58A GeV)+Ag Strahlzeit.

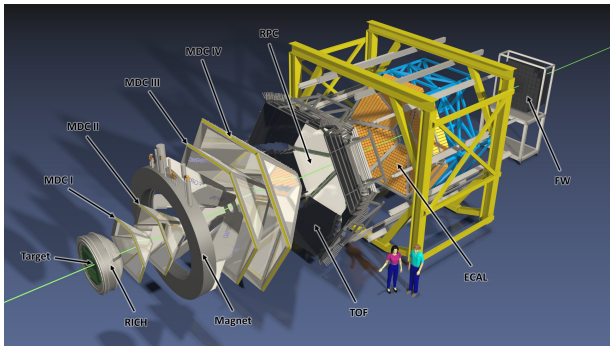

Abbildung 7.2.: Schematische Abbildung des HADES Experiments - Siehe Abbildung 2.2.

7.3. Analysemethoden

In Kapitel 3 werden verschiedenste Methoden und Verfahren zur Durchführung der Analysen, die in dieser Arbeit entwickelt oder überarbeitet wurde, beschrieben. Darunter fallen zunächst die Kalibrierung der START und VETO Detektoren welche für fast alle HADES Analysen unerlässlich sind, da der START Detektor die Kollisionszeit bestimmt welche bei allen weiteren Zeitmessungen als Referenzzeit benötigt wird. Das Verfahren besteht aus zwei Schritten: Zunächst werden die konstanten Verzögerungen zwischen den Streifen des START und Feldern des VETO Detektors durch individuelle Offsets ausgeglichen. Im zweiten Schritt werden diese Offsets für jeden einzelnen *Run* der Strahlzeit unter Verwendung der gemessenen Flugzeiten und Impulse von π^- Spuren angepasst. Nach der Kalibrierung erreicht der START Detektor eine Zeitauflösung von circa 50 ps.

Als nächstes wird das Verfahren zur Erkennung problematischer *Events* beschrieben welches ebenfalls aus zwei Schritten besteht: Zunächst werden neun vordefinierte Kriterien getestet und *Events*, die mindestens eins nicht erfüllen, verworfen. Im zweiten Schritt wird die Leistung des gesamten Detektorsystems und der Rekonstruktionsverfahren für jeden einzelnen *Run* der Strahlzeit anhand der mittleren Menge an Proton, π^+, π^- and $e^+ + e^-$ Spuren pro *Event* im Vergleich zum täglichen Durchschnitt bewertet. Alle *Runs*, bei denen ein Wert eine festgelegte relative Abweichung überschreitet, werden verworfen. Danach werden noch Selektionskriterien auf die Spuren innerhalb der *Events* angewendet. Diese Kriterien dienen dazu Spuren die sich aus einer falschen Kombination von Detektorhits zusammensetzen und keinem echten Teilchen entsprechen zu verwerfen.

Als nächstes werden die Verfahren zur Identifikation von Protonen, π^+, π^- und ^{3}He Spuren anhand der gemessenen Impulse und Flugzeiten bzw. spezifischen Energieverluste beschrieben. In beiden Fällen wurden die Standardverfahren in diesem Projekt für eine höhere Präzision verbessert. Für die Selektion unter Verwendung der Flugzeiten wurde die neue Größe a eingeführt welche zusammen mit der berechneten Masse ein kartesisches Koordinatensystem bildet, welches wiederum eine präzise impulsunabhängige Selektion der Massepeaks ermöglicht. Für die Selektion unter Verwendung der spezifischen Energieverluste in den MDC Detektoren wurden die entsprechenden Impulsintervalle zum Ersten Mal mit einer logarithmischen asymmetrischen Gaus Funktion gefittet welche eine präzise Selektion selbst bei hohen Energieverlusten und niedrigen Impulsen möglich macht.

Im folgenden Abschnitt wird das Verfahren zur Abschätzung der Zentralität anhand gemessener Größen beschrieben. Grundsätzlich ist das Verfahren identisch zu dem welches bereits für Au(1.23A GeV)+Au Kollisionen in [16] angewendet wurde, aber es wurde speziell für die analysieren Ag(1.58A GeV)+Ag Kollisionen angepasst. Dabei wird ein geometrischen Glauber Modell [134] zusammen mit dem „wounded nucleon“ Modell [67] verwendet um die Anzahl an RPC und TOF Detektorhits für einen gegebenen Impactparameter abzuschätzen und damit die 0-30 % zentralsten *Events* in drei gleich große Zentralitätsklassen zu unterteilen.

Die verbleibenden Abschnitte von Kapitel 3 befassen sich mit Methoden die vorrangig zur Rekonstruktion schwach zerfallender Hadronen benötigt werden. Dies beginnt mit den OVD Topologien die eine Folge der verhältnismäßig langen Lebensdauern bei schwachen Zerfällen sind. Anhand der Topologie werden sechs Parameter definiert die eine Unterschei-

dung von zufälligen Kombinationen und echten Tochterteilchenkombinationen schwach zerfallender Hadronen ermöglichen. Die meisten dieser Parameter hängen von der Position des Kollisionsvertex ab. Dieser wird mittels des Eventvertex angenähert, der über die in Abschnitt 3.7 beschriebene Methode zur Erreichung einer höheren Präzision als bei der Eventrekonstruktion bestimmt. Ein weiterer Parameter wird aus der AP Methode abgeleitet. Hierzu werden die charakteristischen AP Ellipsen zum Ersten Mal in Polarkoordinaten interpretiert wobei der Azimutalwinkel den Parameter APAngle bildet. Trotz der starken Reduktion falschen Signale sowohl bei direkt detektierten Teilchen als auch bei rekonstruierten durch die beschriebenen Methoden verbleibt stets ein Untergrund der abgeschätzt und abgezogen werden muss. Bei direkt detektierten Teilchen erfolgt die Abschätzung mittels eines Interpolationsverfahrens des entsprechenden Masseintervals. Bei rekonstruierten Teilchen wird der kombinatorische Untergrund mithilfe der *Mixed-Event* Methode abgeschätzt. Letztlich wird noch die Anwendung eines ANN zur Identifikation schwach zerfallender Hadronen beschrieben. Das Verfahren ist weitestgehend identisch mit dem aus [170], wurde allerdings verbessert indem der damals verwendete Impuls des Mutterteilchens durch den Parameter APAngle ersetzt wurde. Außerdem wurden verschiedene Crosschecks durchgeführt um das ideale ANN Setup zu bestimmen.

7.4. Analyseergebnisse

Kapitel 4 befasst sich mit den tatsächlichen Analysen der Emission von Protonen sowie die Produktion von Λ Hyperonen, K^0_S Mesonen, $^3_\Lambda$H Hyperkernen und Ξ^- Hyperonen unter Verwendung der beschriebenen Methoden. Nur die Protonen werden direkt in den Detektoren gemessen. Die Menge an Hintergrundtracks in der Proton Masseregion und somit die Menge an tatsächlichen Protontracks wird mit einer speziellen neu entwickelten Methode unter Verwendung mehrerer *cubic Spline* Interpolationen bestimmt. Zusammen mit simulierten Protonen des Generators Pluto, die in simulierte UrQMD *Events* implementiert wurden und zur Abschätzung von Akzeptanz- und Effizienzverlusten genutzt werden, wird die Emission von Protonen multi-differentiell als Funktion von Transversalimpuls, Rapidität und Zentralität analysiert. Die resultierenden Spektren werden mit SR Modell Funktionen (Siehe Abschnitt 1.4) zur Extrapolation gefittet um volle 4π Produktionsraten sowie die Modellparameter T_{Eff} und β zur Beschreibung der Emission zu erhalten.

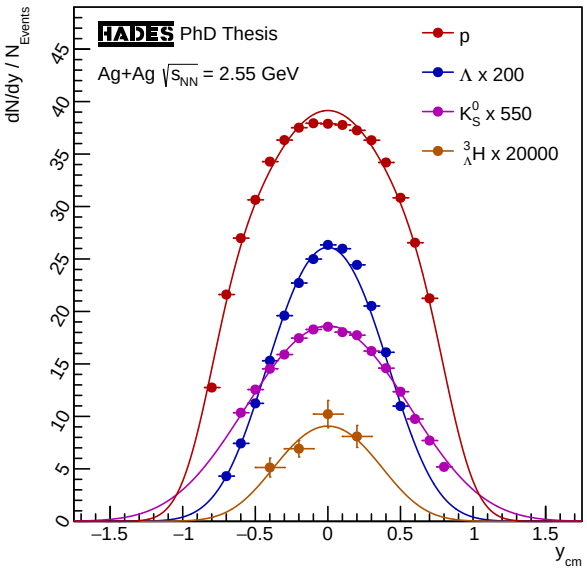

Abbildung 7.3.: Rapiditätsspektren von Protonen, Λs, K^0_S und $^3_\Lambda$H und deren Modellfunktionen - Siehe Abbildungen 4.4, 4.14, 4.24 und 4.34.

Die Analysen von Λ Hyperonen und K^0_S Mesonen sind weitestgehend identisch. Zunächst wird das Training der zur Trennung von Signalen und kombinatorischem Untergrund

verwendeten ANNs beschrieben. Unter deren Verwendung werden in einem iterativen Optimierungsverfahren die Selektionskriterien für Signale mit maximierter Signifikanz bestimmt. Als nächstes wird damit eine Messung der Lebensdauern beider Teilchen durchgeführt und die Ergebnisse werden mit den Literaturwerten verglichen um die Akzeptanz- und Effizienzkorrekturen welche mit simulierten Λ Hyperonen und K^0_S Mesonen des Generators Pluto, die in reale *Events* nach der Methode aus Abschnitt 2.3.4 implementiert wurden, durchgeführt werden zu überprüfen. Bei beiden Teilchen sind die gemessenen Lebensdauern innerhalb ihrer Unsicherheiten konsistent mit den Literaturwerten. Schlussendlich wird die Produktion beider Teilchen multi-differentiell als Funktion von Transversalimpuls, Rapidität und Zentralität analysiert. Die resultierenden Spektren werden mit DIS Modell Funktionen (Siehe Abschnitt 1.4) zur Extrapolation gefittet um volle 4π Produktionsraten sowie den Modellparameter T_{Eff} zur Beschreibung der Emission zu erhalten.

Zum ersten Mal konnte in dieser Arbeit das ${}^3_\Lambda$H in Schwerionenkollisionen bei $\sqrt{s_{NN}} = 2.55$ GeV über seinen Zwei-Körper-Zerfall rekonstruiert werden. Zunächst wird wieder das Training des ANN und die Optimierung der Selektionskriterien beschrieben. Aufgrund der niedrigen Menge von nur ≈ 1000 rekonstruierten ${}^3_\Lambda$H ergeben sich leider große statistische Unsicherheiten. Erneut wird eine Lebensdauermessung durchgeführt. Das Ergebnis von $(253 \pm 24 \pm 42)$ ps wird in Kapitel 5 mit anderen Messungen verglichen um zur Lösung des ${}^3_\Lambda$H Lebensdauerrätsels beizutragen. Es ist konsistent mit kürzlichen Messungen der ALICE [12] und der STAR [6] Kollaboration sowie der Lebensdauer freier Λ Hyperonen. Schlussendlich wird auch die Produktion von ${}^3_\Lambda$H multi-differentiell analysiert. Aufgrund der niedrigen Menge an Signalen werden die zentralitätsabhängigen Produktionsraten unabhängig von der multi-differentiellen Analyse als Funktion von Transversalimpuls und Rapidität, welche nur für die 0-25 % zentralsten *Events* durchgeführt wird, bestimmt. Es zeigt sich dass die gemessenen ${}^3_\Lambda$H von einer Quelle bei *Mid-Rapidity* produziert werden.

Zusätzlich zu den ${}^3_\Lambda$H wurden auch die Ξ^- Hyperonen zum ersten Mal erfolgreich in Schwerionenkollisionen bei $\sqrt{s_{NN}} = 2.55$ GeV rekonstruiert. In diesem Fall besteht das Rekonstruktionsverfahren aus der Rekonstruktion zweier aufeinander folgender schwacher Zerfälle, da Ξ^- Hyperonen kaskadenartig zerfallen. Auch nach allen Optimierungsverfahren übersteigt das beste Signal nicht die Signifikanzschwelle von 5σ. Aus diesem Grund werden sowohl eine Produktionsrate als auch eine obere Produktionsgrenze bestimmt. Die obere Grenze liegt bei 0.81×10^{-4} und die Produktionsrate bei $(0.36 \pm 0.11) \times 10^{-4}$ Ξ^- Hyperonen pro *Event*. Die Größenordnung dieser Raten ist vergleichbar mit vorherigen Analysen im selben Energiebereich [7, 30, 170].

7.5. Interpretation der Ergebnisse

Im letzten Kapitel 5 werden die Ergebnisse aus Kapitel 4 interpretiert. Im ersten Abschnitt werden die Produktionsraten von reinen Λ und Σ Hyperonen unter Verwendung der gemessenen $(\Lambda+\Sigma^0)$ und K^0_S Produktionsraten und der Erhaltung der Strangenessquantenzahl in der starken Wechselwirkung abgeschätzt. Die Isospin-Asymmetrie als Konsequenz der unterschiedlichen Menge an up- und down-Quarks in den kollidierenden Kernen wird mit einer einfachen Annäherung berücksichtigt. Der Vergleich der K^0_S Produktionsraten mit vorläufigen K^+ Produktionsraten aus [122] zeigt dass die Annäherung zumindest für die

0-10 % zentralsten *Events* funktioniert. Überraschenderweise steigt das Verhältnis von Σ^0 und Λ Produktionsraten zu peripheren *Events* an was sich durch Σ + N Reaktionen erklären ließe. Die Rekonstruktion von Σ^0 Hyperonen in [61] wird diesbezüglich zu mehr Klarheit beitragen.

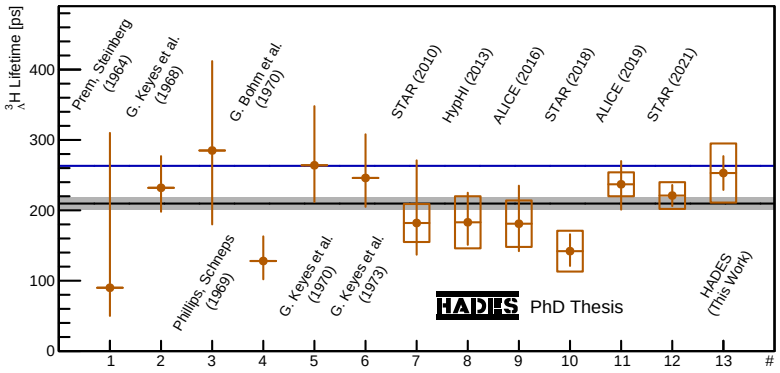

Abbildung 7.4.: $^3_\Lambda$H Lebensdauermessungen - Siehe Abbildung 5.9.

Im zweiten Abschnitt werden die Produktionsraten von Λ Hyperonen, K^0_S Mesonen und $^3_\Lambda$H bei *Mid-Rapidity* sowie das Verhältnis von Ξ^- und Λ Hyperonen mit Daten von verschiedensten Kollisionssytemen und Energien verglichen. Die Produktionsraten von Λ Hyperonen und K^0_S Mesonen passen perfekt zu den vorhandenen Daten und weisen auf einen exponentiellen Anstieg der Produktionsraten in der Nähe der NN Schwellenenergie hin. Im Falle der $^3_\Lambda$H existieren leider nur sehr wenige Messungen bei *Mid-Rapidity*. Dennoch passt die gemessene Produktionsrate gut zu den existierenden Daten und der thermischen Modellvorhersage. Auch das gemessene Ξ^- zu Λ Verhältnis passt gut zu den verfügbaren Messungen, obgleich weitere Interpretationen aufgrund der geringen Menge an Daten in dem Energiebereich schwierig sind.

Im dritten Abschnitt wird die Skalierung der Produktionsraten von Λ Hyperonen, K^0_S und K^+ Mesonen und $^3_\Lambda$H mit $\langle A_{Part} \rangle$ untersucht. Bei Au(1.23A GeV)+Au Kollisionen hat sich gezeigt dass die Produktionsraten „seltsamer“ Hadronen proportional zu $\langle A_{Part} \rangle^\alpha$ mit einem gemeinsamen Exponenten $\alpha = 1.45 \pm 0.06$ skalieren [18]. Trotz der höheren Energie der Ag(1.58A GeV)+Ag Kollisionen skalieren die Λ Hyperonen und K^0_S und K^+ Mesonen mit einem vergleichbaren Exponenten $\alpha = 1.44 \pm 0.03$. Die Produktionsrate der $^3_\Lambda$H hingegen skaliert deutlich stärker mit einem Exponenten $\alpha = 2.84 \pm 0.32$. Diese wichtige Beobachtung lässt sich erklären wenn die $^3_\Lambda$H aus an der Kollision beteiligten Nukleonen gebildet werden.

Im vierten Abschnitt wird die longitudinale Asymmetrie des Feuerballs, die aus der Tatsache folgt dass die kollidieren Kerne in der Kollisionzone nicht vollständig gestoppt werden, zentralitätsabhängig untersucht. Die Analyse wird durchgeführt indem die Rapiditätsspektren von Λ Hyperonen, und K^0_S Mesonen im Normalfall und nach Koordinatensystemrotationen verglichen werden. Es zeigt sich dass der Feuerball in x- und y-Richtung isotrop ist während die z-Richtung deutlich größere Breiten aufweist. Des Weiteren nehmen die transversalen Breiten zu peripheren *Events* ab, während die longitudinalen Breiten ansteigen, da die Kerne in zentralen Kollisionen stärker gestoppt werden.

Im fünften Abschnitt werden die transversalen und longitudinalen Spektren von Protonen und Λ Hyperonen aus Au(1.23A GeV)+Au und Ag(1.58A GeV)+Ag Kollisionen verglichen. Es zeigt sich dass in beiden Kollisionssystemen die Protonen einen größeren Blast und eine niedrigere effektive Temperatur als die Λ Hyperonen aufweisen. Der Unterschied ist bei den Au(1.23A GeV)+Au Kollisionen deutlich stärker als bei den Ag(1.58A GeV)+Ag

Kollisionen was als Folge des höheren $\sqrt{s_{NN}}$ bei den Ag+Ag Kollisionen verstanden werden kann. Dieselbe Beobachtung wurde bereits am AGS Beschleuniger um das Jahr 2000 [79] gemacht, allerdings nicht weiter interpretiert.

Im letzten sechsten Abschnitt wird die gemessene ${}^{3}_{\Lambda}\mathrm{H}$ Lebensdauer mit anderen Messungen verglichen um zur Lösung des ${}^{3}_{\Lambda}\mathrm{H}$ Lebensdauerrätsels beizutragen was bereits in Abschnitt 7.4 diskutiert wurde. Abbildung 7.4 zeigt den entsprechenden Vergleich.

7.6. Ausblick

Im Rahmen des FAIR Phase-0 Forschungsprogramms wurde das HADES Experiment verbessert, unter anderem durch die neuen MAPMTs und FEEs für den RICH Detektor die auch beim RICH Detektor des zukünftigen CBM Experiments zum Einsatz kommen. Durch dieses Upgrade wurde die Detektionseffizienz von Elektronen und Positronen signifikant erhöht [20]. Außerdem wurde der neue ECAL Detektor gebaut welcher die direkte Messung von Photonen ermöglicht. In Kombination sind durch diese Upgrades präzisere Messungen elektromagnetischer Sonden als je zuvor möglich. Kürzlich wurde das HADES Experiment weiterhin durch ein Trackinsystem in vorwärts Richtung erweitert, welches aus vier STSs, die für das zukünftige $\overline{\mathrm{P}}$ANDA Experiment entwickelt wurden, und einem fRPC Detektor besteht. Dadurch wurde die geometrische Akzeptanz bei vorwärts Rapiditäten stark erhöht, wodurch insbesondere die Messung exklusiver Kanäle in elementaren Reaktion verbessert wird. Des Weiteren sind Upgrades des aktuellen CTS Systems, sowie der FEEs der MDC Detektoren unter Verwendung von PASTTREC Chips geplant [179].

Bis heute hat die HADES Kollaboration sechs Messungen im Rahmen des FAIR Phase-0 Forschungsprogramms vorgeschlagen. Die erste davon war die Messung von Ag(1.58A GeV)+Ag Kollisionen und wurde im März 2019 durchgeführt. Im Februar 2022 ist aktuell eine vierwöchige Messung von p(4.5 GeV)+p Kollisionen mit HADES geplant. Die Ziele dieser Messung umfassen die Erforschung elektromagnetischer und schwacher Hyperonenzerfälle, die Erforschung der Produktion mehrfach „seltsamer“ Hyperonen und ϕ Mesonen sowie die Produktion von Hadronen als Referenzmessung für die Messung von p(4.5 GeV)+Ag Kollisionen, die allerdings noch keinen Termin haben. Außerdem ist ein Strahlenergiescan von Au+Au Kollisionen bei 800, 600, 400 und 200 GeV pro Nukleon geplant. Primäres Ziel dieser Messung ist die Erforschung der Hyperonenproduktion weit unterhalb der Schwellenenergie in isolierten NN Kollisionen sowie die Erweiterung der Ausfrierkurve im QCD Phasendiagramm bei den höchsten erreichbaren baryochemischen Potentialen. Weiterhin ist die Messung von d+p Kollisionen bei Strahlenergien von 1.00, 1.13, 1.25 und 1.75 GeV pro Nukleon und von π+CH_2, π+C und π+Ag Kollisionen geplant, allerdings ebenfalls noch ohne Termin.

A. Appendix

A.1. Uncertainty Analysis

A core principle of quantum mechanics is that due to Heisenberg's uncertainty principle, the state of a system cannot be infinitely precise defined. Within these uncertainties only statistical statements are possible, which is why most quantum mechanical processes, like for example particle decays, show a statistical nature. The same holds true if the outcome of a process cannot be predicted because either the initial state or the underlying mechanisms are unknown. Therefore, the statistical uncertainties of a measurement always need to be taken into account and propagated through the entire analysis chain onto the final results within this thesis.

At the beginning of most analyses a count rate N is measured. If the underlying process is of statistical nature, the probability distribution of the outcome N in multiple independent measurements is given by the Poisson-distribution A.1 with the expectation value μ.

$$P_{\mu}(n) = \frac{\mu^n}{\Gamma(n)} \cdot \exp(-\mu) \tag{A.1}$$

It can be shown that the standard deviation σ, which is a measure for the dispersion of N, is $\sqrt{\mu}$ in case of a Poisson-distribution. Therefore, the statistical uncertainty of a count rate N is defined as $\sqrt{N}$. For large expectation values μ the Poisson distribution can be approximated by a Gaussian-distribution A.2 with $\sigma = \sqrt{\mu}$.

$$P_{\mu,\sigma}(x) = \frac{1}{\sigma\sqrt{2\pi}} \cdot \exp\left(-\frac{(x-\mu)^2}{2\sigma^2}\right) \tag{A.2}$$

Thus, the statistical uncertainty of a count rate N can be assumed to be symmetrical. Furthermore, the probability of the count rate exceeding its actual value by n times its statistical uncertainty can be calculated by integrating the Probability Density Function (PDF) of the Gaussian-distribution like shown in Equation A.3 where $\mathrm{erf}(x)$ represents the Gaussian error function:

$$P(N \in [\mu \pm n\sigma]) = \frac{1}{\sqrt{2\pi}} \cdot \int_{-n}^{n} \exp\left(-\frac{x^2}{2}\right) dx = \mathrm{erf}\left(\frac{n}{\sqrt{2}}\right) \tag{A.3}$$

In case a quantity x carrying the Gaussian uncertainty Δx is transformed by a functional correlation $f(x)$, the uncertainty needs to be propagated. According to the Gaussian law, the uncertainty propagation is described by Equation A.4 in case x is a one dimensional quantity:

$$\Delta f\left(x\right) = \frac{df\left(x\right)}{dx}\Delta x \tag{A.4}$$

For the propagation $f\left(x\right)$ is approximated to be linear in the range $[x \pm \Delta x]$, since only the first order derivative is taken into account. Although this is potentially problematic in case of a strong non-linearity of $f\left(x\right)$, the Gaussian law of uncertainty propagation is used as a common standard.

In case of a n dimensional quantity $\vec{x}$, also correlations between the uncertainties of the multiple dimensions need to be taken into account. An example for correlated uncertainties are the ones of the parameters of a functional correlation which is fitted to a given distribution. In this case, the Gaussian law of uncertainty propagation results in Equation A.5:

$$\Delta f\left(\vec{x}\right) = \sqrt{\left(\vec{\nabla} f\left(\vec{x}\right)\right)^{T} \times M_{COV} \times \left(\vec{\nabla} f\left(\vec{x}\right)\right)} \tag{A.5}$$

In this equation M_{COV} represents the quadratic $n \times n$ covariance matrix. Its diagonal entries ($\mathrm{i} = \mathrm{j}$) correspond to the squared uncertainties of the individual dimensions of $\vec{x}$ and the entries apart from the diagonal ($\mathrm{i} \neq \mathrm{j}$) correspond to the correlated uncertainty of the i^{th} and j^{th} dimension of $\vec{x}$. Thus, in case the uncertainties of the individual dimensions are uncorrelated, all entries apart from the diagonal are 0 and Equation A.5 can be simplified to Equation A.6:

$$M_{COV} = \begin{pmatrix} \left(\Delta x_1\right)^2 & 0 & \cdots & 0 \\ 0 & \left(\Delta x_2\right)^2 & \cdots & 0 \\ \vdots & \vdots & \ddots & \vdots \\ 0 & 0 & \cdots & \left(\Delta x_n\right)^2 \end{pmatrix} \Rightarrow \Delta f\left(\vec{x}\right) = \sqrt{\sum_{i}^{n} \left(\frac{\partial f\left(\vec{x}\right)}{\partial x_i}\Delta x_i\right)^2} \tag{A.6}$$

An example for uncorrelated uncertainties are the uncertainties of two independently counted rates M and N. In case the correlations between the individual dimensions are unknown, the maximum uncertainty of $f\left(x\right)$ can be calculated by replacing the sum of squares in Equation A.6 by a sum of absolutes resulting in Equation A.7:

$$\Delta f\left(\vec{x}\right) = \sum_{i}^{n} \left|\frac{\partial f\left(\vec{x}\right)}{\partial x_i}\Delta x_i\right| \tag{A.7}$$

It is obvious that due to the underlying approximations the presented equations are only suited for Gaussian distributed uncertainties. While statistical uncertainties are Poisson distributed and therefore in the limit of large expectation values Gaussian distributed, in case of systematic uncertainties, the underlying distribution is often unknown. Therefore, the propagation of systematic uncertainties using the presented equations yields an approximate for the actual uncertainty at best.

A.2. χ^2 Values

There are multiple slightly different definitions of χ^2 values as well as effective χ^2 values used in literature. This section describes the χ^2 implementations of the ROOT framework [150] which are consistently used throughout this thesis.

The χ^2 value is one of the most commonly used methods to quantify the accordance between two datasets of same length. For the two datasets a_i and b_i of length N it is defined by Equation A.8. A lower χ^2 value corresponds to a better accordance between the datasets. Therefore, two equal datasets yield a value of 0.

$$\chi^2 = \sum_i^N (a_i - b_i)^2 \tag{A.8}$$

Concerning distributions, the datasets can be understood as different values corresponding to the same set of points x_i. In that case the full datasets are $(x, a)_i$ and $(x, b)_i$, where x can be multidimensional. Furthermore, the datasets can correspond to a functional correlation with the definition $(x, f(x))_i$, where $f(x)$ is required to be a one dimensional quantity. Using these prerequisites, the χ^2 value can also be used to quantify the accordance between a distribution $(x, a)_i$ and functional correlation $f(x)$, which is described by Equation A.9:

$$\chi^2 = \sum_i^N (a_i - f(x_i))^2 \tag{A.9}$$

If the first dataset is a given distribution and the second dataset a functional correlation with free parameters, the χ^2 value can be used to find the optimal parameters to describe the distribution. This procedure is called χ^2 minimization and is a very common application of the χ^2 value. First, the χ^2 value of the distribution and the functional correlation is calculated for multiple variations of the free parameters around their initial values. Second, the parameter set yielding the lowest χ^2 value is selected as ideal. These steps are repeated iteratively with the result of the previous iteration serving as initial parameter values for the current iteration. Once no further reduction in the χ^2 value is achieved, the last found parameter values are selected as the optimal values. Colloquially, the χ^2 minimization is often referred to by "fitting a function to a distribution".

The χ^2 minimization can also be understood as the search for a minimum of a multidimensional surface with the amount of free parameters defining the dimensionality. Obviously, problems occur if the spline has multiple local minima, since it cannot be guaranteed that the found minimum is actually the global minimum. Modern algorithms cope with this by randomly altering the initial parameter values and checking, whether the χ^2 minimization converges at the same parameter values.

Especially in physics, values are not infinitely precise but have at least a statistical uncertainty. This has to be taken into account when calculating the χ^2 value to increase the importance of values with low uncertainties and decrease it in case of high uncertainties. Therefore, an effective χ^2 value as defined by Equation A.10 is used for the distribution $(x, a)_i$ with the statistical uncertainties Δa_i and the functional correlation $f(x)$.

$$\chi^2 = \sum_i^N \frac{\left(a_i - f\left(x_i\right)\right)^2}{\Delta a_i^2} \tag{A.10}$$

In case also the x_i values have statistical uncertainties, they are propagated according Equation A.4 using the Gaussian law of uncertainty propagation (cf. Appendix A.1) and are added quadratically to the uncertainties Δa_i resulting in Equation A.11. In case of multidimensional x values the propagation is performed assuming uncorrelated uncertainties according to Equation A.6.

$$\chi^2 = \sum_i^N \frac{\left(a_i - f\left(x_i\right)\right)^2}{\Delta a_i^2 + \left(\frac{\partial f}{\partial x}\left(x_i\right)\Delta x_i\right)^2} \tag{A.11}$$

Binned distributions pose another problem: Since the bin values correspond to an x range instead of a single x value, the value of $f\left(x\right)$ at bin center can only be used if the distribution is linear within the bins. In case of non-linearity, the function needs to be integrated over the bin ranges and normalized to the bin volumes. Equation A.12 defines the χ^2 value for a binned distribution $\left(x, a\right)_i$ with the statistical uncertainties Δa_i and bin ranges of $x_i \pm \delta x_i$ as well as the functional correlation $f\left(x\right)$.

$$\chi^2 = \sum_i^N \frac{\left(a_i - \int_{x_i-\delta x_i}^{x_i+\delta x_i} f\left(x\right) dx / \int_{x_i-\delta x_i}^{x_i+\delta x_i} dx\right)^2}{\Delta a_i^2} \tag{A.12}$$

Yet another modification needs to be taken into account to be able to compare the χ^2 values of different datasets or functional correlations. Due to the sum over all points, datasets with more points yield higher χ^2 values at same relative accordance. In addition, functional correlations with more free parameters can be adjusted to a larger variety of distributions. Both effects can be coped with by dividing the χ^2 value by the Number of Degrees of Freedom (NDF). They are equal to the length of the dataset minus the amount of free parameters of the functional correlation. The resulting value χ^2 / NDF can be understood as the average χ^2 value per data point and can be compared across different datasets and functional correlations.

A.3. Lorentz-Vectors and Invariant Masses

At relativistic energies, the total momentum which is the magnitude of the three dimensional momentum vector depends on the frame in which it is measured and is therefore not Lorentz-invariant. By adding a fourth dimension to the three dimensional momentum vector equal to the energy, a so called Lorentz-vector or four-vector is formed. It's definition is given by Equation A.13 with the component of the momentum vector $p_{x,y,z}$ and the energy E as well as the imaginary unit i. For simplicity the speed of light is omitted in all equations of this section.

$$\vec{P} = \begin{pmatrix} E \\ ip_x \\ ip_y \\ ip_z \end{pmatrix} \tag{A.13}$$

Lorentz-vectors use a special metric, diverging from the standard Euclidean metric, to calculate their magnitudes. One possibility to express this, is to precede the momentum components with the imaginary unit i. This results in a Lorentz-invariant magnitude equal to the rest mass m_0 as shown in Equation A.14 utilizing the relativistic energy-momentum relation 1.2:

$$\left|\vec{P}\right| = \sqrt{E^2 - p_x^2 - p_y^2 - p_z^2} = \sqrt{p^2 + m_0^2 - p^2} = m_0 \tag{A.14}$$

In particle decays, the Lorentz-vectors of the multiple daughter particles add up to the Lorentz-vector of the mother particle, due to their Lorentz-invariance. Thus, the rest mass of a hypothetical mother particle with the daughter particles numbered by the index i, also called invariant mass m_{inv}, can be calculated via Equation A.15:

$$m_{inv} = \sqrt{\left(\sum_i E_i\right)^2 - \left(\sum_i p_{xi}\right)^2 - \left(\sum_i p_{yi}\right)^2 - \left(\sum_i p_{zi}\right)^2} \tag{A.15}$$

In particle collisions, the invariant mass of the colliding particles has another special meaning: It is equal to the amount of energy available in the CM system of the particles $\sqrt{s}$, which is an important quantity for the production of particles as discussed in Section 1.3.2. In a fixed-target collision, where the target particle of mass m_t rests in the laboratory system and the projectile particle of mass m_p and energy E_p collides with it, Equation A.15 yields Equation 1.4 to calculate $\sqrt{s}$.

Disclaimer: A similar description is used in [170].

A.4. Transverse Momentum and Transverse Mass

The transverse momentum is an important property of particles emerging from particle collisions. Conventionally, it is defined as the proportion of the total momentum vector perpendicular to the longitudinal beam axis and can be calculated via Equation A.16 with the particle's total momentum p and the polar angle ϑ:

$$p_t = p \cdot \sin(\vartheta) \tag{A.16}$$

Since conventionally the beam axis is equal to the longitudinal z-axis, initially the colliding particles carry no transverse momentum. However, interactions between them result in the emission of particles carrying also transverse momentum. As a result, the transverse momenta distributions are not contaminated by remnants of the initial momenta and therefore provide access to the properties of the system emitting the particles.

As an alternative to the transverse momentum, often the transverse mass is used. It can be understood as the hypothetical mass of a particle if it had no longitudinal momentum / if it total momentum was equal to its transverse momentum. The transverse mass of a particle with the rest mass m_0, the transverse momentum p_t, the energy E and the longitudinal momentum p_l is defined by Equation A.17

$$m_t = \sqrt{m_0^2 + p_t^2} = \sqrt{E^2 - p_l^2} \tag{A.17}$$

The equality between the two formulations can be shown by the relativistic energy-momentum relation 1.2. As it can be seen from the first formulation, the transverse mass is always larger or equal to the rest mass of a particle. Because of that, often the reduced transverse mass $m_t - m_0$ starting at 0 $\mathrm{MeV/c^2}$ is used instead.

Furthermore, it shows that the relation between the transverse momentum and transverse mass is non-linear. In particular at low transverse momenta significantly below the rest mass of a particle, the transverse mass is only weakly connected to the transverse momentum. Thus, low transverse masses span a rather large transverse momentum interval.

Disclaimer: A similar description is used in [170].

A.5. Rapidity

In relativistic physics, the rapidity w is commonly used instead of the regular velocity β because it is a Lorentz-additive quantity. Thus, the transformations between a resting reference frame and a relativistically moving frame can be described by a simple addition / subtraction of the rapidity of the moving frame inside the reference frame. The analogy between the rapidity w and the velocity β of a particle is demonstrated by the first definition is Equation A.18. The second alternative definition utilizes the energy E and the momentum p instead:

$$w = \operatorname{artanh}(\beta) = \frac{1}{2} \cdot \ln\left(\frac{E+p}{E-p}\right) \tag{A.18}$$

Concerning relativistic particle collision physics like they are studied in this thesis, the rapidity is commonly defined by the velocity in longitudinal direction. The definition of this modified rapidity y is given by Equation A.19 using the energy E and the longitudinal momentum p_l of the particle:

$$y = \frac{1}{2} \cdot \ln\left(\frac{E+p_l}{E-p_l}\right) \tag{A.19}$$

This alternative definition is advantageous as the coordinate system is commonly chosen such that its longitudinal direction is equal to the beam axis. Thus, for the colliding particles as well as their common CM system, in the reference laboratory frame both definitions of the rapidity are identical. Furthermore, the transformations between the laboratory frame, in which the particles are measured, and the CM system of the collision, in which the particles are emitted / produced, can be described by a simple addition / subtraction of the rapidity of the CM system in the laboratory frame. This rapidity is also called mid-rapidity y_{cm} and is defined by Equation A.20 in case of a fixed-target heavy-ion collision with the energy E_p and momentum p_p of a projectile nucleon:

$$y_{cm} = \frac{1}{4} \cdot \ln\left(\frac{E_p+p_p}{E_p-p_p}\right) \tag{A.20}$$

A further advantage of the modified definition of the rapidity y is that it is independent from the transverse momentum / mass which are discussed in Appendix A.4. In multi-differential analyses of the kinematic distributions of particles, the rapidity y can therefore be used to describe the emission pattern in longitudinal direction independent from the transverse direction. Combined with the definition of the transverse mass from Equation A.17 the relations given by Equation A.21 can be deduced:

$$\begin{aligned} p_l &= m_t \cdot \sinh(y) \\ E &= m_t \cdot \cosh(y) \end{aligned} \tag{A.21}$$

A.6. Off-Vertex-Decay Parameter

The following list summarizes the parameters used to recognize OVDs in this thesis either by fixed selection criteria or by evaluating the parameters using an ANN as described in Section 3.10:

Dau1VD: Distance of Closest Approach (DCA) / Vertex Distance (VD) between the trajectory of daughter particle 1 and the primary event vertex.

Dau2VD: Distance of Closest Approach (DCA) / Vertex Distance (VD) between the trajectory of daughter particle 2 and the primary event vertex.

MotVD: Distance of Closest Approach (DCA) / Vertex Distance (VD) between the trajectory reconstructed for the mother particle and the primary event vertex.

VDX: Distance between the reconstructed decay vertex and the primary event vertex (Decay length of the mother particle).

MTD: Distance of Closest Approach (DCA) / Vertex Distance (VD) between the trajectories of the two daughter particles.

A: Opening angle between the trajectories of the two daughter particles (Only used for the mixed-event background description).

APAngle: Azimuthal angle in the Armenteros-Podolanski (AP) α-$p_\perp$-plane as defined in Section 3.8 (Only used as an input parameter to the ANNs).

The first six parameters are of geometrical nature and are defined in Section 3.6. As stated in Section 3.9, the sixth parameter A is required to assure a proper description of the combinatorial background using the mixed-event technique. Since it potentially influences the invariant mass distribution obtained for the anticipated mother particle species it is not used to optimize the reconstructed signal neither by fixed selection criteria nor an ANN. The seventh parameter APAngle is based on the Armenteros-Podolanski method and is defined in Section 3.8. Unlike the other parameters, no fixed selection criteria are applied on it, thus it is only used as an input for the ANNs.

In case a particle decays via a cascade of multiple individual decays, like for example the Ξs, the individual decays are numbered in the order they are reconstructed which means the last occurring decay is numbered 1 and an according prefix (Dec1, Dec2, etc.) is added to the names of the parameters. For more details on the definitions of the parameters see Sections 3.6, 3.8 and 3.10. For more details on how the described methods are applied in the actual particle reconstructions see Sections 4.2.1, 4.3.1, 4.4.1 and 4.5.1.

A.7. Particle Selection Criteria

Table A.1 summarizes the selection criteria used to identify particles in this work. All of the listed criteria are applied in addition to the standard track selection criteria described in Section 3.3. The Polarity (Pol.) refers to the sign of electric charge which is determined from the direction of the bending in the magnetic field. The mass of a measured track is calculated from the measured momentum and velocity via Equation 3.1. The quantity a is the additional parameter introduced in Section 3.4.1 to construct a Cartesian coordinate system with the measured mass as one of the axes. Furthermore, in this section, the 2D momentum velocity (p-β) selections for Weak Decay Daughters (WDDs) are described. The 2D momentum specific energy loss (p-dE/dx) selections are described in Section 3.4.2. χ^2_{RK} and MMQ are track quality parameters described in Section 2.3.3. The column "Additional" refers to tables listing further selection criteria used in the corresponding analysis like for example criteria on OVD topology parameter.

Please refer to Sections 4.1 to 4.5 for details on the various analyses conducted.

Particles		**Pol.**	**Mass [MeV/c²]**	***a***	**2D Selection**	**χ^2_{RK}**	**MMQ**	**Additional**
Free p		+	—	—	3σ p-dE/dx	Additional		Table 4.2
Λ	**p**	+	—	0.40 - 2.10	WDD p-β	< 400	< 3	Table 4.5
	π^-	−	—	0.65 - 1.05				
K^0_S	**π^+**	+	—	0.70 - 1.40	WDD p-β	< 400	< 3	Table 4.8
	π^-	−	—					
$^3_\Lambda$H	**^{3}He**	+	1270 - 1520	0.50 - 2.00	^{3}He p-dE/dx	< 400	< 3	Table 4.10
	π^-	−	—	0.65 - 1.05	WDD p-β			
Ξ⁻	**p(Λ)**	+	—	0.72 - 1.51	WDD p-β	< 400	< 3	Table 4.12
	π^-(Λ)	−	—	0.84 - 1.04				
	Λ		Additional	0.78 - 1.65	—	—	—	
	π^-	−	—	0.87 - 1.05	WDD p-β	< 400	< 3	

Table A.1.: Summary of the criteria used to identify particle tracks in this work in addition to the standard track selection criteria described in Section 3.3. The 2D momentum specific energy loss (p-dE/dx) selections are described in Section 3.4.2 and the 2D momentum velocity (p-β) selections for Weak Decay Daughters (WDDs) in Section 3.4.1. The column "Additional" refers to tables listing further selection criteria used in the corresponding analysis.

A.8. Multi-Differential Analysis Spectra

In the sections of Chapter 4 describing the multi-differential analysis of protons, Λ hyperons, K^0_S mesons and ${}^3_\Lambda H$, only a selected set of mass spectra and the resulting spectra from one centrality class are shown for reasons of space. This section displays the full set of mass spectra from the most central centrality class for Λ hyperons, K^0_S mesons and ${}^3_\Lambda H$ as well as the multi-differential analysis spectra from the remaining centrality classes analyzed in this work. Table A.2 gives for each particle and each centrality class the references to the figures displaying the corresponding multi-differential yields. The mid-rapidity transverse momentum spectra as well as the rapidity spectra after transverse integration are displayed in Figures 4.5, 4.15 and 4.25 respectively.

Centrality	**Protons**	**Λ Hyperons**	**K^0_S Mesons**	**${}^3_\Lambda H$ Hypernuclei**
0-10 %	4.2 and 4.3	4.13 and 4.12	4.22 and 4.23	**0-25 %**: 4.31 and 4.33
10-20 %	A.1	A.10	A.20	
20-30 %	A.2	A.10	A.21	

Table A.2.: References to the figures displaying the multi-differential yields of protons, Λ hyperons and K^0_S mesons from the centrality classes of the 0-30 % most central Ag(1.58A GeV)+Ag events.

The mass spectra of Λ hyperons are displayed in Figures A.3 to A.9, the mass spectra of K^0_S in Figures A.12 to A.19 and the mass spectra of ${}^3_\Lambda H$ in Figures A.22 and A.23. In these plots the y-axes are omitted for space reasons. All spectra marked by a red $\times$ are rejected for the multi-differential analyses - See Sections 4.2.3 and 4.3.3 for details. The figures displaying the multi-differential analysis results have always the same structure: The plot in the upper panel of the figure displays the multi-differential yields of the corresponding particle after normalization and correction for acceptance and efficiency losses. The x-axes display the transverse momentum and the y-axes display the rapidity in the CM system of the collision. In case of the proton spectra, the green-frame marks the part of the phase-space covered by the RPC detector and the blue-frame the part covered by the TOF detector.

The plots in the lower left of the figures display the same data like the plots in the upper panel, but with one individual transverse momentum spectrum per rapidity interval. The rapidity intervals in the backward hemisphere are depicted as full markers and the corresponding intervals from the forward hemisphere as hollow markers. The mid-rapidity interval is depicted by the symbol $*$. For better visibility the rapidity spectra are scaled by factors 10^x. Furthermore, the model functions used to perform the transverse extrapolation are displayed. The plots in the lower right of the figures displays the ratios between the model functions and the transverse momentum spectra. For better visibility the ratios are shifted by $\pm$x. For each rapidity interval a black line is depicted which represents a ratio of 1. For all particles and all centralities a fair accordance between the spectra and the model functions is observed.

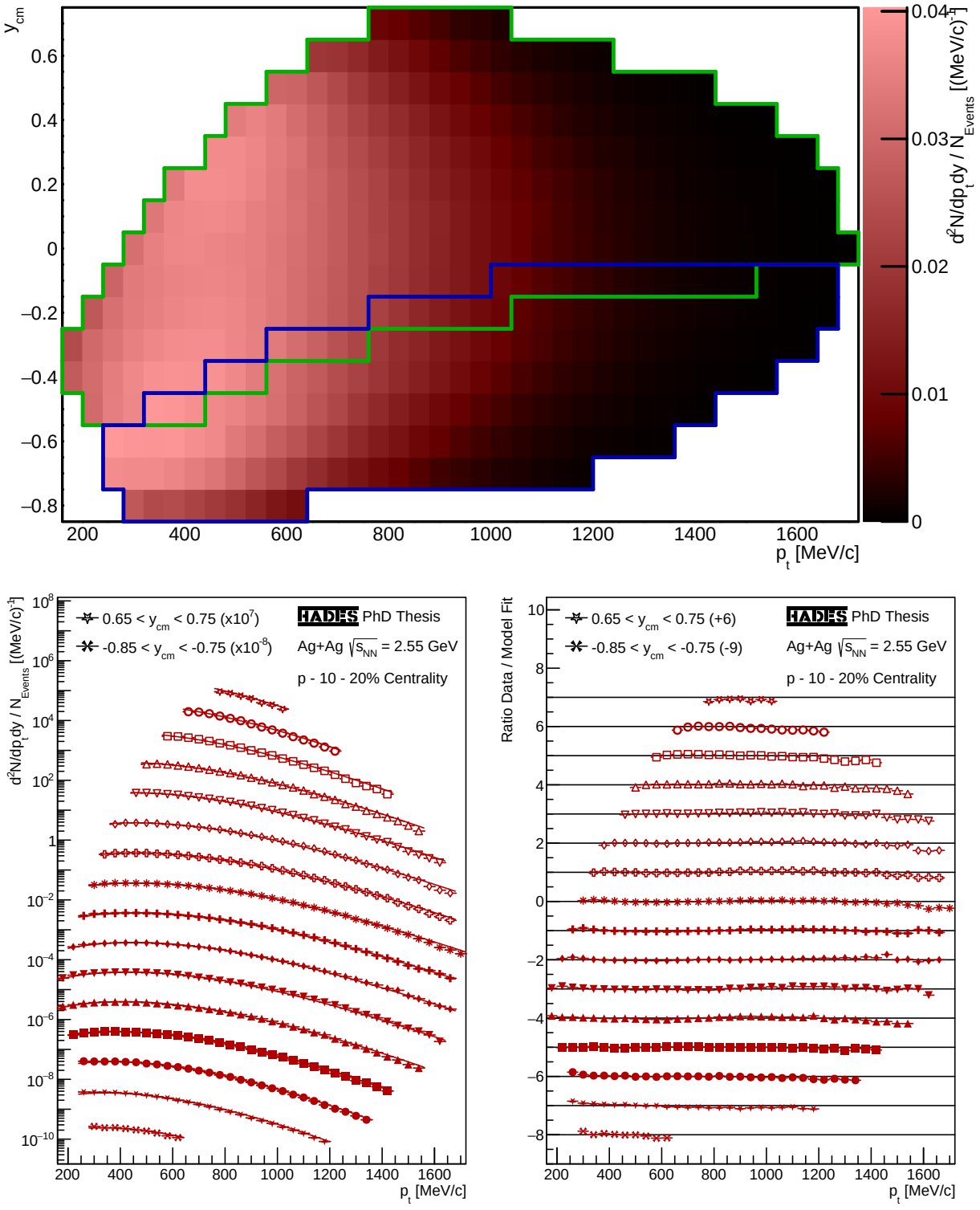

Figure A.1.: Corrected and normalized emission rates (upper panel) and transverse momentum spectra (lower left) of protons from the 10-20 % most central Ag(1.58A GeV)+Ag events as well as their ratios to the SR fit functions (lower right).

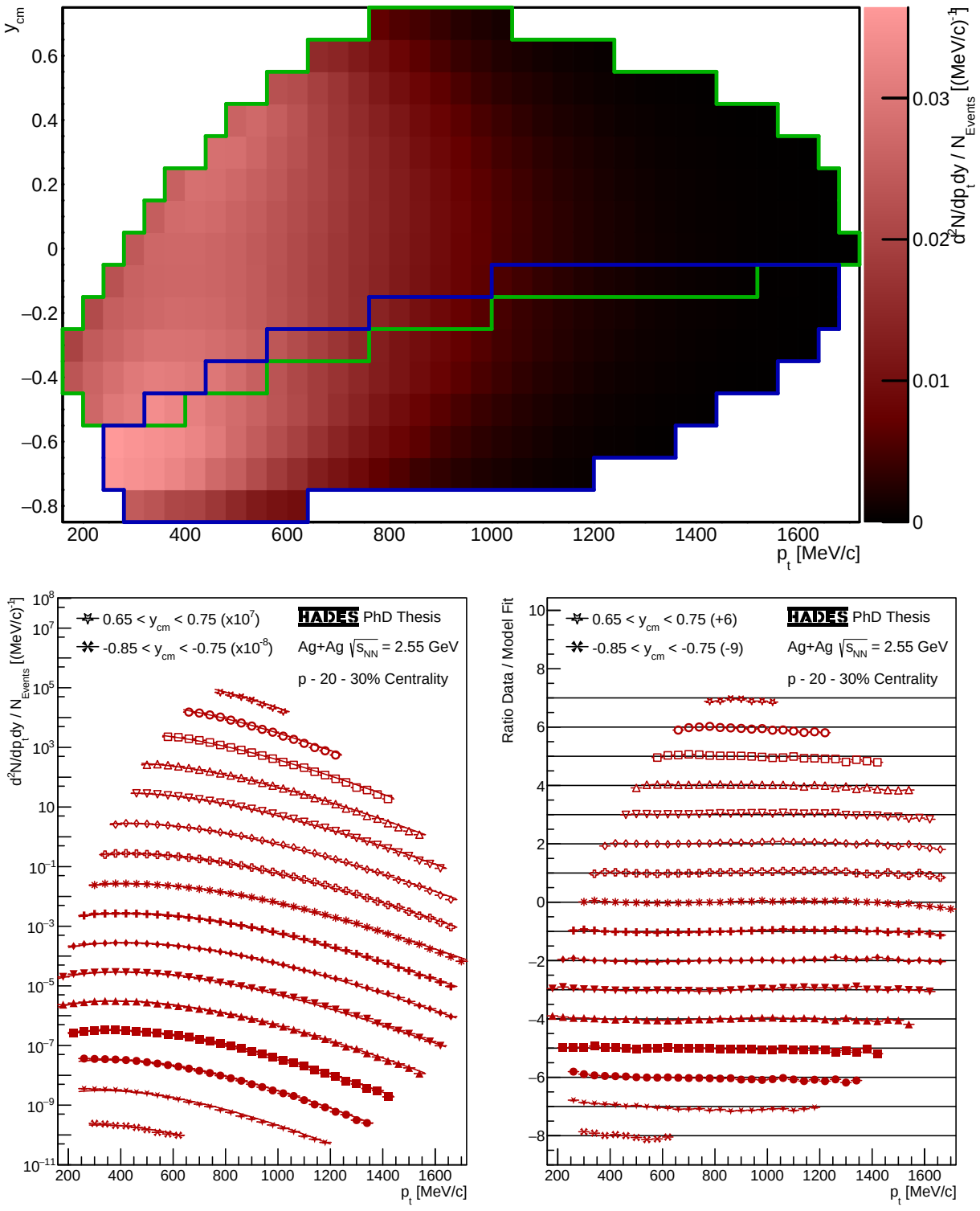

Figure A.2.: Corrected and normalized emission rates (upper panel) and transverse momentum spectra (lower left) of protons from the 20-30 % most central Ag(1.58A GeV)+Ag events as well as their ratios to the SR fit functions (lower right).

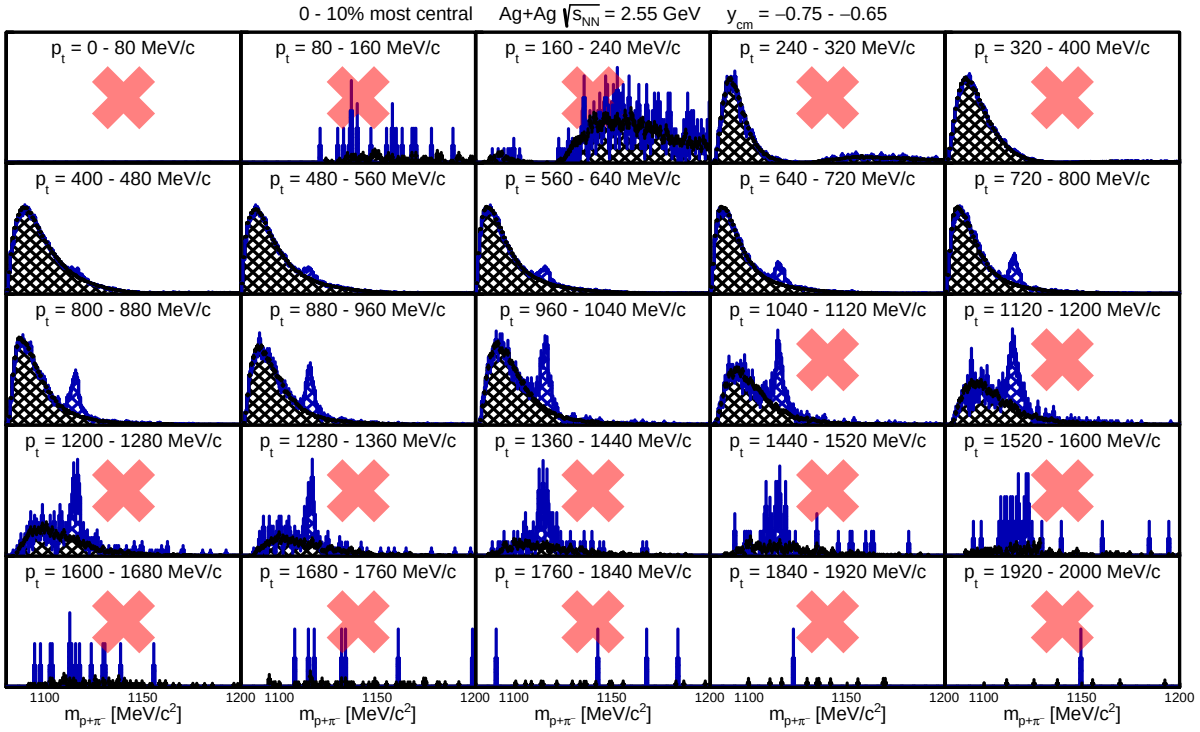

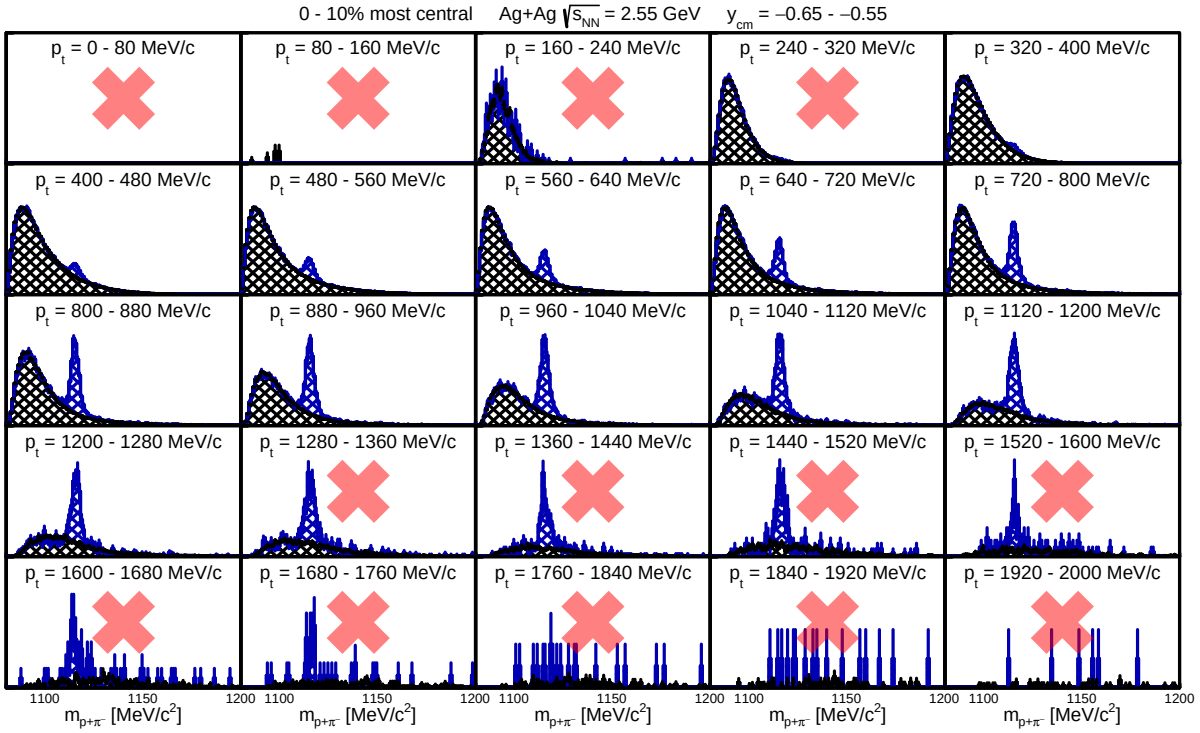

Figure A.3.: Invariant mass distributions of p-π^- pairs for all transverse momentum intervals and the rapidity intervals y_{cm} = –0.75 - –0.65 and –0.65 - –0.55 from the 0-10 % most central Ag(1.58A GeV)+Ag events.

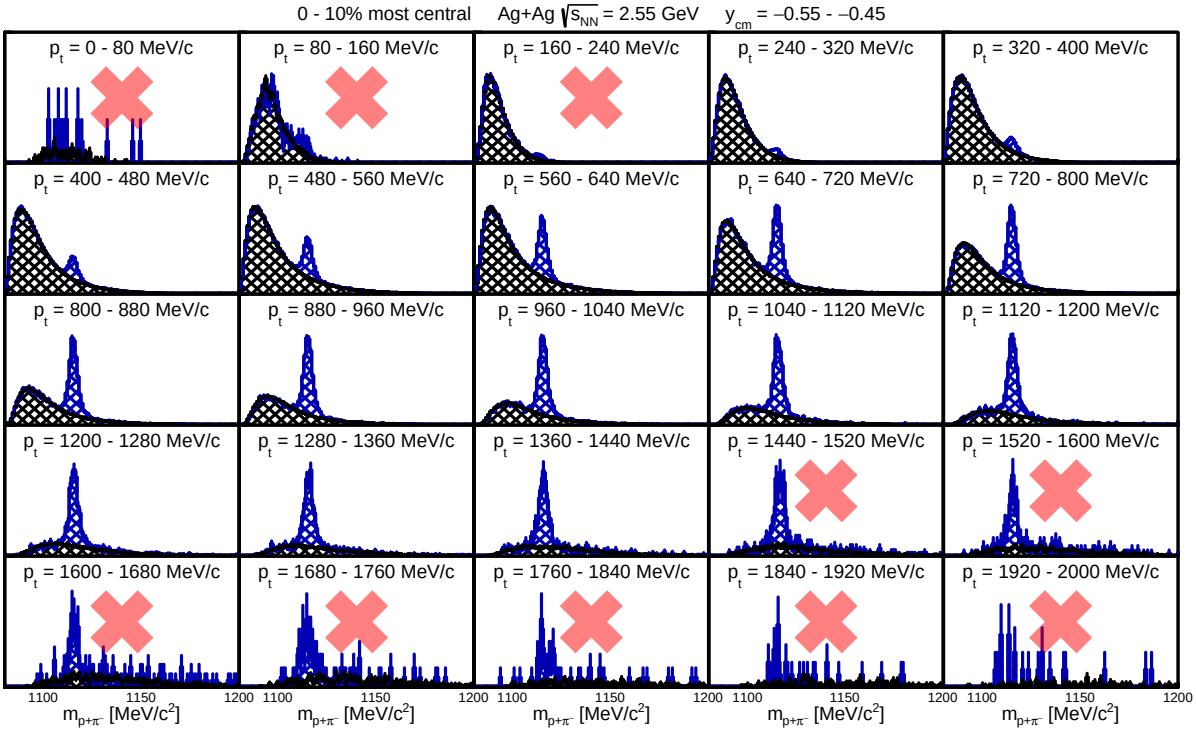

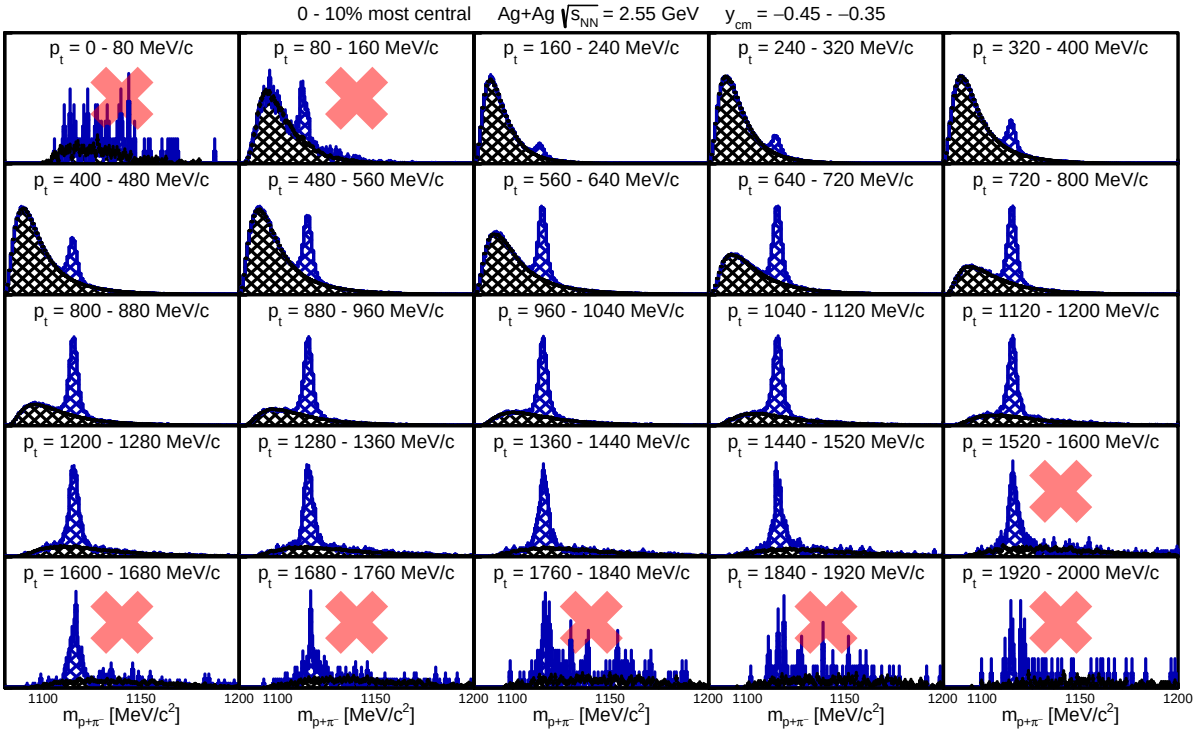

Figure A.4.: Invariant mass distributions of p-π^- pairs for all transverse momentum intervals and the rapidity intervals y_{cm} = –0.55 - –0.45 and –0.45 - –0.35 from the 0-10 % most central Ag(1.58A GeV)+Ag events.

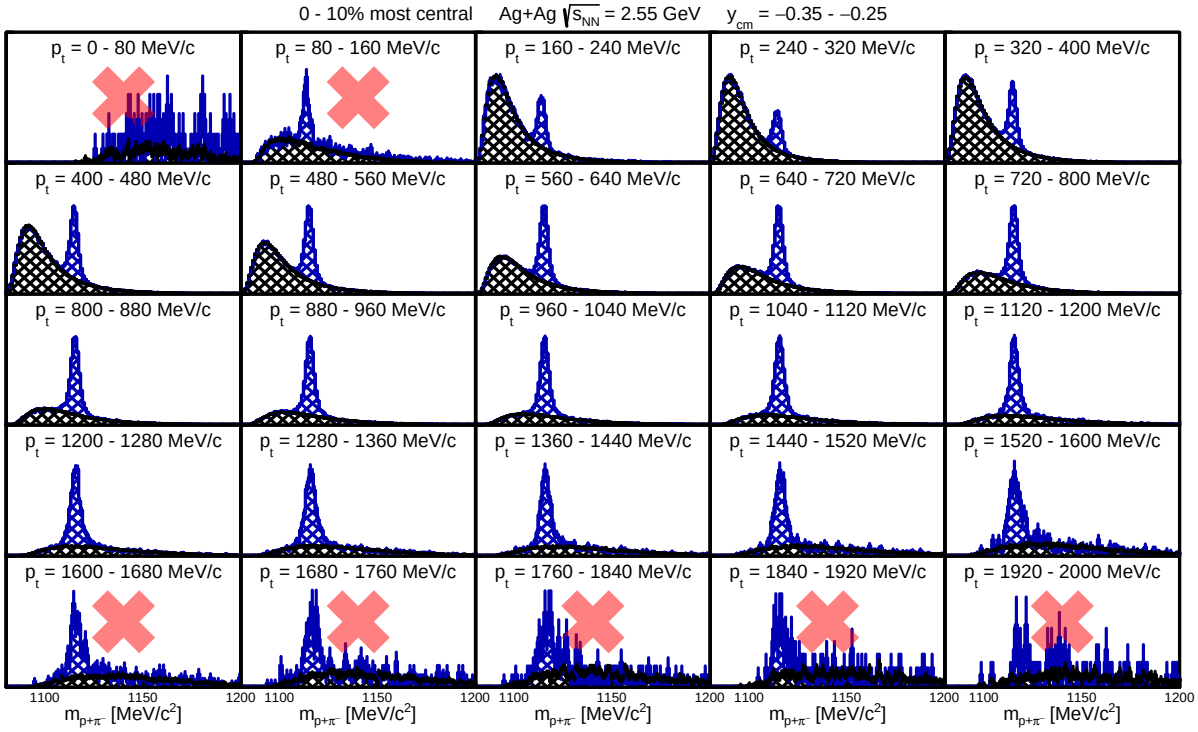

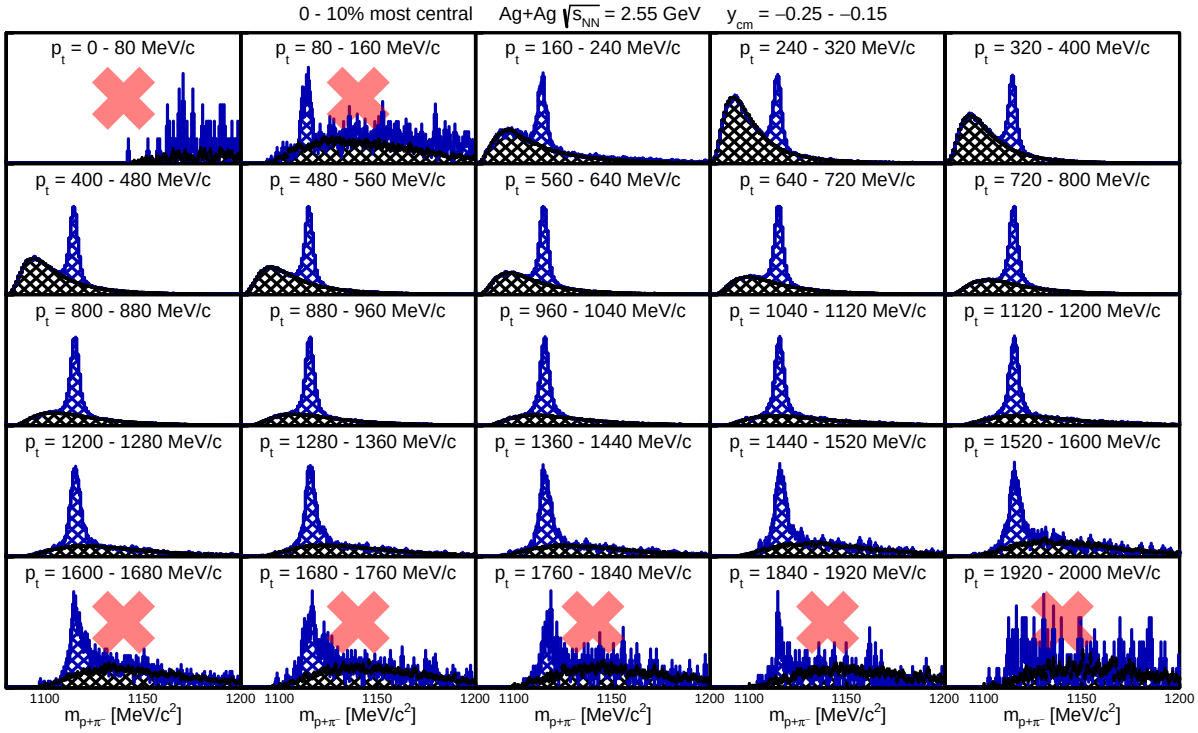

Figure A.5.: Invariant mass distributions of p-π^- pairs for all transverse momentum intervals and the rapidity intervals y_{cm} = –0.35 - –0.25 and –0.25 - –0.15 from the 0-10 % most central Ag(1.58A GeV)+Ag events.

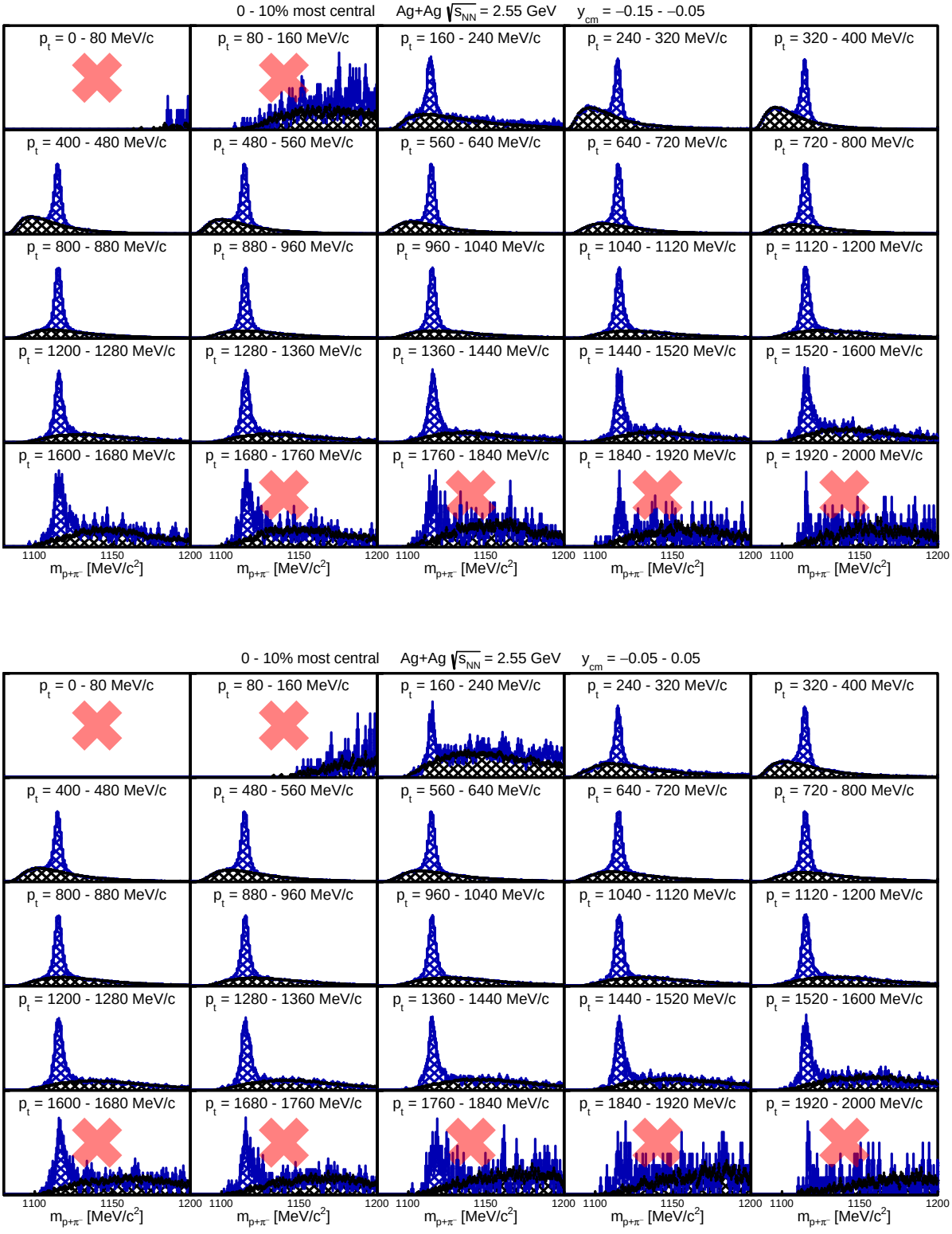

Figure A.6.: Invariant mass distributions of p-π^- pairs for all transverse momentum intervals and the rapidity intervals y_{cm} = –0.15 - –0.05 and –0.05 - 0.05 from the 0-10 % most central Ag(1.58A GeV)+Ag events.

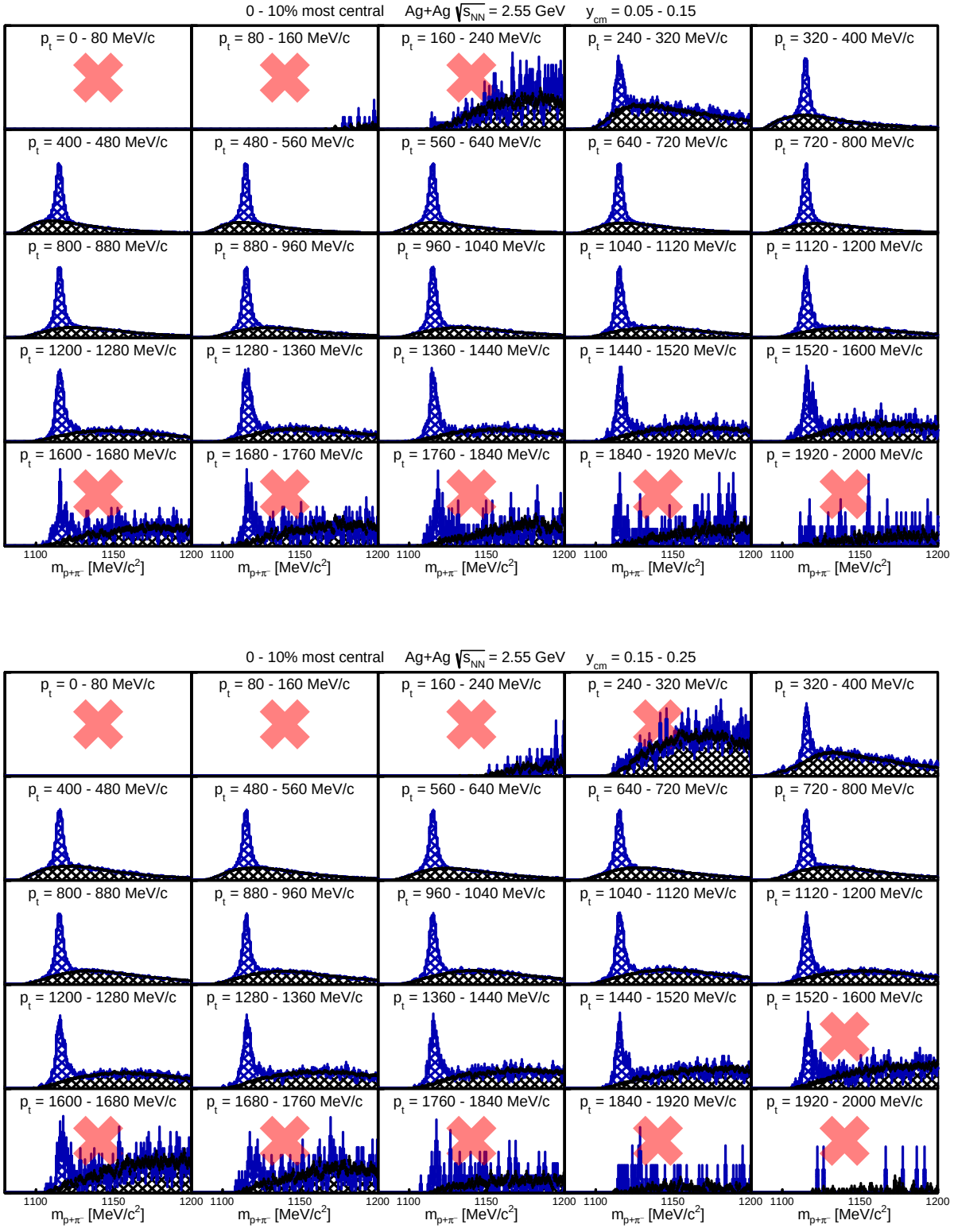

Figure A.7.: Invariant mass distributions of p-π^- pairs for all transverse momentum intervals and the rapidity intervals y_{cm} = 0.05 - 0.15 and 0.15 - 0.25 from the 0-10 % most central Ag(1.58A GeV)+Ag events.

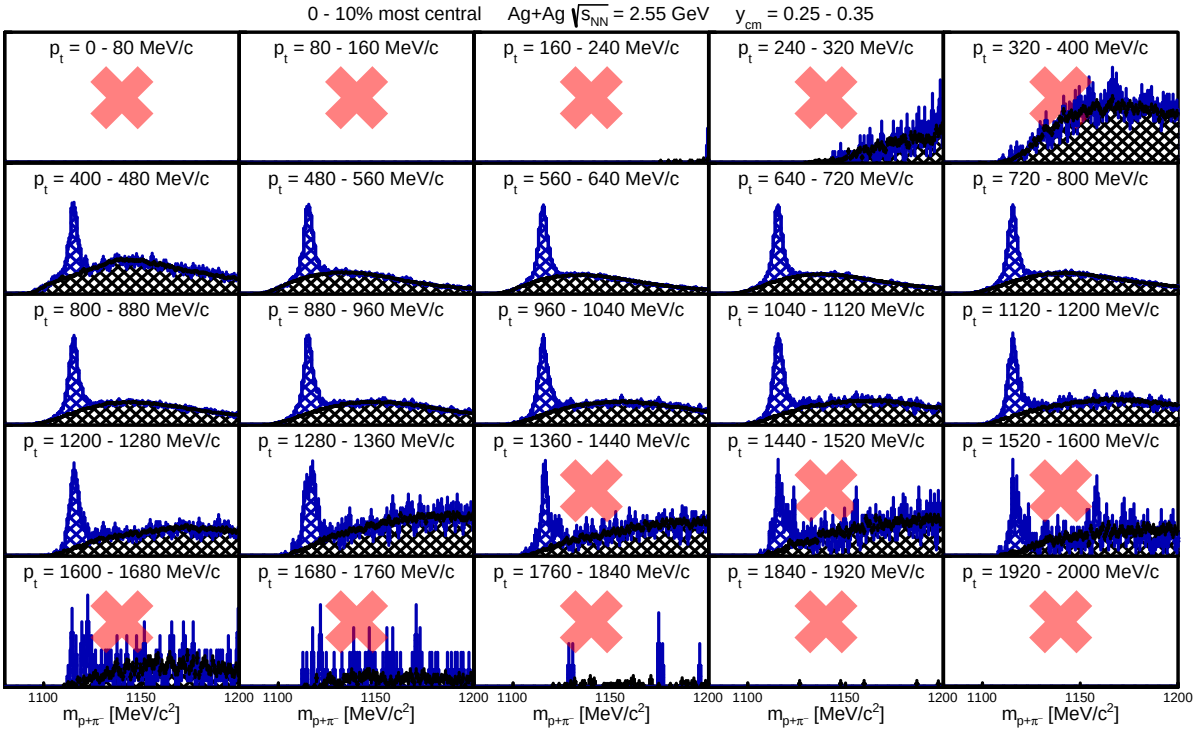

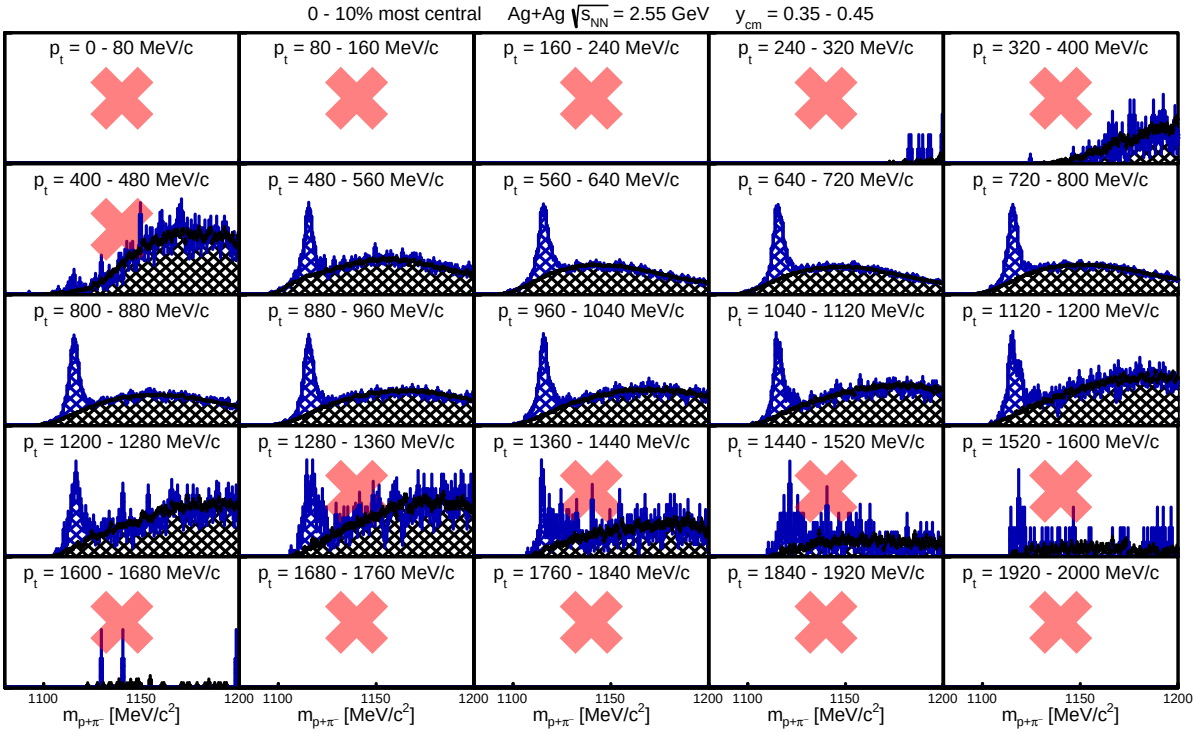

Figure A.8.: Invariant mass distributions of p-π^- pairs for all transverse momentum intervals and the rapidity intervals y_{cm} = 0.25 - 0.35 and 0.35 - 0.45 from the 0-10 % most central Ag(1.58A GeV)+Ag events.

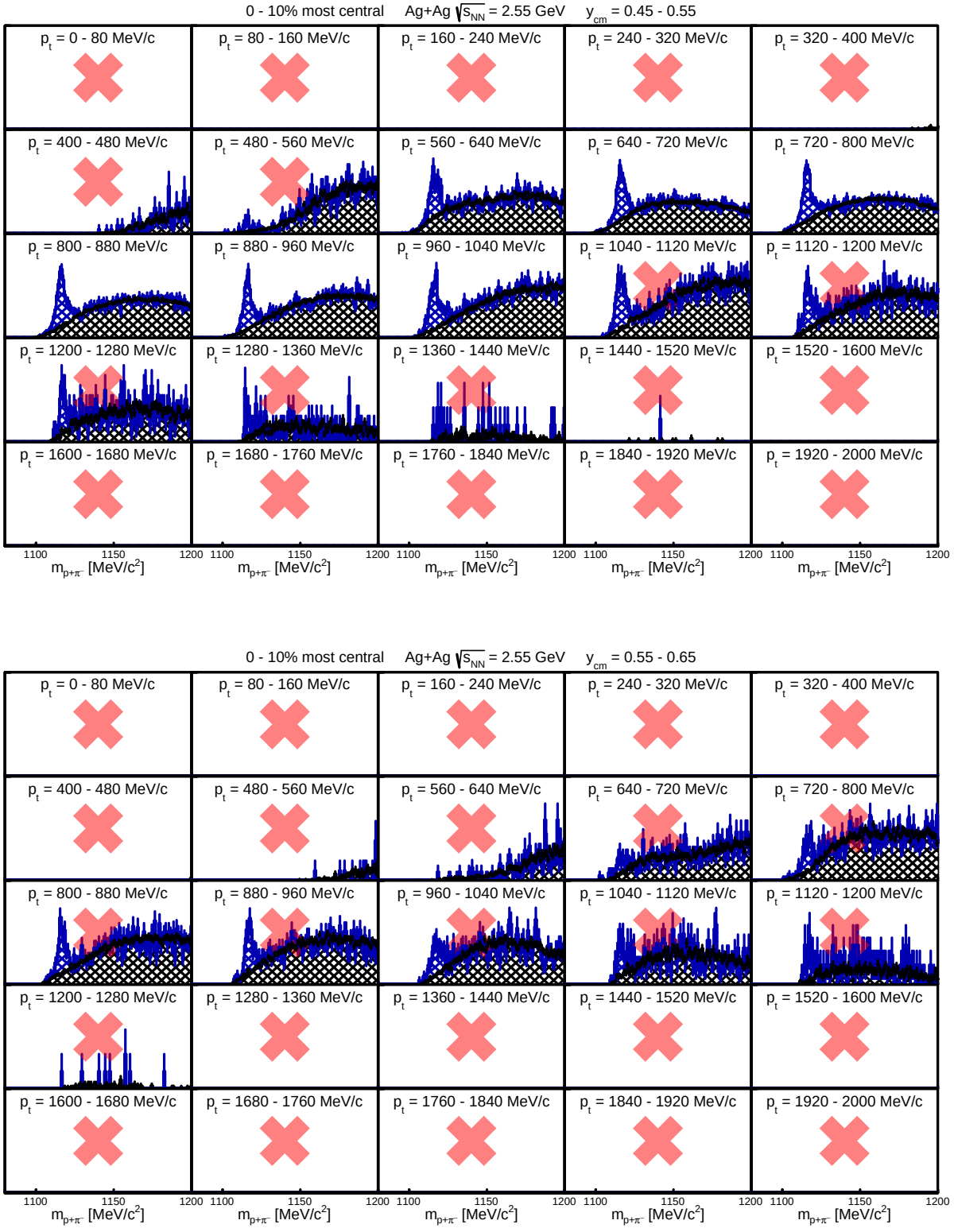

Figure A.9.: Invariant mass distributions of p-π^- pairs for all transverse momentum intervals and the rapidity intervals y_{cm} = 0.45 - 0.55 and 0.55 - 0.65 from the 0-10 % most central Ag(1.58A GeV)+Ag events.

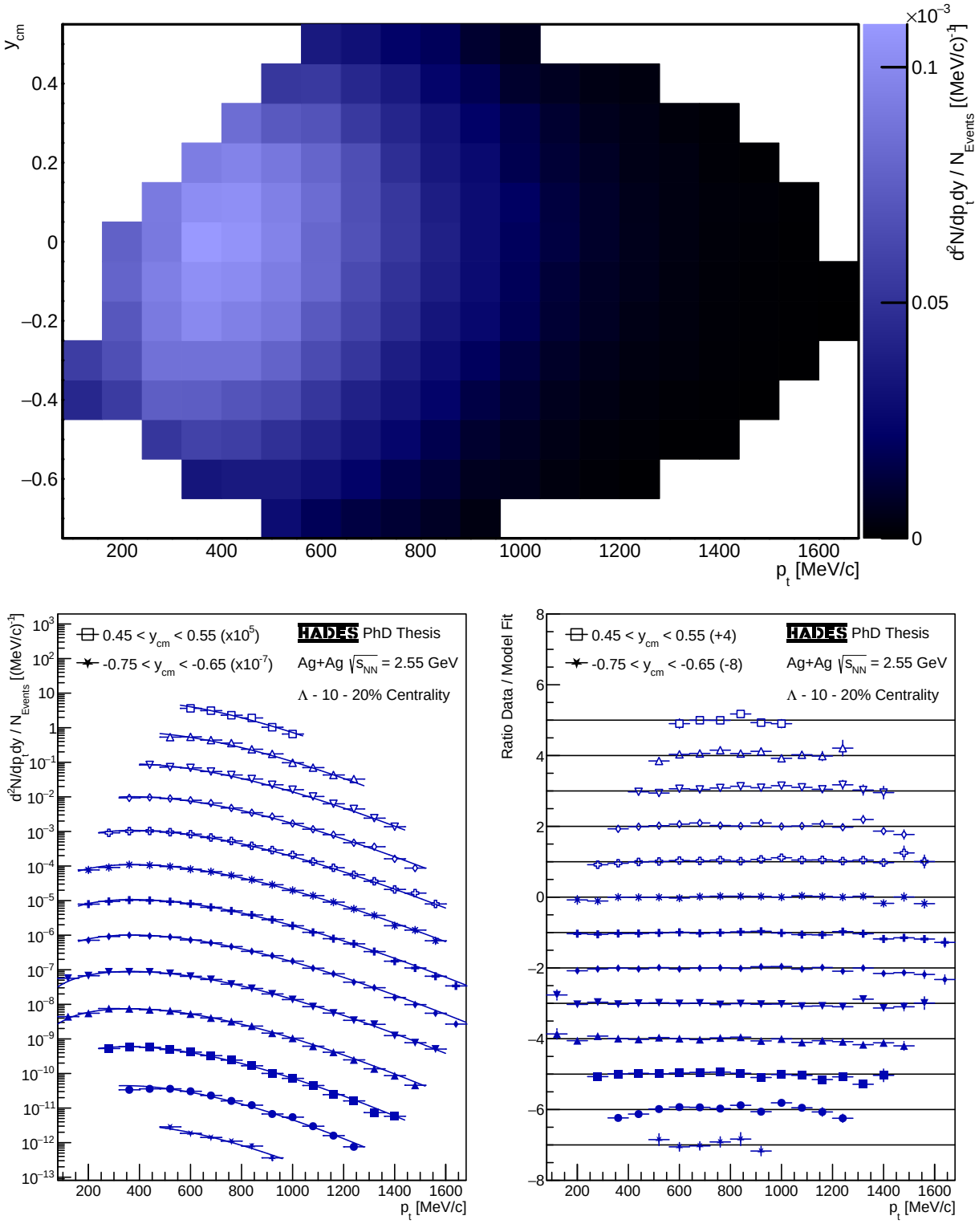

Figure A.10.: Corrected and normalized emission rates (upper panel) and transverse momentum spectra (lower left) of Λ hyperons from the 10-20 % most central Ag(1.58A GeV)+Ag events as well as their ratios to the DIS fit functions (lower right).

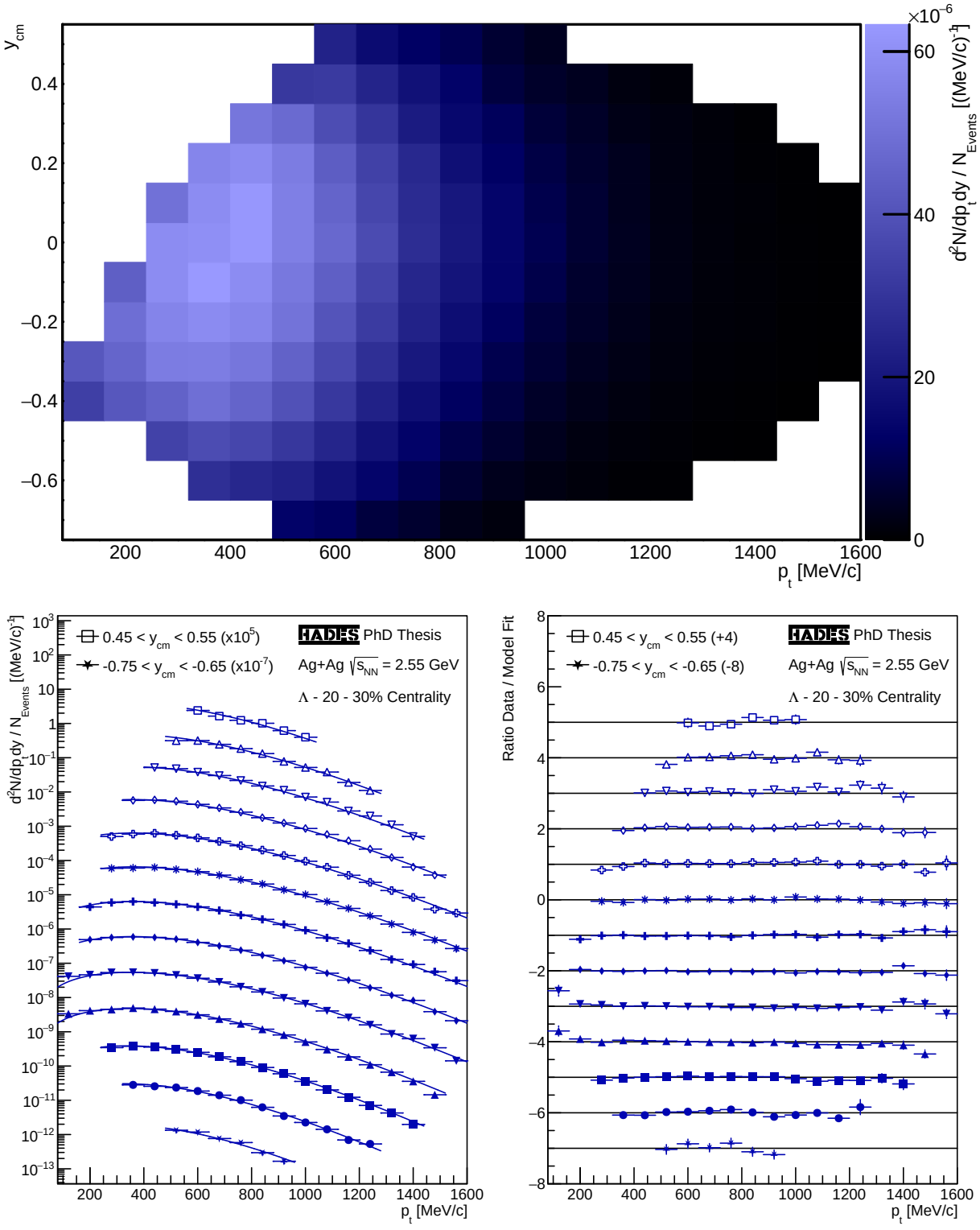

Figure A.11.: Corrected and normalized emission rates (upper panel) and transverse momentum spectra (lower left) of Λ hyperons from the 20-30 % most central Ag(1.58A GeV)+Ag events as well as their ratios to the DIS fit functions (lower right).

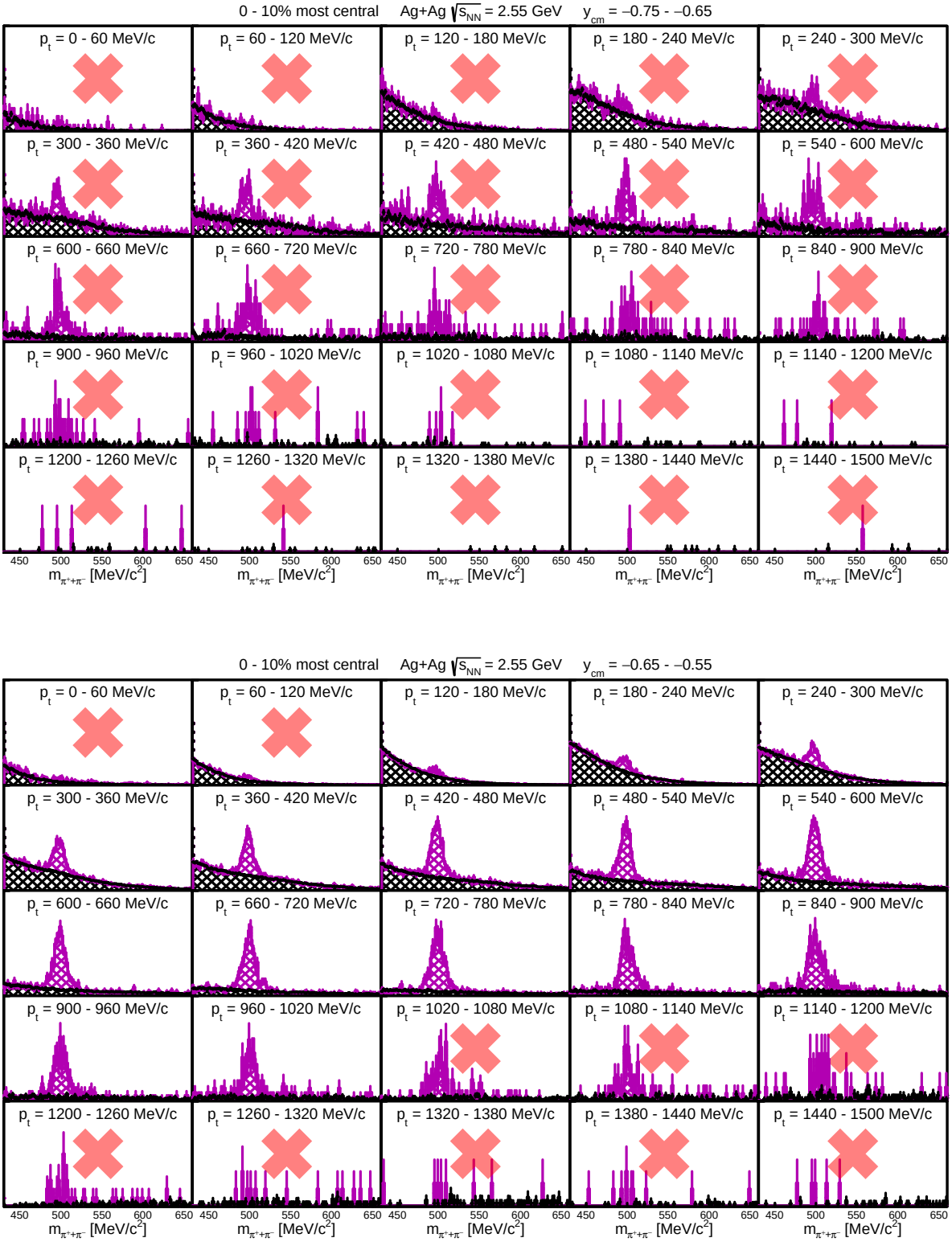

Figure A.12.: Invariant mass distributions of π^+-π^- pairs for all transverse momentum intervals and the rapidity intervals y_{cm} = –0.75 - –0.65 and –0.65 - –0.55 from the 0-10 % most central Ag(1.58A GeV)+Ag events.

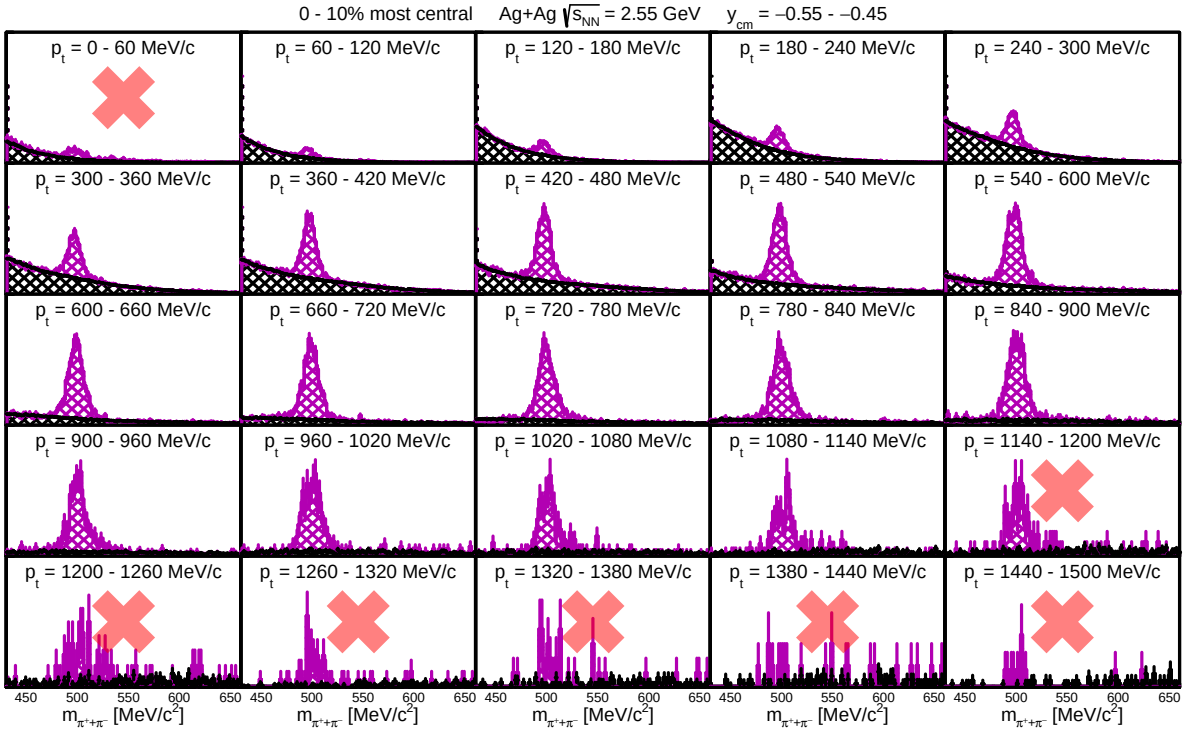

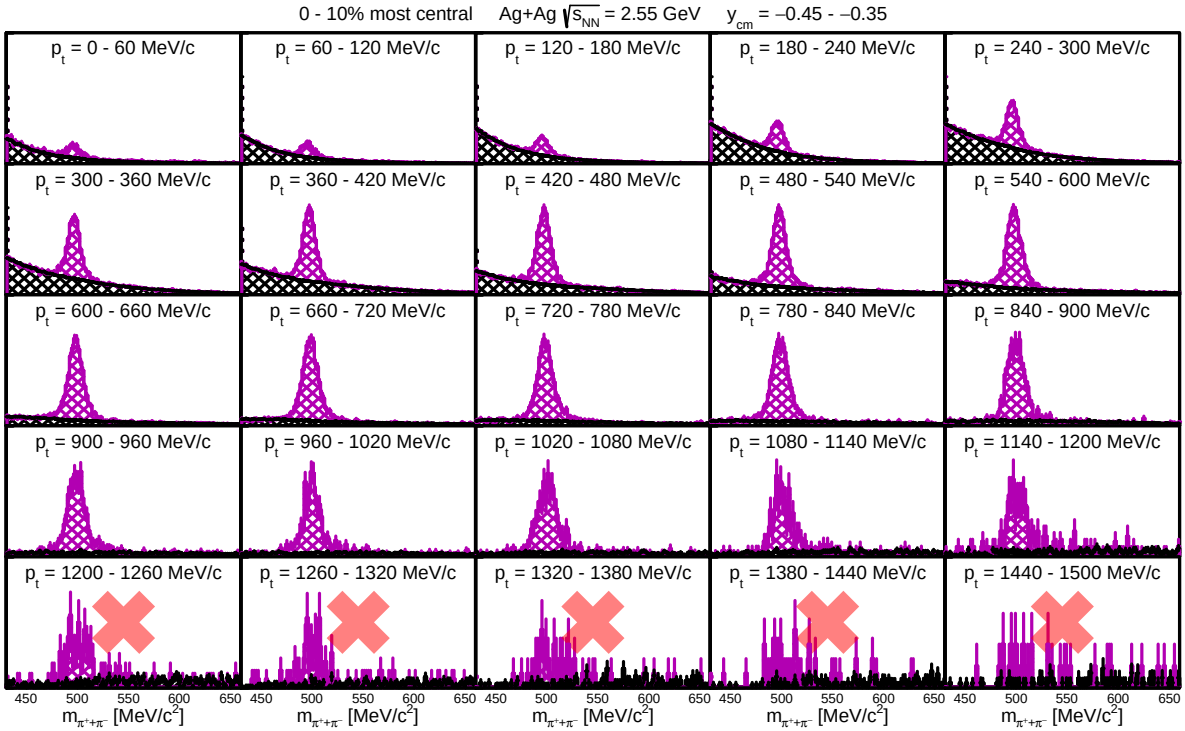

Figure A.13.: Invariant mass distributions of π^+-π^- pairs for all transverse momentum intervals and the rapidity intervals y_{cm} = –0.55 - –0.45 and –0.45 - –0.35 from the 0-10 % most central Ag(1.58A GeV)+Ag events.

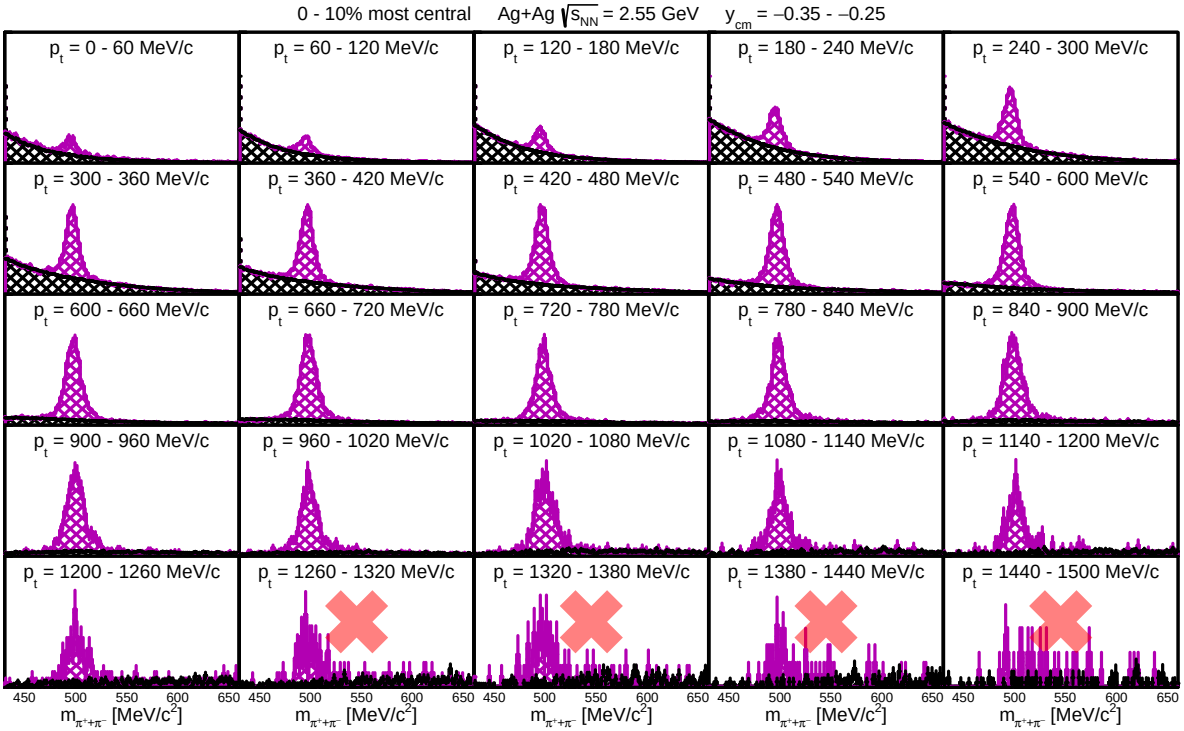

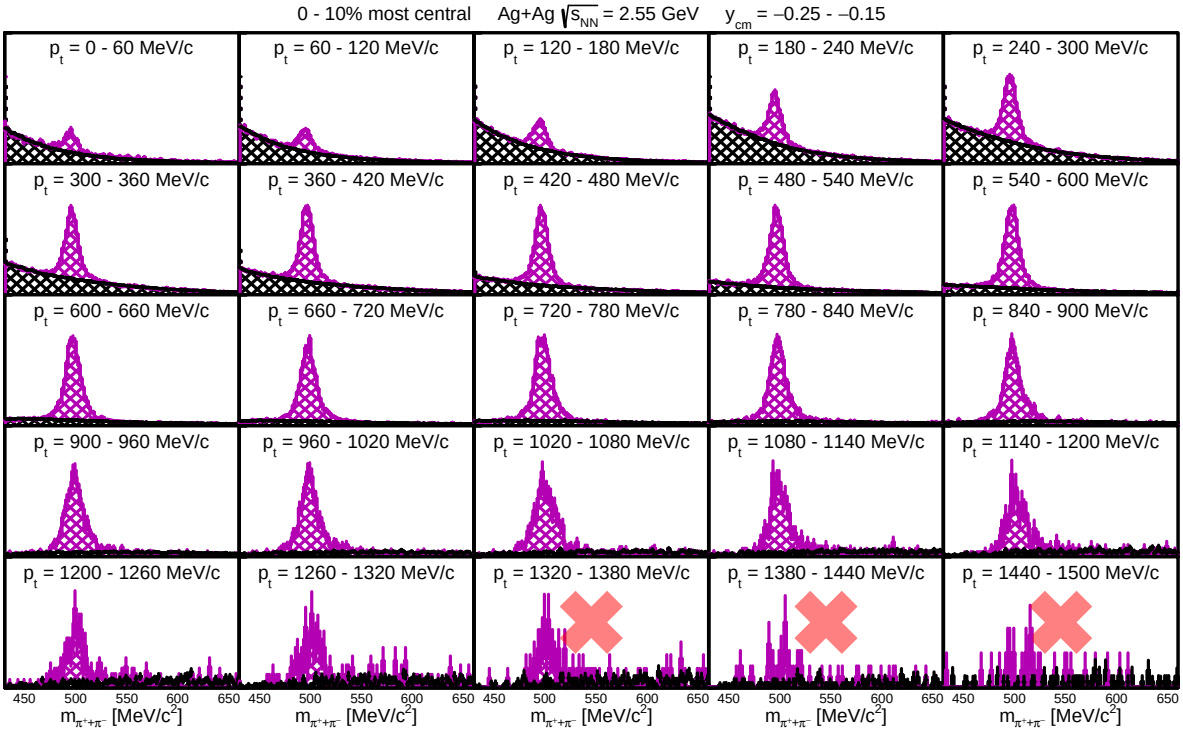

Figure A.14.: Invariant mass distributions of π^+-π^- pairs for all transverse momentum intervals and the rapidity intervals y_{cm} = –0.35 - –0.25 and –0.25 - –0.15 from the 0-10 % most central Ag(1.58A GeV)+Ag events.

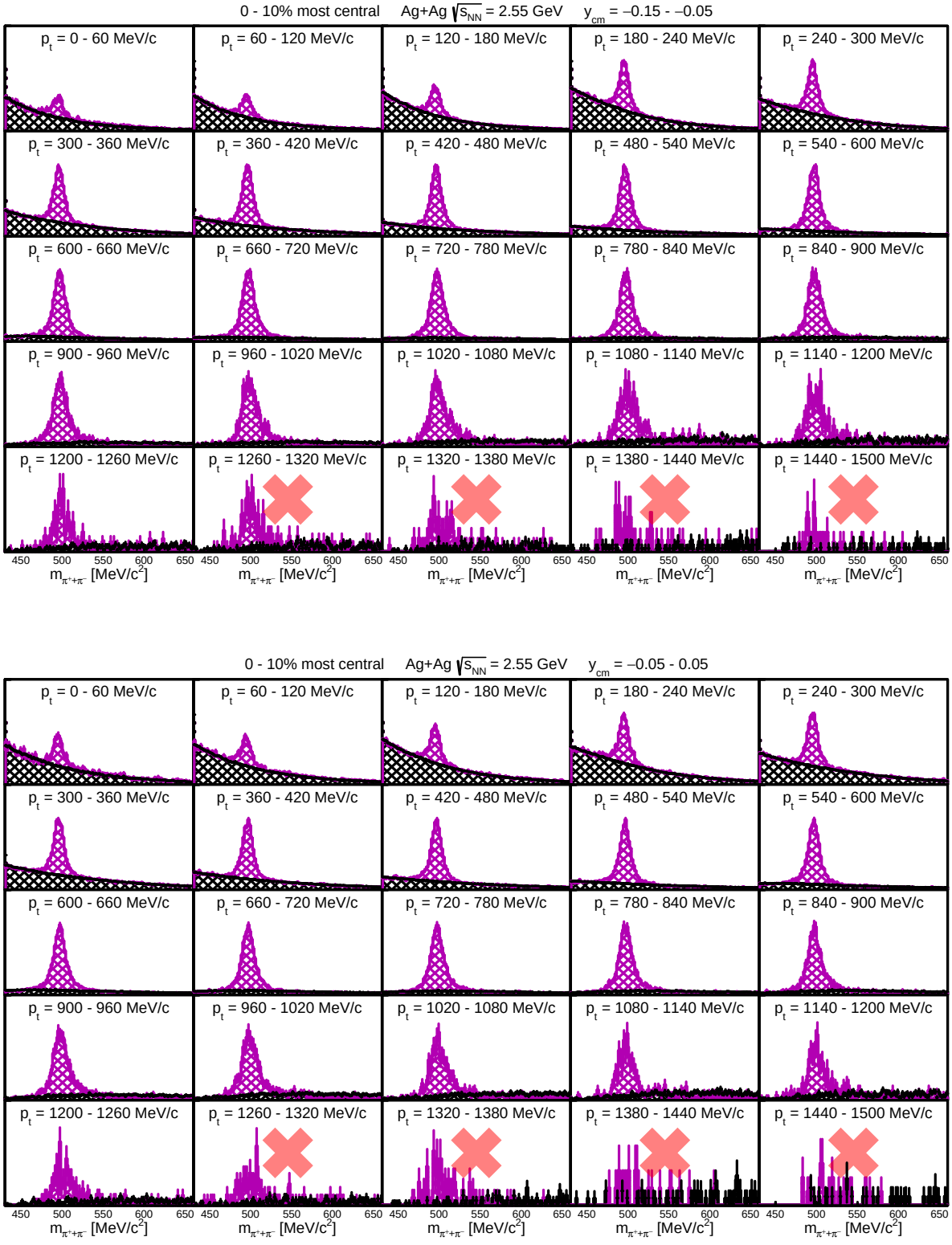

Figure A.15.: Invariant mass distributions of π^+-π^- pairs for all transverse momentum intervals and the rapidity intervals y_{cm} = –0.15 - –0.05 and –0.05 - 0.05 from the 0-10 % most central Ag(1.58A GeV)+Ag events.

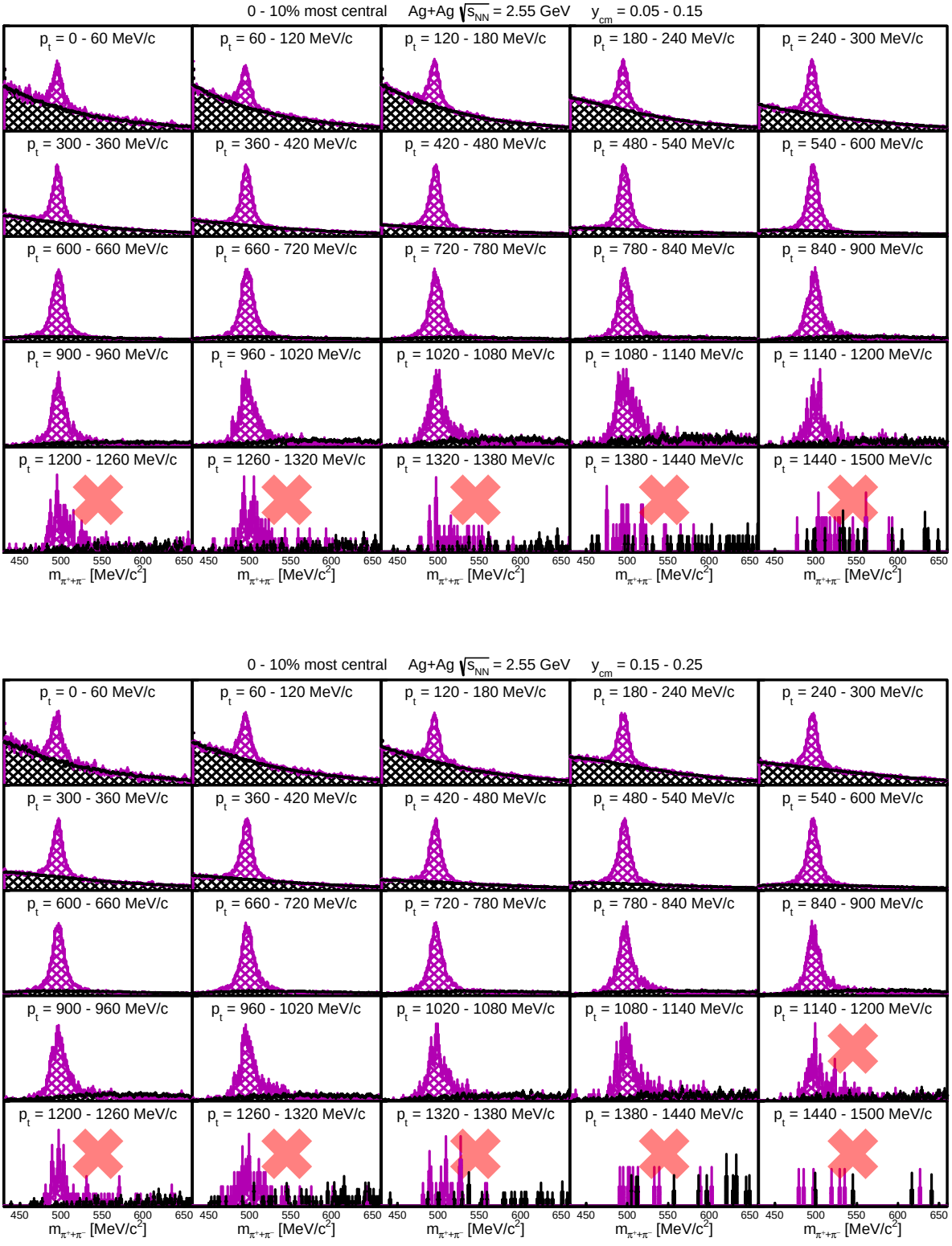

Figure A.16.: Invariant mass distributions of π^+-π^- pairs for all transverse momentum intervals and the rapidity intervals y_{cm} = 0.05 - 0.15 and 0.15 - 0.25 from the 0-10 % most central Ag(1.58A GeV)+Ag events.

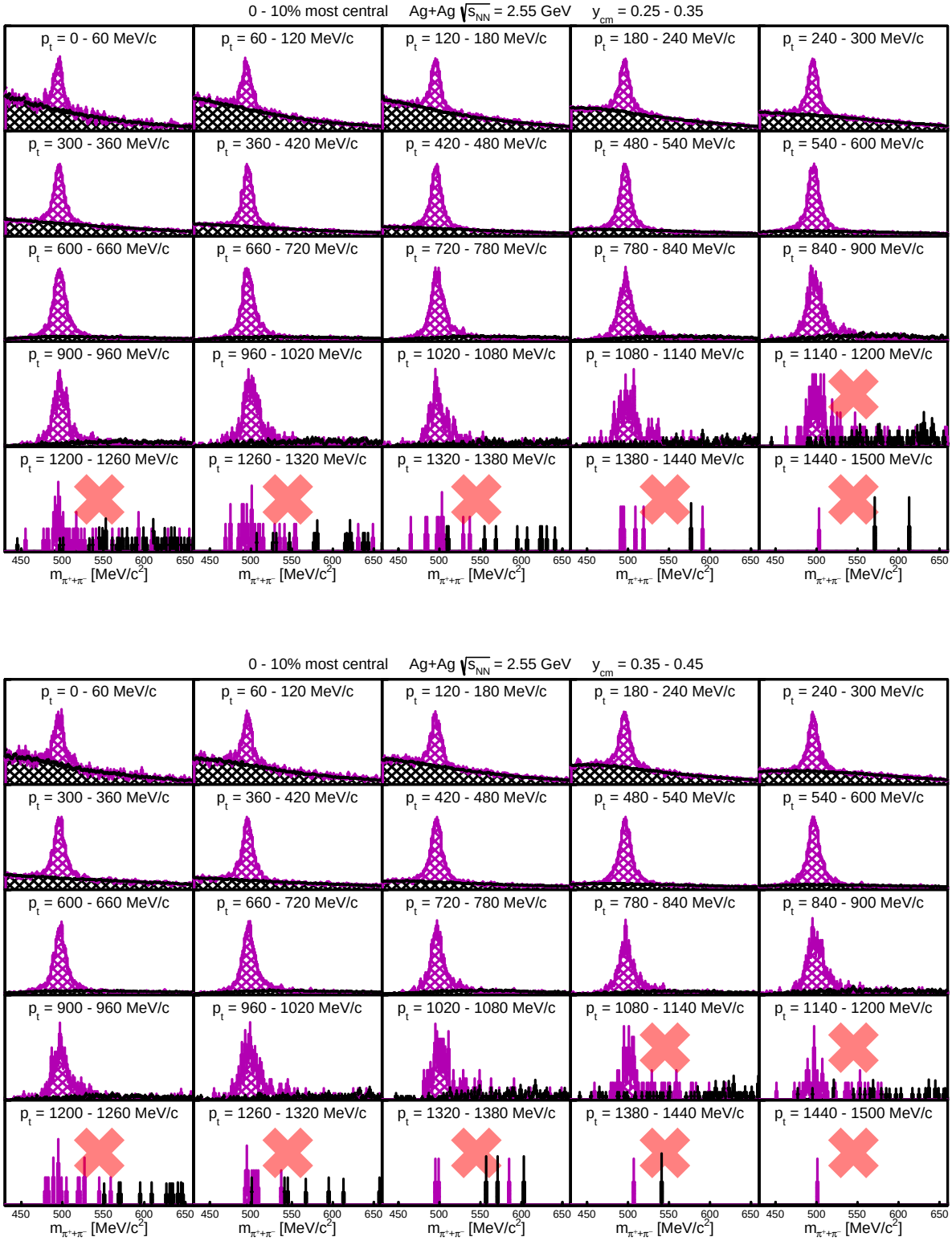

Figure A.17.: Invariant mass distributions of π^+-π^- pairs for all transverse momentum intervals and the rapidity intervals y_{cm} = 0.25 - 0.35 and 0.35 - 0.45 from the 0-10 % most central Ag(1.58A GeV)+Ag events.

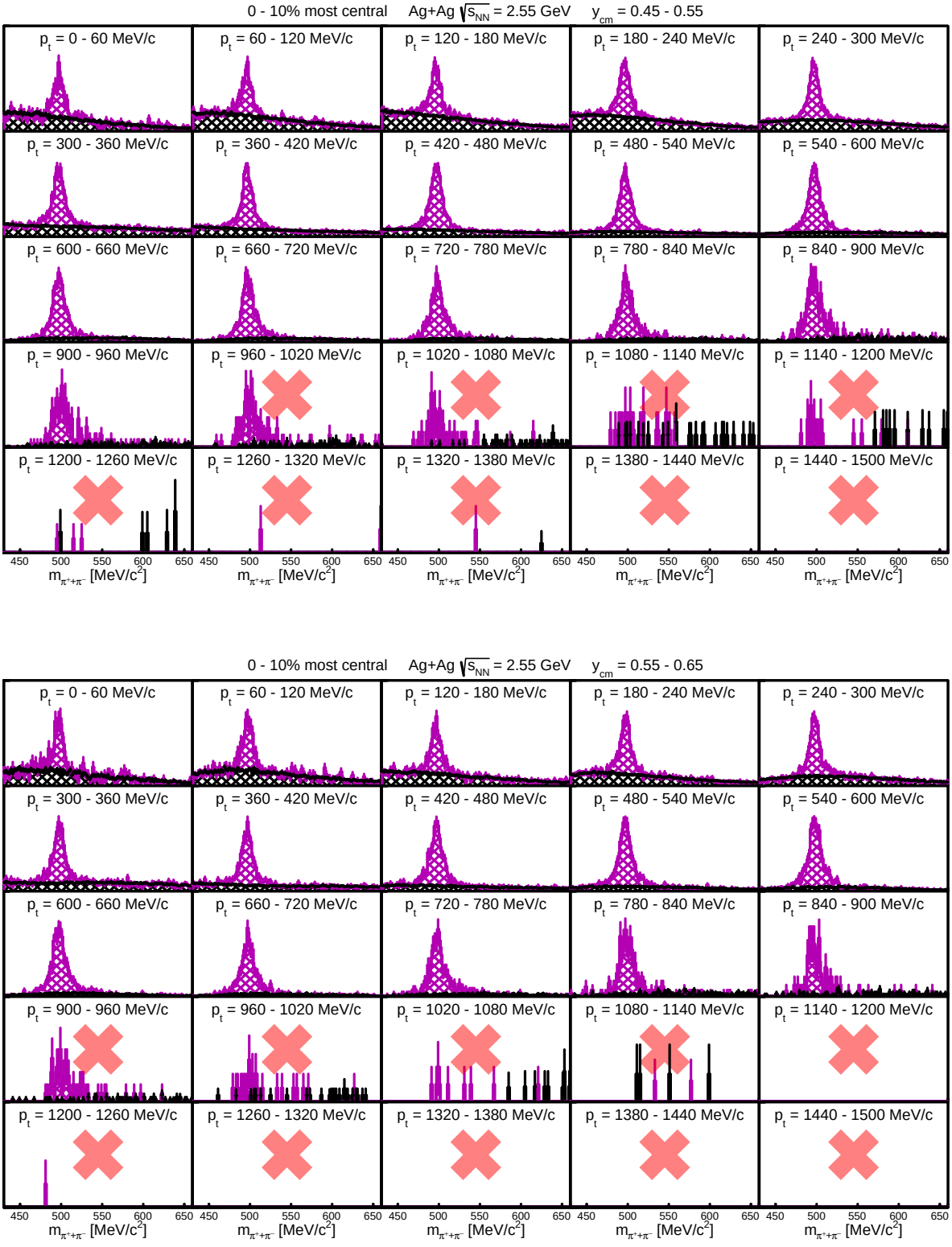

Figure A.18.: Invariant mass distributions of π^+-π^- pairs for all transverse momentum intervals and the rapidity intervals y_{cm} = 0.45 - 0.55 and 0.55 - 0.65 from the 0-10 % most central Ag(1.58A GeV)+Ag events.

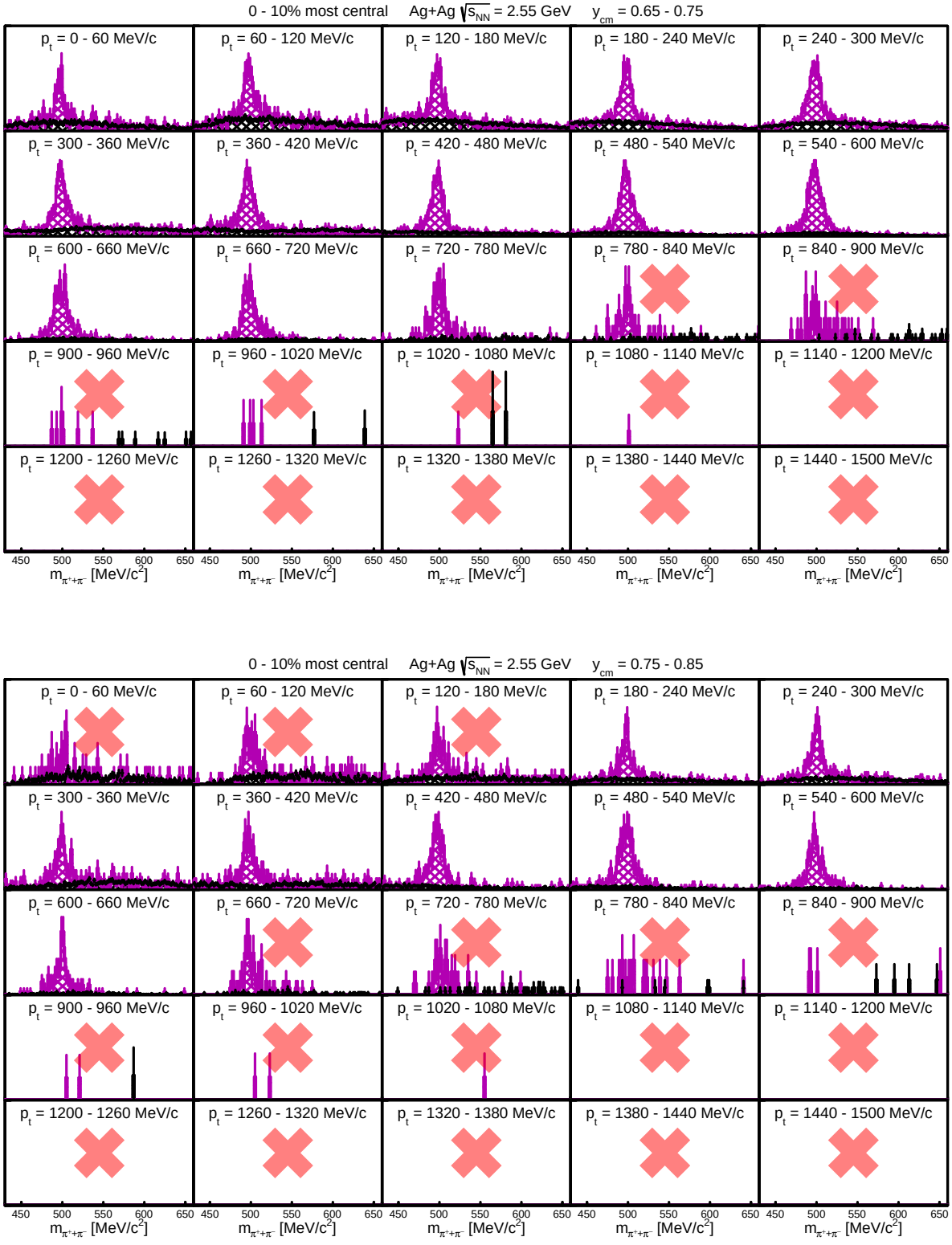

Figure A.19.: Invariant mass distributions of π^+-π^- pairs for all transverse momentum intervals and the rapidity intervals y_{cm} = 0.65 - 0.75 and 0.75 - 0.85 from the 0-10 % most central Ag(1.58A GeV)+Ag events.

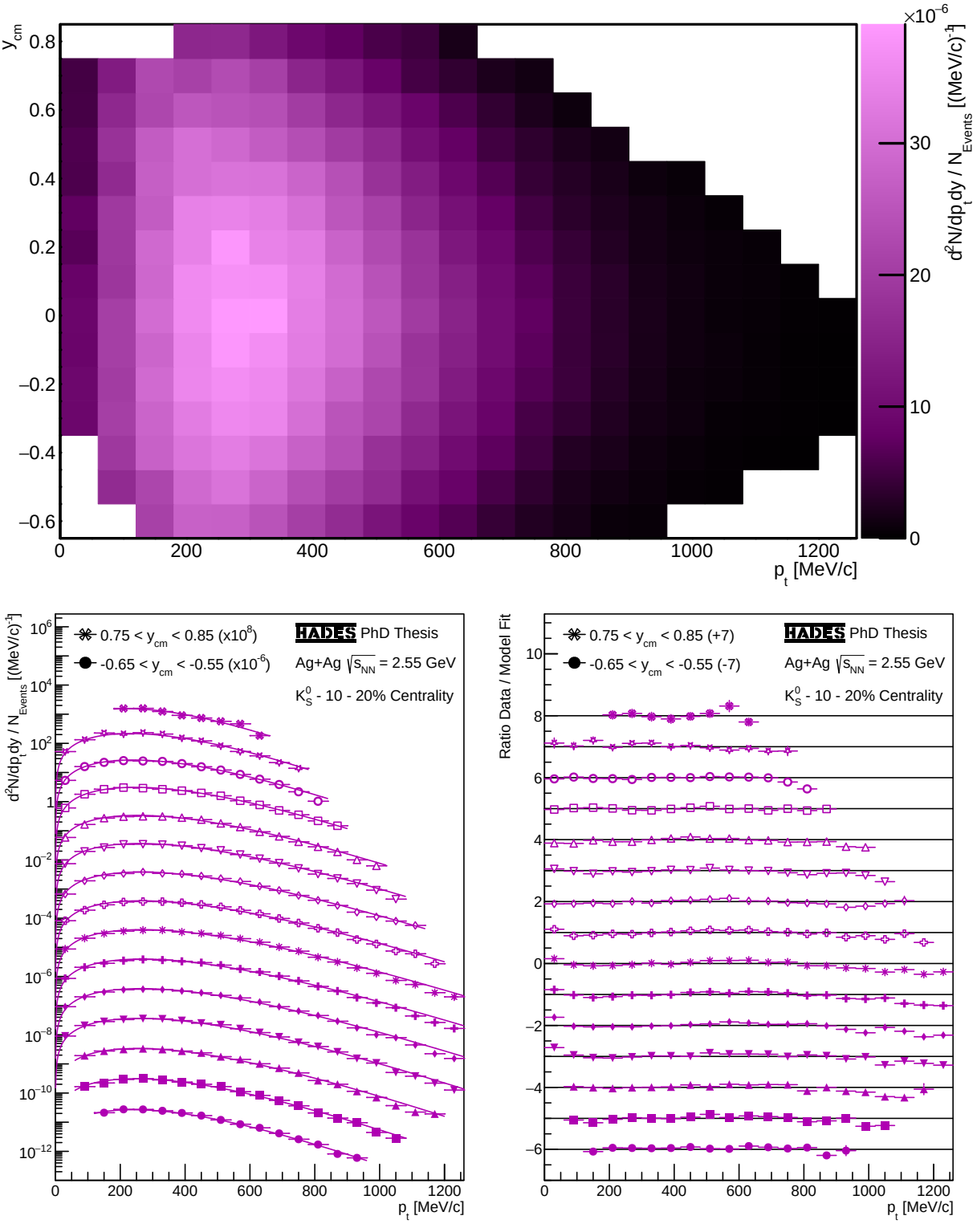

Figure A.20.: Corrected and normalized emission rates (upper panel) and transverse momentum spectra (lower left) of K^0_S mesons from the 10-20 % most central Ag(1.58A GeV)+Ag events as well as their ratios to the DIS fit functions (lower right).

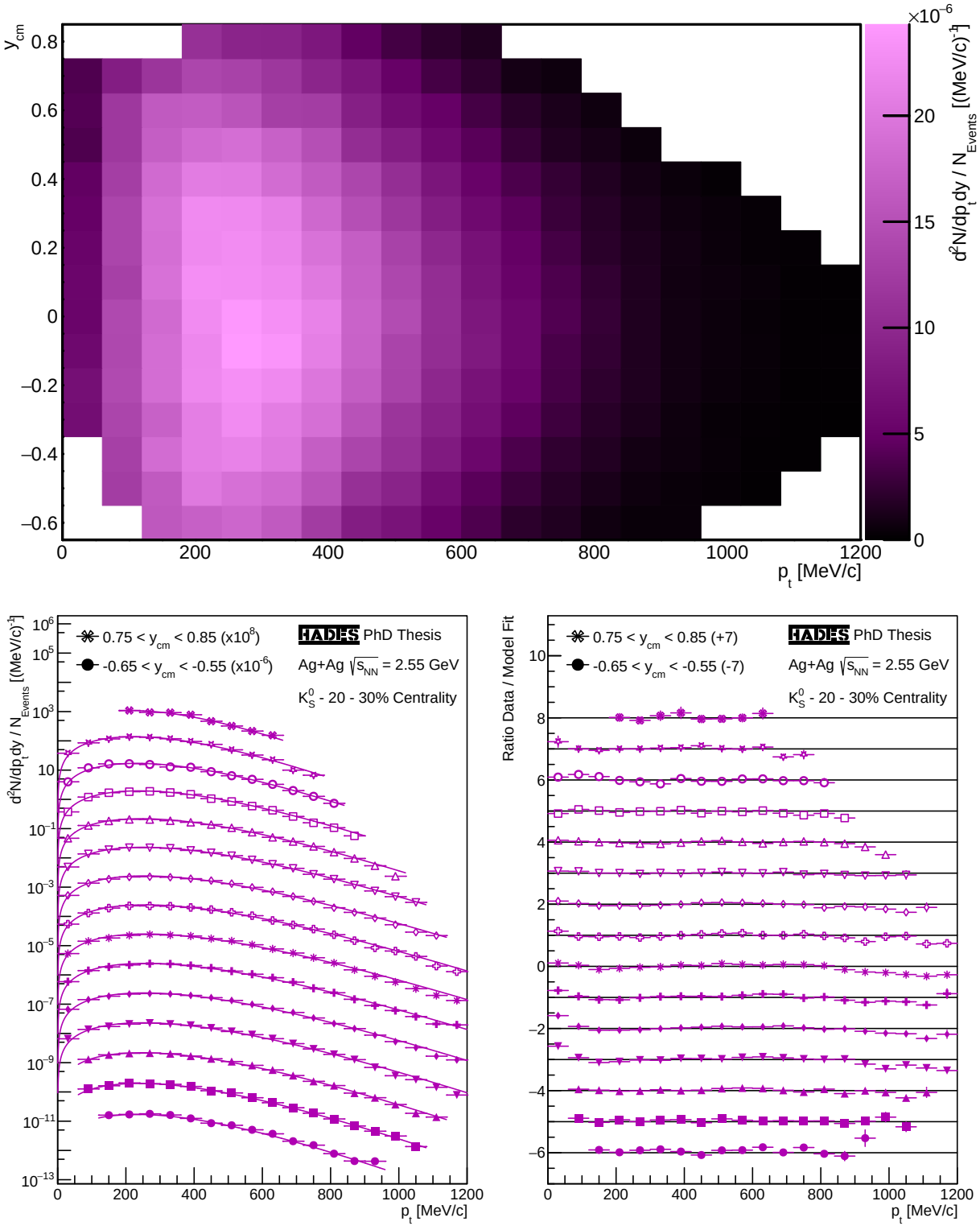

Figure A.21.: Corrected and normalized emission rates (upper panel) and transverse momentum spectra (lower left) of K^0_S mesons from the 20-30 % most central Ag(1.58A GeV)+Ag events as well as their ratios to the DIS fit functions (lower right).

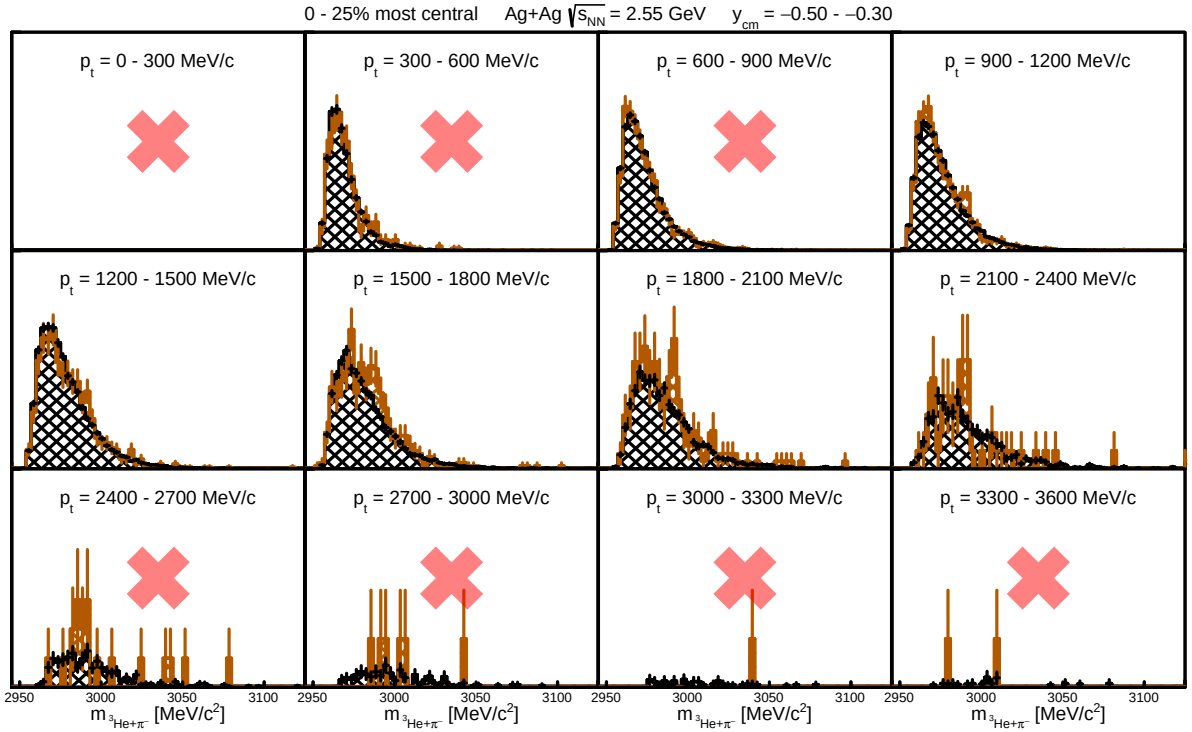

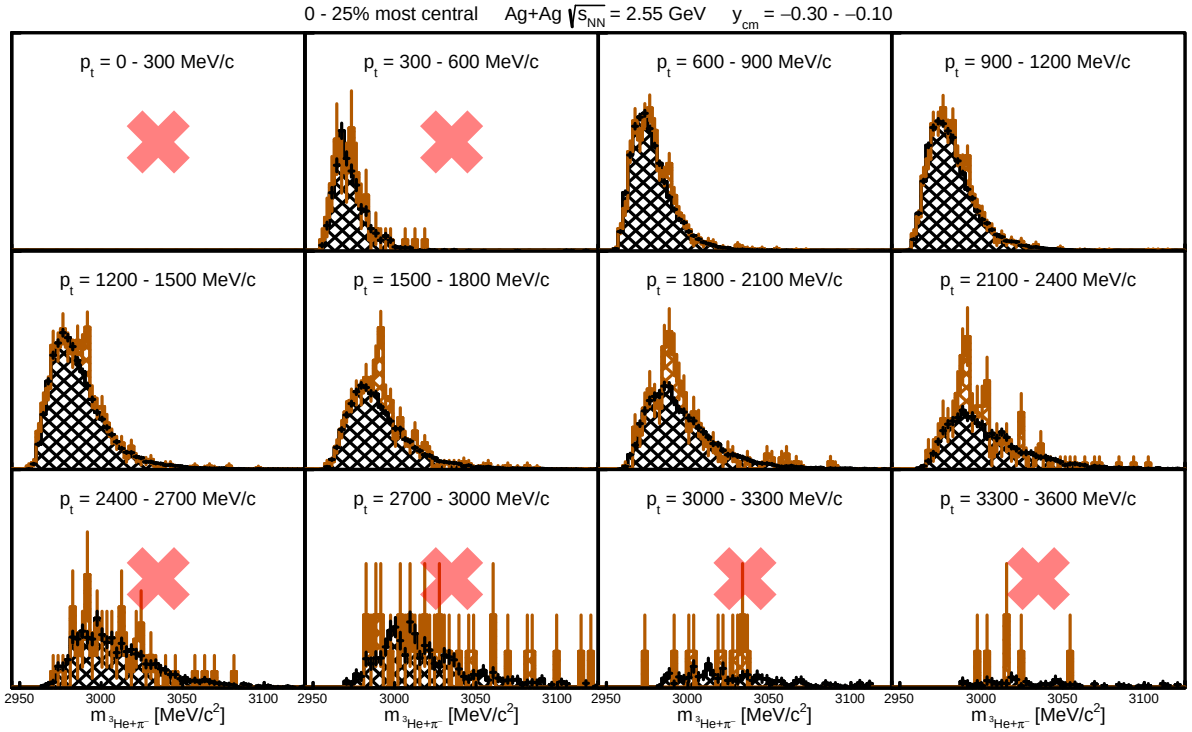

Figure A.22.: Invariant mass distributions of ^{3}He-π^- pairs for all transverse momentum intervals and the rapidity intervals y_{cm} = –0.5 - –0.3 and –0.3 - –0.1 from the 0-25 % most central Ag(1.58A GeV)+Ag events.

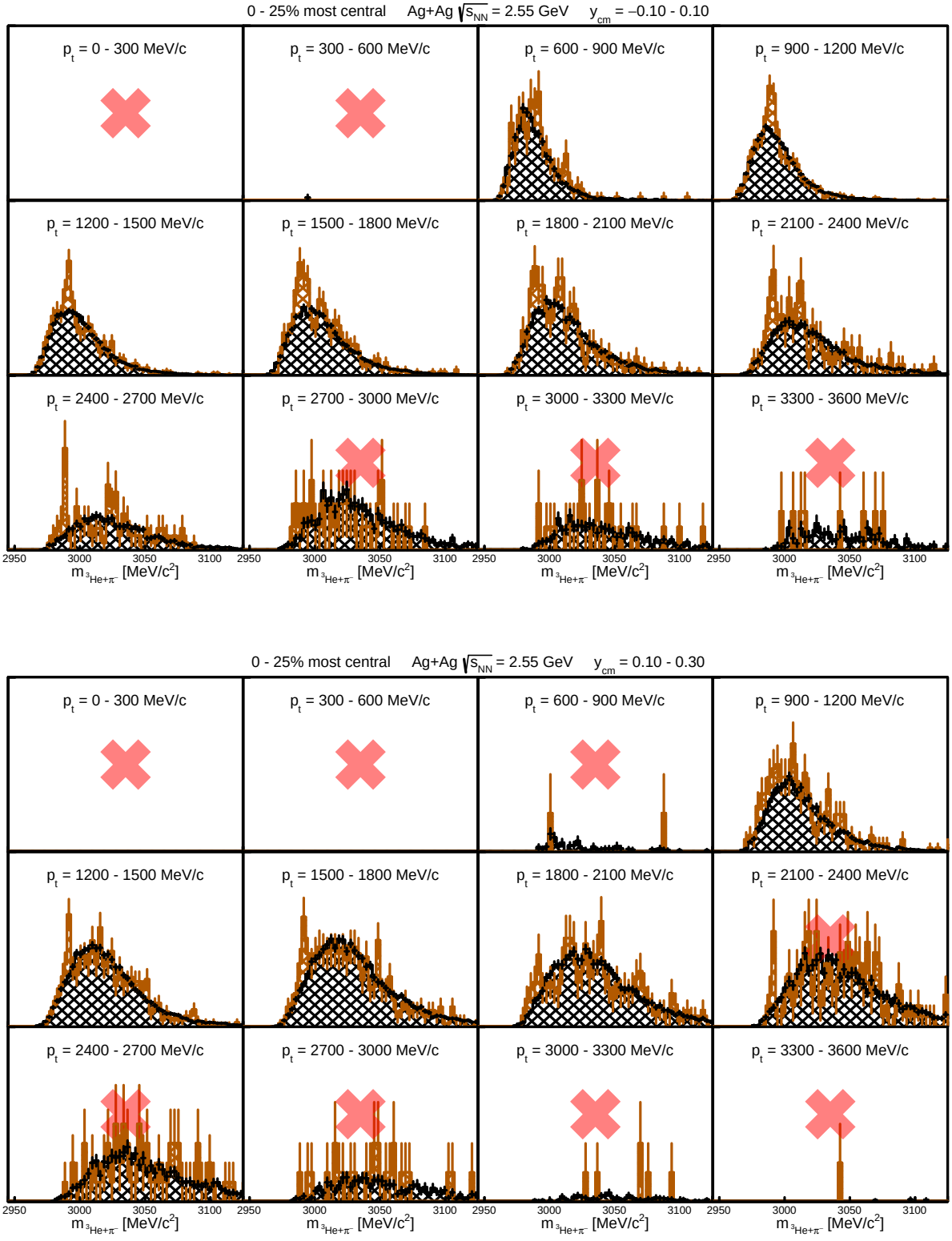

Figure A.23.: Invariant mass distributions of ^{3}He-π^- pairs for all transverse momentum intervals and the rapidity intervals y_{cm} = –0.1 - 0.1 and 0.1 - 0.3 from the 0-25 % most central Ag(1.58A GeV)+Ag events.

List of Figures

List of Tables

List of Acronyms and Apronyms

ADC . . . . Analog to Digital Converter
AGS . . . . Alternating Gradient Synchrotron
ALICE . . . A Large Ion Collider Experiment [3]
ANN . . . . Artificial Neural Network
AP . . . . . Armenteros-Podolanski method [147]
ASD . . . . Amplifier-Shaper-Discriminator
ASIC . . . . Application-Specific Integrated Circuit
ATLAS . . A Toroidal LHC ApparatuS [1]
BDT . . . . Boosted Decision Tree
BFGS . . . Broyden-Fletcher-Goldfarb-Shannon
BNL . . . . Brookhaven National Laboratory
BP . . . . . Back Propagation
BR . . . . . Branching Ratio
BT . . . . . BackTracking
CAD . . . . Computer Aided Design
CBM . . . . Compressed Baryonic Matter experiment [11]
CDF . . . . Cumulative Distribution Function
CERN . . . *Conseil Européen pour la Recherche Nucléaire* (European Organization for Nuclear Research)
CL . . . . . Confidence Level
CM . . . . . Center of Mass
CMOS . . . Complementary Metal-Oxide-Semiconductor
CMS . . . . Compact Muon Solenoid [77] / Center of Mass System
COSY . . . COoler SYnchrotron
CPT . . . . Chiral Perturbation Theory
CTS . . . . Central Trigger System
CVD . . . . Chemical Vapor Deposition method
DAC . . . . Digital to Anlaog Converter
DAQ . . . . Data AcQuisition
DCA . . . . Distance of Closest Approach
DIS . . . . . Double Isotropic-Statistical model
DLS . . . . . DiLepton Spectreometer [182]
DNN . . . . Deep Neural Network
DPG . . . . *Deutsche Physikalische Gesellschaft* (German Physical Society)
DSR . . . . Double Siemens-Rasmussen model
DST . . . . Data Summary Tape
EB . . . . . Event Builder
ECAL . . . Electromagnetic CALorimeter
EoS . . . . . Equation of State
EOS . . . . Equation Of State experiment [151]
ESR . . . . Experimental Storage Ring
eV . . . . . electron Volt
FAIR . . . . Facility for Antiproton and Ion Research
FEE . . . . . Front-End Electronic
FOPI . . . . FOur PI experiment [156]
FPGA . . . Field-Programmable Gate Array
fRPC . . . . forward RPC
FRS . . . . . FRagment Separator
FW . . . . . Forward Wall
FWHM . . Full Width at Half Maximum
GEANT . . GEometry And TRacking [73]
GeV . . . . . Giga electron Volt
GiBUU . . Giessen Boltzmann-Uehling-Uhlenbeck project [74]
GNU . . . . GNU's Not UNIX
GSI . . . . . *Gesellschaft für SchwerIonenforschung* Helmholtz Center for Heavy-Ion Research
GSL . . . . . GNU Scientific Library [92]
HADES . . High Acceptance DiElectron Spectrometer [32]
HIC . . . . . Heavy-Ion Collision
HLD . . . . HADES List mode Data
HSD . . . . Hadron String Dynamics model [76]
HV . . . . . High Voltage
HYDRA . . HADES sYstem for Data Reduction and Analysis
IIS . . . . . Integrated Isotropic-Statistical model
IPU . . . . . Image Processing Unit
IQMD . . . Isospin-dependent Quantum Molecular Dynamics model [105]
IR . . . . . InfraRed
IS . . . . . Isotropic-Statistical model
ISR . . . . . Integrated Siemens-Rasmussen model
JINR . . . . Joint Institute for Nuclear Research
k-NN . . . . k-Nearest Neighbour classifier
KaoS . . . . Kaon Spectrometer [166]
keV . . . . . kilo electron Volt
LAN . . . . Local Area Network
LBNL . . . Lawrence Berkeley National Laboratory
LD . . . . . Linear Discriminant analysis
LEP . . . . . Large Electron-Positron collider
LGAD . . . Low Gain Avalanche Diode /

	Detector
LH_2	Liquid Hydrogen
LHC	Large Hadron Collider
LIP	*Laboratorio de Instrumentacao e Fisica Experimental de Particulas* (Laboratory of instrumentation and Experimental Particle Physics)
LO	Leading Order
LSB	Least Significant Bit
LV	Low Voltage
MAP	MAximum ionizing Particle
MAPMT	Multi-Anode PhotoMultiplier Tube
MAMI	*MAinzer MIkrotron*
MB	Minimum Bias
MC	Monte-Carlo
MDC	Mini Drift Chamber
MEP	MEdium ionizing Particle
META	Multiplicity Electron Trigger Array
MeV	Mega electron Volt
MIP	Minimum Ionizing Particle
MLP	Multi Layer Perceptron
MMQ	META Match Quality
MTD	Minimum Track Distance
MVA	MultiVariate Analysis
MVD	Micro Vertex Detector
NBD	Negative Binomial Distribution
NDF	Number of Degrees of Freedom
NLO	Next to Leading Order
NN	Nucleon-Nucleon / Neural Network
NNLO	Next to Next to Leading Order
OVD	Off-Vertex-Decay
PAC	Program Advisory Committee
$\overline{\text{P}}$ANDA	antiProton ANihilation at DArmstadt experiment [129]
PASTTREC	$\overline{\text{P}}$ANDA STT REadout Chip
PCB	Printed Circuit Board
PDE	Probability Density Estimator
PDE-RS	PDE using Range-Search approach
PDF	Probability Density Function
PHENIX	Pioneering High Energy Nuclear Interaction eXperiment [27]
PID	Particle IDentification
PMF	Probability Mass Function
PMT	PhotoMultiplier Tube
PT	Physics Trigger
PWA	Partial Wave Analysis
QA	Quality Assessment
QCD	Quantum Chromo Dynamics
QED	Quantum Electro Dynamics
QGP	Quark Gluon Plasma
R^3B	Reactions with Relativistic Radioactive Beams experiment
RICH	Ring Imaging CHerenkov detetctor
RMS	Root Mean Square
ROC	Receiver Operating Characteristic
RPC	Resistive Plate Chamber
SHINE	SPS Heavy Ion and Neutrino Experiment
SHM	Statistical Hadronization Model [72]
SIS18	*SchwerIonenSynchrotron 18 Tm* (Heavy-Ion Synchrotron 18 Tm)
SIS100	*SchwerIonenSynchrotron 100 Tm* (Heavy-Ion Synchrotron 100 Tm)
SMASH	Simulating Many Accelerated Strongly-interacting Hadrons model [178]
SPPS	Super Proton antiProton Synchrotron
SPS	Super Proton Synchrotron
SR	Siemens-Rasmussen model
STAR	Solenoidal Tracker At RHIC [104]
STS	Strawtube Tracking Station
STT	Straw Tube Tracker
SVM	Support Vector Machine
TAPS	Two-Three-Arm Photon Spectrometer [140]
TDC	Time to Digital Converter
TDR	Technical Design Report
TeV	Tera electron Volt
TPC	Time Projection Chamber
TRB	Trigger and Readout Board
TRD	Transition Radiation Detector
TF	TensorFlow [5]
TMVA	Toolkit for MultiVariate Data Analysis with ROOT [109]
ToF	Time of Flight
TOF	Time Of Flight detetor
ToT	Time over Threshold
UFSD	Ultra-Fast Silicon Detector
UNILAC	UNIversal Linear ACcelerator
UNIX	UNIpleXed information and computing system
UrQMD	Ultra relativistic Quantum Molecular Dynamics model [59, 69]
UV	UltraViolet
VD	Vertex Distance
VDM	Vector Dominance Model
WDD	Weak Decay Daughter

Bibliography

[1] G. Aad *et al.* ATLAS Collaboration - The ATLAS Experiment at the CERN Large Hadron Collider - *JINST* **3** (2008) S08003.

[2] G. Aad *et al.* ATLAS Collaboration - Observation of a new particle in the search for the Standard Model Higgs boson with the ATLAS detector at the LHC - *Phys.Lett.B* **716** (2012) 1-29 - arXiv:1207.7214 [hep-ex] (2012).

[3] K. Aamodt *et al.* ALICE Collaboration - The ALICE experiment at the CERN LHC - *JINST* **3** (2008) S08002.

[4] K. Aamodt *et al.* ALICE Collaboration - Strange particle production in proton-proton collisions at $\sqrt{s}$ = 0.9 TeV with ALICE at the LHC - *Eur.Phys.J.C* **71** (2011) 1594 - arXiv:1012.3257 [hep-ex] (2010).

[5] M. Abadi, A. Agarwal, P. Barham, E. Brevdo, Z. Chen *et al.* - TensorFlow: Large-scale machine learning on heterogeneous systems (2015) - Software available from `https://tensorflow.org` - 10.5281/zenodo.4724125.

[6] M. Abdallah *et al.* STAR Collaboration - Measurements of ${}^{3}_{\Lambda}$H and ${}^{4}_{\Lambda}$H Lifetimes and Yields in Au+Au Collisions in the High Baryon Density Region - *Phys.Rev.Lett.* **128** (2022) 20, 202301 - arXiv:2110.09513 [nucl-ex] (2021).

[7] M.S. Abdallah *et al.* STAR Collaboration - Probing Strangeness Canonical Ensemble with K^-, ϕ and Ξ^- Production in Au+Au Collisions at $\sqrt{s_{NN}}$ = 3 GeV - *Phys.Lett.B* **831** (2022) 137152 - arXiv:2108.00924 [nucl-ex] (2021).

[8] B.B. Abelev *et al.* ALICE Collaboration - K^0_S and Λ production in Pb-Pb collisions at $\sqrt{s_{NN}}$ = 2.76 TeV - *Phys.Rev.Lett.* **111** (2013) 222301 - arXiv:1307.5530 [nucl-ex] (2013).

[9] B.B. Abelev *et al.* ALICE Collaboration - Multi-strange baryon production at mid-rapidity in Pb-Pb collisions at $\sqrt{s_{NN}}$ = 2.76 TeV - *Phys.Lett.B* **728** (2014) 216-227 Erratum: *Phys.Lett.B* **734** (2014) 409-410 - arXiv:1307.5543 [nucl-ex] (2013).

[10] B.I. Abelev *et al.* STAR Collaboration - Observation of an Antimatter Hypernucleus - *Science* **328** (2010) 58-62 - arXiv:1003.2030 [nucl-ex] (2010).

[11] T. Ablyazimov *et al.* CBM Collaboration - Challenges in QCD matter physics - The scientific program of the Compressed Baryonic Matter experiment at FAIR - *Eur.Phys.J.A* **53** (2017) 3, 60 - arXiv:1607.01487 [nucl-ex] (2016).

[12] S. Acharya *et al.* ALICE Collaboration - ${}^{3}_{\Lambda}$H and $\overline{{}^{3}_{\Lambda}\mathrm{H}}$ lifetime measurement in Pb-Pb collisions at $\sqrt{s_{NN}}$ = 5.02 TeV via two-body decay - *Phys.Lett.B* **797** (2019) 134905 - arXiv:1907.06906 [nucl-ex] (2019).

[13] J. Adam *et al.* ALICE Collaboration - ${}^{3}_{\Lambda}\mathrm{H}$ and $\overline{{}^{3}_{\Lambda}\mathrm{H}}$ production in Pb-Pb collisions at $\sqrt{s_{NN}}$ = 2.76 TeV - *Phys.Lett.B* **754** (2016) 360-372 - arXiv:1506.08453 [nucl-ex] (2015).

[14] J. Adam *et al.* STAR Collaboration - Strange hadron production in Au+Au collisions at $\sqrt{s_{NN}}$ = 7.7, 11.5, 19.6, 27, and 39 GeV - *Phys.Rev.C* **102** (2020) 3, 034909 - arXiv:1906.03732 [nucl-ex] (2019).

[15] J. Adamczewski-Musch *et al.* HADES Collaboration - Proposals for experiments at SIS18 during FAIR Phase-0 - HADES 102 p. (2017) [10.15120/GSI-2019-00976].

[16] J. Adamczewski-Musch *et al.* HADES Collaboration - Centrality determination of Au+Au collisions at 1.23A GeV with HADES - *Eur.Phys.J.A* **54** (2018) 5, 85 - arXiv:1712.07993 [nucl-ex] (2017).

[17] J. Adamczewski-Musch *et al.* HADES Collaboration, - Deep sub-threshold ϕ production in Au+Au collisions - *Phys.Lett.B* **778** (2018) 403-407 - arXiv:1703.08418 [nucl-ex] (2017).

[18] J. Adamczewski-Musch *et al.* HADES Collaboration - Sub-threshold production of K^{0}_{S} mesons and Λ hyperons in Au+Au collisions at $\sqrt{s_{NN}}$ = 2.4 GeV - *Phys.Lett.B* **793** (2019) 457-463 - arXiv:1812.07304 [nucl-ex] (2018).

[19] J. Adamczewski-Musch *et al.* HADES Collaboration - Directed, Elliptic, and Higher Order Flow Harmonics of Protons, Deuterons, and Tritons in Au+Au Collisions at $\sqrt{s_{NN}}$ = 2.4 GeV - *Phys.Rev.Lett.* **125** (2020) 262301 - arXiv:2005.12217 [nucl-ex] (2020).

[20] J. Adamczewski-Musch *et al.* TRB Collaboration - Status of the CBM and HADES RICH projects at FAIR - *Nucl.Instrum.Meth.A* **952** (2020) 161970.

[21] L. Adamczyk *et al.* STAR Collaboration - Elliptic flow of identified hadrons in Au+Au collisions at $\sqrt{s_{NN}}$ = 7.7-62.4 GeV - *Phys.Rev.C* **88** (2013) 014902 - arXiv:1301.2348 [nucl-ex] (2013).

[22] L. Adamczyk *et al.* STAR Collaboration - Measurement of elliptic flow of light nuclei at $\sqrt{s_{NN}}$ = 200, 62.4, 39, 27, 19.6, 11.5, and 7.7 GeV at the BNL Relativistic Heavy Ion Collider - *Phys.Rev.C* **94** (2016) 3, 034908 - arXiv:1601.07052 [nucl-ex] (2016).

[23] L. Adamczyk *et al.* STAR Collaboration - Bulk Properties of the Medium Produced in Relativistic Heavy-Ion Collisions from the Beam Energy Scan Program - *Phys.Rev.C* **96** (2017) 4, 044904 - arXiv:1701.07065 [nucl-ex] (2017).

[24] L. Adamczyk *et al.* STAR Collaboration - Measurement of the ${}^{3}_{\Lambda}\mathrm{H}$ lifetime in Au+Au collisions at the BNL Relativistic Heavy Ion Collider - *Phys.Rev.C* **97** (2018) 5, 054909 - arXiv:1710.00436 [nucl-ex] (2017).

[25] J. Adams *et al.* STAR Collaboration - Scaling Properties of Hyperon Production in Au+Au Collisions at $\sqrt{s_{NN}}$ = 200 GeV - *Phys.Rev.Lett.* **98** (2007) 062301 - arXiv:nucl-ex/0606014 (2006).

[26] K. Adcox *et al.* PHENIX Collaboration - Measurement of the Lambda and anti-Lambda particles in Au+Au collisions at $\sqrt{s_{NN}}$ = 130 GeV - *Phys.Rev.Lett.* **89** (2002) 092302 - arXiv:nucl-ex/0204007 (2002).

[27] K. Adcox *et al.* PHENIX Collaboration - PHENIX detector overview - *Nucl.Instrum.Meth.A* **499** (2003) 469-479.

[28] C. Adler *et al.* STAR Collaboration - Midrapidity Λ and $\overline{\Lambda}$ production in Au+Au collisions at $\sqrt{s_{NN}}$ = 130 GeV - *Phys.Rev.Lett.* **89** (2002) 092301 - arXiv:nucl-ex/0203016 (2002).

[29] C. Adler *et al.* STAR Collaboration - Kaon production and kaon to pion ratio in Au+Au collisions at $\sqrt{s_{NN}}$ = 130 GeV - *Phys.Lett.B* **595** (2004) 143-150 - arXiv:nucl-ex/0206008 (2002).

[30] G. Agakishiev *et al.* HADES Collaboration - Deep sub-threshold Ξ^- production in Ar+KCl reactions at 1.76A GeV - *Phys.Rev.Lett.* **103** (2009) 132301 - arXiv:0907.3582 [nucl-ex] (2009).

[31] G. Agakishiev *et al.* HADES Collaboration - ϕ decay: A Relevant source for K^- production at SIS18 energies? - *Phys.Rev.C* **80** (2009) 025209 - arXiv:0902.3487 [nucl-ex] (2009).

[32] G. Agakishiev *et al.* HADES Collaboration - The High-Acceptance Dielectron Spectrometer HADES - *Eur.Phys.J.A* **41** (2009) 243-277 - arXiv:0902.3478 [nucl-ex] (2009).

[33] G. Agakishiev *et al.* HADES Collaboration - Hyperon production in Ar+KCl collisions at 1.76A GeV - *Eur.Phys.J.A* **47** (2011) 21 - arXiv:1010.1675 [nucl-ex] (2010).

[34] G. Agakishiev *et al.* HADES Collaboration - An upper limit on hypertriton production in collisions of Ar(1.76A GeV)+KCl - *Eur.Phys.J.A* **49** (2013) 146 - arXiv:1310.6198 [nucl-ex] (2013).

[35] G. Agakishiev *et al.* HADES Collaboration - Subthreshold Ξ^- Production in Collisions of p(3.5 GeV)+Nb - *Phys.Rev.Lett.* **114** (2015) 21, 212301 - arXiv:1501.03894 [nucl-ex] (2015).

[36] G. Agakishiev *et al.* HADES Collaboration - Statistical hadronization model analysis of hadron yields in p+Nb and Ar+KCl at SIS18 energies - *Eur.Phys.J.A* **52** (2016) 6, 178 - arXiv:1512.07070 [nucl-ex] (2015).

[37] M. Agari - Hyperon Production in Proton-Nucleus Collisions at a Center-of-Mass Energy of $\sqrt{s_{NN}}$ = 41.6 GeV at HERA-B and Design of Silicon Microstrip Detectors for Tracking at LHCb - PhD Thesis Universität Dortmund (2006).

[38] M.M. Aggarwal *et al.* STAR Collaboration - An Experimental Exploration of the QCD Phase Diagram: The Search for the Critical Point and the Onset of Deconfinement - arXiv:1007.2613 [nucl-ex] (2010).

[39] M.M. Aggarwal *et al.* STAR Collaboration - Strange and Multi-strange Particle Production in Au+Au Collisions at $\sqrt{s_{NN}}$ = 62.4 GeV - *Phys.Rev.C* **83** (2011) 024901 - arXiv:1010.0142 [nucl-ex] (2010).

[40] C. Agodi, A. Bassi, R. Bassini, G. Bellia, M. Benovic *et al.* - The HADES time-of-flight wall - *Nucl.Instrum.Meth.A* **492** (2002) 14-25.

[41] S. Ahmad, B.E. Bonner, C.S. Chan, J.M. Clement, S.V. Efremov *et al.* - Lambda production by 11.6A GeV/c Au beam on Au target - *Phys.Lett.B* **382** (1996) 35-39 Erratum: *Phys.Lett.B* **386** (1996) 496-496.

[42] C. Alt *et al.* NA49 Collaboration - Energy dependence of Λ and Ξ production in central Pb+Pb collisions at A-20, A-30, A-40, A-80, and A-158 GeV measured at the CERN Super Proton Synchrotron - *Phys.Rev.C* **78** (2008) 034918 - arXiv:0804.3770 [nucl-ex] (2008).

[43] E. Andersen *et al.* WA97 Collaboration - Strangeness enhancement at mid-rapidity in Pb Pb collisions at 158-A-GeV/c - *Phys.Lett.B* **449** (1999) 401-406.

[44] A. Andronic *et al.* FOPI Collaboration - Excitation function of elliptic flow in Au+Au collisions and the nuclear matter equation of state - *Phys.Lett.B* **612** (2005) 173-180 - arXiv:nucl-ex/0411024 (2004).

[45] A. Andronic, P. Braun-Munzinger and J. Stachel - Hadron production in central nucleus-nucleus collisions at chemical freeze-out - *Nucl.Phys.A* **772** (2006) 167-199 - arXiv:nucl-th/0511071 (2005).

[46] A. Andronic, P. Braun-Munzinger, K. Redlich and J. Stachel - Decoding the phase structure of QCD via particle production at high energy - *Nature* **561** (2018) 7723, 321-330 - arXiv:1710.09425 [nucl-th] (2017).

[47] E. Annala, T. Gorda, A. Kurkela, J. Nättilä and A. Vuorinen - Evidence for quark-matter cores in massive neutron stars - *Nature Phys.* **16** (2020) 9, 907-910 - arXiv:1903.09121 [astro-ph.HE] (2019).

[48] T. Anticic *et al.* NA49 Collaboration - Λ and $\overline{\Lambda}$ production in central Pb-Pb collisions at 40A GeV, 80A GeV and 158A GeV - *Phys.Rev.Lett.* **93** (2004) 022302 - arXiv:nucl-ex/0311024 (2003).

[49] F. Antinori *et al.* WA97 Collaboration - Production of strange and multistrange hadrons in nucleus-nucleus collisions at the SPS - *Nucl.Phys.A* **661** (1999) 130-139.

[50] F. Antinori *et al.* NA57 Collaboration - Energy dependence of hyperon production in nucleus-nucleus collisions at SPS - *Phys.Lett.B* **595** (2004) 68-74 - arXiv:nucl-ex/0403022 (2004).

[51] F. Antinori *et al.* NA57 Collaboration - Rapidity distributions around mid-rapidity of strange particles in Pb-Pb collisions at 158A GeV/c - *J.Phys.G* **31** (2005) 1345-1357 - arXiv:nucl-ex/0509009 (2005).

[52] F. Antinori *et al.* NA57 Collaboration - Enhancement of hyperon production at central rapidity in 158-A-GeV/c Pb-Pb collisions - *J.Phys.G* **32** (2006) 427-442 - arXiv:nucl-ex/0601021 (2006).

[53] H. Appelshäuser *et al.* NA49 Collaboration - Baryon Stopping and Charged Particle Distributions in Central Pb+Pb Collisions at 158 GeV per Nucleon - *Phys.Rev.Lett.* **82** (1999) 2471-2475 - arXiv:nucl-ex/9810014 (1998).

[54] B. Arnoldi-Meadows - Reconstruction of Hypertriton in Au+Au collisions at 1.23A GeV with HADES via the Two-Body Decay Channel - Bachelor Thesis Goethe Universität Frankfurt (2019).

[55] M. Asakawa and K. Yazaki - Chiral Restoration at Finite Density and Temperature - *Nucl.Phys.A* **504** (1989) 668-684.

[56] A.R. Baden *et al.* GSI-LBL Collaboration - The Plastic Ball Spectrometer: An Electronic 4π Detector With Particle Identification - *Nucl.Instrum.Meth.* **203** (1982) 189.

[57] A. Barducci, R. Casalbuoni, S. De Curtis, R. Gatto and G. Pettini - Chiral Symmetry Breaking in QCD at Finite Temperature and Density - *Phys.Lett.B* **231** (1989) 463-470.

[58] A. Barducci, R. Casalbuoni and G. Pettini - Chiral phases of QCD at finite density and temperature - *Phys.Rev.D* **49** (1994) 426-436.

[59] S.A. Bass, M. Belkacem, M. Bleicher, M. Brandstetter, L. Bravina *et al.* - Microscopic Models for Ultrarelativistic Heavy Ion Collisions - *Prog.Part.Nucl.Phys.* **41** (1998) 225-370 - arXiv:nucl-th/9803035 (1998).

[60] F. Becattini, J. Steinheimer, R. Stock and M. Bleicher - Hadronization conditions in relativistic nuclear collisions and the QCD pseudo-critical line - *Phys.Lett.B* **764** (2017) 241-246 - arXiv:1605.09694 [nucl-th] (2016).

[61] M. Becker - Search for the Σ^0 in Ag+Ag at 1.58A GeV via photon conversion method - Master Studies Justus-Liebig-Universität Giessen (Work in Progress).

[62] D. Belver, A. Blanco, P. Cabanelas, N. Carolino, E. Castro *et al.* - The HADES RPC inner ToF wall - *Nucl.Instrum.Meth.A* **602** (2009) 687-690.

[63] D. Belver - The Front-End Electronics of the HADES timing RPCs wall: design, development and performances analysis - PhD Thesis Universidade de Santiago de Compostela (2009).

[64] J. Berges and K. Rajagopal - Color superconductivity and chiral symmetry restoration at nonzero baryon density and temperature - *Nucl.Phys.B* **538** (1999) 215-232 - arXiv:hep-ph/9804233 (1998).

[65] M. Berglund and M.E. Wieser - Isotopic compositions of the elements 2009 (IUPAC Technical Report) - *Pure and Applied Chemistry* **83.2** (2011) 397-410.

[66] T. Bhattacharya, M.I. Buchoff, N.H. Christ, H.-T. Ding, R. Gupta *et al.* - QCD Phase Transition with Chiral Quarks and Physical Quark Masses - *Phys.Rev.Lett.* **113** (2014) 8, 082001 - arXiv:1402.5175 [hep-lat] (2014).

[67] A. Bialas, M. Bleszynski and W. Czyz - Multiplicity Distributions in Nucleus-Nucleus Collisions at High-Energies - *Nucl.Phys.B* **111** (1976) 461-476.

[68] A. Blanco, D. Belver, P. Cabanelas, J. Diaz, P. Fonte *et al.* - RPC HADES-ToF wall cosmic ray test performance - *Nucl.Instrum.Meth.A* **661** (2012) S114-S117.

[69] M. Bleicher, E. Zabrodin, C. Spieles, S.A. Bass, C. Ernst *et al.* - Relativistic Hadron-Hadron Collisions in the Ultra-Relativistic Quantum Molecular Dynamics Model - *J.Phys.G* **25** (1999) 1859-1896 - arXiv:hep-ph/9909407 (1999).

[70] G. Bohm, J. Klabuhn, U. Krecker, F. Wysotzki, G. Coremans *et al.* - On the lifetime of the ${}^{3}_{\Lambda}$H hypernucleus - *Nucl.Phys.B* **16** (1970) 46-52 Erratum: *Nucl.Phys.B* **16** (1970) 523-523.

[71] W.H. Bragg and R. Kleeman - On the α particles of radium, and their Loss of Range in passing through various Atoms and Molecules - *Philos.Mag.* **10** (1905) 318.

[72] P. Braun-Munzinger, K. Redlich and Johanna Stachel - Particle production in heavy ion collisions - *Quark-Gluon Plasma* **3**, pp. 491-599 (2004) - arXiv:nucl-th/0304013 (2003).

[73] R. Brun, F. Bruyant, M. Maire, A.C. McPherson and P. Zanarini - GEANT 3 - CERN-DD-EE-84-1 (1987).

[74] O. Buss, T. Gaitanos, K. Gallmeister, H. van Hees, M. Kaskulov *et al.* - Transport-theoretical Description of Nuclear Reactions - *Phys.Rept.* **512** (2012) 1-124 - arXiv:1106.1344 [hep-ph] (2011).

[75] J. Bystricky, P. La France, F. Lehar, F. Perrot, T. Siemiarczuk and P. Winternitz - Energy dependence of nucleon-nucleon inelastic total cross-sections - *J.Phys.France* **48** (1987) 1901-1924.

[76] W. Cassing and E.L. Bratkovskaya - Hadronic and electromagnetic probes of hot and dense nuclear matter - *Phys.Rept.* **308** (1999) 65-233.

[77] S. Chatrchyan *et al.* CMS Collaboration - The CMS Experiment at the CERN LHC - *JINST* **3** (2008) S08004.

[78] S. Chatrchyan *et al.* CMS Collaboration - Observation of a New Boson at a Mass of 125 GeV with the CMS Experiment at the LHC - *Phys.Lett.B* **716** (2012) 30-61 - arXiv:1207.7235 [hep-ex] (2012).

[79] P. Chung, J.M. Alexander, N.N. Ajitanand, M. Anderson, D. Best *et al.* - Lambda flow and Lambda p correlation in Au + Au collisions at AGS energies - *J.Phys.G* **27** (2001) 293-299.

[80] P. Chung *et al.* E895 Collaboration - Near threshold production of the multistrange Ξ^- hyperon - *Phys.Rev.Lett.* **91** (2003) 202301 - arXiv:nucl-ex/0302021 (2003).

[81] J. Cleymans, H. Oeschler, K. Redlich and S. Wheaton - Comparison of chemical freeze-out criteria in heavy-ion collisions - *Phys.Rev.C* **73** (2006) 034905 - arXiv:hep-ph/0511094 (2005).

[82] D. Clowe, M. Bradac, A.H. Gonzalez, M. Markevitch, S.W. Randall, C. Jones and D. Zaritsky - A direct empirical proof of the existence of dark matter - *Astrophys.J.Lett.* **648** (2006) L109-L113 - arXiv:astro-ph/0608407 (2006).

[83] M. Creutz - Quarks, gluons and lattices - ISBN: 0521244056.

[84] S. Date, M. Gyulassy and H. Sumiyoshi - Nuclear Stopping Power at High-Energies - *Phys.Rev.D* **32** (1985) 619.

[85] C.B. Dover and G.E. Walker - The Interaction of Kaons with Nucleons and Nuclei - *Phys.Rept.* **89** (1982) 1-177.

[86] G.J. Feldman and R.D. Cousins - A Unified Approach to the Classical Statistical Analysis of Small Signals - *Phys.Rev.D* **57** (1998) 3873-3889 - arXiv:physics/9711021 [physics.data-an] (1997).

[87] A. Forster *et al.* KaoS Collaboration - Review of the results of the KaoS collaboration - *J.Phys.G* **31** (2005) 6, S693-S700 - arXiv:nucl-ex/0411045 (2004).

[88] A. Forster, F. Uhlig, I. Bottcher, D. Brill, M. Debowski *et al.* - Production of K^+ and of K^- Mesons in Heavy-Ion Collisions from 0.6 to 2.0A GeV Incident Energy - *Phys.Rev.C* **75** (2007) 024906 - arXiv:nucl-ex/0701014 (2007).

[89] G. Fricke and K. Heilig - Nuclear Charge Radii Landolt-Börnstein - Group I Elementary Particles, Nuclei and Atoms, Vol. 20 (2004) pp. 1-4.

[90] H. Fritzsch, M. Gell-Mann and H. Leutwyler - Advantages of the Color Octet Gluon Picture - *Phys.Lett.B* **47** (1973) 365-368.

[91] I. Fröhlich, L. Cazon, T. Galatyuk, V. Hejny, R. Holzmann *et al.* - Pluto: A Monte Carlo Simulation Tool for Hadronic Physics - *PoS* ACAT (2007) 076 - arXiv:0708.2382 [nucl-ex] (2007).

[92] M. Galassi *et al.* - GNU Scientific Library Reference Manual (3rd Ed.) - ISBN 0954612078 (2021).

[93] T. Galatyuk, M. Golubeva, F. Guber, A. Ivashkin, A. Kugler *et al.* - Tests of the Electromagnetic Calorimeter for HADES Experiment at GSI - *KnE Energ.Phys.* **3** (2018) 162-169.

[94] M. Gell-Mann - The Eightfold Way: A Theory of strong interaction symmetry - CTSL-20, TID-12608 (1961).

[95] M. Gell-Mann - A Schematic Model of Baryons and Mesons - *Phys.Lett.* **8** (1964) 214-215.

[96] A.C. Genz and A.A. Malik - Remarks on algorithm 006: An adaptive algorithm for numerical integration over an N-dimensional rectangular region - *J.Comput.Appl.Math.* **6** (1980) 4, 295-302.

[97] J.W. von Goethe - *Faust. Der Tragödie erster Teil* (1808).

[98] K.A. Goulianos - Diffractive Interactions of Hadrons at High-Energies - *Phys.Rept.* **101** (1983) 169.

[99] E. Gross and O. Vitells - Trial factors for the look elsewhere effect in high energy physics - *Eur.Phys.J.C* **70** (2010) 525-530 - arXiv:1005.1891 [physics.data-an] (2010).

[100] GSI Helmholtz Center for Heavy-Ion Research - GSI-FAIR Scientific Reports - GSI Report 2019-1 127 p. (2019) [10.15120/GSI-2019-00545],
GSI Report 2018-1 453 p. (2018) [10.15120/GSI-2017-01856],
GSI Report 2017-1 486 p. (2017) [10.15120/GR-2017-1],
GSI-Report 2016-1 395 p. (2016) [10.15120/GR-2016-1],
GSI Report 2015-1 557 S. (2015) [10.15120/GR-2015-1],
GSI Report 2014-1 452 S. (2014) [10.15120/GR-2014-1].

[101] `https://www.gsi.de/en/researchaccelerators/accelerator_facility/` - Webpage accessed on the 15.11.2021.

[102] A.M. Halasz, A.D. Jackson, R.E. Shrock, M.A. Stephanov and J.J.M. Verbaarschot - On the phase diagram of QCD - *Phys.Rev.D* **58** (1998) 096007 - arXiv:hep-ph/9804290 (1998).

[103] J.W. Harris, G. Odyniec, H.G. Pugh, L.S. Schroeder, M.L. Tincknell *et al.* - Pion Production in High-energy Nucleus Nucleus Collisions - *Phys.Rev.Lett.* **58** (1987) 463-466.

[104] J.W. Harris *et al.* STAR Collaboration - The STAR experiment at the relativistic heavy ion collider - *Nucl.Phys.A* **566** (1994) 277C-285C.

[105] C. Hartnack, R.K. Puri, J. Aichelin, J. Konopka, S.A. Bass *et al.* - Modeling the many body dynamics of heavy ion collisions: Present status and future perspective - *Eur.Phys.J.A* **1** (1998) 151-169 - arXiv:nucl-th/9811015 (1998).

[106] R. Hensch - Modelling hadron yields and spectra from Au+Au collisions at 1.23A GeV based on macroscopic parameters - Master Thesis Goethe Universität Frankfurt (2019).

[107] N. Herrmann *et al.* FOPI Collaboration - Strangeness production at (sub)threshold energies - *J.Phys.G* **37** (2010) 094036.

[108] F. Hildenbrand and H.W. Hammer - Lifetime of the hypertriton - *Phys.Rev.C* **102** (2020) 064002 - arXiv:2007.10122 [nucl-th] (2020).

[109] A. Hoecker, P. Speckmayer, J. Stelzer, J. Therhaag, E. von Toerne *et al.* - TMVA - Toolkit for Multivariate Data Analysis - CERN-OPEN-2007-007 (2007).

[110] J.H. Hubbell and S.M. Seltzer - X-Ray Mass Attenuation Coefficients - NISTIR 5632 (2004).

[111] H. Huck - *Rekonstruktion des Hypertritons über den Drei-Körper-Zerfall in Au+Au Kollisionen bei 1,23A GeV* - Bachelor Thesis Goethe Universität Frankfurt (2018).

[112] H. Huck - *Emission leichter Kerne aus semi-zentralen Au+Au Kollisionen bei 1.23A GeV* - Master Thesis Goethe Universität Frankfurt (To be published).

[113] M. Juric, G. Bohm, J. Klabuhn, U. Krecker, F. Wysotzki *et al.* - A new determination of the binding-energy values of the light hypernuclei (15>=a) - *Nucl.Phys.B* **52** (1973) 1-30.

[114] H. Kamada, J. Golak, K. Miyagawa, H. Witala and W. Gloeckle - Pi mesonic decay of the hypertriton - *Phys.Rev.C* **57** (1998) 1595-1603 - arXiv:nucl-th/9709035 (1997).

[115] D.B. Kaplan and A.E. Nelson - Strange Goings on in Dense Nucleonic Matter - *Phys.Lett.B* **175** (1986) 57-63.

[116] B. Kardan - Centrality Determination at 1.23A GeV Gold-Gold Collisions and Readout-Electronics for the HADES Calorimeter - Diploma Thesis Goethe Universität Frankfurt (2015).

[117] F. Karsch - Lattice QCD at high temperature and density - *Lect.Notes Phys.* **583** (2002) 209-249 - arXiv:hep-lat/0106019 (2001).

[118] G. Keyes, M. Derrick, T. Fields, L.G. Hyman, J.G. Fetkovich *et al.* - New Measurement of the ${}^{3}_{\Lambda}$H Lifetime - *Phys.Rev.Lett.* **20** (1968) 819-821.

[119] G. Keyes, M. Derrick, T. Fields, L.G. Hyman, J.G. Fetkovich *et al.* - Properties of ${}^{3}_{\Lambda}$H - *Phys.Rev.D* **1** (1970) 66-77.

[120] G. Keyes, J. Sacton, J.H. Wickens and M.M. Block - A measurement of the lifetime of the ${}^{3}_{\Lambda}$H hypernucleus - *Nucl.Phys.B* **67** (1973) 269-283.

[121] P. Klaus - UrQMD Viewer - `https://github.com/pklaus/urqmd-viewer`.

[122] M. Kohls - Reconstruction and Analysis of Charged Kaons and ϕ from Ag+Ag Collisions at 1.58A GeV measured with HADES - PhD Thesis Goethe Universität Frankfurt (To be published).

[123] G. Kornakov - New Advances and developments ob the RPC ToF wall of the HADES experiment at GSI - PhD Thesis Universidade de Santiago de Compostela (2012).

[124] M.W. Kutta - *Beitrag zur näherungweisen Integration totaler Differentialgleichungen - Z.Math.Phys.* **46** (1901) 435-453.

[125] C.H. Lee, G.E. Brown, D.P. Min and M. Rho - An Effective chiral Lagrangian approach to kaon - nuclear interactions: Kaonic atom and kaon condensation - *Nucl.Phys.A* **585** (1995) 401-449 - arXiv:hep-ph/9406311 (1994).

[126] Y. Leifels *et al.* FOPI Collaboration - Strangeness production in heavy ion collisions: Constraining the KN -potential in medium - *J.Phys.Conf.Ser.* **420** (2013) 012019.

[127] B. Lommel - Private communication (2021).

[128] X. Lopez *et al.* FOPI Collaboration - Subthreshold production of Sigma(1385) baryons in Al + Al collisions at 1.9A GeV - *Phys.Rev.C* **76** (2007) 052203 - arXiv:0710.5007 [nucl-ex] (2007).

[129] M.F.M. Lutz *et al.* $\overline{\text{P}}$ANDA Collaboration - Physics Performance Report for $\overline{\text{P}}$ANDA: Strong Interaction Studies with Antiprotons - arXiv:0903.3905 [hep-ex] (2009).

[130] A. Maire - *Production des baryons multi-étranges au LHC dans les collisions proton-proton avec l'expérience ALICE* - PhD Thesis Université de Strasbourg (2011).

[131] A. Mangiarotti *et al.* FOPI Collaboration - Sub-threshold phi-meson yield in central ^{58}Ni+^{58}Ni collisions - *Nucl.Phys.A* **714** (2003) 89-123 - arXiv:nucl-ex/0209012 (2002).

[132] J. Markert - *Untersuchung zum Ansprechverhalten der Vieldraht-Driftkammern niedriger Massenbelegung des HADES Experimentes* - PhD Thesis Goethe Universität Frankfurt (2005).

[133] J. Michel - Development and Implementation of a New Trigger and Data Acquisition System for the HADES Detector - PhD Thesis Goethe Universität Frankfurt (2012).

[134] M.L. Miller, K. Reygers, S.J. Sanders and P. Steinberg - Glauber modeling in high energy nuclear collisions - *Ann.Rev.Nucl.Part.Sci.* **57** (2007) 205-243 - arXiv:nucl-ex/0701025 (2007).

[135] M. Morháč, J. Kliman, V. Matoušek, M. Veselský and I. Turzo - Identification of peaks in multidimensional coincidence γ-ray spectra - *Nucl.Instrum.Meth.A* **443** (2000) 108-125.

[136] E.R. Most, L.J. Papenfort, V. Dexheimer, M. Hanauske, S. Schramm, H. Stöcker and L. Rezzolla - Signatures of quark-hadron phase transitions in general-relativistic neutron-star mergers - *Phys.Rev.Lett.* **122** (2019) 6, 061101 - arXiv:1807.03684 [astro-ph.HE] (2018).

[137] C. Müntz - Private communication (2020).

[138] M. Nabroth - Private communication (2021).

[139] M. Nabroth - Emission pattern of charged pions from Ag+Ag collisions at 1.58A GeV - Master Thesis Goethe Universität Frankfurt (To be published).

[140] R. Novotny *et al.* TAPS Collaboration - The BaF_2 photon spectrometer TAPS - *IEEE Trans.Nucl.Sci.* **38** (1991) 379-385.

[141] O. Pechenov and V. Pechenov - Tracking Status for Mar 2019 - Talk on HADES Collaboration Meeting XXXVIII in Dresden-Rossendorf (2020).

[142] R.E. Phillips and J. Schneps - Lifetimes of Light Hyperfragments. II - *Phys.Rev.* **180** (1969) 1307.

[143] K. Piasecki *et al.* FOPI Collaboration - Strangeness production in heavy-ion collisions around 2A GeV in FOPI - *J.Phys.Conf.Ser.* **312** (2011) 022019.

[144] K. Piasecki *et al.* FOPI Collaboration - Influence of ϕ mesons on negative kaons in Ni+Ni collisions at 1.91A GeV beam energy - *Phys.Rev.C* **91** (2015) 5, 054904 - arXiv:1412.4493 [nucl-ex] (2014).

[145] J. Pietraszko, T. Galatyuk, V. Grilj, W. Koenig, S. Spataro and M. Träger - Radiation damage in single crystal CVD diamond material investigated with a high current relativistic ^{197}Au beam - *Nucl.Instrum.Meth.A* **763** (2014) 1-5.

[146] C. Pinkenburg *et al.* E895 Collaboration - Production and collective behavior of strange particles in Au+Au collisions at 2A GeV - 8A GeV - *Nucl.Phys.A* **698** (2002) 495-498 - arXiv:nucl-ex/0104025 (2001).

[147] J. Podolanski and R. Armenteros - Analysis of V-events - *Phil.Mag.* **45** (1954) 13-30.

[148] M. Post, S. Leupold and U. Mosel - Hadronic spectral functions in nuclear matter - *Nucl.Phys.A* **741** (2004) 81-148 - arXiv:nucl-th/0309085 (2003).

[149] R.J. Prem and P.H. Steinberg - Lifetimes of Hypernuclei, ${}^{3}_{\Lambda}$H, ${}^{4}_{\Lambda}$H, ${}^{5}_{\Lambda}$H - *Phys.Rev.* **136** (1964) B1803.

[150] F. Rademakers, P. Canal, A. Naumann, O. Couet, L. Moneta *et al.* - ROOT Data Analysis Framework - 10.5281/zenodo.848818.

[151] G. Rai, A. Arthur, F. Bieser, C.W. Harnden, R. Jones *et al.* - A TPC Detector for the Study of High Multiplicity Heavy Ion Collisions - *IEEE Trans.Nucl.Sci.* **37** (1990) 56-64.

[152] C. Rappold, E. Kim, D. Nakajima, T.R. Saito, O. Bertini *et al.* - Hypernuclear spectroscopy of products from ^{6}Li projectiles on a carbon target at 2A GeV - *Nucl.Phys.A* **913** (2013) 170-184 - arXiv:1305.4871 [nucl-ex] (2013).

[153] C. Rappold, T.R. Saito, O. Bertini, S. Bianchin, V. Bozkurt *et al.* - Hypernuclear production cross section in the reaction of ^{6}Li + ^{12}C at 2A GeV - *Phys.Lett.B* **747** (2015) 129-134.

[154] C. Ratti - Lattice QCD and heavy ion collisions: a review of recent progress - *Rept.Prog.Phys.* **81** (2018) 8, 084301 - arXiv:1804.07810 [hep-lat] (2018).

[155] W. Reisdorf *et al.* FOPI Collaboration - Nuclear stopping from 0.09A GeV to 1.93A GeV and its correlation to flow - *Phys.Rev.Lett.* **92** (2004) 232301 - arXiv:nucl-ex/0404037 (2004).

[156] J. Ritman *et al.* FOPI Collaboration - The FOPI detector at SIS18/GSI - *Nucl.Phys.B Proc.Suppl.* **44** (1995) 708-715.

[157] C.D.T. Runge - *Über die numerische Auflösung von Differentialgleichungen* - *Math.Ann.* **46** (1895) 167-178.

[158] P. Salabura *et al.* HADES Collaboration - HADES: A High Acceptance DiElectron Spectrometer - *Acta Phys.Polon.B* **27** (1996) 421-440.

[159] O. Scavenius, A. Mocsy, I.N. Mishustin and D.H. Rischke - Chiral phase transition within effective models with constituent quarks - *Phys.Rev.C* **64** (2001) 045202 - arXiv:nucl-th/0007030 (2000).

[160] T. Scheib - Rekonstruktion des Hypertritons in Ar+KCl bei 1,76A GeV mit HADES - Master Thesis Goethe Universität Frankfurt (2012).

[161] T. Scheib - Λ and K^0_S Production in Au+Au Collisions at 1.23A GeV - PhD Thesis Goethe Universität Frankfurt (2017).

[162] A.M. Schmah - *Produktion von Seltsamkeit in Ar+KCl Reaktionen bei 1.756A GeV mit HADES* - PhD Thesis Technische Universität Darmstadt (2008).

[163] K. Schmidt-Sommerfeld - *Konzeptstudie für eine Photomultiplierauslese des Tscherenkow-detektors im HADES Experiment* - Master Thesis Thechnische Universität München (2014).

[164] E. Schnedermann, J. Sollfrank and U.W. Heinz - Thermal phenomenology of hadrons from 200A GeV S+S collisions - *Phys.Rev.C* **48** (1993) 2462-2475 - arXiv:nucl-th/9307020 (1993).

[165] H. Schuldes - Charged Kaon and ϕ Reconstruction in Au+Au Collisions at 1.23A GeV - PhD Thesis Goethe Universität Frankfurt (2016).

[166] P. Senger *et al.* KaoS Collaboration - The KAON spectrometer at SIS18 - *Nucl.Instrum.Meth.A* **327** (1993) 393-411.

[167] E.V. Shuryak - Quark-Gluon Plasma and Hadronic Production of Leptons, Photons and Psions - *Phys.Lett.B* **78** (1978) 150, *Sov.J.Nucl.Phys.* **28** (1978) 408, *Yad.Fiz.* **28** (1978) 796-808.

[168] P.J. Siemens and J.O. Rasmussen - Evidence for a blast wave from compress nuclear matter - *Phys.Rev.Lett.* **42** (1979) 880-887.

[169] S. Spies - *Simulationen zur Produktion geladener Teilchen unter ALICE-TRD Trigger-Bedingungen* - Bachelor Thesis Goethe Universität Frankfurt (2016).

[170] S. Spies - *Rekonstruktion schwacher Zerfälle in Au+Au Kollisionen bei 1,23A GeV* - Master Thesis Goethe Universität Frankfurt (2018).

[171] S. Spies - Λ and K^0_S Analysis in AuAu - Talk on *DPG Frühjahrstagung* in Munich (2019).

[172] P. Spiller, M. Bai, J. Blaurock, O. Boine-Frankenheim, O. Dolinskyy *et al.* - Status of the FAIR Project - *Proceedings of IPAC* (2018).

[173] J. Stachel, A. Andronic, P. Braun-Munzinger and K. Redlich - Confronting LHC data with the statistical hadronization model - *J.Phys.Conf.Ser.* **509** (2014) 012019 - arXiv:1311.4662 [nucl-th] (2013).

[174] J. Stumm - A Systematic Statistical Model Analysis of HADES Au+Au Data at 1.23A GeV - Master Thesis Goethe Universität Frankfurt (2019).

[175] M. Szala - Hadron Production and Propagation in Au+Au Collisions at 1.23A GeV - PhD Thesis Goethe Universität Frankfurt (To be published).

[176] L. Toth - Additive Quark Model with Six Flavors - *Czech.J.Phys.B* **30** (1980) 56-63.

[177] V. Vovchenko, B. Dönigus, B. Kardan, M. Lorenz and H. Stoecker - Feed-down contributions from unstable nuclei in relativistic heavy-ion collisions - *Phys.Lett.B* **809** (2020) 135746 - arXiv:2004.04411 [nucl-th] (2020).

[178] J. Weil, V. Steinberg, J. Staudenmaier, L.G. Pang, D. Oliinychenko *et al.* - Particle production and equilibrium properties within a new hadron transport approach for heavy-ion collisions - *Phys.Rev.C* **94** (2016) 5, 054905 - arXiv:1606.06642 [nucl-th] (2016).

[179] M. Wiebusch - Towards new Front-End Electronics for the HADES Drift Chamber System - PhD Thesis Goethe Universität Frankfurt (2019).

[180] Wolfram Alpha LLC - Wolfram|Alpha - `https://www.wolframalpha.com/` (2021).

[181] G. Xie *et al.* STAR Collaboration - Light and strange hadron production and anisotropic flow measurement in Au+Au collisions at $\sqrt{s_{NN}} = 3$ GeV from STAR - arXiv:2108.05424 [nucl-ex] (2021).

[182] A. Yegneswaran, S. Beedoe, J. Bystricky, J. Carroll, S. Christo *et al.* - The Dilepton spectrometer - *Nucl.Instrum.Meth.A* **290** (1990) 61-75.

[183] G. Zweig - An SU(3) model for strong interaction symmetry and its breaking. - CERN-TH-401, CERN-TH-412, NP-14146, PRINT-64-170 (1964).

[184] P.A. Zyla *et al.* Particle Data Group - Review of Particle Physics - *Prog.Theor.Exp.Phys.* **2020** 8, 083C01.

Legal Remarks

This print version contains minor changes, not relevant in terms of content, compared to the version submitted to the doctoral office.